Microfluidic microwave resonant sensors

David James Rowe

A thesis submitted to Cardiff University
for the degree of Doctor of Philosophy

June 2012

Declaration

This work has not previously been accepted in substance for any degree and is not concurrently submitted in candidature for any degree.

Signed…… (candidate) Date……

Statement 1

This thesis is being submitted in part fulfilment of the requirements for the degree of PhD.

Signed…… (candidate) Date……

Statement 2

The work present in this thesis is all my own and carried out under the supervision of Prof. Adrian Porch, Prof. David Barrow and Dr. Chris Allender except the experimental data in chapter 5, which were collected by Mr. Sultan al-Malki at Cardiff University. Other sources are acknowledged by explicit references.

Signed…… (candidate) Date……

Statement 3

I hereby give consent for my thesis, if accepted, to be available for photocopying and for inter-library loan, and for the title and summary to be made available to outside organisations.

Signed…… (candidate) Date……

ACKNOWLEDGEMENTS

The work presented in this thesis would not have been possible without the assistance of many people. I am deeply indebted to my supervisors Prof. Adrian Porch, Prof. David Barrow and Dr. Chris Allender, and their collective willingness to allow my research to roam between different disciplines. Prof. Porch's vast knowledge and understanding have been invaluable over the past three years. I am particularly grateful for his patience in helping me relate my observations to underlying physical principles. Moreover, his intuition and approach to teaching have inspired me to continue in academia. Prof. Barrow has not only given excellent guidance on all aspects of my work, but kept me focussed and been a constant source of motivation. His attitude has been instrumental in my academic development. Dr. Allender has provided essential experimental advice and has been a constant font of ideas. His fresh perspective and propensity for asking 'why?' have made me far more well-rounded as a researcher than I could have otherwise hoped for. Additionally, my thanks go to Mr. Sultan al-Malki, who collected the experimental data of chapter 5 as part of his BEng project.

Many thanks go out to my friends and colleagues for their patience and support over the years: to Dan Slocombe, Jack Naylon, Nelo Dehghan and Alex Morgan for being an absolute pleasure to work with, and to Amy McLaughlin, James Parker, Rob Smith, Oliver Burrows and many other long-suffering friends who have always been there when a beer was required. I would like to thank my parents, Sue and Nick, and siblings, Lucy and Josh, for their continuous love and encouragement. Finally, I owe a special thanks to my partner Laura Dundas for being quite simply brilliant throughout.

ABSTRACT

Matter can be identified by its interaction with electromagnetic fields. This can be described by its dielectric and magnetic properties, which typically vary with respect to frequency in the microwave region. Microwave-frequency spectroscopy is capable of making non-contact, non-destructive, non-invasive and label-free measurements with respect to time. It can be used to characterise all states of matter and combinations thereof, such as colloids and microparticulate suspensions. Sensors based upon this technology therefore have great potential for (bio)chemical and industrial point-of-sampling applications where existing measurement techniques are insufficiently portable, low-cost or sensitive. Microfluidics is the manipulation of fluids within microscale geometries. This gives rise to phenomena not observed at the macroscale that can be exploited to achieve enhanced control of fluid flow. This means that microfluidic techniques can be used to perform complex chemistry in a completely sealed environment with minimal reagent consumption. Hence, microfluidics offers an ideal sample interfacing method for a microwave-frequency sensor. This work is concerned with developing novel, low-cost and highly sensitive probes that be easily integrated into a microfluidic device for performing on-chip sample preparation and diagnostics for generic (bio)chemical and industrial point-of-sampling applications. To this end, several novel microwave resonant structures were designed, optimised and integrated into microfluidic devices in order to characterise a variety of liquid-phase samples.

Table of contents

1. INTRODUCTION

Electrically charged particles will experience a force when placed in an electric field [1]. Any material will therefore interact with an applied electric field due to a subatomic structure comprised, at least in part, of electrically charged particles. Although there are several mechanisms by which such action can occur, the net result is usually identical: depolarisation. The applied electric field distorts the molecular charge distribution of the material, inducing an opposing (depolarising) electric field that reduces the applied field within the material [2]. Permittivity is the factor by which the external field is reduced.

Charge redistribution is an inherently dynamic situation that depends on factors such as dipole moment, size and molecular mass. One can imagine how the same depolarisation mechanism (e.g. distortion of the electron cloud) may occur at different speeds for different molecules. Similarly, different depolarisation mechanisms (e.g. electron cloud distortion versus dipolar reorientation) may occur at different speeds when acting upon the same molecule [2]. If the applied electric field is alternating, it follows that the induced depolarisation will depend upon its frequency.

Since the movement of electric charge within an electric field implies there is work done, the redistribution of charge is a dissipative process. This gives rise to a lag between the applied polarising electric field and the induced depolarising electric field. Permittivity is complex-valued to account for the phase difference between

the applied and induced fields [3], [4]. From this simple physical description, the real component of permittivity quantifies polarisability, or how effectively a material can reduce electric field, and the imaginary component quantifies power dissipation associated with lossy depolarisation mechanisms.

1.1. Dielectric spectroscopy

Dielectric spectroscopy is the measurement of complex permittivity with respect to frequency. It is a method unaffected by the state of matter of the material under test, and has been demonstrated for solids [5], liquids [6] and gases [7]. The sample must occupy a region of electric field, but the propagation of electromagnetic radiation means the sample does not necessarily have to be in contact with electrodes or a waveguide. Importantly, the interaction between the applied electric field and the material under test is virtually instantaneous. The frequency with which measurements can be taken is a function of how fast data can be read with current instrumentation rather than the speed of the depolarisation mechanisms [8].

Dielectric spectroscopy is therefore capable of making non-contact, non-destructive, non-invasive and label-free measurements in real-time and with respect to time. In the case of liquids and particulate suspensions [9], dielectric spectroscopy is unaffected by matrix opacity. Such advantages contrast with more ubiquitous spectroscopy techniques, but have not necessarily been realised in one device.

1.2. Microfluidics

Microfluidics is concerned with the manipulation of fluids confined within microscale structures [10]. The simplest such structure - a channel – will typically have cross-sectional dimensions in the order of microns, although its length may be much longer. Such confinement causes the proportional contributions of various forces to fluid behaviour to change in comparison to the macroscale situation, leading to otherwise unobtainable fluid behaviour. The most notable effect is probably the increasing dominance of viscous forces. This allows laminar

(non-turbulent) flow, which in turn allows many of the subsequent fluid manipulation capabilities.

1.3. Context

The properties and potential advantages of dielectric spectroscopy are hugely enabling. To date, however, dielectric spectroscopy has remained something of a specialised technique owing to the difficulty of interfacing liquid samples in a high-throughput, robust and repeatable manner. There have been some efforts to incorporate microfluidic techniques for an improved method of sample interfacing [9], [11–20], but these have encountered various drawbacks in terms of both microfluidics and microwave design. The overriding objective of this project is to better exploit the potential advantages of dielectric spectroscopy with a holistic approach incorporating microwave engineering, microfluidics, and biochemistry influences.

The presented devices are applicable to solid or gaseous samples, but the concern of this work is primarily with liquid-phase systems for biochemical and pharmaceutical applications. Solid-phase experiments (e.g. *in vivo* human tissue characterisation) are equally feasible, but are only discussed with regards to future opportunities.

1.4. Aims and objectives

1.4.1. Aim

The aim of this project is to develop microwave-frequency measurement techniques that can be integrated directly into a widely compatible 'lab-on-a-chip' device for performing on-chip sample preparation and diagnostics for generic (bio)chemical and industrial point-of-sampling applications.

1.4.2. Objectives

- Identification of a suitable sensing technology for low cost, highly sensitive, point-of-sampling characterisation of liquid and microparticulate suspension samples.

- Development of robust, low cost and easy to fabricate sensor geometries.
- Optimisation of the sensor geometries for maximum sensitivity.
- Identification, development and optimisation of a sensor for simultaneous dielectric and magnetic characterisation of liquid-phase samples.
- Identification of suitable microfluidic interfaces for the sensing structures.
- Characterisation of liquid and microparticulate suspension samples with the developed sensors.
- Characterisation of liquid-phase chemical processes with respect to time.
- Proof-of-principle demonstration of the deconvolution of the electric and magnetic properties of a liquid-phase sample.
- Development of a suitable user interface to allow a non-expert user to operate the sensors.
- Proposition of further enhancements to the developed sensors.

1.5. Original contributions

There are five novel aspects to this work, which are briefly described in subsections 1.5.1 to 1.5.5.

1.5.1. Evanescently-perturbed coaxial resonator

First, there are two main ways for obtaining permittivity spectra: broadband methods and resonant methods. A broadband device measures a continuous permittivity spectrum, whereas a resonant technique measures permittivity at a single frequency with greatly improved accuracy and sensitivity [21], [22]. An overmoded coaxial resonator capable of taking permittivity measurements at numerous discrete frequencies has been demonstrated for the first time. This technique can obtain frequency dependence information (akin to a broadband technique) with the improved accuracy of a resonant technique. This structure was based upon an optimised coupling structure for performing transmission measurements from a single end of a half-wavelength coaxial resonator.

1.5.2. Resonant sensor microfluidic interface

Second, the evanescently-perturbed coaxial resonator has been embedded in a compression-sealed polytetrafluoroethylene (PTFE) microfluidic device. Based upon measurements of a serial dilution of acetonitrile in toluene, we have demonstrated a limit of detection and resolution orders of magnitude greater than other attempts to integrate dielectric spectroscopy techniques into microfluidic systems. Other microfluidic functionalities have also been demonstrated. These include mixing and the generation of segmented flow for continuous liquid-phase molecular extraction.

1.5.3. Graphical user interface

The third novel aspect of this work is the graphical user interface that (a) vastly simplifies the measurement procedure to make it suitable for a non-expert user, and (b) allows permittivity spectra to be measured with respect to time. This is a powerful technique with many further applications. It has been demonstrated for the *in situ* quantification of non-specific binding events as a dissolved species is extracted by a suspended phase. A further anticipated application of this technique is to monitor molecularly imprinted polymer binding events without the need for fluorescent labelling or the sieving process required to assess the quantity of bound target via HPLC.

1.5.4. Capillary-perturbed coaxial resonator

Fourth, the resonant coaxial sensor was modified to allow electric and magnetic field effects to be measured simultaneously but in isolation from each other. Virtually all current resonator techniques do not separate electric and magnetic properties, but rely on the assumption that the two behave independently. This is not valid, as one may expect from Faraday's law of induction. This device was used to measure various salt solutions, which interact with both electric and magnetic fields via different mechanisms. This method also allowed different cations and different anions to be distinguished. Further applications include the *in situ* monitoring of functionalised magnetic nanoparticle binding events.

1.5.5. Improved split-ring resonator

Fifth, a modified split ring resonator formed from square cross-section silver wire was also developed as an extremely simple structure for enhanced dielectric sensing. Owing to its inductive coupling, it is also suitable for simultaneously heating and sensing. When integrated into a microfluidic platform, its miniaturisable electronics mean it has great potential as a portable, handheld device.

1.6. Thesis overview

The usual ordering of chapters did not seem entirely appropriate because this work details the development of several measurement techniques, each requiring its own methods, results and discussion. Therefore, Chapters 3 through 5 each describe an individual measurement technique, where all have self-contained methods, results and discussion sections. Chapter 3 charts the development of a novel coupling structure that allowed transmission measurements to be taken from one end of an open-ended half-wavelength coaxial resonator. This coupling allowed the evanescent field at the other end of the resonator to be perturbed at multiple frequencies and in various ways; most notably, with a compression-sealed PTFE microfluidic device. Chapter 4 also discusses a coaxial resonator, but one perturbed in a different fashion. A sample-filled microfluidic capillary was passed through the centre of the resonator in holes drilled perpendicularly to the conductor axes. This method of coupling allowed electric and magnetic field effects to be measured simultaneously but independently at multiple frequencies. Chapter 5 presents the design of a modified split-ring resonator, which increased field confinement and thereby sensitivity. Although measurements could only be performed at a single frequency, such geometry was extremely simple and well suited to selectively heating a sample at the same time as characterising it. A general discussion of the three techniques follows in Chapter 6, which forms comparative arguments from which the conclusions and suggestions of future work of Chapter 7 are drawn.

1.7. Publications

The following articles have been published throughout the course of this work:

1.7.1. Journal publications

D. J. Rowe, A. Porch, D. A. Barrow, and C. J. Allender, "Microfluidic microwave sensor for simultaneous dielectric and magnetic characterisation," *IEEE Transactions on Microwave Theory and Techniques*, accepted for publication.

D. J. Rowe, A. Porch, D. A. Barrow, and C. J. Allender, "Microfluidic device for compositional analysis of solvent systems at microwave frequencies," *Sensors and Actuators B: Chemical*, vol. 169, pp. 213-221, 2012.

D. J. Rowe, A. Porch, D. A. Barrow, and C. J. Allender, "Novel coupling structure for the resonant coaxial probe," *IEEE Transactions on Microwave Theory and Techniques*, vol. 60, no. 6, pp. 1699-1708, 2012.

1.7.2. Conference publications

D. J. Rowe*, A. Porch, D. A. Barrow, and C. J. Allender, "Dielectric analysis of microfluidic systems with an integrated microwave resonant device," in *Proc. EuMC 2011*, 2011, pp. 607-10 *[* presenter, oral]*.

D. J. Rowe*, A. Porch, D. A. Barrow, and C. J. Allender, "Non-contact label-free dielectric spectroscopy of single- and multi-phase microfluidic systems," in *Proc. MicroTAS 2011*, Seattle, 2011, pp. 891-3 *[* presenter, poster]*.

D. J. Rowe*, A. Porch, D. A. Barrow, and C. J. Allender, "Integrated microwave resonant device for dielectric analysis of microfluidic systems," *Journal of Physics: Conference Series*, vol. 310, 012004, Aug. 2011 *[* presenter, oral]*.

D. J. Rowe*, J. Naylon, A. Porch, D. A. Barrow, and C. J. Allender, "Microwave resonant sensor for real-time continuous-flow measurements of microfluidic systems," in *Proc. MicroTAS 2010*, Groningen, 2010, pp. 1004-6 *[* presenter, poster]*

2. THEORY AND LITERATURE

2.1. Spectroscopic methods

The *Handbook of Spectroscopy* provides a general definition of spectroscopy as 'the science that deals with interactions between electromagnetic radiation and matter' [23]. A spectroscopic technique is one that uses knowledge of such interactions to infer knowledge of material properties from observed changes in the spectra of an irradiated material. There are an uncountable number of ways of achieving such a feat, but most methods fall into several main categories. In order for the microwave-frequency techniques of this thesis to have any value, they must be placed in context with alternative methods.

An aim of this work is to develop highly sensitive measurement techniques for a non-expert user to generate useful, usable information. A generic diagnostic device should be capable of operating in a wide range of environments where samples cannot readily be shipped to a laboratory for further assessment: at a hospital bedside, at a crime scene, in a food processing plant, or at an exploratory oil well, for example. These can be described as point-of-sampling applications. In these instances, predetermined knowledge of the material under test cannot be assumed, so a generic diagnostic device must be able to operate blindly. This could be imagined as a biochemical alternative to the multimeter. The spectroscopic methods under discussion shall be evaluated in relation to this aim. It is obvious that with any spectroscopic technique, sensitivity (i.e. the minimum measurable

change of a measurand) is of secondary importance if a rigorous measurement cannot be performed under the required conditions.

Spectroscopic methods can be subdivided in various ways, according to the frequency of operation, the mechanism of interaction between electromagnetic radiation and matter, and the type of matter being interrogated. For the purposes of comparing them with microwave-frequency techniques, the following principal categories of spectroscopy shall be considered in subsections 2.1.1 through 2.1.6: absorption, emission, scattering, impedance, nuclear magnetic resonance (NMR) and mass spectrometry (MS).

Before detailed considerations of each technique, it is useful to qualitatively compare them in terms of cost, size, sampling rate and sensitivity. This was performed by comparing available data from the websites of various instrumentation manufacturers to loosely define each parameter. For example, typical instrument sizes could be defined as either miniaturised, handheld, benchtop or room sized. Figure 2.1 shows (a) cost versus size and (b) sampling rate versus sensitivity per unit sample volume.

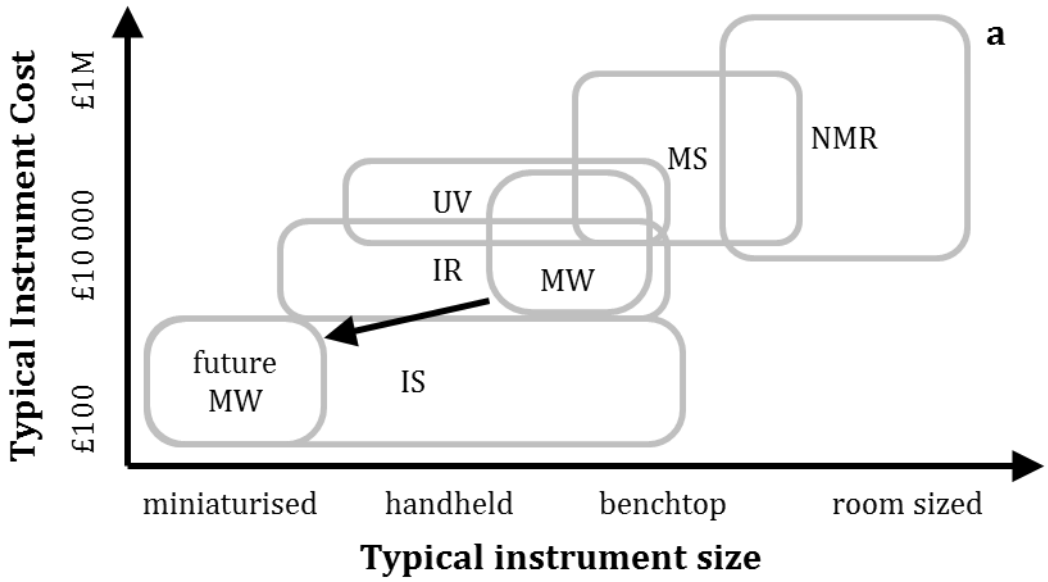

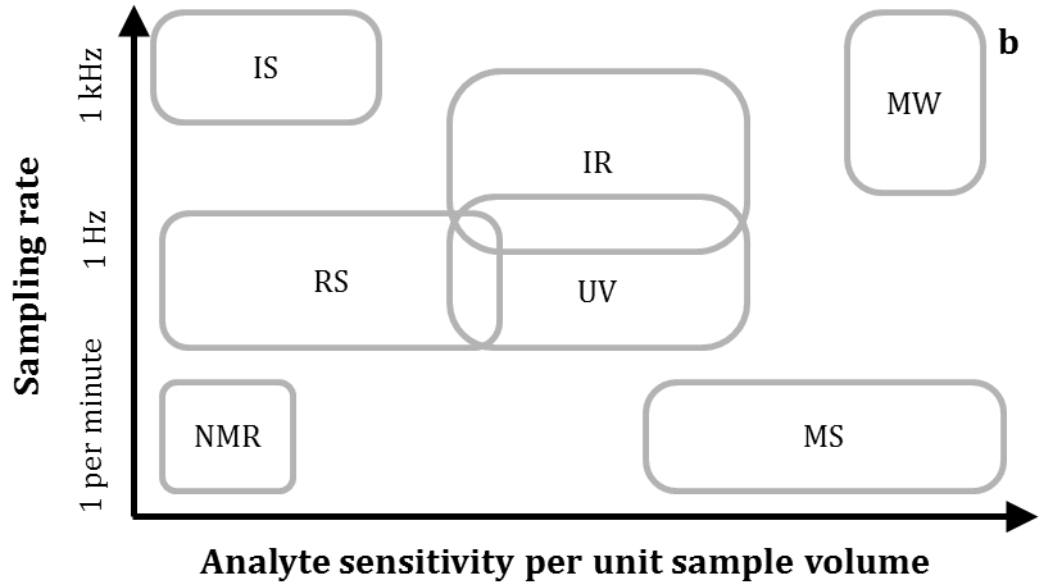

*Figure 2.1: Comparisons of typical instrument parameters for the following spectroscopies: mass spectroscopy (MS), nuclear magnetic resonance (NMR), Raman scattering (RS), ultraviolet absorption (UV), infrared absorption (IR), microwave-frequency resonators (MW) and impedance spectroscopy (IS). (***a***) shows a qualitative comparison of cost versus size, where future microwave techniques currently under development at Cardiff University are also shown. (***b***) shows sampling rate versus sensitivity per unit sample volume, where sampling rate is the number of measurements that can be performed per second. Note that sensitivity is evaluated with respect to an analyte suitable for detection with that particular spectroscopy. Also note that 'impedance spectroscopy' represents low frequency techniques but not microwave frequency techniques, which are labelled separately.*

Other current research efforts at Cardiff University include the miniaturisation of microwave-frequency spectroscopy instrumentation. Note that smaller and cheaper instrumentation is already available for such measurements, but these lack the precision of vector network analyser-based implementations. It is *high precision* microwave instrumentation that current research is seeking to miniaturise.

2.1.1. Absorption spectroscopy

Absorption spectroscopy refers to a class of techniques that use wavelength-dependent energy absorption to identify a sample under test. When a known

source of radiation is focussed upon a sample, radiation intensity will reduce at certain wavelengths that have energies corresponding to the bandgap of the sample. Such measurements can be taken across the entire electromagnetic spectrum, but are most commonly encountered at ultraviolet-visible (UV-VIS) and infrared (IR) wavelengths.

The energy of a photon (*E)* is related to the frequency of its associated electromagnetic wave (v) according to the wave-particle duality, and can be described by the Planck relation:

$$E = hv, \tag{2.1}$$

where h is Planck's constant. This is usually rewritten in terms of wavenumber (k), the reciprocal of wavelength (λ), according to:

$$k = \frac{1}{\lambda} = \frac{v}{c}, \tag{2.2}$$

where c is the vacuum speed of light. Wavenumber is commonly quoted in units of cm^{-1}. Depending on the application, frequency may be scaled by 2π to give angular frequency in units of rad s^{-1} and wavenumber in units of rad m^{-1}.

Within a molecular structure, charge carriers in the ground state can transition to an excited state if sufficient energy is transferred to the system. These transitions could, for example, be electronic, rotational or vibrational. Consider a sample irradiated with electromagnetic radiation. If the wavenumber of incident radiation is such that its energy corresponds to a particular transition within the sample under test, the radiation will be absorbed and the transition would occur. This situation is illustrated in Figure 2.2. The transmitted intensity of the sensing radiation will decrease at this particular wavenumber. It is therefore possible to identify molecules by plotting transmittance with respect to wavenumber, where transition-specific absorptions will be characteristic to particular molecules.

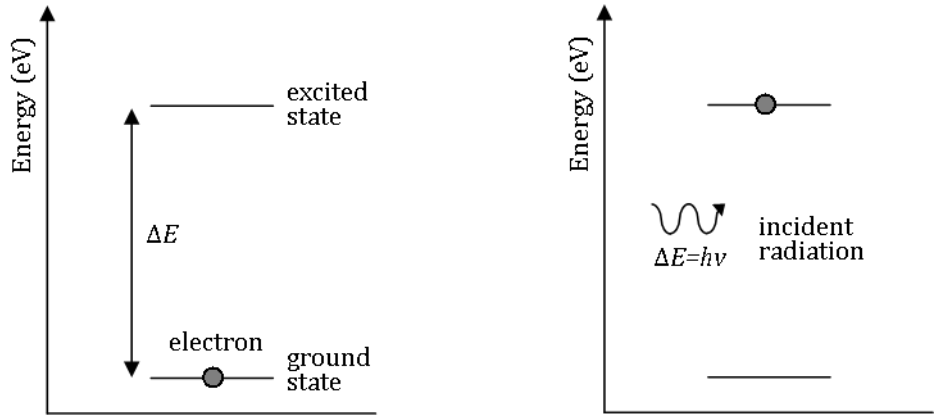

Figure 2.2: Energy diagram showing electron excitation from a ground state to an excited state from photon absorption. This occurs when the frequency of incident radiation is such that photon energy hν corresponds to the transition energy ΔE.

Absorption spectroscopy remains an extremely popular technique in analytical chemistry. The absorption of radiation at a particular wavelength corresponds to an excitation of a particular energy transition. For example, infrared absorption usually corresponds to vibrations of bound atoms, which cause deformations in the length and angle of bonds between atoms. The (mid-)infrared region is taken as wavenumbers in the region of 400 – 4000 cm^{-1}, where the near- and far-infrared regions exist above and below this range, respectively. The absorption of organic compounds will typically occur at wavenumbers in the region of 1500 – 4000 cm^{-1}, although absorptions do exist down to 500 cm^{-1}; the heavier atoms found in inorganic compounds give rise to absorptions at significantly lower wavenumbers.

Ultraviolet and visible wavelength absorptions have contributions from both electronic and vibrational transitions. For example, carbon-carbon bonds demonstrate peak absorption at a wavelength of approximately 200 nm, where the peak may shift with respect to wavelength due to the presence of other chemical groups. UV-VIS techniques are commonly used with respect to time in conjunction with liquid chromatography methods. Chromatographic methods act to separate liquid mixtures by exploiting differences in propagation velocities through a stationary phase. The UV-VIS spectroscopy data allows the identification and quantification of each analyte as it separates according to its retention time.

There are significant obstacles to implementing absorption spectroscopy techniques outside of the laboratory. Perhaps most importantly, liquid-phase measurements cannot be performed if a solid-phase suspension is present due to scattering of the excitation radiation. This necessitates the extraction and purification of the sample, which is often a skilled procedure requiring knowledge of the sample itself. Absorption spectroscopy is therefore not generally suitable for a generic 'point-of-sampling' diagnostic device.

A notable exception to the problem of scattering has been demonstrated by a method for the diagnosis of HIV [24] and of HIV and syphilis [25], which performed an immunoassay by exploiting the opacity of a silver film to infer analyte concentration. Disease-specific antigens were used to immobilise pathogens at different detection regions. Flows of gold nanoparticle-conjugated antibodies and silver reagents resulted in the formation of a silver film in the presence of the pathogen. The opacity of the film was a function of its thickness, which in turn was shown to be a function of the immobilised antibody concentration. Concentration could therefore be inferred from changes in absorption as measured by a laser diode and optical detector. Separating antigens into different detection regions allowed simultaneous screening of multiple pathogens. This method demonstrated a unique way of obtaining quantitative data from absorption measurements. It is good example of how microfluidics can aid analytical procedures (as discussed in Section 2.4.3), but also illustrates how a functionalised detection technique (which is inherently single use) cannot be used for any other purpose. This enforces the point that absorption spectroscopy is not suitable for a generic point-of-sampling diagnostic device.

2.1.2. Emission spectroscopy

Photons can be emitted upon the relaxation of an excited state to the ground state, or possibly to a less energetic excited state. This provides an alternative spectroscopic method: emission spectroscopy. The initial excitation can occur due to thermal or electromagnetic effects; the spectrum of spontaneous emission due to thermal excitation at any nonzero temperature is referred to as the blackbody spectrum.

Fluorescence spectroscopy is the particular case of emission spectroscopy where states are excited with electromagnetic radiation (in a fashion similar to absorption spectroscopy) before relaxing to less energetic excited states before the ground electronic state via smaller intermediary transitions. It is obvious from Equations 2.1 and 2.2 that smaller transitions will result in the emission of longer wavelength radiation. The observed spectra will therefore be in a different region of the electromagnetic spectrum (e.g. visible) compared to the excitation radiation (e.g. UV). However, many materials do not naturally fluoresce. In biological and biochemical applications, therefore, this technique is commonly used in conjunction with fluorescent markers, or fluorophores. For example, it is possible to add single fluorescent molecules to individual DNA fragments or to individual RNA [26]. Target concentration can then be quantified by the intensity of the fluorescence due to the marker.

This not only requires predetermined knowledge of the system, but could alter the chemistry of the liquid system being interrogated. The requirements for knowledge of the system, for target-specific biomarkers and for pure samples with no solid suspension, mean that emission spectroscopy methods are also unsuitable for a generic point-of-sampling diagnostic device.

2.1.3. Scattering spectroscopy

There are two main phenomena that are exploited in scattering spectroscopy: Rayleigh scattering and Raman scattering. Both cause the angle and polarisation of incident radiation to vary; they are distinguished by whether the wavelength of scattered radiation changes. The elastic process, where wavelength does not change because energy has been conserved, is Rayleigh scattering. The inelastic process, where wavelength changes because the scattered radiation is of a different energy to the incident radiation, is Raman scattering. In Rayleigh scattering, the excitation and relaxation transitions are the same, albeit in difference directions. Raman scattering occurs when the excitation and relaxation transitions are of different magnitude. The different frequencies that occur as a consequence of Raman scattering (referred to as Raman bands) collectively form a Raman spectrum.

There are many different subsets of both types (differentiated, for example, by whether Raman bands are at longer or shorter wavelengths than that of the incident radiation), but several generalisations apply to all. Perhaps most significantly, the nature of the sensing mechanism means it is unsuitable for inhomogeneous samples. The entirety of *The Raman Effect* (to which the reader is referred for a comprehensive treatment of the various types of scattering and their associated spectroscopies [27]) is restricted to situations where 'monochromatic radiation… is incident on systems such as dustfree, transparent gases and liquids, or optically perfect, transparent solids, [so that] most of it is transmitted without change but, in addition, some scattering of the radiation occurs' [27]. This necessitates a requirement for very high sample purity that is not readily achievable in the field: a device incorporating scattering spectroscopy would not be practical for the quantitative characterisation of contaminants in an industrial process, for example. The above quote also implies that only a small fraction of the incident radiation will scatter by either the Raman or Rayleigh mechanism. The measureable intensity of such phenomena will be of significantly lower magnitude than absorption phenomena, for example, so scattering spectroscopies consequently require far more sensitive instrumentation (*cf.* Figure 2.1). This is another prohibitive factor when considering portable spectroscopic techniques for low-cost, point-of-sampling applications.

2.1.4. Impedance spectroscopy

Impedance spectroscopy methods are concerned with how materials reduce electric field. They can also be used for the equivalent quantification of magnetic field interactions (magnetisation), although such methods are far less common. A possible reason for this is that magnetic measurements are inherently less widely useful than electric field measurements since all matter exhibits nonzero electric susceptibility but a most matter has far smaller magnetic susceptibility.

How a reduction in electric field is quantified typically relies on the frequency region of interest: as impedance or conductivity at low frequencies (10^{-4} – 10^{6} Hz); as permittivity at radio, microwave and terahertz frequencies (10^{6} – 10^{13} Hz) and as refractive index at optical frequencies and beyond (>10^{13} Hz). These are not

truly independent spectroscopic techniques because each of these quantities can be calculated from the others according to [28]:

$$\tilde{n} = c\sqrt{\mu\varepsilon}, \tag{2.3}$$

where $\tilde{n}$ is complex refractive index, permeability $\mu = \mu_0\tilde{\mu}$ and permittivity $\varepsilon = \varepsilon_0\tilde{\varepsilon}$. $\tilde{\mu}$ is complex relative permeability and $\tilde{\varepsilon}$ is complex relative permittivity. Both of these quantities vary with frequency. Permittivity is also a function of conductivity, as explained in the following paragraphs. μ_0 is vacuum permeability, ε_0 is vacuum permittivity, $j = \sqrt{-1}$ and vacuum speed of light $c = (\varepsilon_0\mu_0)^{-1/2}$.

It is convenient to talk about impedance spectroscopy methods in terms of complex permittivity since it is a meaningful quantity over all frequencies; refractive index is conventionally used at IR to UV frequencies and conductivity at low frequencies because there is no conductivity contribution above the low GHz region. Impedance spectroscopy is usually referred to as dielectric spectroscopy when used to determine complex permittivity.

Complex permittivity can be expressed as:

$$\tilde{\varepsilon} = \varepsilon_1 - j\left(\varepsilon_2 + \frac{\sigma}{\omega}\right). \tag{2.4}$$

ε_1 is a measure of polarisability, or how much an applied electric field is reduced by the depolarisations it induces with a material; ε_2 is a measure of dielectric loss, and arises as a consequence of the induced polarisation lagging behind the applied electric field. ω is angular frequency. For a lossy material (i.e. one that is imperfectly insulating), the imaginary component of permittivity also varies as a function of conductivity. For highly conducting media, one occasionally sees the definition $\varepsilon_2 = \sigma/\omega$. For the purposes of this work, it is useful to distinguish between conducting and non-conducting loss mechanisms, so the definition of complex permittivity according to Equation 2.4 will be used throughout. A detailed study of the origins and implications of ε_1 and ε_2 can be found in Section 2.2.1. For the purposes of comparing dielectric spectroscopy with other measurement techniques, it is sufficient to say that these quantities exhibit

frequency dependencies according to the dynamics of the various polarisation mechanisms that can contribute to complex permittivity.

The polarisation mechanisms that contribute to complex permittivity are, in ascending order of their speed of response to a polarising electric field: ionic, dipolar, atomic and electronic. Their contributions to the real component of permittivity are shown in Figure 2.3.

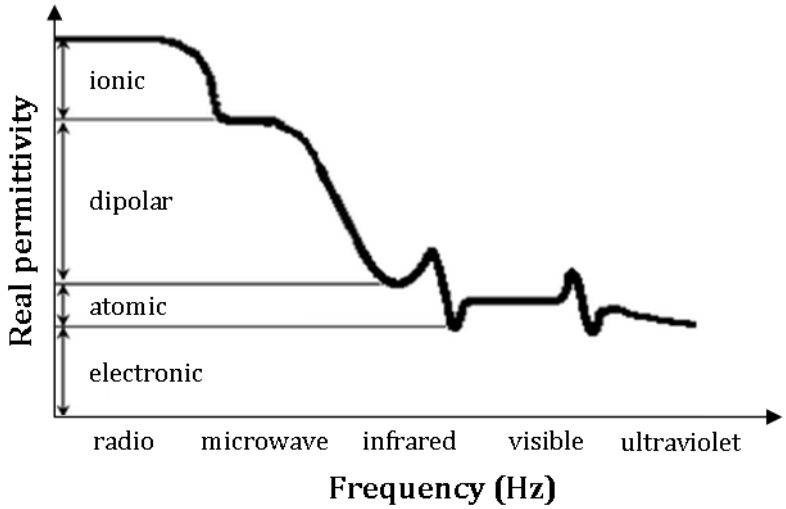

Figure 2.3: The contribution of various polarisation mechanisms to the real component of permittivity with respect to frequency (adapted from [29]). Approximate frequency regions are also labelled.

Each mechanism will lag behind the polarising field to a greater or lesser extent because of some small but finite inertia associated with the displacement of electric charges. At low frequencies, all of these mechanisms will contribute to permittivity. That is, polarisation will occur via all mechanisms so the reduction in applied electric field is maximised. As the frequency of the polarising electric field increases, the lag associated with ionic polarisation becomes sufficiently large that the ions can no longer redistribute throughout the material under test, so the permittivity contribution of that particular mechanism falls away. In the microwave region, the lag associated with the reorientation of electric dipoles becomes large enough that its permittivity contribution also reduces. Similar effects happen for atomic and electronic polarisation distortions at infrared and ultraviolet frequencies, respectively. A more detailed description of the concepts of polarisation and permittivity can be found in Section 2.2.1.

Ionic polarisations dominate the low frequency impedance spectroscopy response and so commonly find usage in electrochemical applications, where the ionic behaviour at the electrode-electrolyte interface is of interest [30].

2.1.5. NMR spectroscopy

Protons and neutrons are (composite) fermions and therefore exhibit spin. A nucleus is comprised of protons and neutrons and thus will have an overall spin; a quantised value described by the spin quantum number I. Generally, when a nucleus has even numbers of protons and neutrons, $I = 0$. If there are an odd number of protons or neutrons, as found in many isotopes, then $I \neq 0$. Since a nonzero spin implies an angular momentum, there will be a magnetic moment associated with moving charges. If the nucleic spins are aligned with a static magnetic field and then subjected to a MHz-frequency pulse, properties of the nucleus can be inferred from the frequency of absorption, which corresponds to the precession frequency of the nucleus under test. Such information is inferred from the fact that, in aligning with the static field, the spin will precess about the direction of the applied field; the precession frequency (termed the Larmor frequency) is isotope-specific and typically in the radiofrequency region. The nuclear magnetic resonance that the method is named for is the radiation absorption that occurs when the nucleus is subject to a pulse at the Larmor frequency. The Larmor frequency is affected by a vast number of other parameters, including the spins of other nuclei in close proximity. In one sense, the difficulty of deconvolving such a complex system could be prohibitive, but in another sense the level of detail obtainable makes NMR an attractive prospect.

The two most common NMR-active isotopes used in NMR spectroscopy are ^{1}H and ^{13}C. The former is somewhat simpler as ^{1}H is the major isotope of hydrogen whereas ^{12}C is the major isotope of carbon, but ^{13}C-NMR still finds widespread use in organic chemistry applications. NMR spectroscopy can also be divided into solution and solid-state (in the physics rather than the electronics sense of the phrase) techniques. The principle of detection remains the same for both: each isotope has a clearly defined resonance (in the order of MHz) that will shift by a specific amount (in the order of 100 Hz) in relation to a standard (such as

tetramethylsilane) depending on the presence of other chemical groups. Note that ^{13}C-NMR shifts are typically ten times greater than ^{1}H shifts. The nuclear magnetic resonance frequencies of some common isotopes in a static magnetic field of 9.4 T are given in Table 2.1 [31].

Table 2.1: Nuclear magnetic resonance frequencies, v, of some common isotopes for a magnetic flux density of 9.4 T.

Isotope	^{1}H	^{2}H	^{13}C	^{19}F	^{31}P
v (MHz)	400.0	61.4	100.6	376.5	162.1

NMR spectroscopy is not affected by radiation scattering or sample opacity in the same fashion as absorption and emission spectroscopies. It does, however, remain a prohibitively expensive method. One contributing factor is the need for very uniform and large magnetic fields (9.4 T is typical), required because signal-to-noise ratio is a function of field strength [32]. A recent study of various spectroscopic techniques for characterising suspensions in microfluidic devices concluded that NMR was most realistically suitable prospect given the amount of useful data that could be obtained, despite the cost [33]. The cost and requirement for NMR-active isotopes are incommensurate with the aims and motivation of this project.

2.1.6. Mass spectrometry (MS)

Mass spectrometry differentiates between free gaseous ions according to their mass/charge ratio, which is determined by how their motion in vacuum is affected by electromagnetic fields. There are various methods of implementing this approach, but all operate on the same principle. The Lorentz force equation for the force **F** experienced by a particle of charge Q and velocity **v** in electric field **E** and magnetic flux density **B** is:

$$\mathbf{F} = Q(\mathbf{E} + \mathbf{v} \times \mathbf{B}). \qquad 2.5$$

Newton's second law for the force **F** experienced by a mass m undergoing acceleration **a** is:

$$\mathbf{F} = m\mathbf{a}. \qquad 2.6$$

It is obvious from Equations 2.5 and 2.6 that the acceleration force experienced by an ion due to electric and magnetic fields is dependent on both mass and charge. Note that this acceleration is a vector so it also has an associated direction. Equations 2.5 and 2.6 can be set equal to each other to obtain:

$$\frac{m}{Q}\mathbf{a} = \mathbf{E} + \mathbf{v} \times \mathbf{B}. \qquad 2.7$$

Typically, electric and magnetic fields are used to redirect an ion beam so that it impacts upon a detector. Varying field strength will therefore alter which ions are directed at the detector depending on their mass/charge ratio, meaning the ratio can be inferred from knowledge of field strength variation.

Many of the experimental difficulties encountered in mass spectrometry are because the sample must be gaseous and ionised. To ionise a sample and transfer it to the gas-phase non-destructively is particularly difficult for labile biomolecules. The development of new ionisation techniques in recent years have gone some way to alleviating these problems. 'Soft' ionisation techniques do not result in the fragmentation of the sample molecules, which is of critical importance for the ability to characterise complex biomolecules and for retaining their functionality. Electrospray ionisation and laser desorption are two examples of such techniques. The developers of these techniques (John Fenn and Koichi Tanaka, respectively) shared half of the Nobel Prize in Chemistry in 2002 for their contributions to mass spectrometry. However, the measurement process requires extensive sample preparation, much of which will be specific to the material under test. This means mass spectrometry is unsuitable for generic, point-of-sampling applications, despite the high sensitivity and resolution. This argument is amply illustrated in the qualitative cost versus size and sampling rate versus sensitivity comparisons shown in Figure 2.1.

2.2. Microwave-frequency spectroscopy

This thesis concentrates on microwave-frequency impedance measurements. The majority of this work is concerned with dielectric characterisation, although magnetic characterisation will also be considered. This section of the literature

review begins with a discussion of the concepts of permittivity and permeability (Section 2.2.1) before a treatment of existing dielectric and magnetic measurement techniques (Sections 2.2.2 through 2.2.5). Measurement techniques that incorporate microfluidic sample interfaces are discussed in Section 2.5 after the principles of microfluidics are introduced in Section 2.4.

Dielectric spectroscopy has been demonstrated to be an extremely useful metrological technique for various applications in industry and throughout the biological, chemical and pharmaceutical sciences [12], [34–38]. However, the majority of recently developed techniques utilise bulk measurements without considering the method of sample interfacing in great detail. This is understandable given that, for the purposes of research, a measurement technique can be demonstrated without characterising a vast number of samples. However, it seems that many engineers underestimate the sheer number of measurements that must be taken in the fields of research where their technique is purportedly useful. In these situations, manually filling a waveguide with tens of millilitres of solution is not practical. Ignoring the need for a high throughput and low-volume sample interface required by modern liquid-phase science could be a reason why dielectric spectroscopy techniques are not more widely used. These techniques have great potential given the available information and possibility of non-destructive, non-invasive, non-contact and label-free measurements of multi-phase liquid systems [12], [34], [37], [39–41]. These measurements are also unaffected by matrix opacity, which is a key shortcoming in optical spectroscopy techniques. However, existing dielectric spectroscopy setups remain impractical and prone to experimental error and have been unable to establish themselves as standard laboratory tools.

Microwave-frequency measurements (around 1 GHz and upwards, i.e. cm-scale wavelengths) are ideal for characterizing solvent systems because it is within this region that many dipolar molecular relaxations can be observed. At these frequencies, complex permittivity is dominated by electric dipole interactions with an applied electric field, meaning ionic and electronic effects can be discounted. This is of particular significance with respect to lower frequency measurement techniques, where electrode polarisation effects are particularly problematic [42].

The effects of dissolved species upon such dipolar relaxations can also be quantified through microwave-frequency measurements, as demonstrated for a variety of mixtures [41], [43–46].

It should be noted that dielectric spectroscopy can theoretically be used to directly distinguish between any molecules with differing charge distribution. One exception to this is with enantiomers, where the chirality of two molecules means they will not be distinguishable using sinusoidal electromagnetic fields. This is discussed in more detail in Section 2.6.1, where a method for indirectly identifying the chirality of a molecule based upon its biological function is also considered.

2.2.1. Measurands, defined

Given that this work is based upon measurements of complex permittivity and complex permeability, it seems prudent to discuss the origins and implications of these quantities.

Permittivity is best described by first considering the behaviour matter in a static (time-invariant) electric field, before extending the description to incorporate time-variant behaviour. A similar approach was taken in the texts of Fröhlich [3] and Hasted [4].

Consider a parallel plate capacitor of separation d and plate surface area A, where d is much smaller than the width and length of the plates. If a potential difference is applied to the plates, an equal and opposite charge will accumulate on each plate. This gives rise to an electric field (which will act in the direction of positive charge to negative charge) between the plates. However, if a non-conducting (i.e. dielectric) material is placed between the plates, polarisation charges will accumulate on the surfaces of the dielectric to reduce the electric field. If the dielectric material is of static relative permittivity ε_S, the applied electric field $\mathbf{E}_0$ will reduce by a factor of ε_S:

$$\mathbf{E} = \mathbf{E}_0/\varepsilon_S. \qquad 2.8$$

The polarisation charges accumulate as a result of electron cloud distortion. No charge flows as there are no free electrons, but the bound electrons are displaced

due to their Coulombic attraction to the positively charged plate of the capacitor. This distortion means there is a finite displacement between the electron cloud and the positive ion core of each molecule, which can be interpreted as an induced dipole moment. If electric field is uniform within the material, the induced charges will cancel out with adjacent molecules. If electric field is not uniform, the polarisation will vary throughout the volume of the material so the induced charges do not completely cancel. The remaining charges are termed volume polarisation charges. However, at the edge of the dielectric there are no adjacent particles to cause the net charge to sum to zero, so surface polarisation charges form. This situation is illustrated in Figure 2.4.

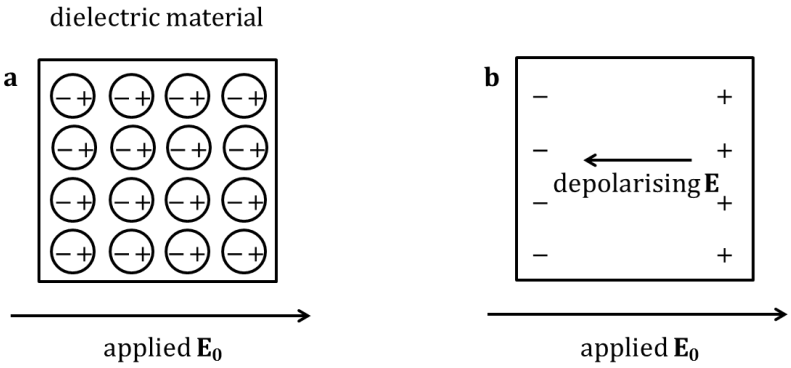

*Figure 2.4: Cross-sectional diagram of a dielectric material in an applied electric field, showing (***a***) how electric dipoles are induced and (***b***) the formation of surface polarisation charges.*

The macroscopic polarisation **P** is defined as dipole moment per unit volume:

$$\mathbf{P} = n\mathbf{p}, \tag{2.9}$$

where n is the number of atoms per unit volume and **p** is the individual dipole moment of each atom. The charge accumulated at each of the end surfaces of the material shown in Figure 2.4 Q_{pol} is:

$$Q_{\mathrm{pol}} = \mathbf{P}A, \tag{2.10}$$

where A is the area of each end surface. It follows that the incremental area element $d\mathbf{A}$ experiences an accumulated charge of dQ_{pol}:

$$dQ_{\text{pol}} = \mathbf{P} \bullet d\mathbf{A}. \qquad 2.11$$

Note that polarisation charges only develop on surfaces that are not parallel to the electric field. This is evident from the dot product in Equation 2.11, where the surface polarisation charge is maximised when the surface and polarisation are perpendicular, and is zero when the surface and polarisation are parallel. It can be shown empirically that polarisation is related to the total electric field inside the material. Specifically, polarisation is proportional to the applied electric field minus the induced depolarising field. The constant of proportionality is the electric susceptibility χ_e, which can be written in terms of permittivity by $\chi_e = \varepsilon_s - 1$. The relationship between polarisation and electric field can be expressed as:

$$\mathbf{P} = \chi_e \varepsilon_0 \mathbf{E} = (\varepsilon_s - 1)\varepsilon_0 \mathbf{E}, \qquad 2.12$$

where ε_0 is vacuum permittivity $\simeq 8.854 \times 10^{-12}$ Fm^{-1} and ε_S is the (dimensionless) static relative permittivity of the material. Electric flux density **D** can be defined as:

$$\mathbf{D} = \varepsilon_s \varepsilon_0 \mathbf{E} = \varepsilon_0 \mathbf{E} + \mathbf{P}. \qquad 2.13$$

This quantity is useful because it is defined in terms of free charges only; it is independent of induced polarisation charges.

Consider now the case where the potential difference applied across the parallel plate capacitor is time variant.

$$\mathbf{E} = \mathbf{E}_0 \cos \omega t, \qquad 2.14$$

where ω is angular frequency and t is time. Assuming any initial transients have passed and the dielectric-filled parallel plate capacitor is being excited with **E** according to Equation 2.14 in the steady state, it follows that **D** will also exhibit periodicity. This does not necessarily have to be (and indeed probably will not be) in phase with **E**. A phase shift δ can be described by:

$$\mathbf{D} = \mathbf{D}_0 \cos(\omega t - \delta) = \mathbf{D}_1 \cos \omega t + \mathbf{D}_2 \sin \omega t, \quad 2.15$$

where

$$\mathbf{D}_1 = \mathbf{D}_0 \cos \delta \text{ and } \mathbf{D}_2 = \mathbf{D}_0 \sin \delta. \quad 2.16$$

The quantities of $\mathbf{D}_0$ and $\mathbf{E}_0$ are usually proportional to each other, although their quotient ($\mathbf{D}_0/\mathbf{E}_0$) can be expected to exhibit some frequency dependence. We can therefore introduce two different components of permittivity according to:

$$\mathbf{D}_1 = \varepsilon_1 \varepsilon_0 \mathbf{E}_0 \text{ and } \mathbf{D}_1 = \varepsilon_2 \varepsilon_0 \mathbf{E}_0, \quad 2.17$$

where ε_1 and ε_2 are functions of frequency. Combining Equations 2.16 and 2.17:

$$\tan \delta = \frac{\varepsilon_2}{\varepsilon_1}, \quad 2.18$$

where δ is the phase lag between **D** and **E**, and also between **E** and **P**. The quantity $\tan \delta$ is known as the loss tangent. ε_1 and ε_2 are the real and imaginary components of permittivity, as introduced in Equation 2.4. They can be shown to quantify the energy stored and the energy dissipated by a dielectric, respectively. This can be demonstrated by considering a lossy dielectric between the plates of the parallel plate capacitor. This can be described by an equivalent circuit comprised of an ideal, lossless capacitor with a shunt conductance.

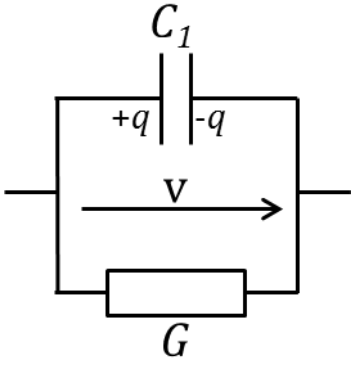

Figure 2.5: Equivalent circuit of a lossy capacitor, where C_1 and G are ideal. Charges of ±q will accumulate on the plates of the capacitor according to Q=CV.

Consider the circuit in Figure 2.5 with an applied periodic voltage $v = V_0 e^{j\omega t}$. This will cause a charge $q = Q_0 e^{j(\omega t - \delta)}$. The effective capacitance C is given by:

$$j\omega C = j\omega C_1 + G$$

$$\rightarrow C = C_1 - jG/\omega = C_1 - jC_2, \qquad 2.19$$

where $-jC_2 = -jG/\omega$. The stored charge is therefore $q = C\mathrm{v} = (C_1 - jC_2)\mathrm{v}$. Thus, the time-averaged stored energy $\langle U \rangle$ is:

$$\langle U \rangle = \tfrac{1}{4} C_1 {V_0}^2 = \tfrac{1}{4}\mathrm{Re}\{q\mathrm{v}^*\} \equiv \tfrac{1}{4} Q_0 V_0 \cos\delta, \qquad 2.20$$

and the time-averaged power dissipated $\langle W \rangle$ is:

$$\langle W \rangle = \tfrac{1}{2} G {V_0}^2 = \tfrac{1}{2}\omega C_2 {V_0}^2 = \tfrac{-1}{2}\omega\ \mathrm{Im}\{q\mathrm{v}^*\} \equiv \tfrac{1}{2}\omega Q_0 V_0 \sin\delta. \qquad 2.21$$

From this, it can be seen that for a lossless capacitor (i.e. when $C = C_1$), $\delta = 0$ so voltage and charge are in phase and no power is dissipated. However, power will be dissipated if there is a conductivity term associated with the dielectric according to Equation 2.21. The greater the value of G and therefore of C_2, the greater the phase lag δ and the associated power dissipated. Power dissipation is a direct consequence of the phase lag between charge and voltage. Considering a dielectric material experiencing an applied electric field, the phase lag between polarisation and electric field (and consequently ε_1 and ε_2; *cf.* Equation 2.18) similarly implies power dissipation.

We can perform the following substitutions: $q \rightarrow \mathbf{D}, v \rightarrow \mathbf{E}$ and (energy/power) $\rightarrow$ (energy/power) per unit volume. This means that $\mathbf{E} = E_0 e^{j\omega t}$ and $\mathbf{D} = D_0 e^{j(\omega t - \delta)}$. Using Equation 2.13, it is possible to rewrite the time-averaged expressions for stored energy and power dissipated (Equations 2.20 and 2.21) for a lossy dielectric:

$$\langle U \rangle = \tfrac{1}{4}\mathrm{Re}\{\mathbf{D}\mathbf{E}^*\} \equiv \tfrac{1}{4} D_0 E_0 \cos\delta = \tfrac{1}{4}\varepsilon_1\varepsilon_0 {E_0}^2, \qquad 2.22$$

$$\langle W \rangle = \tfrac{-1}{2}\omega\ \mathrm{Im}\{\mathbf{D}\mathbf{E}^*\} \equiv \tfrac{1}{2}\omega D_0 E_0 \sin\delta = \tfrac{1}{2}\omega\varepsilon_2\varepsilon_0 {E_0}^2. \qquad 2.23$$

Clearly, the energy stored in a lossy dielectric is a function of ε_1 and the power dissipated is a function of ε_2. There are three main polarisation mechanisms through which a dielectric material can interact with an electric field: ionic, dipolar

and electronic. The two components of permittivity are the sum total of the contributions of each process to electric energy storage and power dissipation. The frequency dependencies of ε_1 and ε_2 arise from inertial terms associated with redistributing charged particles of finite mass. It follows that at sufficiently high frequencies, none of the depolarisation mechanisms can possibly occur. Under these circumstances, the dielectric will not store additional energy or dissipate power. Relative permittivity will reduce to unity and there will be no difference between **D** and **E**.

A similar process can be applied to magnetisable materials in a region of magnetic field. The macroscopic magnetisation **M** is defined as magnetic moment per unit volume:

$$\mathbf{M} = n\mathbf{m}, \tag{2.24}$$

where n is the number of magnetic dipoles per unit volume and **m** is the individual dipole moment of each atom. A basic view of the atom is of electrons moving in orbitals around a nuclear core, where the movement of charge constitutes current and gives rise to magnetic effects according to Maxwell's equations. The atomic scale magnetic moments of a material will attempt to reorientate with magnetic field if the material is placed in a region of magnetic field. This is analogous to how electric charge responds to an applied electric field. Specifically, magnetisation is proportional to the applied magnetic field **H**, where the constant of proportionality is the magnetic susceptibility χ_m. This can be expressed as:

$$\mathbf{M} = \chi_m \mathbf{H} = (\mu_r - 1)\mathbf{H}, \tag{2.25}$$

where μ_r is the (dimensionless) relative permeability of the material. The magnetic flux density **B** can be introduced in terms of magnetic field and subsequently expressed in terms of magnetic field and magnetisation:

$$\mathbf{B} = \mu_r \mu_0 \mathbf{H} = \mu_0(\mathbf{H} + \mathbf{M}), \tag{2.26}$$

where μ_0 is vacuum permeability, defined as $\mu_0 = 4\pi \cdot 10^{-7}$ Hm^{-1}. It is obvious from Equation 2.26 that magnetisation can be thought of as the difference between magnetic flux density and magnetic field. Note that **H** is normally considered the

derived field, as **D** is similarly derived from **E**. This is because **B** and **E** can normally be used to fully describe electric and magnetic fields using Maxwell's equations if sources of current density and charge density are known. For this reason, the relationships between **B** and **H** (Equation 2.26) and between **D** and **E** (Equation 2.13) are referred to as the constitutive relations.

The relative permeability of a magnetic (or magnetisable) material differs from relative permittivity in several key respects. Firstly, it is not unusual for permeability to be greater than or less than unity. Materials with these properties that do not exhibit a permanent magnetic moment are known as paramagnetic and diamagnetic, respectively. Naturally-occurring dielectric materials do not exhibit sub-unity permittivity and synthetic dielectrics rarely do so over a significant portion of the electromagnetic spectrum. Secondly, some materials retain a magnetic moment after the applied magnetic field has been removed. These materials are known as ferromagnetic. This property depends on the magnitude of the applied field and, as such, differs from the permanent dipole moment due to molecular charge distribution. The relative permeability therefore exhibits some form of memory, known as hysteresis. Thirdly, permeability is generally a far smaller quantity than permittivity (with the exception of many ferromagnets).

As electric fields store energy, so do magnetic fields. Permeability can be used to quantify the difference between magnetic field and magnetic flux density, and will therefore be complex valued if there is a phase lag between the two. This can be demonstrated according to the following substitutions: $q \rightarrow \mathbf{B}, v \rightarrow \mathbf{H}$ and (energy/power) → (energy/power) per unit volume. This means that $\mathbf{H} = H_0 e^{j\omega t}$ and $\mathbf{B} = B_0 e^{j(\omega t - \delta)}$. Using Equation 2.13 and taking the loss tangent $\tan\delta = \mu_2/\mu_1$ for complex relative permeability $\mu_r = \mu_2 + j\mu_2$, it is possible to rewrite the time-averaged expressions for stored energy and power dissipated (Equations 2.20 and 2.21) for a lossy magnetic material:

$$\langle U \rangle = \frac{1}{4}\mathrm{Re}\{\mathbf{B}\mathbf{H}^*\} \equiv \frac{1}{4}B_0 H_0 \cos\delta = \frac{1}{4}\mu_1\mu_0 {H_0}^2, \qquad 2.27$$

$$\langle W \rangle = \frac{-1}{2}\omega\ \mathrm{Im}\{\mathbf{B}\mathbf{H}^*\} \equiv \frac{1}{2}\omega B_0 H_0 \sin\delta = \frac{1}{2}\omega\mu_2\mu_0 {H_0}^2. \qquad 2.28$$

As discussed in Sections 75 and 77 of [47], the frequencies at which the values of ε and μ disperse (that is, exhibit frequency dependence) may be completely different. If a measurement technique is to characterise both parameters, it is therefore prudent to select a frequency range most appropriate for measuring permittivity rather than permeability given that all matter will have an electric field response but not all matter will have a magnetic field response.

2.2.2. Broadband dielectric spectroscopy

The most common method for performing broadband dielectric spectroscopy is the coaxial reflectance sensor, as originally reported by Misra [48]. Propagating waves were reflected by the open-circuited termination of a coaxial line, where the reflection was shown to be a function of aperture admittance. This, in turn, was shown to be a function of the permittivity of the material occupying the evanescent field in the region immediately outside of the probe aperture (i.e. where propagating waves were not supported). This was achieved by matching the modes inside and outside the transmission line, which must have the same distribution at the aperture; a detailed analysis of various aperture admittance models and the subsequent effects on sensitivity was reported in [49].

An example application for this technique is to monitor oil contaminants (and thereby oil quality), which is of obvious interest to the oil and petroleum industries. A broadband coaxial reflectance cell has been demonstrated for this purpose [50], [51]. This technique exhibits low uncertainty over a large frequency range for bulk samples, which is particularly beneficial for hydrocarbons that have dielectric dispersions over many orders of magnitude of frequency. However, this work did not quantify the concentration of contaminants and required the sample to be in contact with a metal transmission line, reducing the number of compatible solvents and biological species that could be characterised using this technique. This problem is common to many coaxial reflectance techniques; the use of a separating layer to prevent the sample under test from coming into contact with the sensor forms a multi-layer geometry and vastly increases the complexity of the analytical problem.

A similar approach allows permittivity to be quantified using a coplanar transmission line geometry, which has been demonstrated using measurements of a solvent of known permittivity (butanol) [52]. This technique benefits from being low cost and easy to fabricate, and offered performance comparable to that of a commercially available broadband coaxial probe. However, the large tolerances associated with the fabrication technique used by the authors led to decreased measurement accuracy.

A related microwave-frequency transmission line technique was functionalised for biological specificity and used to (qualitatively) distinguish between surface-bound macromolecules [53]. The transmission line was surface functionalised with guanine bases, which allowed other nucleic acids to be qualitatively distinguished based upon whether hybridisation occurred. The occurrence of such an event could be inferred from a change in the dielectric properties of the transmission line. This method was sensitive to picomolar concentrations of nucleic acids; an impressive limit of detection achieved because the interactions were restricted to the two-dimensional surface of the transmission line. However, the functionalised transmission line could not be used to quantify the number of occupied binding sites or the complex permittivity of the sample. The use of functionalised conductors is a tremendously powerful technique but makes the sensor entirely application-specific. This factor, coupled with the reduced chemical and biological compatibility inherent to any functionalised technique, means such a method is not appropriate for this project.

Another problem encountered with broadband techniques is the requirement for careful and frequent calibration of the measurement equipment used to interrogate the sensor. It is for this reason that resonant techniques are sometimes preferred as they have a lesser dependence on Vector Network Analyser (VNA) calibration and therefore have lower systematic error. This is important if the 'black box' dielectric spectroscopy aims of this project are considered. Calibration-dependent techniques are not suitable for the non-specialist user who wishes to analyse a sample in the field without having to perform an intricate and rigorous calibration. This is of particular significance when such a calibration would need to be performed at least once an hour.

Alternative broadband techniques have been suggested to alleviate this problem. One example was based upon propagation constant measurements [54]; another was based upon raw (uncalibrated) S-parameter measurements [55]. These methods still suffer from fluid interfacing problems as encountered for other broadband techniques: both methods utilise a liquid-filled section of waveguide. Such approaches have reduced chemical and biological compatibility (as well as exposing the waveguide to potentially corrosive materials) and are not appropriate for high-throughput applications.

2.2.3. Resonant dielectric spectroscopy

Resonant dielectric spectroscopy offers advantages over the broadband equivalent in two main respects: by having improved sensitivity through increased signal-to-noise ratio (SNR) [8] and lesser susceptibility to systematic errors due to a lesser dependence on careful network analyser calibration [22]. However, resonant techniques are inferior in that they cannot be used to characterise continuous permittivity spectra, although it is possible to use several modes to obtain multi-frequency information. It is not possible to state that broadband or resonant techniques are universally superior, so an informed deliberation is necessary. However, it should be noted that dielectric dispersions in the microwave region vary slowly with frequency so highly detailed spectral information is not necessary. This decision requires thorough knowledge of the available measurement techniques and some knowledge of the application. The latter requirement encompasses information such as the approximate dielectric and magnetic properties (or lack thereof) of the material under test; whether the sample is solid or fluidic, and how it could be interfaced to the sensor.

There are many different structures that can be used to form electromagnetic resonators. For the sake of brevity, only five of the most common geometries are discussed here: cavities, dielectric resonators, hairpin cavities, split-ring cavities and coaxial resonators. Each is discussed in turn.

There are three commonly used types of cylindrical cavity resonator: TM_{010} mode, TE_{011} mode and re-entrant. Schematic views of each are shown in Figure 2.6.

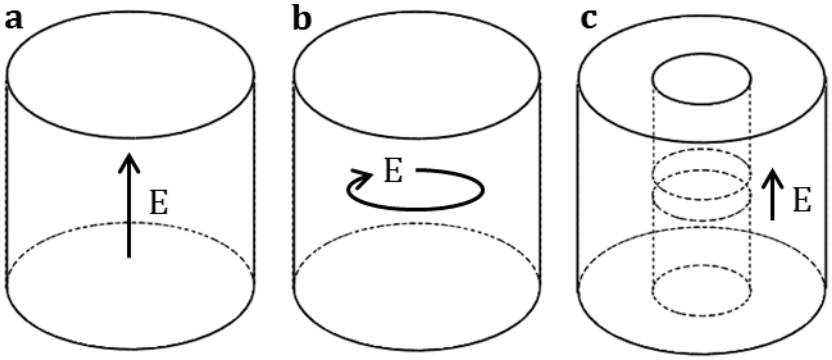

*Figure 2.6: Schematic views of (***a***)* TM_{010} *mode, (***b***)* TE_{011} *mode and (***c***) re-entrant cavities.*

The TM_{010} mode has the lowest frequency resonance. It is therefore the most easily distinguishable mode and, as a consequence, the most commonly used. The electric field lines run parallel to the cylinder axis, where the field magnitude diminishes radially to zero at the cylindrical side-wall, as shown in Figure 2.6 **a**. The magnetic field lines form concentric circles about the cylinder axis. The most common way of perturbing this resonator is to position a cylindrical sample (either a solid rod or a fluid-filled tube) along the axis. This occupies maximum electric field and causes minimal depolarisation as the cylindrical sample does not cross any electric field lines so charge cannot accumulate on its surface and thereby oppose the inducing electric field. Higher order TM_{0n0} modes can also be perturbed in this fashion, although incidences of degeneracy (where modes overlap in the transmission spectrum of the resonator) are increasingly common at higher frequencies. From experience, it is difficult to identify and reliably use more than two of these modes.

TE_{011} mode cavities have azimuthal (circularly-polarised) electric field lines circulating about the cavity axis, as shown in Figure 2.6 **b**. The electric field magnitude decays to zero at the cylindrical side-walls. This field distribution is particularly suitable for disc-shaped samples oriented parallel to the ends of the cavity, where the sample radius should be (at least approximately) the same as that of the cavity. This is obviously unsuitable for capillaries or microfluidic chips (where microchannels run through a bulk substrate), although such cavities do also exhibit high quality factors. More significantly, however, is the fact that this

mode is always degenerate with the TM_{111} mode, necessitating some form of filtering.

Re-entrant cavities are a special case of the TM_{010} cavity, where cylindrical conductors protrude inwards from the top and bottom of the cavity to approximate a short-circuited coaxial transmission line with an gap in the inner conductor. This situation is shown in Figure 2.6 **c**. A thick disc-shaped sample may then be inserted into this gap in a similar manner to the TE_{011} mode cavity. The gap approximates a parallel plate capacitor, albeit one with a large separation in comparison with the surface area. Re-entrant cavities therefore have large fringing electric fields. This can lead to large uncertainties in real permittivity measurements unless the effects of the fringing fields are reduced or removed via numerical modelling [22] or careful calibration.

All cavities have high quality factors and are therefore suitable for characterising low loss materials. However, resonant frequency is set by the cylindrical cavity dimensions which, for microwave frequency operation, are fairly large (centimetres to tens of centimetres). It would be possible to use narrow fluidic capillaries for perturbation along the TM_{010} cavity axis. The resonant frequency of this mode is independent of length but the quality factor (and therefore sensitivity) is not. This results in an undesirable compromise as a long length is necessary for decent quality factors but results in poor spatial resolution.

Dielectric resonators are formed from discs of high permittivity, low loss materials. Such techniques can be broadly subdivided into the follow types: $TE_{01\delta}$ mode, whispering gallery mode and split-post.

Other TM and hybrid modes could be used for sensing, but the $TE_{01\delta}$ mode dielectric resonator remains the most common choice for sensing [56] as it has one of the lowest frequency resonances and is consequently one of the most accessible modes. The delta subscript refers to the fact that the height of the resonator is much less than the half-wavelength of the resonance. The high permittivity of the resonator allows propagation along the axis of the resonator but not beyond the ends of the cylinder, where instead there are rapidly decaying evanescent fields.

This situation is similar to a dielectric rod waveguide supporting a propagating TE_{01} mode where a short length of the dielectric rod is of much higher permittivity than the surrounding regions [57]. The low resonant frequency of the $TE_{01\delta}$ mode resonator is a consequence of the fact that this mode can support a standing wave of half-wavelength many times larger than the height of the dielectric cylinder. For a resonator of fixed dimensions, the $TE_{01\delta}$ mode will clearly be of lower resonant frequency than higher order modes with additional half-wavelengths confined within the resonator.

However, unlike cavity resonators, the fields are not completely confined within the dielectric resonator. The $TE_{01\delta}$ mode has azimuthal (circularly-polarised) electric field. There are also evanescent fields outside of the dielectric material that allow power to be coupled in to and out of the resonator. This is in contrast with cavity resonators, which require invasive couplings in order to access the electromagnetic fields. Note that this type of resonator has to be contained within a cavity (where its resonances have to be distinguished from those of the cavity) in order to prevent excessive radiative losses and resultant drop in quality factor [22].

The whispering gallery mode is formed when a wave experiences total internal reflection in such a way that it forms a standing wave just inside the circumference of the dielectric resonator. This leads to greatly increased evanescent electric field confinement, meaning the cavity required for the $TE_{01\delta}$ mode can be dispensed with. Note that such modes are typically at much higher frequencies than the $TE_{01\delta}$ mode (resonances at 36 GHz and 170 GHz were demonstrated in [16]) and, as such, may be unsuitable for interrogation the low GHz region where the dielectric dispersions of many solvents can be observed.

Split-post dielectric resonators are, as the name would suggest, formed from two dielectric resonators oriented so that each resonator has one of its flat edges parallel and closely separated from the other [22]. Again, this structure must be contained within a cavity. The two dielectric discs exhibit a coupled $TE_{01\delta}$ resonance, which gives rise to an azimuthal (circularly-polarised) evanescent

electric field in the gap between the two resonators. Disc-shaped samples can then be inserted into the gap.

All dielectric resonators exhibit high sensitivity. The split-post dielectric resonator is extremely simple to construct and remains a popular metrological technique. However, they usually require solid, disc-shaped samples (where uncertainty can be a function of the machining quality of the sample itself) and are difficult to perturb with microchannels. A recent example went some way to addressing this issue, where a circular microchannel was milled in the top of a sapphire disc. This was then bonded to another disc to seal the channel and to form a split-post dielectric resonator with its gap perturbed by the microchannel [17]. This has an advantage over many microfluidic dielectric spectroscopy techniques in that the channel runs parallel to electric field and therefore does not cause any depolarisation. However, the method used to bond the device together (to form the fluidic seal) resulted in such a large drop in quality factor that the expense incurred in fabricating the device was not justified by its sensitivity. This is exacerbated by the difficulty in machining quartz.

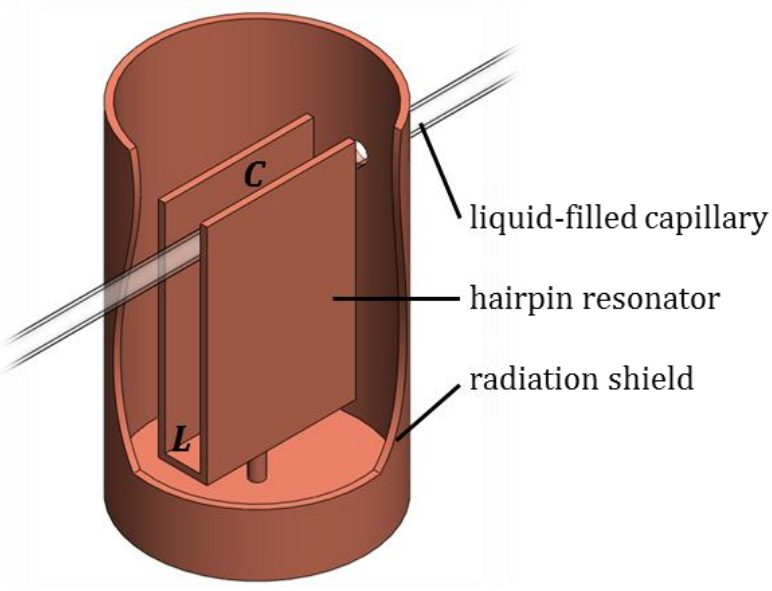

Figure 2.7: Schematic cutaway view of the λ/4 hairpin resonator mounted in a radiation shield perturbed with a liquid-filled quartz capillary. The capacitive and inductive regions are labelled C and L, respectively. The resonator is mounted inside the cavity on a copper post and inductively coupled using loop-terminated coaxial feedlines (not shown).

A hairpin resonator can be constructed from a metal sheet formed into a flat-bottomed U-shape configuration, as shown in Figure 2.7. This type of structure would usually be contained within a radiation shield to prevent excessive losses from reducing quality factor to an unusable level. The electric field region of largest magnitude and highest uniformity is located at the open end of the hairpin. This can be perturbed with a fluid-filled PEEK capillary, as demonstrated in [18]. Similarly, magnetic sensing could be performed by passing the capillary through a region of high magnetic field (i.e. the inductive region, as labelled in Figure 2.7). This structure exhibits excellent field confinement as the electric field has high uniformity within the hairpin plates but decays rapidly outside of them. However, the sensitivity of this device suffers as the microchannel is oriented perpendicularly to electric field and therefore experiences depolarisation. Additionally, this structure offers limited microfluidic functionality and is not robust enough (given the long length of suspended capillary) for point-of-sampling applications.

Schematic views of the typical implementations of the split ring resonator (distinguished by whether the resonator is planar) are shown in Figure 2.8.

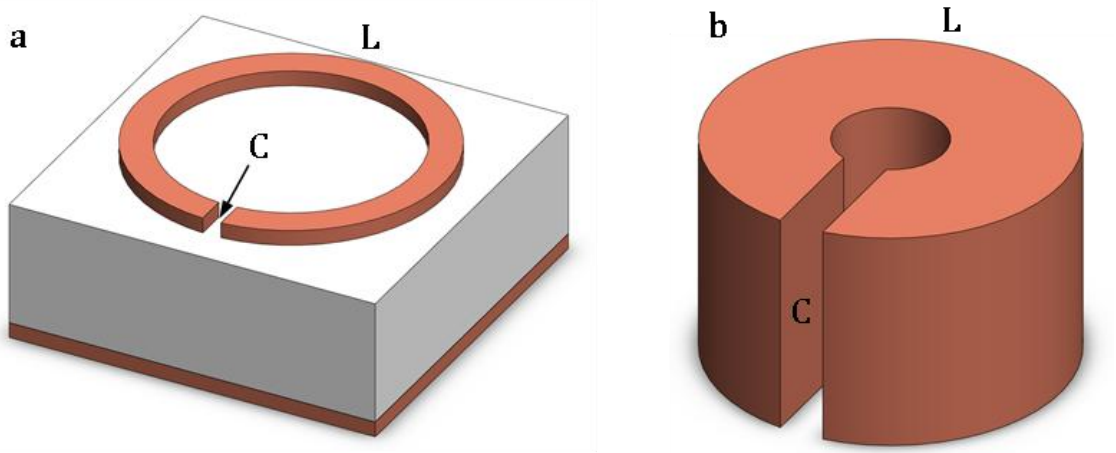

Figure 2.8: Typical implementations of the split-ring resonator. **a** *shows a planar structure and* **b** *shows an alternative fabricated from a conducting tube, where the approximate locations of the inductive (L) and capacitive (C) regions are also labelled. Note that the capacitive regions are strictly in the gap of the split rings.*

A (square) example of Figure 2.8 **a** was described in [19]. Thin film samples could be detected when deposited in the capacitive loop gap region. It did not exhibit high sensitivity due to low quality factors associated with high conductor losses. These arose from having conductors thinner than the skin depth at such frequencies (thereby causing increased resistivity) and by using a square ring (where all corners caused current bunching and further increased resistivity). An example of Figure 2.8 **b** is described in [58]. It was perturbed with a liquid sample in a similar fashion to the hairpin resonators by passing a PEEK capillary through the gap in the resonator. The loop gap is the region where electric field is highest, of uniform magnitude and perpendicular to the axis of the capillary. The planar example had large fringing fields so any material in the loop gap would only occupy a small fraction of the electric field. The non-planar alternative addressed this by increasing the surface area of the faces bounding the loop gap. This has a large sensing volume that is inappropriate for microfluidic perturbation as the dimensions of the loop gap faces will generally be much bigger than any microchannel.

Liquid-filled quarter-wavelength coaxial resonators have been used to evaluate the electrical properties of several solvents [59]. This method is suitable for through-flow measurements, although the dimensions of the resonator mean that a microfluidic interface could not be used. The frequency of interrogation was set by the length of the resonator, meaning that multi-frequency measurements required the use of different resonators. A disadvantage shared with many of the other dielectric spectroscopy techniques discussed above was that the sample was required to be in contact with a copper transmission line.

2.2.4. Related techniques

Other spectroscopic techniques that also exploit material interactions with a microwave-frequency electric field have been combined with microfluidic techniques.

A microwave interferometer is a device that measures the difference between waves that have traversed a sample-perturbed transmission line and a reference transmission line by virtue of their interference. Such a device has been used to

perform differential measurements of sample-filled and reference liquid reservoirs in order to determine the composition of ethanol-water and methanol-water mixtures [60]. Note that measurements could only be performed at a single frequency. This technique was demonstrated with large changes in molar fraction (≥ 5%), which yield correspondingly large (and easily detectable) changes in permittivity. The composition of a biological sample (for example, changes in blood glucose concentration) could reasonably be expected to vary by orders of magnitude less than this.

A Coulter counter for measuring the number density of biological cells has been implemented using MHz frequency impedance measurements [61]. A potential problem with this approach is the high power dissipated in the sample during measurement. This could be exploited for the purposes of heating as delivering power at a certain frequency will dissipate energy according to the dielectric loss of the liquid at that frequency. This could prove to be an efficient and selective method for *in situ* temperature control of liquids whilst simultaneously characterising the sample. Serendipitously, the peak in imaginary permittivity of many common solvents occurs in the microwave-frequency region.

However, with respect to [61], μW power levels are considerable for low-volume (microfluidic) samples and could lead to misleading or ambiguous results. This problem will be most significant for liquids with highly temperature-dependent permittivity, and for mixtures composed of fluids with different temperature dependencies. This method also requires the sample to be in contact with a metal electrode, which reduces biological and chemical compatibility. Similar cell counting devices have also been implemented using GHz frequency measurements [62], [63]. The permittivity contribution of ionic content will decrease as the frequency of measurement increases. Therefore, these methods typically have a better signal-to-noise ratio than lower frequency techniques. This has the additional benefit of implying that any measured change can be attributed to changes in capacitance due to the presence of cells. The inability to quantitatively characterise material properties other than size means that such methods are of limited use for point-of-sampling applications. However, combining cell counting methods with dielectrophoretic techniques meant that different cells could be

distinguished. For example, the ability to distinguish between viable and non-viable yeast cells was demonstrated in [63]. This method requires predetermined knowledge of the differences in permittivity between the suspended cells and the suspending medium. The lack of directly accessible and quantitative information for an arbitrary sample means this approach is not suitable for generic point-of-sampling applications.

2.2.5. Magnetic spectroscopy

All matter must have a non-zero electric susceptibility since only a vacuum can have zero susceptibility. A magnetic material must therefore exhibit dielectric properties, and vice versa for a dielectric material. Given that both electric and magnetic susceptibility affect the response of a resonator measurement, it is therefore desirable to deconvolve the contributions of the electric and magnetic properties of the material under test. The change in complex resonant frequency can be rewritten to acknowledge such dependencies:

$$\Delta\tilde{f}(\tilde{\varepsilon},\tilde{\mu}) = \Delta f_0 - \mathrm{j}\frac{1}{2}\Delta f_\mathrm{B}, \tag{2.29}$$

where complex permittivity $\tilde{\varepsilon}$ is defined as $\tilde{\varepsilon} = \varepsilon_1 - \mathrm{j}\varepsilon_2$, where ε_1 is permittivity and ε_2 dielectric loss. Complex permeability is similarly defined to be $\tilde{\mu} = \mu_1 + \mathrm{j}\mu_2$, where μ_1 is permeability and μ_2 magnetic loss. This type of expression quantifies perturbation theory, which is used to extract material properties from resonator measurements. It is necessary to introduce it here for the purposes of discussing magnetic microwave-frequency spectroscopy, but perturbation theory is discussed in more detail in Section 2.3.

This work is generally restricted to isotropic samples, although anisotropic samples (including microflows of extremely diffuse suspensions) would simply require directional dependency of the function $\Delta\tilde{f}$. Expressions of the same form as Equation 2.1 apply to all modes if additional harmonics of an overmoded resonator are considered.

Magnetic materials are the most obvious type of sample requiring electric and magnetic deconvolution. For microfluidic characterisation, such samples clearly

have to be liquid- or gas-phase; note that magnetic liquids are usually suspensions where the suspended particles are magnetic but the carrier phase is not. Of particular significance is blood, where erythrocytes have a magnetic response due to the iron content of haemoglobin [64]. Oxygenated (diamagnetic), deoxygenated and methaemoglobin (both paramagnetic) each exhibit a different magnetic moment and can be separated by an applied magnetic field in suspension [65]. These measurements took place in an artificially simple liquid system. It is proposed that the ability to extract as much information from a sample with as little preparation as possible is important for point-of-sampling applications. To be able to characterise the dielectric and magnetic properties of a liquid could be tremendously useful for clinical applications.

However, such electric and magnetic deconvolution is also necessary for any medium that exhibits a coupled permittivity and permeability response. For example, a detailed theoretical treatment of simultaneous polarisation and magnetisation in chiral media is included in [66]. The coupled response of ionic solutions is another example, and will be used extensively in this work. This response arises because mobile charge carriers interact with both an applied electric field and the induced electric field due to an oscillating magnetic field.

Electric and magnetic deconvolution can be achieved with numerous measurement techniques, both broadband and resonant. Broadband transmission/reflection waveguide measurements are well established for such deconvolution. The seminal Nicolson-Ross-Weir method uses measurements of four parameters (the amplitude and phase of both power reflection S_{11} and transmission S_{21}) to determine complex permittivity and permeability [67–69]. Such methods are often applied to metamaterials research [70–72] in order to demonstrate a negative index of refraction, which requires knowledge of both complex permittivity and complex permeability.

Similar broadband approaches have also been adopted in disciplines outside of metamaterials research. For example, the complex permittivity and permeability of other solids [68], [73], liquids [74] and ferrofluids [75–79] have also been demonstrated. There are, however, several shortcomings with these works.

Whilst the problem was formulated in terms of both permittivity and permeability in [73], [74], only permittivity measurements of non-magnetic and non-ionic samples were experimentally verified. Of the ferrofluid characterisation methods, only two [75], [78] consider permittivity as well as permeability.

A ferrofluid is a colloidal suspension of superparamagnetic nanoparticles with an appropriate surfactant coating to prevent aggregation and allow the formation of a monodisperse suspension. See Section 2.6.3 for more information. Note that ferrofluids are a specific subset of magnetic liquids. Suspensions such as the paramagnetic and diamagnetic erythrocytes usually fall under the more generic label of 'magnetic liquids'.

The techniques described in [68], [70–79] are all broadband and are therefore less suitable for low concentration detection in comparison with resonant techniques, assuming an equivalent form of deconvolution is possible. These broadband methods are therefore inappropriate for the biochemical and pharmaceutical applications of this work due to decreased accuracy and sensitivity. The advantages of resonant techniques are indeed noted by [74] and discussed in detail in the section 2.2.3 and in [21], [22].

The deconvolution of electric and magnetic field effects can also be achieved with resonant measurement techniques. The simplest implementation is realised through positioning the sample in such a way that it only occupies either electric field or magnetic field depending on which mode of the resonator (i.e. which frequency) is interrogated. Peñaranda-Foix et al. [80] have gone some way to achieving deconvolution by exploiting the field distributions of a split cavity resonator. However, full deconvolution is not achieved because, despite the magnetic properties being isolated at certain frequencies, the electrical properties are not separated from the magnetic properties.

A split cavity resonator is formed from a cylinder halved along its height so that a solid slab of material can be placed between the two (symmetric) halves. This can be excited in the same way as a normal cavity resonator, but requires an extended analytical treatment due to incomplete field confinement in gap between the two

halves of the cavity. In [80], TE_{0np} modes are used. Magnetic field is maximised within the sample region when odd values of p are selected (termed "odd" modes), whereas electric field is minimised. Likewise, both the electric and magnetic fields are maximised within the sample region when even values of p are used (termed "even" modes). This only partially addresses the issue of deconvolution because the magnetic properties of the sample can be measured independently of the electrical properties but the electrical properties cannot be directly isolated from the magnetic properties. This may be acceptable if the variation of magnetic properties varied by a known amount within the interrogated frequency range, but any requirement for predetermined knowledge is unacceptable for a generic device to be used for analysing arbitrary samples with minimal preparation.

It would be possible to estimate the isolated electrical properties of a sample by comparing the responses of electromagnetically- and magnetically-perturbed modes, but the two measurements must necessarily be taken at different frequencies. This approach would entirely negate the use of multi-modal information for extracting frequency dependence information for permittivity and permeability. Although not explicitly stated in [80], complex permittivity is not (and cannot be) measured independently of varying permeability. Additionally, the imaginary component of permeability is ignored in [80]. This is perhaps understandable given that the imaginary component is normally fairly small, but it also means the certain sources of dielectric loss (i.e. dipolar and ionic polarisation) cannot be distinguished from each other.

Another cavity perturbation method has also been developed for extracting permittivity and permeability simultaneously [81–83]. If more than two or three modes are to be interrogated using this method, multiple sections of waveguide must be used. It is also dependent on careful calibration. For these reasons, such a setup is not suitable for the intended biochemical and pharmaceutical applications of this work, or for operation by a non-expert user.

2.3. Perturbation theory

Perturbation theory is usually derived in a manner similar to that set out below. This approach is also followed by [84–86]. The quality factor of a resonator is

defined as the ratio of energy stored U to power dissipated P at angular frequency ω $(= 2\pi f)$.

$$Q = \omega \frac{\langle U \rangle}{\langle P \rangle}, \tag{2.30}$$

where angle brackets denote a time-averaged quantity. Resonant frequency is denoted as ω_0. Frequencies close to resonance can be expressed as $\omega = \omega_0 + \Delta\omega$, where $\Delta\omega \ll \omega_0$. It can be shown that a lossy resonator of resonant frequency ω_0 is equivalent to a lossless resonator of complex resonant frequency $\tilde{\omega}$ [57]:

$$\tilde{\omega} = \omega_0 \left(1 + j\frac{1}{2Q}\right), \tag{2.31}$$

for frequencies $\omega = \omega_0 + \Delta\omega$ where $\Delta\omega$ is small. This can alternatively be expressed in terms of half-power bandwidth $f_B = f_0/Q$. Small perturbations of the resonator fields (in terms of permittivity, permeability or shape) will affect a change in complex resonant frequency, which can be written as [84–86]:

$$\frac{\tilde{\omega} - \tilde{\omega}_0}{\tilde{\omega}} = \frac{-\int_V (\Delta\varepsilon \mathbf{E} \cdot \mathbf{E_0^*} + \Delta\mu \mathbf{H} \cdot \mathbf{H_0^*})\, dV}{\int_V (\varepsilon \mathbf{E} \cdot \mathbf{E_0^*} + \mu \mathbf{H} \cdot \mathbf{H_0^*})\, dV}, \tag{2.32}$$

where the subscript 0 denotes an unperturbed quantity. $\Delta\varepsilon$ is the change in permittivity due to perturbation relative to the permittivity of the region occupied by the resonator field $\varepsilon = \varepsilon_r \varepsilon_0$; likewise for the change in permeability $\Delta\mu$. If it is assumed that the perturbed fields have the same distribution as the unperturbed ones, then Equation 2.32 can be reduced to:

$$\frac{\tilde{\omega} - \tilde{\omega}_0}{\tilde{\omega}} \approx \frac{-\int_V (\Delta\varepsilon |\mathbf{E}_0|^2 + \Delta\mu |\mathbf{H}_0|^2)\, dV}{\int_V (\varepsilon |\mathbf{E}_0|^2 + \mu |\mathbf{H}_0|^2)\, dV}. \tag{2.33}$$

The assumption that the fields remain the same is an approximation that does not hold for large perturbations (i.e. where the sample is of high permittivity or occupies a significant volume fraction of the resonator fields). Alternative inversion techniques will be explored in subsequent sections to account for calculation errors arising from such distortions.

Note that the denominator terms in Equation 2.33 are related to the energies stored within the electric and magnetic fields. For non-magnetic media, Equation 2.33 can be rewritten in terms of induced dipole moment and stored (electric) energy $U = U_e = \frac{1}{2}\varepsilon_0 \int_V |\mathbf{E}|^2 \, dV$:

$$\frac{\widetilde{\omega} - \widetilde{\omega}_0}{\widetilde{\omega}} \approx \frac{pE_0}{4U}. \tag{2.34}$$

Both sides are complex valued. It is useful to expand the left-hand side of this equation in terms of centre frequency and quality factor:

$$\mathrm{Re}\left(\frac{\widetilde{\omega} - \widetilde{\omega}_0}{\widetilde{\omega}}\right) \approx \frac{\tilde{f} - \tilde{f}_0}{\tilde{f}} = \frac{\Delta\tilde{f}}{\tilde{f}}, \tag{2.35}$$

$$\mathrm{Im}\left(\frac{\widetilde{\omega} - \widetilde{\omega}_0}{\widetilde{\omega}}\right) \approx \frac{1}{Q} - \frac{1}{Q_0} = \Delta Q^{-1}, \tag{2.36}$$

where $\tilde{f}$ and $\tilde{f}_0$ are the perturbed and unperturbed centre frequencies in units of Hertz. Together with Equations 2.9 and 2.12 (to relate dipole moment to permittivity), Equations 2.34 – 2.36 can be used to evaluated the dielectric properties of a material through measurements of resonator centre frequency and bandwidth. Specifically, the changes in the real and imaginary components of normalised complex frequency shift correspond to the real and imaginary components of polarisability (and therefore to permittivity) of the material under test.

Generally, the change in normalised complex resonant frequency is proportional to sample polarisability and hence to sample permittivity. However, the relationship between complex resonant frequency and permittivity is generally non-linear due to non-negligible field distortions caused by a sample. It is necessary to be able to describe this relationship in order to calculate the dielectric (and possibly magnetic) properties. This can be achieved in several ways: by analytical, numeric and empirical means. The analytical approach requires accurate modelling of the sample polarisability and of the resonator geometry. The numeric approach estimates the complex resonant frequency variation with permittivity using an appropriate simulation method such as finite element modelling. The empirical approach uses measurements of materials of known permittivity to interpolate an

inversion function or to populate a look up table, as long as complex resonant frequency varies smoothly with permittivity.

However, electric and magnetic field perturbation is dependent on the resonator geometry, the mode of excitation and the sample polarisability. The sample polarisability is affected by both its dielectric properties and its shape. Hence, the inversion of complex frequency measurements to complex permittivity values is unique to each resonant sensor and, to a lesser extent, the material under test. There is no universally superior method of measurement inversion as each has its own advantages and disadvantages, so this too depends on the resonator and the sample. It is therefore inappropriate to further discuss the use of perturbation theory for measurement inversion at this point. Each of the sensors developed during this project utilise perturbation theory in a different way, and specifics of such considerations will be dealt with individually for each resonant sensor.

2.4. Microfluidics

Microfluidics is the study of methods for miniaturised flow. This is usually achieved by confining small volumes (10^{-9} – 10^{-18} L) of fluids within channels that have cross-sections of micron-scale dimensions [87], although the length of the channels may be much greater. Various forces influence fluid flow, but the proportional influence of each force varies as the scale of confinement is reduced. Several phenomena arise as a consequence of such confinement. Perhaps most importantly, laminar flow can reduce the effects of turbulence and thereby allow fluid behaviour to be more accurately predicted and more precisely controlled in comparison with macroscale approaches. This level of control offers unprecedented potential for experiment automation and regulation within an enclosed system. Taken together with the obvious reductions in sample volume, equipment footprint, health hazards and the scope for human error, microfluidic techniques are ideal for improved fluid handling throughout many disciplines of science.

2.4.1. Basic principles

Various types of forces influence fluid flow. The most influential forces exerted on a fluid confined within a channel will be body (e.g. gravitational), inertial, viscous and surface forces. Ratios of these values (which are necessarily dimensionless) can be used to assess which forces dominate the others. Certain ratios can be seen to be dependent on some characteristic length of the channel, and are therefore useful measures for examining the non-linear behaviour of fluids at different length scales. Of such measures, the most important one is probably the Reynolds number x_{Re}. This quantifies the ratio of inertial forces to viscous forces:

$$x_{\mathrm{Re}} = \frac{v\rho}{\mu L}. \qquad 2.37$$

Unfortunately, several of these variables are assigned the same letters used for other electromagnetic variables elsewhere in this thesis. The appropriate variable should be clear from the context but, generally, it will refer to the electromagnetic variable rather than the fluid variable unless otherwise stated. v is flow velocity, ρ is density, μ is dynamic viscosity and L is the characteristic length of the channel, which is typically the radius for circular cross-sections. Equation 2.37 may also be written in terms of the kinematic viscosity $\mathrm{v} = \mu/\rho$.

Laminar flow will occur when viscous forces dominate the inertial. Clearly, this situation is described by a low Reynolds number. A laminar flow is one where the fluid flows in layers with little or no lateral motion. This is shown in Figure 2.9 **a**. Two fluids are eluted into a common channel before being separated into two outlet channels (a so-called 'H-cell'); laminar flow is preserved throughout. That lack of lateral motion means that mixing can only occur via diffusion across the interface between the two flows. If the two flows were the same liquid, and a dissolved species were introduced into one of the inlets, the mixing would be a function of the diffusion coefficient (diffusivity) and the length of the path where the two adjacent flows were in contact with each other. This is illustrated in Figure 2.9 **b** and **c**. In case **b**, there is a dissolved species of arbitrary diffusivity introduced into inlet 2. The path length is insufficient to allow complete mixing to occur (i.e. where the analyte concentration would be equal across both flows after some time *t*, assuming constant inflow velocity). Hence, both outlets have different

analyte concentrations, and each outlet exhibits a lateral concentration gradient due to the length of time taken for the analyte to diffuse. In case **c**, there is a dissolved species introduced in the same manner, but of diffusivity fifty times greater. In this instance, the path length is more than enough to allow the concentration to equilibrate. Hence, both outlets have the same analyte concentration.

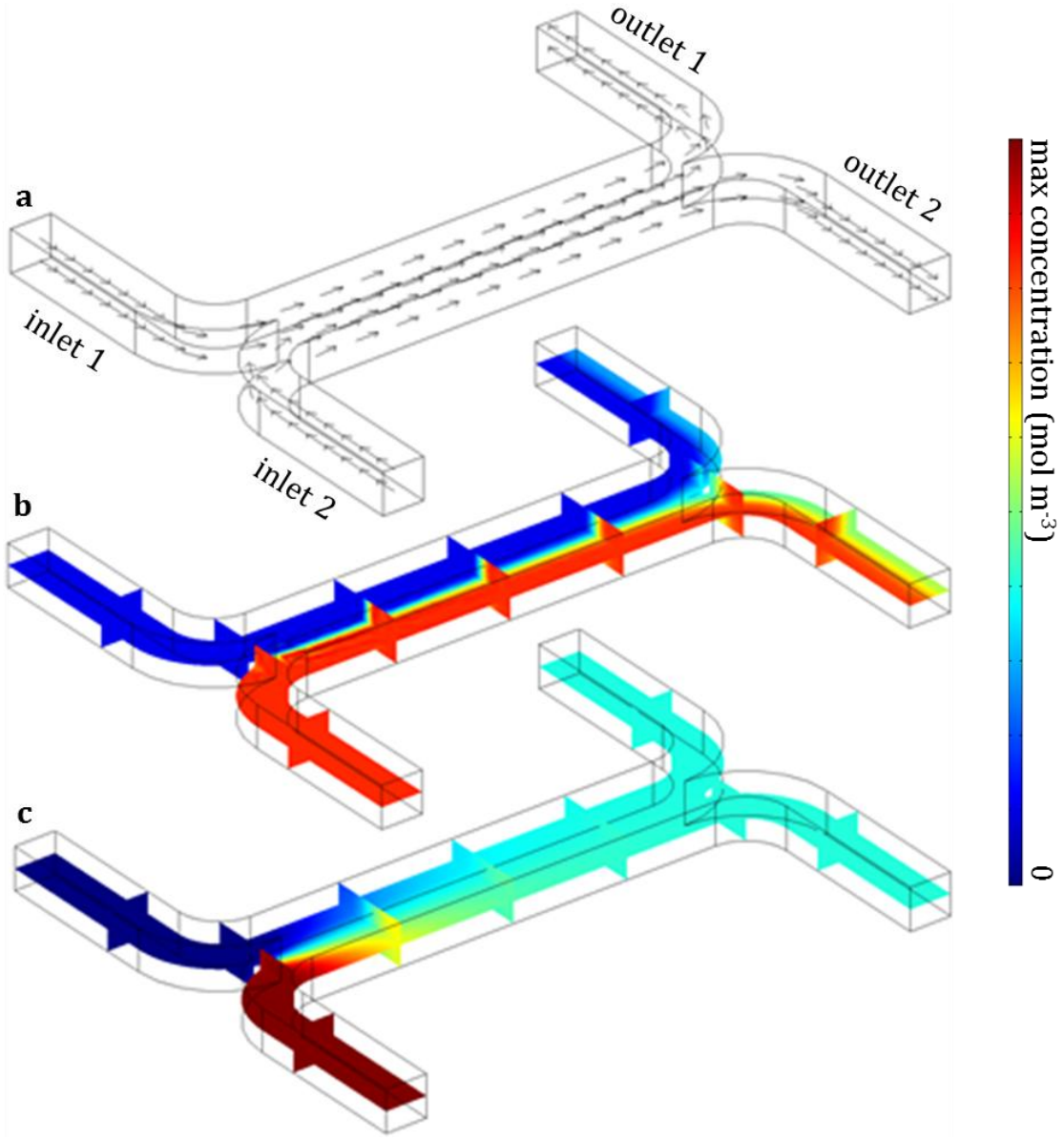

Figure 2.9: Schematic view of microfluidic H-cell modelled in COMSOL, where two inlets are eluted into a common channel before separating into two outlet channels. (a) shows the laminar flow pattern, (b) a colourmap of the concentration of a low diffusivity species introduced in inlet 2 and (c) a similar concentration colourmap for a high diffusivity species introduced in inlet 2. Each inlet and outlet channel has a 100 µm-square cross-section; the main channel has a 200 µm by 100 µm profile.

From this example, it can be seen how laminar flow enables mixing to be controlled simply by varying path length.

2.4.2. Basic techniques

Pumps, mixers, reactors and detectors can all be implemented using microfluidic techniques. Devices incorporating some combination of these on a single platform to perform a specific function are often described as 'lab-on-a-chip', or LoC.

It can be notoriously difficult to ensure mixing of laminar flows, given that diffusion is a relatively slow process. This is somewhat at odds with the purported benefits of microfluidics for fast, high-throughput and automated chemistry. This necessitates the use of mixers, which can be implemented in an active or passive manner. Active mixers use some external energy source to enhance mixing, for example via ultrasound [88], [89] or electrokinetic [90] means.

Conversely, passive approaches utilise the pumping force through particular channel geometries or surface features. Combining two flows at a T-junction, as shown above, is one approach. Other approaches include:

- Meandering channels, where corners and curves in the channel induce Dean flows (at least at high flow rates) that cause lateral flow due to inertial effects. This causes the parallel laminar layers to overlap and interleave and thereby increase mixing [91], [92].
- Parallel lamination, where alternating laminar flows are introduced side by side. Rather than just having one interface between two flows, this vastly increases the surface area across which diffusion can occur.
- Split-and-recombine mixers, where flows are split into smaller channels and subjected to different forces (for example, channels of dissimilar curvature to induce different Dean vortices) to enhance mixing of the entire flow upon recombination [93], [94].

All of the above examples of microfluidic techniques have been concerned with miscible fluids. Eluting immiscible fluids into a common channel gives rise to

multi-phase microfluidics, or segmented flow. Given the dominance of interfacial surface forces in microfluidic channels, it is energetically unfavourable for two immiscible liquids to form a laminar flow because of the large interface between the flows and correspondingly high surface area-to-volume ratio [95]. The lowest possible surface area-to-volume ratio is that of a sphere, so it is energetically favourable for one of the immiscible fluids to form discrete spherical droplets in the other fluid. A variation on this situation is when the diameter of such a sphere is less than one or both of the cross-sectional dimensions of the channel. In this case, the droplet becomes elongated and forms a slug. It is also possible for such slugs to completely occlude the channel; although more commonly one phase is suspended in the other. The potency of multi-phase microfluidics lies in that each partition demonstrates rapid, well-defined internal mixing, and the interface between each segment is continuously refreshed [96]. For example, a multi-phase method for continuous molecular enrichment [97] was recently developed at Cardiff University. A segmented flow incorporating a suspension of solid adsorbent microparticulates in the organic phase was used to accelerate the extraction of a dissolved target in the other, aqueous phase.

In order to fully take advantage of this performance in a practical laboratory or point-of-sampling application, it is necessary to be able to isolate the segmented phases from each other. Therefore, a membrane-free microfluidic device for continuous-flow operation was subsequently developed to separate a segmented flow into its constitutive phases [98]. Total (100% efficient) separation was achieved by exploiting the differences in the wetting characteristics of the two phases, where the lower contact angle phase could flow down small side channels upon the application of a suitable pressure gradient. The combination of molecular enrichment and phase separation techniques allows continuous-flow sample enrichment and purification.

2.4.3. Example applications

To give an exhaustive overview of all applications of microfluidics is beyond the scope of this section. For further information, please see the reviews [87], [96], [99], [100]. Such applications include chemical synthesis, digital fluidic logic and cell manipulation. Amongst the most useful work is in the development of low-

cost systems for the diagnosis of infectious diseases where it is logistically infeasible to use large-scale laboratory equipment, as recently demonstrated for the simultaneous detection of syphilis and HIV using optical detection methods [25]. As noted in [87], microfluidics offers great potential for high-value, high impact applications, but it remains a field of research in its infancy that has not yet made the transition from proof-of-concept experiments to usable, real world devices. The objectives of this project are in line with these perhaps lofty aims, as it seeks to incorporate the many fluid-handling advantages of microfluidics with the useful, miniaturisable methods of dielectric spectroscopy.

2.5. Current microfluidic microwave-frequency spectroscopy

From an interfacing perspective, filling a waveguide with a solvent [101] or dipping a reflectance probe [48] into a solution are acceptable only if there are a small number of samples to be characterised. This is incommensurate with the applications of modern chemistry and biology, where large-scale and high-throughput assays are an indispensible laboratory tool. To utilise the advantages of microfluidics would appear to be an ideal way of implementing a highly controllable, automated fluid interface.

Whilst microwave-frequency dielectric spectroscopy methods are well established, microfluidics is a young but nascent field of research. Hence, attempts to combine the two technologies have only emerged within the last decade. The most commonly encountered method is to perturb the electric field of a coplanar waveguide with a liquid delivered via microfluidic channels in a PDMS substrate [9], [12], [14], [15], [35], [102], where permittivity is extracted via a number of analytical and numeric means. All of these examples bring the sample into contact with the waveguide conductors. This has been done to avoid covering the coplanar waveguide in PDMS, which should be avoided because of its high dielectric loss at microwave frequencies, as noted by [9]. This is problematic for two reasons: no sample that will react with the conductors can be used (reducing biological and chemical compatibility), and the solutions can attack the bond between the conductor and the waveguide substrate. For the coplanar waveguide geometries referenced above, this means that the centre conductor in particular (which is often made as narrow as possible to increase spatial resolution) is fragile and

prone to come away from the substrate, rendering all measurements useless. These problems are known to occur [103] for the devices reported in [14], [35], [102] and could reasonably be anticipated for the others.

There have also been examples of microfluidic whispering gallery mode dielectric resonators. These devices have been perturbed with microfluidic channels [16], droplets [104] and confined nanolitre fluid samples [105]. The resonant microfluidic approaches exhibit very low chemical sensitivity. Despite the fact that resonator measurements should be capable of improved sensitivity in comparison with broadband techniques (as discussed above), they are less sensitive. [104] and [105] are not capable of continuous flow measurements, which would seem to negate much of the usefulness of a microfluidic interface, and reduce chemical compatibility through their use of contact measurements and PDMS substrates.

In addition to this, several other microfluidic techniques have been developed for resonator perturbation at Cardiff University. These include the capillary-perturbed hairpin [18] and split-ring resonators [58], and the split-post dielectric resonator with an embedded microchannel [17], as discussed from a measurement perspective in Section 2.2.3. From a microfluidics perspective, these interfaces are somewhat limited as the resonators would not be able to be integrated directly onto a lab-on-a-chip device. One of the main attractions of microfluidics for the non-expert point-of-sampling applications of this project is that it allows all processing and diagnostics technology to be integrated into one box. To pump a sample off chip to a resonator is by no means an impossible feat, but would seem to add unnecessary complexity. For example, the sample tubing would need to be maintained at the same temperature as both the resonator and the microfluidic chip. Furthermore, experience has proven that some of the most problematic elements of a microfluidic circuit are the fluidic inlet and outlet connections, so adding more is undesirable.

2.6. Chemistry

2.6.1. Chirality

Stereoisomeric molecules are isomers that differ in their spatial arrangement of atoms but not in the order of their bonds or in molecular formula. These are distinct from constitutional isomers, which also have the same molecular formula but differ in the order of their bonds. Stereoisomers can be further subdivided according to the arrangement of their stereocentres, which are atoms asymmetrically bonded to two or more groups where any pair of groups is interchangeable. Stereoisomers can either be enantiomers or diastereoisomers. Two molecules are enantiomers when every stereocentre in one molecule is of the opposite configuration to the equivalent stereocentre in the other molecule. For example, thalidomide exists as two different enantiomers that exhibit some different properties within the human body [106]. Two molecules are diastereoisomers when at least one but not all of the stereocentres in one molecule are of the opposite configuration to the equivalent stereocentres in the other molecule. For example, cocaine exists as different diastereoisomers, which can be useful in distinguishing whether a particular sample is from a natural or synthetic source [107].

A consequence of having oppositely configured stereoisomers is that any two enantiomers will be mirror images of each other but will not be superimposable. A commonly used analogy for describing this situation is a pair of hands, where the hands are equivalent and mirror images of each other but are not rotationally symmetric. However, the polarisability of two enantiomers in an oscillating electric field will be identical. This problem arises because microwave-frequency dielectric spectroscopies typically characterise the rotational movement of molecules with sinusoidally varying fields. Therefore, enantiomers cannot be directly distinguished because their charge distributions dictate that their polarisabilities will be identical, despite rotating in different directions. However, biological function is often enantiomer specific. Enantiomers can therefore be identified if the dielectric properties of a biological species (such as tissue or a membrane) can be interrogated. An example of this is given in [108], where the electrical properties of an erythrocyte membrane are measurably affected by the presence of the D-glucose enantiomer but not the L-glucose enantiomer. Dielectric

spectroscopy can therefore be used to indirectly identify glucose enantiomers due to their biological action or lack thereof via the electrical properties of erythrocyte membranes. A microelectrode device for performing such measurements in demonstrated in [109]. Conversely, diastereoisomers (i.e. not enantiomers) can be directly assessed with dielectric spectroscopy techniques because their charge distributions differ, as demonstrated for arabinose in [110].

2.6.2. Molecular imprinting

Considering recent research at Cardiff University, an area of interest is in the use of molecularly imprinted polymers (MIPs) for specific binding [97], [111–113], as alluded to in Section 2.4.2. MIPs are polymers that, due to the presence of a template molecule during polymerisation, contain recognition sites that will selectively bind to a target ligand [114]. The cavity left in the polymer by the removal of the template retains chemically functional groups spatially arranged in relief of the target. The imprinted site will therefore demonstrate chemical affinity for structures corresponding to that of the target ligand, and so behave as a type of artificial antibody. Although MIPs typically exhibit lower specificity than their biological counterparts, they possess excellent chemical and thermal stability [115] and can be used in a wide range of environments.

Current spectroscopic techniques cannot be used to directly assess specific binding in solution. To be able to perform such characterisation *in situ* (for example, in a continuous microfluidic segmented flow such as in [97]) would be tremendously enabling. For example, if MIPs were to be used in a synthetic purification stage by removing a dissolved species in segmented flow, dielectric spectroscopy could allow automated optimisation of the synthetic procedure by indicating when a set level of binding had been achieved without the need to separate the phases and subsequently perform an assay. The potential for *in situ* continuous flow measurements could dramatically reduce the time taken by such procedures.

Microfluidic dielectric spectroscopy could be capable of performing such measurements, but the large size of MIPs ($\sim$ 4 μm [116]) mean that they are unlikely to exhibit significant dielectric dispersion in the microwave-frequency region (if at all). Therefore, it may transpire that dielectric spectroscopy could be

used to quantify the removal of a measureable target ligand to infer binding rather than directly assessing the occupation of ligand-specific sites.

2.6.3. Magnetic nanoparticles

The applications of magnetic nanoparticles have been the subject of numerous extensive reviews, including ones on therapeutic drug delivery [117], cell targeting [118], magnetic resonance imaging [119], cancer diagnosis [120] and data storage [121]. Simultaneous dielectric and magnetic spectroscopy has been attempted for ferrofluid characterisation [122]. However, resonant microwave-frequency spectroscopy has not been utilised for such applications. It is possible that, if such a technique can be implemented effectively in a microfluidic environment, it could offer an ideal method for performing low-cost but highly accurate point-of-care diagnostics.

2.7. Summary

Various different spectroscopies have been qualitatively compared. Microwave-frequency resonators are an excellent sensing technique for a wide range of (bio)chemical and industrial point-of-sampling applications in terms of speed, cost, sensitivity and potential for miniaturisation. Significantly, such techniques can also be combined with a microfluidic sample interface for precise, automated, and high-throughput measurements, although this potential has not yet been fully realised. The aim of this project is to develop a widely compatible 'lab-on-a-chip' device for fluid identification for a non-expert user.

3. EVANESCENTLY-PERTURBED COAXIAL RESONATOR

The concept of using microwave resonators to measure permittivity and permeability was introduced in the previous chapter. Several key questions were also addressed. Specifically:

- Why use dielectric spectroscopy?
- Why use microwave-frequency dielectric spectroscopy?
- Why use resonant microwave-frequency dielectric spectroscopy?

Dielectric spectroscopy has great potential as an alternative, cost effective spectroscopic technique because of its capabilities for non-contact, non-invasive, non-destructive and label-free measurements of all states of matter and combinations thereof. The microwave frequency region is one where rotational dielectric dispersions are dominant and most obviously observable for solvent-based liquid systems. It is therefore beneficial for a low-cost spectroscopy device for point-of-sampling applications to perform measurements in this region. Performing resonant measurements instead of broadband measurements have benefits in terms of sensitivity and dynamic range, although only being able to perform measurements at a single frequency remains a significant drawback.

This chapter explores the use of an evanescently-perturbed coaxial resonator as an alternative geometry for performing rigorous, repeatable measurements for biochemical applications. To fully justify the chosen measurement technique, the

use of a coaxial resonator as an implementation of a resonant microwave-frequency dielectric spectroscopy technique must also be considered.

For most of the previous examples of microwave resonant sensors, the over-riding design methodology has been to maximise the quality factor Q in order to improve resolution. The motivation for doing this is best explained by considering that heating and sensing are two manifestations of the same phenomenon: the interaction of charged particles with an electric field. Heating occurs when the power dissipated via this interaction is sufficient to raise the temperature of a sample by a measureable degree. The principle of sensing via this interaction requires some power to be dissipated by the sample so that the reflected (or transmitted) signal exhibits a measurable difference due to the properties of the sample. The measurement should be configured to minimise the absolute power dissipated in order to prevent any temperature-dependent properties from being affected. Therefore, for dielectric spectroscopy, it is desirable to minimise the power dissipated but to maximise the proportion of input power that interacts with the sample. For an input power $\mathrm{P_{IN}}$, unperturbed quality factor Q_0 and loaded (i.e. sample-filled) quality factor Q_S, the power dissipated in a sample $\mathrm{P_S}$ is:

$$\mathrm{P_S} = \mathrm{P_{IN}}(1 - Q_\mathrm{S}/Q_0). \qquad 3.1$$

A smaller value of $\mathrm{P_S}$ for a given $\mathrm{P_{IN}}$ will give rise to a smaller measured response, meaning that the device resolution will be reduced. It is therefore necessary to design a sensor so that $\mathrm{P_S}$ is maximised for a given $\mathrm{P_{IN}}$. To do this it is necessary to minimise Q_S, maximise Q_0 or both. The normal design procedure is to focus on the maximisation of Q_0.

Increased Q_0 gives reduced insertion loss (i.e. the peak of a power transmission spectrum of a resonant mode becomes less negative). This, in turn, makes the resonator easier to couple to and increases signal-to-noise ratio. Although useful, this in itself does not increase the sensitivity of a resonator. Improved sensitivity arises from maximising the difference in quality factor between the perturbed and unperturbed states of the resonator. This requires careful design of the resonant sensor, so that the proportional volume of perturbed fields occupied by the sample is maximised.

The coaxial resonator has generally been overlooked in favour of other resonators due to the losses associated with the coaxial geometry. This results in quality factors of approximately 1000, which are lower than for cavity or dielectric resonators but higher than for planar resonators. The losses of the coaxial resonator arise from the dielectric loss of the spacer and from the surface resistance of the conductors. Any form of power dissipation will reduce Q given that Q is proportional to the ratio of energy stored to power loss. Most coaxial cables incorporate a dielectric spacer to keep the axes of the inner and outer conductors coincident. Any spacer with finite dielectric loss ε_2 will dissipate power. A commonly used spacer material is PTFE which has a loss tangent $\tan\delta = \varepsilon_2/\varepsilon_1 \simeq 2.5{\cdot}10^{-4}$ at 1 GHz. One possible method for counteracting this reduction in Q would be to use an air-spaced coaxial line, although this would still require dielectric washers to hold the inner conductor in place. The power dissipation arising due to the surface resistance of the conductors could be reduced by using higher conductivity materials such as silver or a superconductor. Aside from the cost of such an approach, which is likely to be prohibitive for miniaturised point-of-sampling measurement devices, superconductors will have a so-called crossover frequency when their surface resistance becomes comparable to that of a metal, which can occur at microwave frequencies. The use of a superconducting coaxial resonator may therefore not be of any significant advantage although it is dependent on many factors including the temperature of operation. The reader is referred to [123] for a detailed consideration of a coaxial cavity with a superconducting inner conductor.

However, a resonant sensor design procedure would be more complete if it did not focus on the maximisation of Q at the expense of all other experimental considerations. For example, it will be shown that transmission measurements can be used to obtain multi-frequency information from one end of a coaxial resonator, allowing it to be evanescently perturbed at the other end. The sensor can be perturbed in a multitude of ways given that the sensing fields are not located inside the resonator. The first two chapters argue that such an approach is more suitable for the aims of this project.

3.1. Methods

3.1.1. Electromagnetic design

Resonators require one coupling port for reflection measurements and two for transmission. This chapter focuses exclusively on transmission measurements, for which there are several justifications, to show that such measurements allow the use of weak coupling.

Firstly, in weak coupling, the requirement for careful network analyser calibration is reduced as only a minor correction is required to convert quality factor measurements from loaded to unloaded in order to quantify dielectric loss. This is noteworthy considering the eventual aim of developing 'black box' dielectric spectroscopy, where a non-specialist user would be able to collect measurements without knowing the intricacies of the measurement technique or having to perform a rigorous calibration.

Secondly, weak coupling means the coupling structures do not significantly alter the electromagnetic field distribution compared to the empty cavity, making the extraction of coupling-independent resonator parameters easier. This reduces the experimental procedure by enabling the resonance parameters to be extracted unambiguously.

Thirdly, the fact that performing a measurement in transmission rather than reflection removes calibration dependence implies that the measurement does not necessarily have to be performed with a network analyser. This means microwave frequency devices that have attracted funding for mass-production and miniaturisation in other industries (e.g. in wireless communications) could be used to implement the associated technology required for resonator measurements. This gives rise to the potential for low-cost, miniaturised hardware for point-of-sampling applications.

In contrast to the benefits associated with transmission methods, reflection techniques require much stronger coupling to give a measurable resonance. This is because a large insertion loss under weak coupling conditions would give a reflection coefficient too close to 0 dB to allow reliable extraction of experimental

parameters. It is considered poor metrological practice to attempt to measure a weakly-coupled resonance in reflection [22], so it is not possible to directly compare the two methodologies with a single device.

A transmission line resonator is formed when the end conditions of a section of transmission line are such that an incident wave reflects off of both ends to form a standing wave. Consider a transmission line terminated with some arbitrary load Z_L, as shown below.

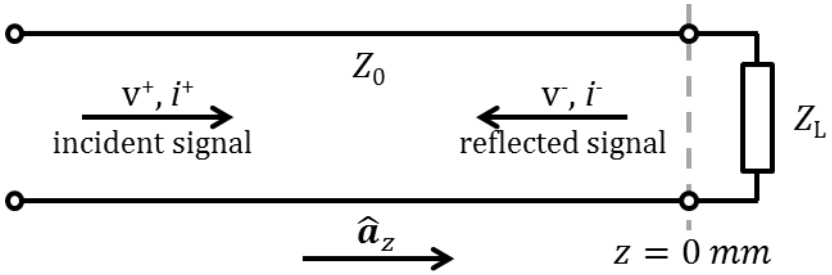

Figure 3.1: Transmission line, where the incident signal is wholly or partially reflected due to mismatch between the line and load impedances.

The incident and reflected voltages are $v^+(z,t) = V_0^+ e^{j(\omega t - \beta z)}$ and $v^-(z,t) = V_0^- e^{j(\omega t + \beta z)}$, respectively. The incident and reflected currents are $i^+(z,t) = V_0^+ e^{j(\omega t - \beta z)}/Z_0$ and $i^-(z,t) = -V_0^- e^{j(\omega t + \beta z)}/Z_0$, respectively. It follows that the load voltage V_L and current I_L are given by:

$$V_L = V_0^+ + V_0^- = (1 + \rho_V)V_0^+, \tag{3.2}$$

$$I_L = I_0^+ + I_0^- = (1 + \rho_I)I_0^+, \tag{3.3}$$

where the voltage reflection coefficient ρ_V at the load is defined as:

$$\rho_V = \frac{V_0^-}{V_0^+} = \frac{Z_L - Z_0}{Z_L + Z_0}, \tag{3.4}$$

and the current reflection coefficient ρ_I at the load is defined as:

$$\rho_I = \frac{I_0^-}{I_0^+} = \frac{Z_0 - Z_L}{Z_0 + Z_L}. \tag{3.5}$$

The inequality $0 \leq |\rho| \leq 1$ holds true for both reflection coefficients. The condition $|\rho| = 0$ implies zero reflection and $|\rho| = 1$ implies complete reflection. Under open circuit conditions (i.e. as $Z_L \to \infty$), $\rho_V = 1$ and $\rho_I = -1$. This means there is maximum load voltage (from Equation 2.1) but zero load current (from Equation 3.3). Therefore if an electromagnetic wave is to be perfectly reflected by an open-circuited transmission line (as required for resonance), the open circuit must correspond to a point in space where the incident wave has maximum electric field and zero magnetic field. Similarly under short circuit conditions (i.e. as $Z_L \to 0$), $\rho_V = -1$ and $\rho_I = 1$. This means there is zero load voltage (from Equation 2.1) but maximum load current (from Equation 3.3). Therefore if an electromagnetic wave is to be perfectly reflected by a short-circuited transmission line, the short circuit must correspond to a point in space where the incident wave has zero electric field and maximum magnetic field.

A section of transmission line will resonate if the end conditions mean an incident wave is repeatedly reflected inside the waveguide in such a way that it constructively interferes by forming a standing wave. Such a resonance is a transverse electromagnetic (TEM) mode because there are no electric or magnetic field components in the direction of propagation. That is, the electric and magnetic field components are transverse to the direction of propagation.

A coaxial TEM resonator can therefore be formed of a section of coaxial line where the end conditions must be comprised of one of three combinations: open-open, short-open or short-short. Cross-sectional schematics of each of these coaxial resonator field distributions are illustrated in Figure 3.2, where the red-white colourmap represents electric field magnitude and the blue-white colourmap represents magnetic field magnitude.

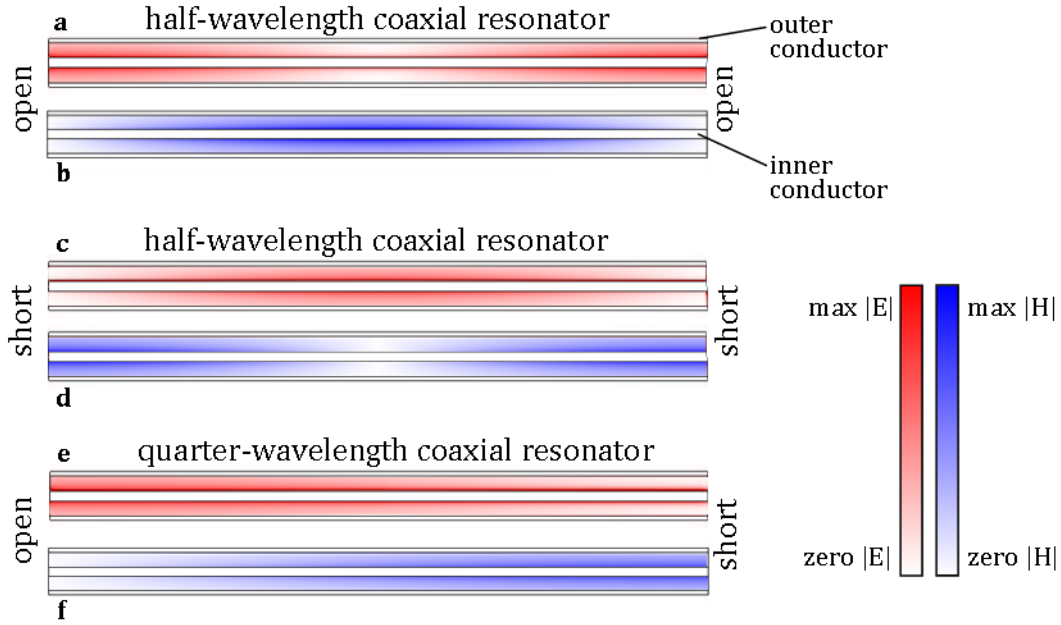

*Figure 3.2: Cross-sectional views of the electric (**a**,**c**,**e**) and magnetic (**b**,**d**,**f**) field distributions for various coaxial resonators. Each one has different end conditions: those shown include open-open (**a**,**b**) and short-short (**c**,**d**) half-wavelength configurations and an open-short (**e**,**f**) quarter-wavelength configuration.*

If both end conditions are the same, the length of the coaxial section will correspond to a half-wavelength of a sinusoidal standing wave because the nodes/antinodes required by the boundary conditions will be a half cycle apart. Likewise a resonator where the end conditions differ requires maximum electric and zero magnetic fields at one end and the opposite situation at the other end. The corresponding nodes/antinodes of a sinusoidal electromagnetic wave will be a quarter of a cycle apart, so the length of such a resonator will correspond to a quarter-wavelength of the standing wave. In both cases these standing waves are of the lowest possible frequency (longest possible wavelength) that can be supported. Both types of resonator will support higher order TEM modes (i.e. harmonics) with shorter wavelengths, which can fit an extra half-wavelength or integer multiple thereof in between the bounded ends of the resonator.

These resonances can be excited if the internal fields of the resonator can be coupled to. This requires a coupling structure of appropriate field distribution to induce an incident wave of appropriate wavelength to resonate within the structure. A structure with both ends short-circuited is necessarily completely

enclosed (i.e. all fields are confined), meaning that such a coupling connection will be inherently invasive and will require some discontinuity in the transmission line. Conversely an open-circuited transmission line will have evanescent fields at both ends of the resonator because it is impossible for the fields to remain completely confined by a structure that has a gap precisely where the maximum electric field is located. Thus a transmission line resonator with open-open end conditions will generally have more easily accessible fields in comparison with a resonator with short-short end conditions. A quarter-wavelength resonator with short-open end conditions may or may not be advantageous, depending on how the structure is coupled to and perturbed. This approach would allow smaller resonators to be used for operation in the same frequency range as the half-wavelength equivalent. However open-circuited half-wavelength resonators are the simplest to couple to and perturb, and are generally used in preference to the alternatives throughout this work.

There are two methods of coupling to resonator fields: via electric field interactions, and via magnetic field interactions. These are referred to as capacitive and inductive couplings, respectively. Capacitive coupling tends to be implemented with an open-ended coaxial termination with a protruding, straight inner conductor, as shown in Figure 3.3 **a**. Inductive coupling is normally formed in a similar fashion, except the protruding inner conductor is curved back on itself to form a loop, as shown in Figure 3.3 **b**.

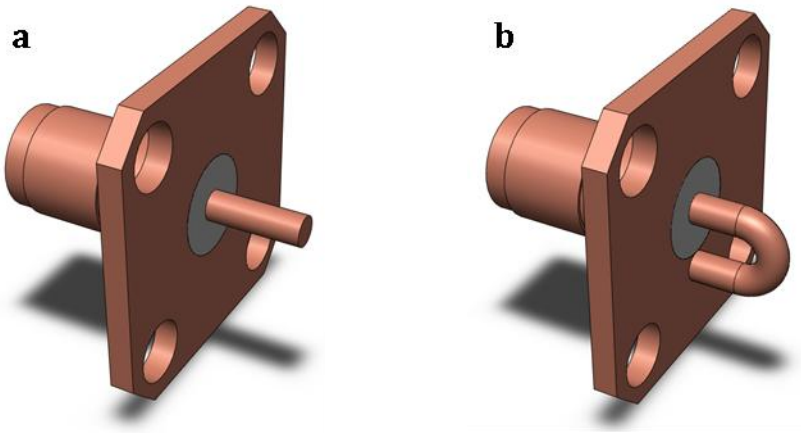

*Figure 3.3: SMA connectors featuring protruding inner conductors for (**a**) capacitive and (**b**) inductive coupling, where the loop would usually be soldered to the ground flange of the connector.*

These can be used to interrogate a resonator by orienting them so that the coupling field distribution corresponds to that of the resonator. Inductive couplings, for example, should be oriented such that the plane of the loop is normal to lines of magnetic field. In comparison with capacitive coupling, inductive coupling loops tend to act as a resonator and generally have a less broadband response due to parasitic modes.

Coaxial cable is comprised of an inner conductor (of radius a), dielectric spacer, and cylindrical outer conductor (of inner radius b). The characteristic impedance Z_0 of this type of transmission line is given by:

$$Z_0 = \frac{\eta_0}{2\pi\sqrt{\varepsilon_r}} \ln\left(\frac{b}{a}\right), \tag{3.6}$$

where η_0 is vacuum impedance and ε_r is the relative permittivity of the dielectric spacer. The resonant frequencies of the TEM modes of an open-circuited half-wavelength coaxial resonator are given by:

$$f_0 = n\frac{c}{2l\sqrt{\varepsilon_r}}, \tag{3.7}$$

where $n \in \mathbb{N}$ is an integer multiple of the fundamental resonance, c is the vacuum speed of light and l is the length of the coaxial resonator.

The inductive coupling loop field pattern is not well suited to coupling to an open-circuited half-wavelength coaxial resonator as the loop has to fit between the conductors in order to be oriented normally to the magnetic field, which is particularly problematic if the coaxial resonator aperture is to be miniaturised. Capacitive coupling is rather easier to achieve for a coaxial resonator, as demonstrated below, and will therefore be used throughout this work.

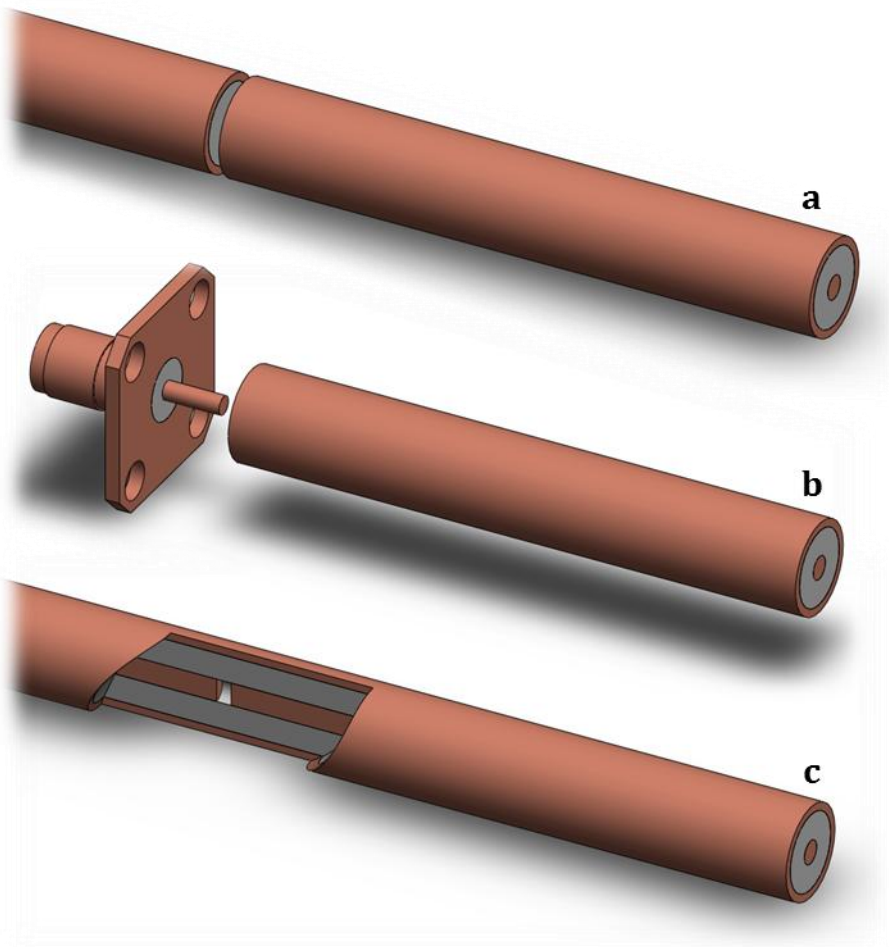

Figure 3.4: 3D schematics of different reflection coupling methods for an open-ended coaxial resonator. **a** *uses an adjacent feedline for capacitive coupling,* **b** *uses an adjacent SMA connector with protruding inner conductor and* **c** *uses a break in the inner conductor to separate the feedline and resonator whilst preventing evanescent field from escaping the confines of the structure and therefore shields it from interference.*

A reflection measurement of an evanescently-perturbed coaxial resonator is much easier to achieve than a transmission measurement because it only requires one port. The simplest method is to position a feedline adjacent and parallel to the resonant section. Several variations of this method are shown in Figure 3.4.

The size of the gap determines the coupling strength. The structure with a common outer conductor between the feedline and resonator would also achieve coupling whilst preventing interference with the coupling field. A colourmap of electric field magnitude for the gap coupled resonator (Figure 3.4 **c**) shows the capacitive coupling interaction in Figure 2.2. Data were obtained from an HF electromagnetics simulation performed in COMSOL Multiphysics (COMSOL, Burlington, MA, USA). The evanescent field, which is sometimes colloquially referred to as the fringing field, will exist a significant distance (sub-mm to mm at microwave frequencies) because the conductor separation b - a is comparable to the length of the resonator l. The resonator is perturbed simply by placing a sample in the evanescent field at one end of the resonator. The evanescent field at the other end allows a capacitive coupling interaction.

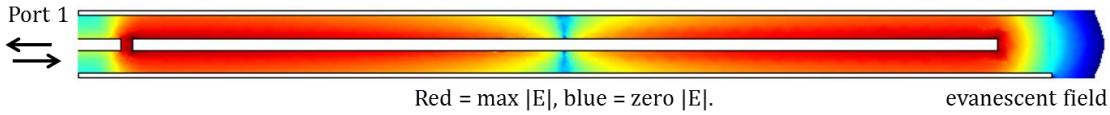

Figure 3.5: Cross-sectional schematic of an open-ended half-wavelength coaxial resonator with a colourmap representing electric field magnitude. A one port reflectance measurement is performed, where the sample occupies the evanescent field at the end of the resonant section.

The dynamic range of the reflectance approach can be increased by taking a transmission measurement, which necessitates the use of two ports. There are numerous ways of achieving this. Several examples can be seen in Figure 3.6.

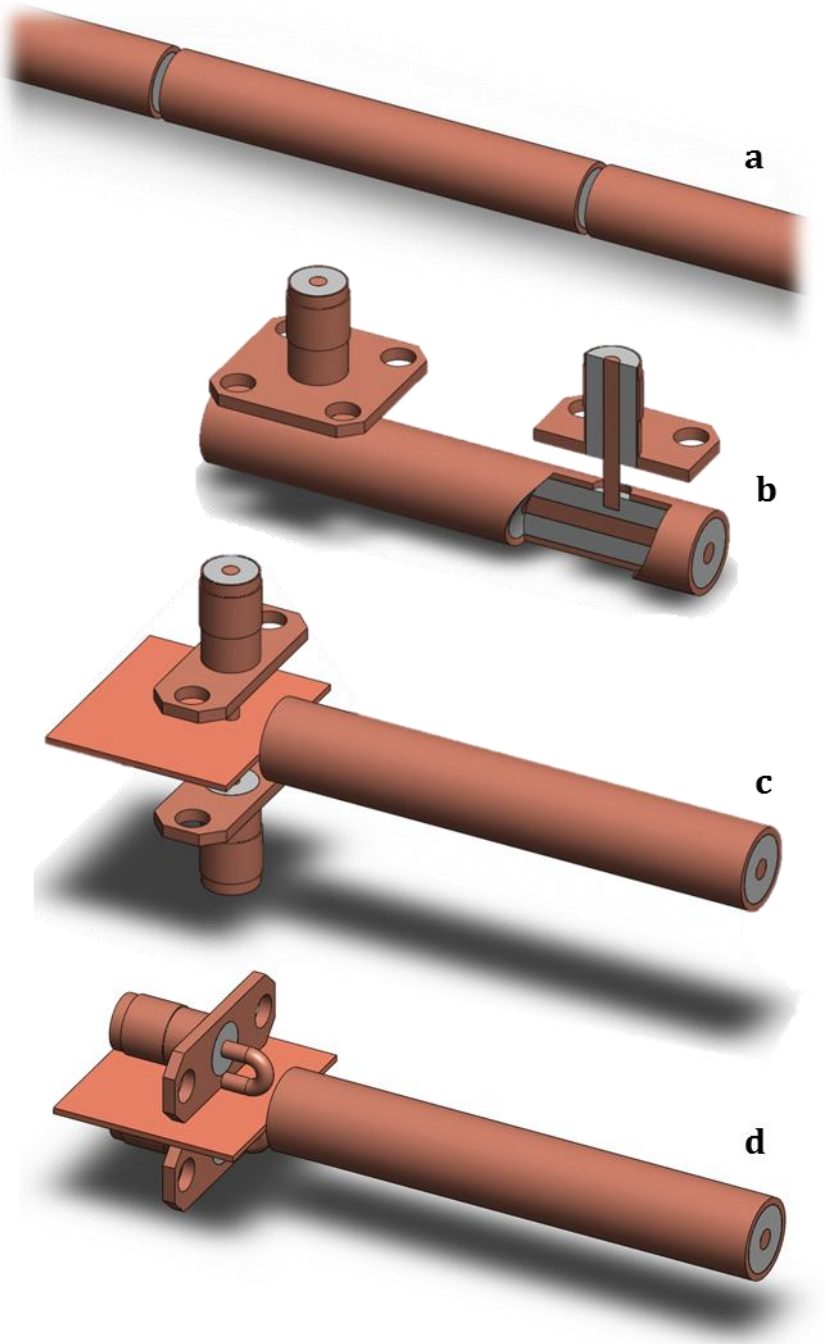

Figure 3.6: 3D schematics of different reflection coupling methods for an open-ended coaxial resonator. All use capacitive coupling except **d**, which uses inductive coupling. **a** *uses adjacent feedlines to couple to the evanescent electric field,* **b** *uses two SMA connectors to invasively interrogate the internal electric field of the resonant TEM mode,* **c** *uses two SMA connectors to couple to the evanescent electric field and* **d** *uses two loop-terminated SMA connectors to couple to the evanescent magnetic field. The ground plane between the connectors in* **c** *and* **d** *is necessary to minimise crosstalk.*

Figure 3.6 **a** shows obvious similarities with Figure 3.4 **a**. In this instance, however, this structure is more difficult to perturb because the evanescent fields at both ends of the resonator are used for coupling. It is possible to pass a capillary through the gap between the resonator and one of the feedlines in order to perturb the coupling field (which is in itself an interesting application), but preliminary simulations have shown this method to be unacceptably sensitive to the capillary position: the dimensional tolerances of capillaries introduce unacceptable uncertainties in the order of ± 10%. However, end coupling is an appropriate and useful configuration for other (differently perturbed) coaxial resonators, as discussed in Chapter 4.

Invasive couplings, where receptacles protrude through holes drilled into the resonant section as in Figure 3.6 **b**, are also possible. This approach maintains the simple perturbation of the reflectance measurement. The invasive coupling approach is fundamentally flawed in that it cannot be used to couple to higher order modes with nodes located adjacent to the receptacles. If the coupling connectors were placed further in from the ends of the probe (which is desirable from an experimental perspective, to allow the probe to be dipped in solution or embedded in a microfluidic device), an increasing number of TEM modes would not be coupled to. This has two effects: it limits the usable frequency range of the measurement device, and will cause false readings for modes with nodes close to the receptacles. This occurs because a dielectric sample typically causes a reduction in resonant frequency, hence causing the nodes to move, which will give a false transmission measurement if a node moves closer to or further away from a receptacle.

In each of these examples it would be possible to perturb a coaxial resonator by passing a sample directly through the resonator or by having a section filled with a sample. However these approaches suffer from high uncertainty due to fabrication tolerances and they require a relatively high sample volume with a low throughput. These factors make such an approach unsuitable for the point-of-sampling applications outlined in the introduction. Reproducibility would be lessened if the filled section had to be disassembled or moved between measurements (e.g. to be cleaned, which is likely to be regularly required given the

large sample volume). This problem is shared by a significant number of other cavity and dielectric resonator techniques.

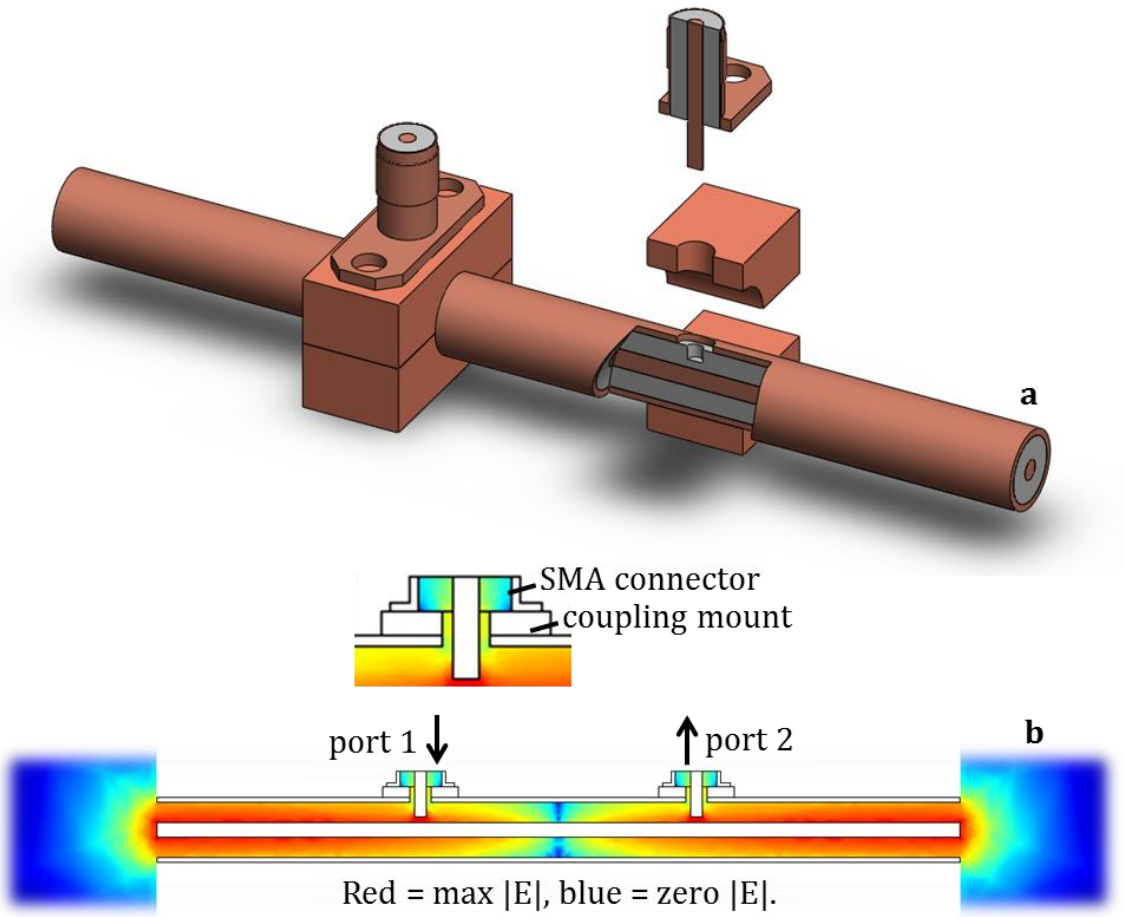

*Figure 3.7: (**a**) 3D schematic of the invasive transmission coupling for an open-ended coaxial resonator and (**b**) logarithmic colourmap of the electric field, demonstrating the capacitive coupling interaction.*

Two further methods of performing transmission measurements of an open-circuited coaxial resonator are shown in Figure 3.6 **c** and **d**. These methods use two connectors to couple to the evanescent field at a single end of the device, which leaves the other end of the device accessible for sensing. This alternative method of coupling necessitates the introduction of a ground plane to minimise crosstalk between the connectors. Otherwise, the connectors would simply couple to themselves and it is unlikely a reading could be obtained from the resonator. The inductive coupling approach shown in **c** will not be used because of the reasons outlined above. Instead, **b** and **d** will be developed further because of their

capability for capacitive coupled transmission measurements and evanescent perturbation.

Open-circuited RG401 50 Ω coaxial cable was used to form the open-ended half-wavelength resonator. It was cut and polished to a length of 8.4 cm, yielding a fundamental resonant frequency of ~ 1.25 GHz according to Equation 3.7. This gives six modes in the frequency region of interest (0.5 to 8.5 GHz) as dictated by the network analyser to be used to characterise the resonator power transmission response. This choice of length was also a suitable compromise between being a practical size and the resonator losses. Losses (which reduce Q and therefore sensitivity) increase as resistivity increases with resonant frequency and so decrease with increasing length. The cable was formed of copper conductors (of 6.35 mm outer diameter) and a polytetrafluoroethylene (PTFE) spacer (of 1.6 mm inner diameter and 5.4 mm outer diameter). These dimensions also set the aperture size and therefore the evanescent sensing field distribution. This diameter cable was chosen to be large enough to allow standard microwave components to be used for the coupling structure (i.e. SMA receptacles at the end of the resonator or protruding in from the side), whilst small enough to be perturbed with a microfluidic channel. A tapered narrowing of the aperture or an elongated and sharpened inner conductor could be used to further localise the evanescent field, which is a method frequently used to improve the spatial resolution of the microwave microscope [124], [125]. It has also recently been demonstrated with an open-ended rectangular waveguide [126], but a tapered aperture was not deemed wholly necessary for this project, particularly due to the additional geometric uncertainty that could be introduced.

A resonant device incorporating a mount that can be used to house invasive couplings is illustrated in the exploded and cross-sectional views of Figure 3.7. The distance of the coupling mount from the end of the probe (and the corresponding recesses drilled in the resonator) were set so that one end of the resonator could be inserted into a standard fluidic T-piece, so that a fluid flow through the fitting would perturb the evanescent field of the resonator. The two connectors must be arranged symmetrically along the length of the resonator to minimise the number of modes that could not be coupled to. The unperturbed end

of the resonator was shielded with a conducting flange to prevent accidental perturbation (which would not be distinguishable from the desired perturbation at the other end of the resonator), which has the fortuitous consequence of increasing field confinement and thereby increasing Q. It is for these reasons that a transmission measurement consisting of one adjacent feedline (cf. Figure 3.4 **a**) and one invasive connector was considered inferior to a design with two invasive couplings.

The inner conductor of each SMA connector and the hole in the coupling mount through which it protrudes essentially form an air-spaced coaxial line. The diameter of the connector conductor is fixed (i.e. of a standard size). Given that cables of 50 Ω characteristic impedance were to be used to connect the resonator to measurement equipment, the diameter of the hole in the coupling mount could therefore be set by Equation 3.6 (in this case, to 3.0 mm).

The coupling strength was set by the length of the inner conductors of the SMA connectors. These were set empirically to give coupling sufficiently weak to not interfere with measurement inversion, but not too weak to render the resonances unusable. In practice this meant achieving an insertion loss of approximately 40 dB for each resonance in the measureable range.

The concept of taking transmission measurements with a capacitive coupling from a single end of the resonator was introduced in Figure 3.6 **c**. This can be implemented using a coupling mount as follows:

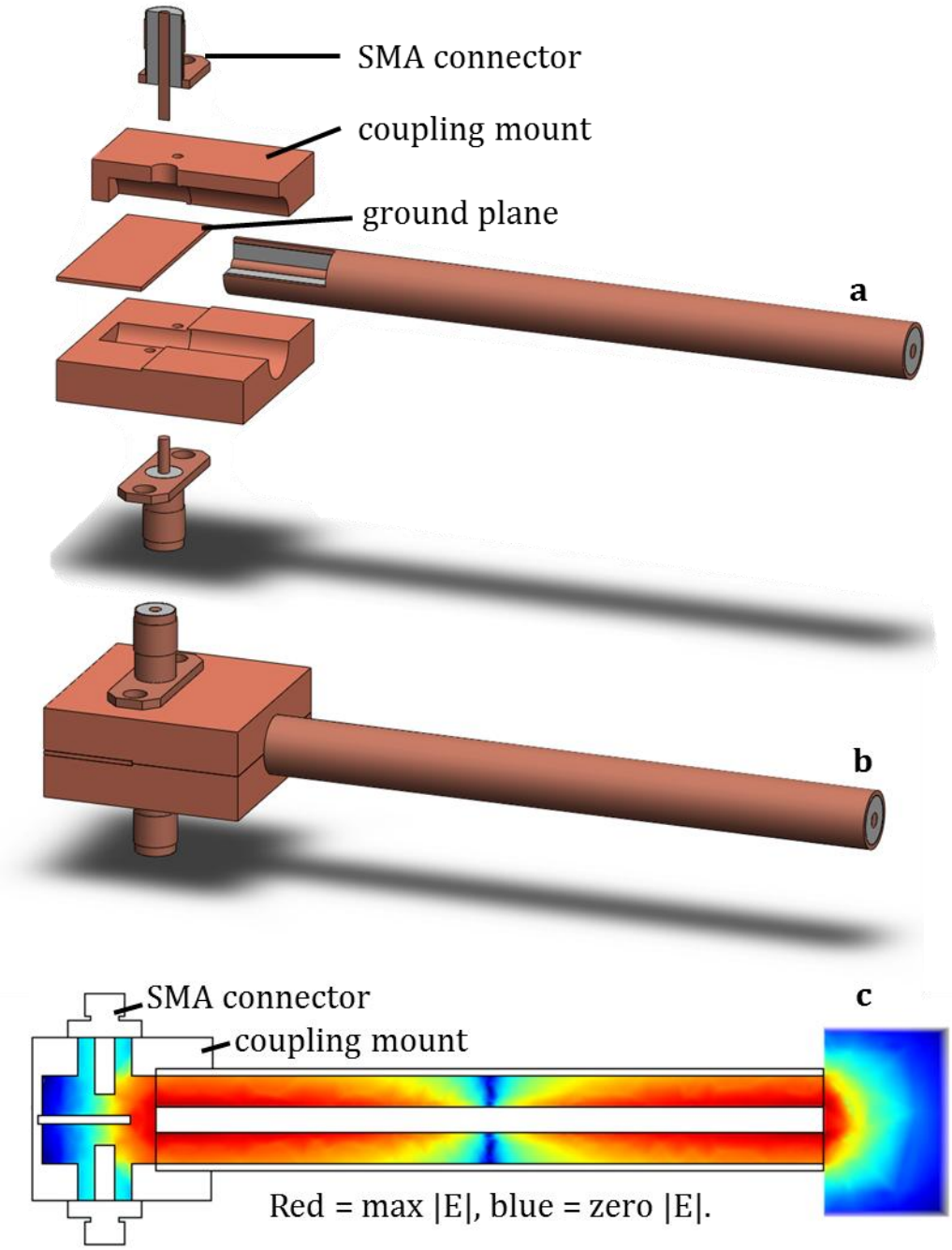

*Figure 3.8: (**a**) 3D exploded schematic of non-invasive transmission coupling for an open-ended coaxial resonator, (**b**) complete 3D schematic of the assembled device and (**c**) logarithmic colourmap of electric field, demonstrating the capacitive coupling interaction.*

Significantly, this demonstrates how single-ended transmission coupling can be achieved in order to free the other end of the resonator for liquid measurement without having to couple at suboptimal points along the length of the resonator. The electromagnetic fields were confined within the structure to prevent

interference. Crosstalk between the coupling receptacles was prevented by the careful positioning of a ground plane to avoid a reduction in dynamic range, which was defined as the difference between the peak of power transmission (at the fundamental resonance) and the noise floor. A series of simulations were used to optimise the coupling mount design. Preliminary simulations showed there were five relevant dimensions that dominated the coupling strength. These are labelled in Figure 3.9.

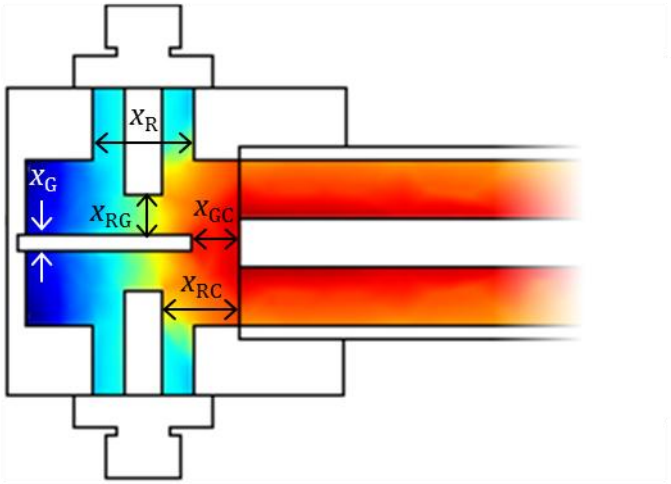

Figure 3.9: Cross-sectional view of the coupling structure showing the dimensions that dominate coupling strength.

Standard gold-plated SMA receptacles were used, and the receptacle housing diameter x_R was set to maintain the 50 Ω characteristic impedance of the feedlines according to the diameter of the receptacle inner conductor (= 1.28 mm). This was chosen for the same reason as with the invasive coupling mount (i.e. to minimise unnecessary reflections by maintaining a characteristic impedance of 50 Ω where possible) and therefore has the same diameter (x_R = 3.0 mm). The coupling coefficient was chosen to be far less than unity (i.e. the structure is very weakly coupled) so that loaded and unloaded Q can be assumed to be identical. This can be interpreted as minimising the dependence of centre frequency and bandwidth on coupling so coupling does not have to be accounted for during the inversion process. Through preliminary simulations, coupling strength was found to be predominantly determined by the resonator-receptacle separation x_{RC}, resonator-ground plane separation x_{GC}, receptacle-ground plane separation x_{RG} and the

ground plane thickness x_G. Additional parameters were also considered: the angle of the coupling receptacles could be tilted so the protruding inner conductor was closer to the resonator, for example. Another modification could be to fork the end of the centre line to give stronger coupling and potentially reduce cross-talk. Cross-sectional field distributions are shown in Figure 3.10 to compare the effects of having a forked rather than a flat profile at the end of the coaxial centre conductor.

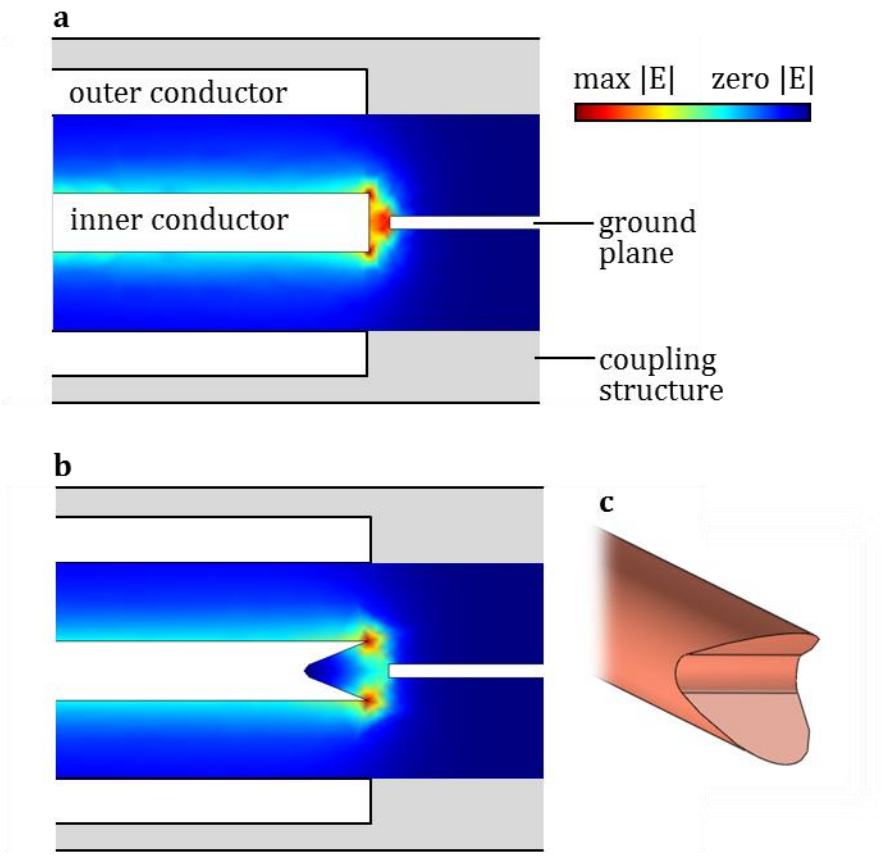

*Figure 3.10: Cross-sectional view of the coupled end of the coaxial resonator, showing the effects of having a flat (**a**) or forked (**b**) centre conductor to achieve field focussing for improved coupling strength. A schematic view showing how the forked end could be formed by cutting away the flat end of a conductor is also shown (**c**).*

However, the five dimensions labelled in Figure 3.9 were sufficient to vary coupling by the desired amount so additional degrees of freedom were not necessary. It is possible that such modifications would be necessary for

applications that require stronger coupling such as increased power handling, but this issue is discussed further in the Future Work section.

Through a series of correlated simulations, the four dimensions were optimised to maximise dynamic range whilst maintaining the weak coupling condition. It was not necessary to sweep x_R as its value was dictated by other considerations. Each dimension was assigned a reasonable set of values (i.e. those that could be machined with the available equipment) and swept with respect to all the other dimensions. The resulting optimised dimensions are given in Table 3.1. These dimensions were used to fabricate the coupling structure with which the results of this paper were obtained.

Table 3.1: Optimised resonator dimensions (resonator-receptacle separation x_{RC}*, resonator-ground plane separation* x_{GC}*, receptacle-ground plane separation* x_{RG} *and the ground plane thickness* x_G*) for the single-ended non-invasive transmission coupling structure, as labelled in Figure 3.9.*

x_{RC}	x_{GC}	x_{RG}	x_G
2.86 mm	0.25 mm	1.25 mm	0.5 mm

In contrast to the alternative coupling structures shown in Figure 3.6, this transmission coupling structure provides single-ended coupling to allow the resonator to be perturbed easily. It also allows coupling to all available TEM modes in the measurable range. Whilst the coupling was optimised for the fundamental mode, all other harmonic TEM modes exhibit the same evanescent field distribution so the probe can be used to obtain multi-frequency information. This is in specific contrast to all other resonator techniques: results will be shown for twelve sensing modes. Electromagnetically coupling different modes simultaneously means that this approach does not require unreliable mechanical adjustments (for example to the length of the resonant section) to access different frequency measurements. By perturbing the evanescent field, this resonator does not need to be disassembled between measurements. It does not suffer from large uncertainties due to the perturbation or coupling methods. The coaxial cable is easily replaceable, should the user wish to access a different frequency range with

a different number of sensing modes. The coupling structure and ground plane were machined from copper.

3.1.2. Microfluidic design

The simplest way of perturbing the evanescent field of an open-ended coaxial resonator with a liquid sample is to dip it in. This approach has commonly been adopted for broadband coaxial probes (*cf.* Literature and Theory chapter), but is generally impractical for high-throughput applications where many samples are to be characterised. In order to have real-world relevance for the intended applications of this project, it must be capable of through-flow measurements of some sort.

The simplest type of flow measurement is to use a fluidic T-piece. This approach is shown in Figure 3.11, which shows a stainless steel fitting (Swagelok, OH, USA).

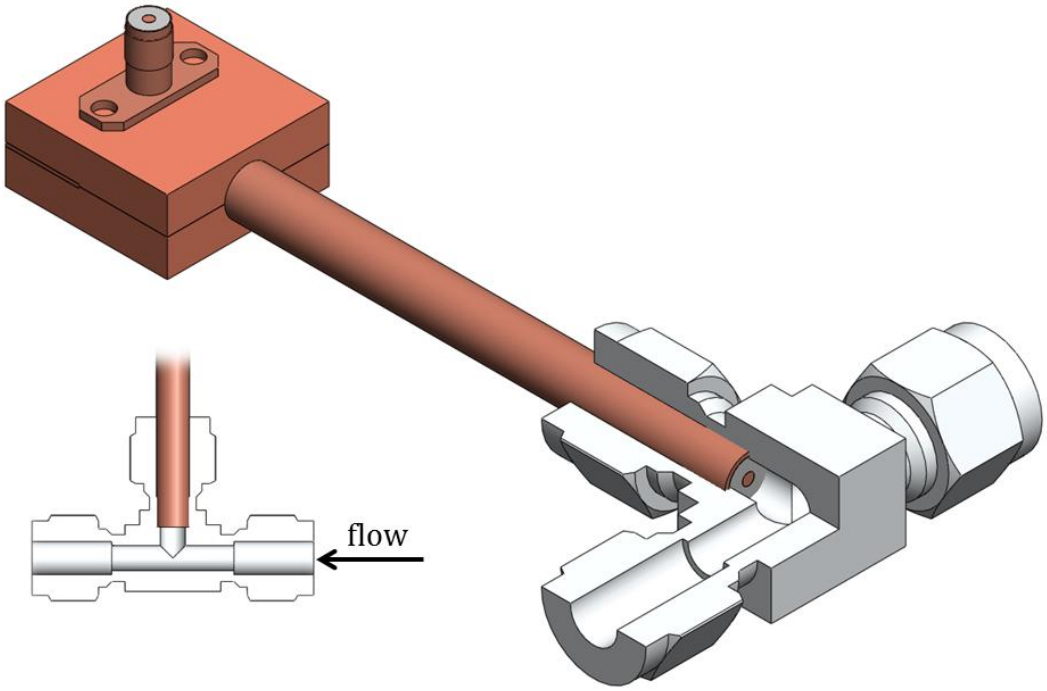

Figure 3.11: Schematic view of a resonant coaxial probe mounted in a fluidic T-piece for simple through-flow measurements.

Each of the T-piece branches is of a quarter-inch diameter. This corresponds to the coaxial resonator probe aperture (as described in the previous section), and also to a widely used size of stainless steel tubing. This approach is extremely simple and

robust, and can easily be implemented in existing flow systems with few modifications. Possible applications include industrial monitoring, where a small feedline could run off of and flow parallel to a reactor for continuous process control. A PTFE disc could be included at the end of the probe (i.e. to sit between the probe aperture and liquid sample) for several reasons. It would improve chemical compatibility due to the chemically inert properties of PTFE; it would also prevent fluid from reacting with the copper conductors or entering the resonator via capillary action. This latter effect would affect the permittivity region occupied by the internal fields and therefore the probe resonances in an uncontrolled fashion.

However, there are drawbacks to using a fluidic T-piece. The sensing volume is large (in the order of ml) and of irregular shape, and the Reynolds number is too high for flow to be laminar. This means that dead volumes could occur at the probe interface, leading to false results where flow composition could be drastically altered but not in the vicinity of the evanescent sensing field. Therefore, using the T-piece is a useful method for proof-of-principle resonator experiments but not for biochemical and pharmaceutical applications.

There are numerous ways of implementing a microfluidic interface, as discussed in the Literature and Theory section. However, an approach based on that demonstrated in [98] was chosen for the resonant coaxial probe for several reasons. The use of a compression-sealed PTFE substrate allows for rapid prototyping of robust microfluidic devices because it can be micromachined with standard circuit board fabrication equipment. Not only does PTFE offer excellent chemical resistance, but it is also preferable to curable resin or glass substrate materials from a microwave measurement perspective because of its extremely low dielectric loss ($\tan\delta \approx 2.5 \times 10^{-4}$). It also has a small relative permittivity (around 2), leading to minimal electric field modification due to its polarisation.

The fact that evanescent field perturbation (or any form of microwave-frequency resonator perturbation) is unaffected by whether a sample is solid, liquid, gas or transparent, means it retains key advantages over optical spectroscopic techniques for on-chip microfluidic characterisation. This method of sample interfacing is

equally capable of characterising suspensions given that the phase separator described in [98] was implemented in a similar compression-sealed PTFE microfluidic device and used to manipulate 2 μm diameter polystyrene beads in suspension. Earlier sections established that resonator perturbation provides a volumetric average of permittivity for a given material under test whilst remaining unaffected by the state of matter of the material. The presence of solid material in a liquid sample is therefore of no consequence as long as an even dispersion of solid material is maintained.

Thus, embedding the resonant coaxial probe in a microfluidic device provides a generic, adaptable method of enabling the potential of dielectric spectroscopy for non-contact and non-invasive measurements of liquids and suspensions. The chosen interface is illustrated below:

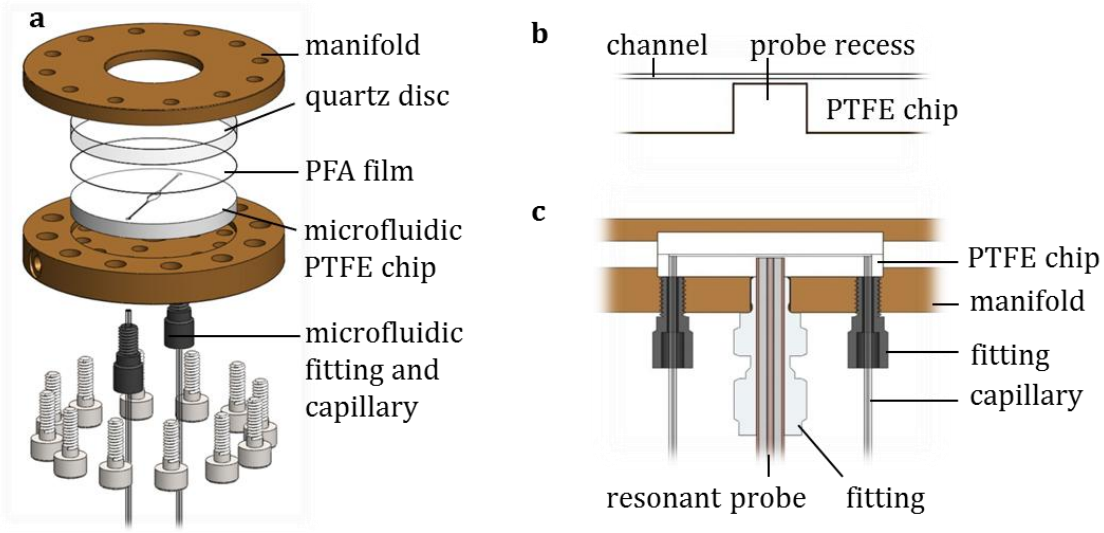

*Figure 3.12: (**a**) Exploded view of the brass compression-seal microfluidic manifold, (**b**) cross-sectional view of the microfluidic PTFE chip and (**c**) cross-sectional view of the integrated microfluidic device with an embedded coaxial resonator.*

An exploded diagram of the compression-seal manifold is shown in Figure 3.12. The microfluidic chip was formed from an appropriate substrate, chosen in this case to be a circular PTFE disc. This enabled microfluidic channels to be milled in the upper side of the disc and a probe recess in the lower side. Such an approach allows many planar microfluidic circuits to be realised whilst providing an interface for the resonant probe. By embedding the probe in the back of a PTFE

chip, a constant volume of liquid sample can be maintained at a constant distance and at a constant temperature. By fixing evanescent field perturbation in this way, any measured changes must be due to changing fluid composition. The device could then be compression-sealed against the coverplate (and gasket layer, included to ensure a reliable seal) within the brass manifold. The rigidity of the manifold and the large number of screws used to provide compression meant the force was evenly distributed across the microfluidic device. A further thin layer of transparent film could also be introduced between the coverplate and manifold to prevent any slight imperfections on the surface of the manifold from shattering the coverplate.

Holes drilled through the device allowed capillaries to be connected via tapped holes in the underside of the manifold. The capillaries could then be attached to external pumping devices as required. The use of appropriate capillary fittings to interface the microfluidic circuit allowed a gas-tight seal to be preserved for the whole device.

The underside of the manifold had a tapped hole in its centre to allow a fluidic fitting (primarily used for quarter-inch stainless steel tubing, but equally useful for RG401 coaxial cable) to screw in and hold the resonant probe rigid with respect to the manifold. The probe itself did not come into contact with the fluid: a 100 μm separating layer of PTFE was kept between the resonator and the microfluidic channel in order to maintain chemical compatibility, to prevent fluid ingress into the resonator and to prevent conductor corrosion. As thin a layer as possible is desirable so that the liquid sample can occupy as much of the evanescent field as possible. This increases the filling factor and therefore the sensitivity of the device. The 100 μm thickness was chosen because it was the smallest feasible gap that could reliably be machined in the microfluidic chip with the available micromachining equipment.

The presence of a separating layer between the resonator and the sample under test meant the geometry was depolarising, as illustrated in Figure 3.13.

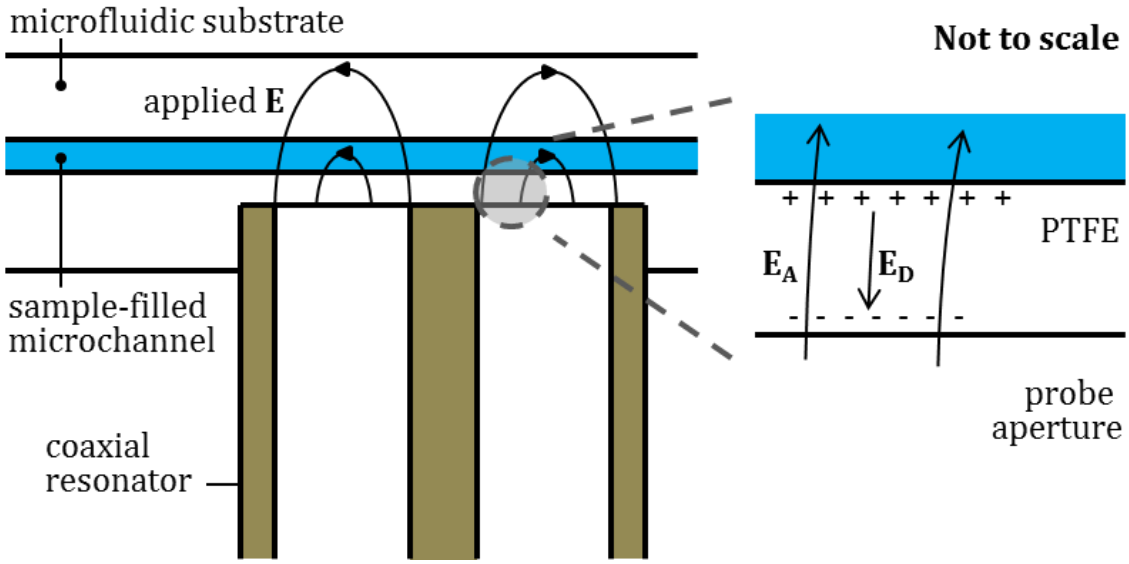

Figure 3.13: Cross-sectional schematic of the depolarising microfluidic interface for the resonant coaxial probe. The exploded view shows induced charges on the PTFE layer separating the probe and the microfluidic channel. These charges are induced by the applied evanescent electric field $\mathbf{E_A}$ *and give rise to an opposing depolarisation field* $\mathbf{E_D}$.

The separating layer between the probe and the microfluidic channel was included for experimental reasons, as described above. Depolarisation was an inevitable consequence of including the separating layer because a boundary between two materials of differing permittivity will accumulate bound (i.e. polarisation) charge under an applied electric field. The depolarising charges cause an opposing electric field that acts to reduce the applied electric field within the material of higher permittivity. To have the probe recess drilled through to the microfluidic channel so that the resonator was in direct contact with the fluidic sample would prevent depolarisation, but would also negate the use of a PTFE microfluidic substrate. This was an unavoidable design constraint, so the resonant device can never be maximally sensitive when implemented in this fashion. The careful design of the coupling structure affords some flexibility with sensing field perturbation, so this compromise is considered acceptable.

The low permittivity and dielectric loss of the PTFE substrate ensures the sample permittivity is not screened. The upper layer of quartz has a significantly higher permittivity. If a coverplate of quartz rather than PTFE is used, there will be

greater field confinement beyond the boundaries of the microfluidic channel given that quartz has a comparably low dielectric loss but higher relative permittivity, thereby increasing sensitivity.

3.1.3. Experimental

Two types of coaxial resonator, using single ended (Figure 3.8) and invasive couplings (Figure 3.7), were fabricated according to the designs outlined in Section 3.1.1. Each structure incorporated copper coupling mounts, gold-plated SMA receptacles and RG401 coaxial cable. The resonant sections of coaxial cable were cut to length and polished with a succession of increasingly fine grit papers. The invasively coupled resonator was cut to a length of 8.4 cm, corresponding to a fundamental resonance of approximately 1.25 GHz. Holes were filed through the outer conductor and a recess was then drilled into the PTFE spacer to allow the extended inner conductor of the SMA connector to protrude into the resonator.

Resonant sections of coaxial cable were cut and polished in the same way for the single ended coupling structure. One advantage of this coupling structure was that the resonant section was interchangeable, so two resonators were used throughout. One resonator had a fundamental resonance of approximately 1.25 GHz to allow comparison with the invasively coupled resonator. A longer resonator of length 17.5 cm with a fundamental resonance of approximately 0.6 GHz was also prepared. This approach provided far more measureable sensing modes in the available frequency region. Note that the coaxial cable could be curved with no significant detrimental effects (as long as a constant cross-section was maintained) to make the complete device less unwieldy.

The first six TEM modes of the 8.4 cm device had quality factors in the region of 800 – 900. The first fifteen modes of the 17.5 cm resonator had Q = 1000 – 1200. The higher frequency resonator was to be used for the characterisation of solvents, solvent-solvent mixtures and segmented flows, whereas the lower frequency resonator was to be used for solute-solvent mixtures. The longer probe was used to interrogate solute-solvent mixtures because of the increased molecular size and the anticipated lower frequency of the associated relaxations and interactions. The coupling structures were machined in-house from block copper. Various

microscope measurements were used to ensure the structure was machined correctly. Both coupling structures were then assembled according to Figure 3.7 and Figure 3.8.

An Agilent E5071B VNA (Agilent, CA, USA) was used to measure the power transmission coefficient of the assembled resonant devices. The shortest, highest quality cables and the fewest, highest quality connectors were used to connect the resonant devices to the VNA. A power transmission spectrum for the shorter 1.25 GHz resonator is shown in Figure 3.14.

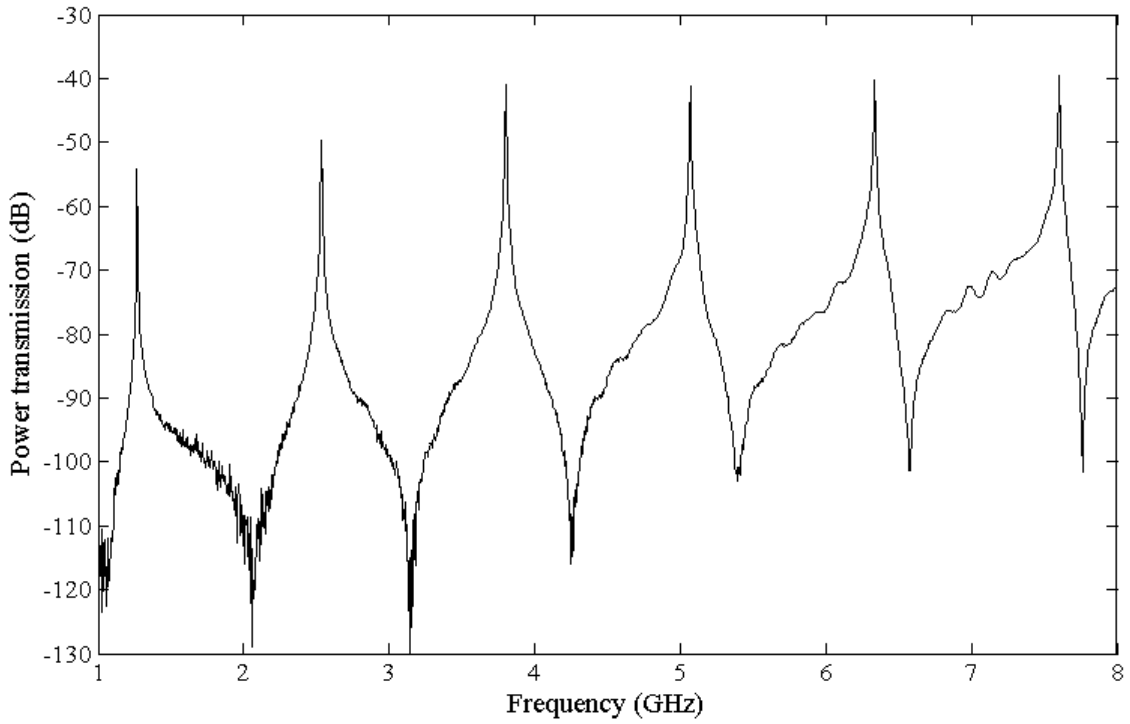

Figure 3.14: Example power transmission spectrum of the 1.25 GHz coaxial resonator, as obtained with a vector network analyzer. The peaks correspond to a fundamental 1.25 GHz resonance and the subsequent five harmonic TEM modes.

This spectrum represents the typical raw data obtained directly from a network analyser. From this type of measurement, centre frequency and quality factor can be extracted. Performing another measurement after the introduction of a sample (which is likely to cause each mode to broaden and shift to the left) allows changes in complex frequency and therefore permittivity to be computed. It is obvious from this figure how much frequency information is available with the overmoded

coaxial resonator technique: the centre of each power transmission peak represents a discrete frequency at which permittivity can be calculated. Note that a lower fundamental frequency (such as that demonstrated by the longer coaxial resonator) would provide more harmonic sensing modes within a given frequency region.

For each measurement, the data were exported to LabVIEW (National Instruments, TX, USA), where a Lorentzian curve was fitted to the peak of each resonance in real-time. The fitted curve data were then used to measure the resonant frequency and bandwidth of all modes. This was done in preference to using bandwidth marker data from the network analyser because the E5071B VNA calculated bandwidth from the points nearest to half power. This is obviously undesirable, so an interpolated method was more appropriate. A very low coupling coefficient ensured that the resonance was undistorted by coupling, so the peak of power transmission at each resonance was Lorentzian. A segmented frequency sweep was used to measure all modes simultaneously, where each segment was maintained at $1.5f_B$ for optimal curve fitting [127]. This means that the peak of each mode of Figure 3.14 was characterised, but the majority of the power transmission data between each peak was not recorded. Excluding the data not required for calculating permittivity allowed an improved sampling rate.

Because the electromagnetic interaction between the evanescent field and the sample is virtually instantaneous, the measurement period is set by the speed of the network analyser and the method used to deliver the sample rather than the evanescent field interaction. The measurement period of this experimental setup was limited by the USB 2.0 data transfer rate from the network analyser and the PC performing the curve fitting algorithms. The maximum measurement rate was 20 Hz. The use of external triggering (for the VNA) could increase this rate to at least 50 Hz, although a PXI implementation of a vector signal generator-vector signal analyser system could markedly improve the measurement rate, to a rate of 1 kHz and beyond [8].

With an appropriate microfluidic system, the chemical composition of the material under test could be changed continuously. This could be achieved with planar mixing techniques on chip, or with some bulk external method.

For the T-piece implementation (Figure 3.11), the resonator was mounted in a standard Swagelok fluidic T-piece with quarter-inch fittings in an identical fashion to stainless steel tubing. A 100 μm PTFE disc was placed at the end of the resonator to prevent fluid ingress and corrosion of the copper conductors, and generally to improve chemical compatibility. This disc meant that it was only the evanescent field at the open end of the resonator that was perturbed with a dielectric sample.

For individual (discrete) measurements, it was not necessary to connect the T-piece into a flow system. Under these circumstances, a reference air measurement was taken first. The probe aperture was then immediately immersed in a large volume (~ 30 ml) of sample solvent to obtain the sample measurement. The sensor was angled to prevent the formation of bubbles at the probe aperture. The temperature of the environment was maintained at 25 °C with a water bath.

For the compression-sealed microfluidic implementation (Figure 3.12), a Protomat C10 milling machine (LPKF, Garbsen, Germany) was used to mill microfluidic channels in a PTFE disc (of 50 mm diameter and 3 mm thickness; Fluorocarbon, Hertford, UK). A smooth finish was then obtained by polishing the surface of the microfluidic chip with a succession of increasingly fine grit papers. The manifold (Figure 3.12 **a**) was precision machined from brass. 1 mm recesses were machined on the inner faces of both parts of the manifold to keep the microfluidic device aligned with its coverplate. In most experiments, coverplates of either quartz or PTFE were used. A 50 μm gasket layer of PFA film (Goodfellow Cambridge, Huntingdon, UK) was required between the PTFE and coverplate to ensure a reliable seal. Other fluoropolymer films of similar thickness were also found to perform this function equally well.

Two microfluidic chips were used for single-phase fluid measurements. The first was comprised of a single straight channel with 400 μm square cross-section. The

second was comprised of a single straight channel with 400 μm square cross-section that widened out above the coaxial resonator to the full width of the probe aperture (≈ 5.4 mm). Another device was used for multi-phase measurements. This was comprised of two inlets combining together at a T-junction, followed by a meandering channel terminating in a single outlet. Segmented flow was generated on-chip through the combination of two immiscible inflows at the T-junction, causing alternating fluid partitions to flow in the orthogonal branch channel and exit the opposite side of the chip after flowing the length of the meandering channel. For the multi-phase flow chip, 400 μm square cross-section channels were used throughout.

The upper portion of the manifold (Figure 3.12 **a**) contained a view hole for monitoring device action, assuming a transparent coverplate was used. The lower portion contained a number of tapped holes to allow fittings to be inserted and tightened against the underside of the PTFE chip. The cross-sectional view of Figure 3.12 **b** shows how capillaries can be situated in through-holes drilled in the PFTE chip and secured with gas-tight fluidic fittings (Upchurch Scientific, WA, USA). FEP capillaries (Upchurch Scientific) were used to connect syringe pumps. KDS 200 series syringe pumps (KD Scientific, MA, USA) were used to pump each individual phase at 50 μl min^{-1}. This flow rate was maintained for multi-phase measurements as well, giving an average multi-phase flow rate of 100 μl min^{-1} for the segmented flow experiments.

HPLC-grade solvents (Sigma Aldrich, MO, USA) were used for all presented experiments. Fresh (previously unopened) samples were used for each test, and were used as supplied. The only exception to this was the use of deionised water, which was obtained from an ELGA Purelab UHQ system for Type I purified water with a resistance of 18.2 MΩ·cm. Where solutes were required, the highest available purity was purchased and used as supplied. Where solutions of varying (decreasing) concentration were required, a serial dilution was performed with the appropriate solvent. Standard health and safety and fluid handling precautions were followed throughout.

3.1.4. Measurement inversion

Generally, complex permittivity can be computed from measured changes in complex frequency (defined in Equation 2.31) via analytical, numerical or empirical means. The analytical approach matches the modes either side of the probe aperture. For example, the internal fields of a broadband coaxial probe are propagating modes whereas the external fields are evanescent modes [128]. This approach is sufficient for simple geometries, such as where the dimensions of the sample are large enough that the probe behaves as if it were exposed to an infinitely large sample. For more complex geometries, such as a microfluidic channel across the probe aperture, such a task becomes much more complicated.

Additionally, certain assumptions do not hold for the evanescently-perturbed coaxial resonator as presented here. For example, a conducting flange is commonly included in broadband measurement techniques. This will approximate to an infinite ground plane (which simplifies the analysis) when the flange is at least four times greater than the aperture width [129].

The inclusion of a conducting flange at the aperture of the evanescently-perturbed coaxial resonator was considered. To date, it has not been possible to fabricate a flanged device that is capable of interrogating a flow system whilst preserving a reliable fluidic seal. One possible solution would be to use a tapered aperture. This would improve spatial resolution by localising the evanescent sensing field in a fashion similar to the microwave microscope [130]. This geometry could behave as if it had an infinite half-plane by preserving the outer diameter of the outer conductor but reducing the other dimensions to narrow the aperture. Such a device could then be implemented in either of the suggested fluidic interfaces, as shown in Figure 3.11 and Figure 3.12. However, inversion techniques were better suited to inverting the measurements performed with the evanescently-perturbed coaxial resonator, as discussed in the following paragraphs.

The numerical inversion method is based upon simulating changes in the complex frequency of a resonant sensor according to a sweep of sample permittivity. This allows permittivity to be estimated from an arbitrary change in complex frequency by interpolating the simulation data. Clearly, this is dependent on the accuracy of

the simulation. This computationally intensive nature of this inversion method means that it is somewhat restrictive. This is particularly significant for the integrated microfluidic sensor shown in Figure 3.12, where the use of a new microfluidic chip would require all simulations to be repeated. However, this would not be as large a problem for industrial process control applications, for example, where the sensor geometry would never change appreciably.

The final inversion method is the empirical approach. This works by a similar principle to the numerical method as it requires the measurement of one or more calibration materials of known permittivity. This allows an inversion function to be interpolated from changes in complex frequency associated with the known values of complex permittivity. It is likely that the inversion function would be non-linear over large changes in permittivity due to the depolarising geometry.

This method is unaffected by uncertainties in any underlying assumptions in the inversion as the calibration and sample measurements are performed in an identical geometry. Any non-linearities due to depolarisation could also been accounted for by using calibration materials with a large range of permittivity. However, the uncertainties of this method are not traceable to international standards so it would be unsuitable for specific tissue absorption measurements of tissue equivalent materials, for example [131].

3.2. Results

3.2.1. Invasively coupled resonator

The resonant frequency and quality factor of the first six TEM modes of the unloaded invasively coupled resonator are shown in Table 3.2.

Table 3.2: Unloaded resonant frequency and quality factor of the first six TEM modes of the unloaded invasively coupled resonator.

Mode	1	2	3	4	5	6
f_0 (GHz)	1.32	2.63	3.94	5.27	6.58	7.88
Q	341	528	341	576	727	327

The complex frequency response of the invasively coupled resonator is shown with respect to percentage volume of acetic acid in toluene in Figure 3.15. Note that the percentage volume refers to the minor component of acetic acid dissolved in the major component of toluene. These data were obtained by dipping the probe a fixed distance (≈ 5 mm) into a bulk sample (≈ 20 ml). This meant a depth greater than 1 cm was maintained between the bottom of the fluid-filled vessel and the probe aperture so the probe behaved as if it were immersed in an infinitely large sample. This was verified by positioning a finger (which is mostly water) a similar distance from the probe aperture: no deviation in complex frequency was detected.

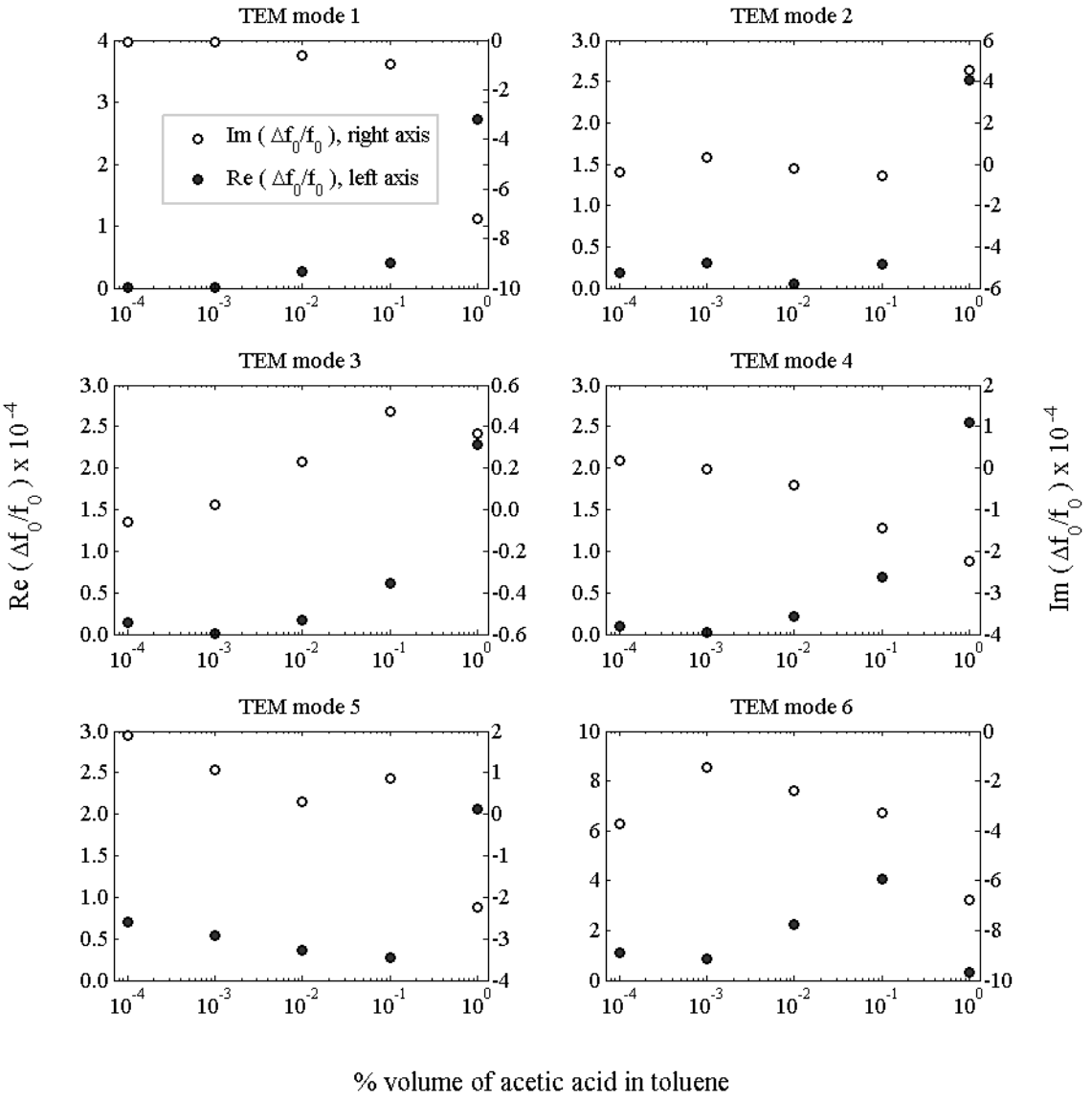

Figure 3.15: Complex frequency response of the invasively coupled coaxial resonator with respect to percentage volume of acetic acid in toluene, where each subplot represents one of the first six TEM modes of the device. The grey markers represent the real component of normalised change in complex resonant frequency, to be read off of the left y-axis. Likewise, the white markers represent the imaginary component of normalised change in complex resonant frequency, to be read off of the right y-axis.

3.2.2. Non-invasively coupled resonator and T-piece fluid interface

Two main sets of results were obtained with the non-invasively coupled resonator using the T-piece fluid interface. These were (a) step changes of fluid composition in real-time in a continuous flow environment and (b) measurements of bulk

solvents to assess sensitivity, stability and the effectiveness of the inversion procedures. In both instances, a 100 μm thick PTFE disc was placed over the end of the resonator and held in place by the fluidic fixture. Solvents were delivered from bulk reservoirs via HPLC pumps.

The device was characterised using measuring microscopes and simulated as accurately as possible to provide a numerical inversion for the continuous flow measurements. The motivation for this was that it was not practical to continually remove and replace the probe for reference air measurements.

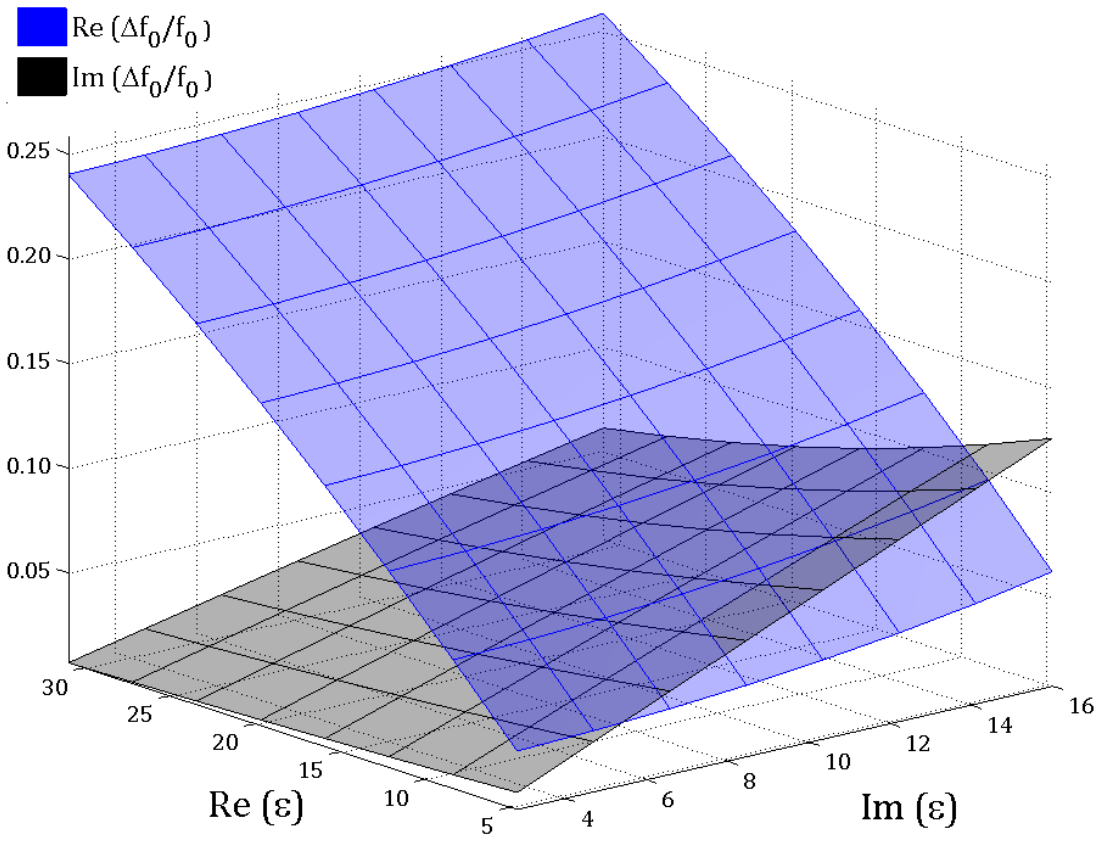

Figure 3.16: Variation in the real (blue surface) and imaginary (grey surface) components of normalised complex frequency of the non-invasively coupled resonant sensor. Data were obtained at the fundamental frequency and plotted with respect to the real and imaginary parts of sample permittivity (ε). Each vertex of the grids represents a simulated data point, and the contour of each grid represents an interpolated function for estimating permittivity between the simulated values.

The device was then used to characterise a continuous flow of toluene and acetic acid, where the amount of acetic acid varied with respect to time. Permittivity values were calculated using the simulated inversion protocol summarised in Figure 3.16.

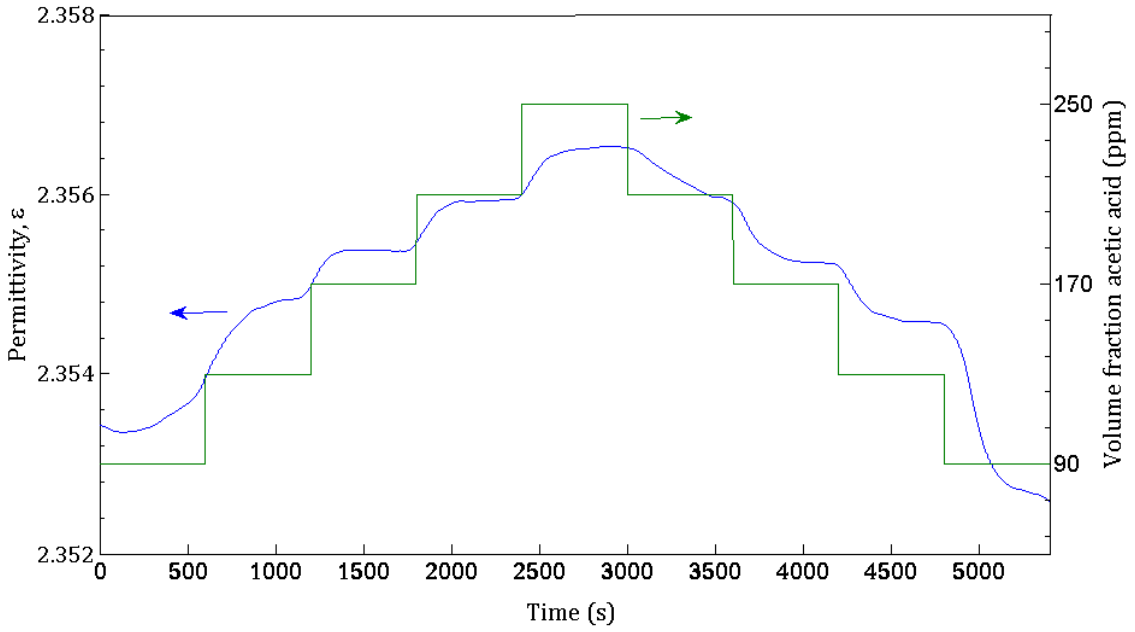

Figure 3.17: The change in sample permittivity (blue trace, to be read off of the left y-axis) as the volume fraction of acetic acid in toluene varies (green trace, to read off of the right y-axis) with respect to time. The parts per million value refers to a minor component of acetic acid and a major component of toluene.

To test the empirical inversion procedure, a series of measurements of bulk solvents were performed. These measurements were performed using a T-piece submerged in a beaker of solvent rather than in a continuous flow system. This was carried out to simplify the measurement process as composition did not need to be varied continuously. This will not affect the performance of the sensor because the entire fluidic system demonstrates great rigidity and the fluidic seals are designed to withstand massive pressures, which are far in excess of those required to perform the measurement shown in Figure 3.17, for example.

Measurements of ethanol, methanol, propan-2-ol and toluene were performed with this setup. Each solvent was of known permittivity, and measurements of the three alcohols were to be used to invert the measurement data of toluene to obtain permittivity values. This forms an alternative approach to simulating data for

obtaining a lookup table for continuous measurement inversion. These solvents were chosen in order to exercise the device over a large and useful range of permittivity. The dielectric dispersion data for the alcohols were obtained from [6], where the frequency-dependent complex permittivity $\tilde{\varepsilon}(f)$ was given by a multi-relaxation Debye model:

$$\tilde{\varepsilon}(f) = \varepsilon_\infty + \sum_{k=1}^{n} \frac{\varepsilon_k - \varepsilon_{\infty k}}{1 + j2\pi f\tau_k}, \qquad 3.8$$

where each of the *n* distinguishable dispersions has a dispersion amplitude $\varepsilon_k - \varepsilon_{\infty k}$ and relaxation time τ_k. ε_∞ is ε_1 in the infinite frequency limit and $\varepsilon_{\infty k} = \varepsilon_{k+1}$. The parameters for ethanol, methanol and propan-2-ol for *n* = 3 are given in Table 3.3. The uncertainty in the real and imaginary components of permittivity of each of the inversion solvents was shown to be ± 3% [6]. Device accuracy will be quantified by comparing measurements of toluene with dielectric dispersion data from [132].

Table 3.3: Debye parameters of the solvents used for resonator measurement inversion.

Solvent	ε_∞	ε_1	τ_1	ε_2	τ_2	ε_3	τ_3
Methanol	2.79	32.50	51.5	5.91	7.09	4.90	1.12
Ethanol	2.69	24.32	163	4.49	8.97	3.82	1.81
Propan-2-ol	2.42	19.40	359	3.47	14.5	3.04	1.96

The raw measurement data of the solvents are shown in Figure 3.18. The inverted permittivity values are shown in Figure 3.19.

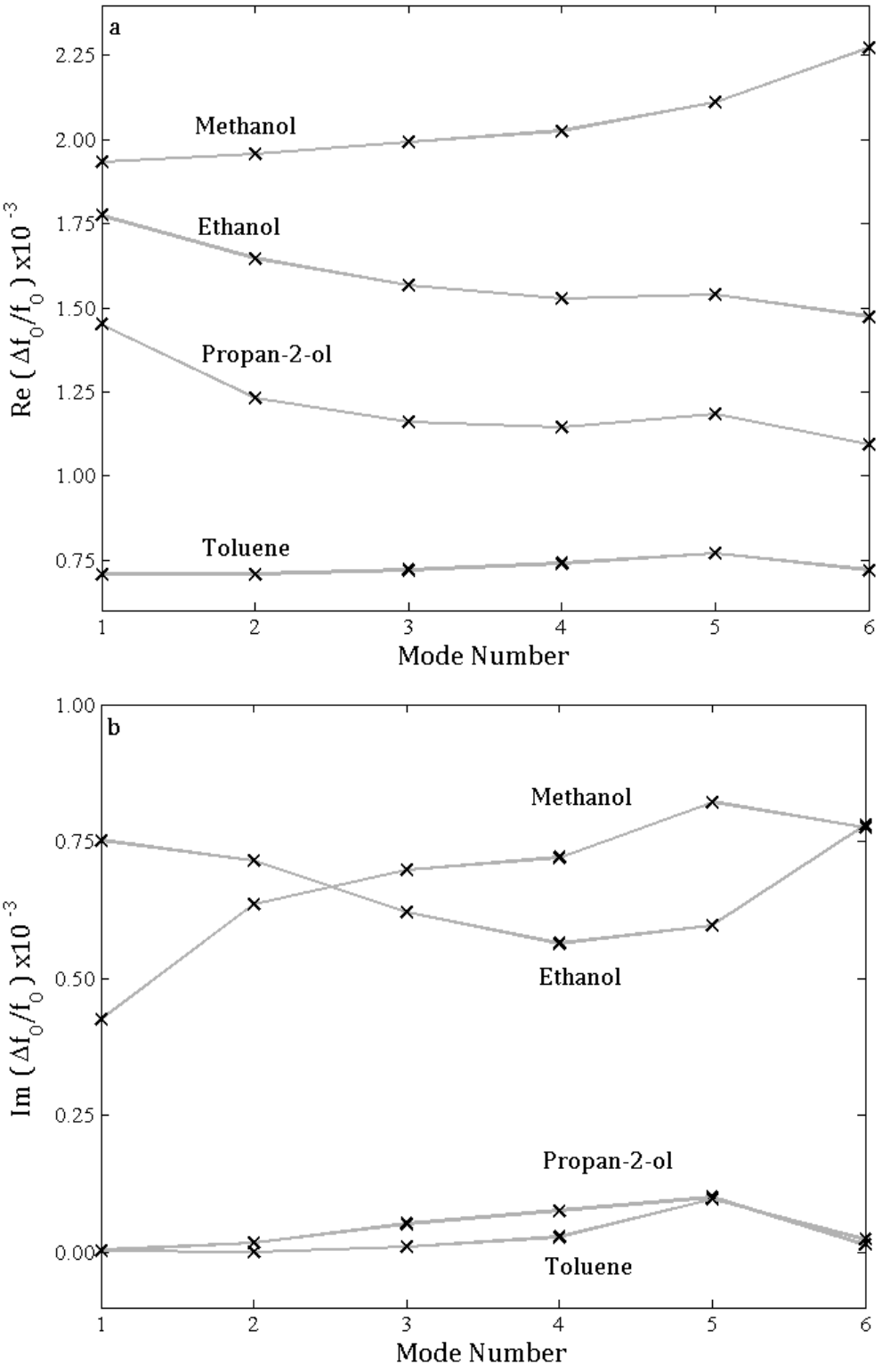

*Figure 3.18: (**a**) Real and (**b**) imaginary components of normalised frequency shift for ethanol, methanol, propan-2-ol and toluene, shown for the first six modes of the device with respect to TEM mode number. These measurements were performed with the T-piece fluid interface and the non-invasively coupled coaxial resonator with a fundamental resonance ≈ 1.25 GHz. Measurement noise is too low for error bars to be appropriate.*

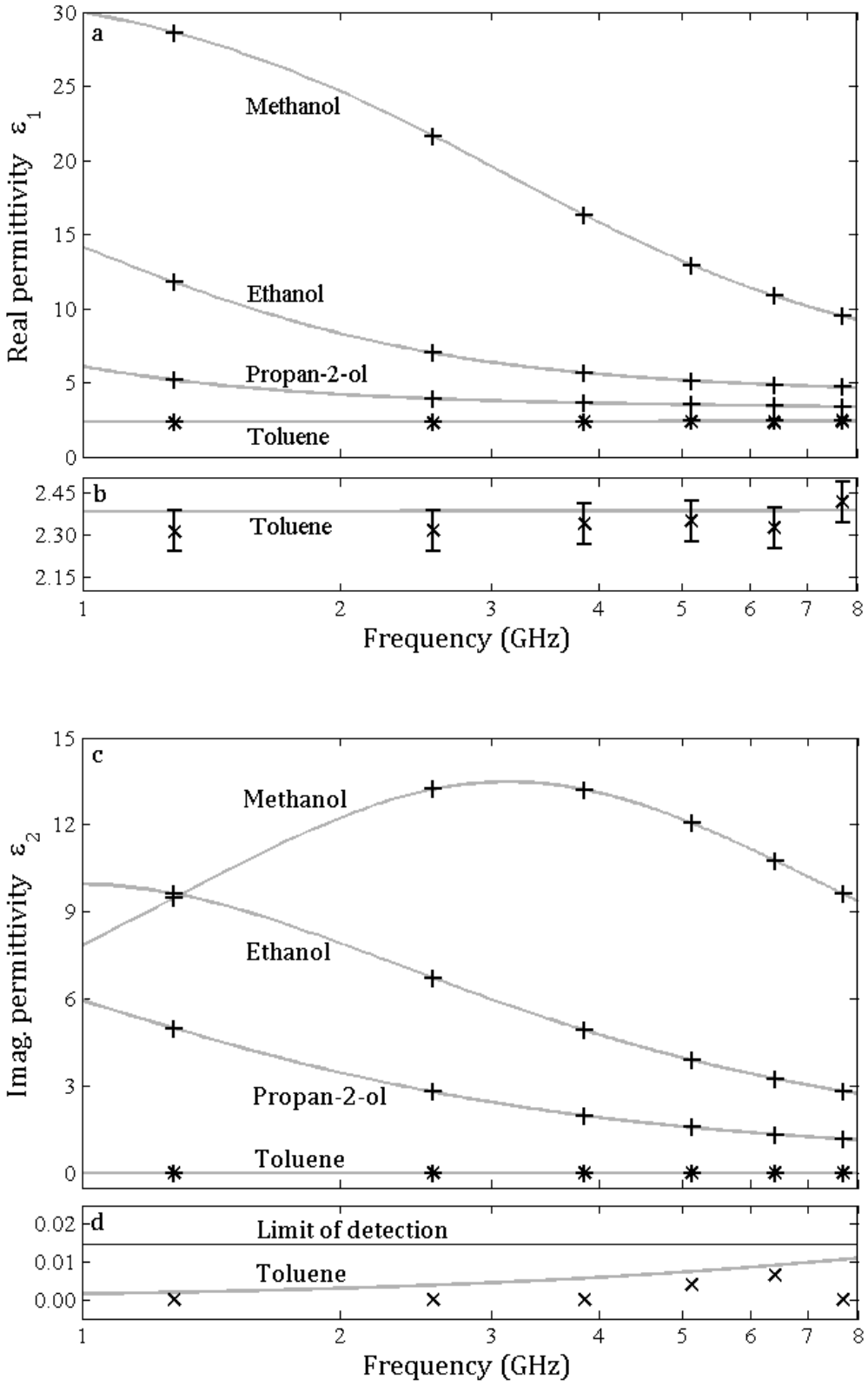

*Figure 3.19: (**a**,**b**) Real and (**c**,**d**) imaginary permittivity spectra for ethanol, methanol, propan-2-ol and toluene, where (**b**) and (**d**) have a finer scale on the y-axis to only represent toluene measurements. Grey lines show Debye spectra obtained from literature; '+' markers show expected permittivity values (i.e. those used to*

*invert toluene measurements) at the measurement frequencies. 'x' markers show permittivity measurements of toluene. Star shapes occur when expected and measured markers overlap. (***b***) shows the real component of toluene measurements to agree with values from literature within the margin of error attributable to the uncertainty of permittivity values from literature. (***d***) shows the dielectric loss of toluene to be below the limit of detection due to measurement noise. This demonstrates why the imaginary component of permittivity of this particular solvent cannot be resolved in this frequency range.*

Statistical parameters for bulk solvent measurements taken with the non-invasively coupled coaxial resonator are given in Table 3.4. Noise was taken as one standard deviation from the mean value. A limit of detection and a resolution at the limit of detection were extrapolated by taking the maximum measurement noise and inverting it to permittivity. The limit of detection (i.e. the minimum change in permittivity that can be distinguished above measurement noise) was obtained directly as this permittivity. The resolution at the limit of detection was taken as the difference between the lowest measurable permittivity and the vacuum permittivity (i.e. $\varepsilon_r = 1$). A series of correlated simulations were used to model fabrication tolerances of the resonator and coupling structure, and the resulting effect on complex resonant frequency. The maximum change was used to estimate the geometric uncertainty, which can be assumed to be the dominant source of uncertainty within the device [21]. However, the empirical method used to invert frequency data (Figure 3.18) to permittivity (Figure 3.19) accounts for geometric uncertainty. Furthermore, this value will be fixed for any given probe so does not need to be considered in the calculation of complex permittivity. The values of maximum measurement noise, limit of detection, resolution and geometric uncertainty are given below.

Table 3.4: Device characteristics for bulk solvent measurements performed in the T-piece fluid interface with the non-invasively coupled coaxial resonator.

x_{RC}	x_{GC}	x_{RG}	x_G
2.86 mm	0.25 mm	1.25 mm	0.5 mm

The performance of the device (including the empirical inversion procedure) can be studied by examining the error in the inverted permittivity measurements of toluene (plotted in Figure 3.19 **b**). The measurement error according to the difference between the measured and expected values of toluene permittivity is given in Table 3.5. Note that only the real component of permittivity is shown; the imaginary component is below the limit of detection.

Table 3.5: Measurement error in the real component of permittivity of toluene. The error in the expected values from literature is 3% [132].

Mode	1	2	3	4	5	6
Expected ε_1	2.384	2.384	2.385	2.386	2.386	2.387
Measured ε_1	2.313	2.316	2.338	2.350	2.324	2.416
Error (%)	2.98	2.88	1.95	1.50	2.60	1.21

3.2.3. Integrated microfluidic device with non-invasively coupled resonator

Figure 3.20 shows permittivity and normalised change in frequency with respect to concentration for a dilution series of acetonitrile in toluene. These data were obtained with the 1.25 GHz non-invasively coupled coaxial resonator embedded in the manifold with a single-phase microfluidic chip and quartz coverpiece. Measurements were performed with respect to pure toluene so that any measured changes would be solely due to acetonitrile. This allowed permittivity values to be calculated according to the assumption that complex frequency varies linearly with permittivity for small changes in permittivity. Each subplot represents one of the first six TEM modes of the device. The traces show the real and imaginary components of both normalised complex frequency shift (to be read off of the left y-axis) and of complex permittivity shift relative to pure toluene (to be read off of the right y-axis. Note that the markers are joined for ease of interpretation but are discrete rather than continuous data. Also note that the complex permittivity of toluene is approximately 2.385 - j0.006 in this frequency range [132].

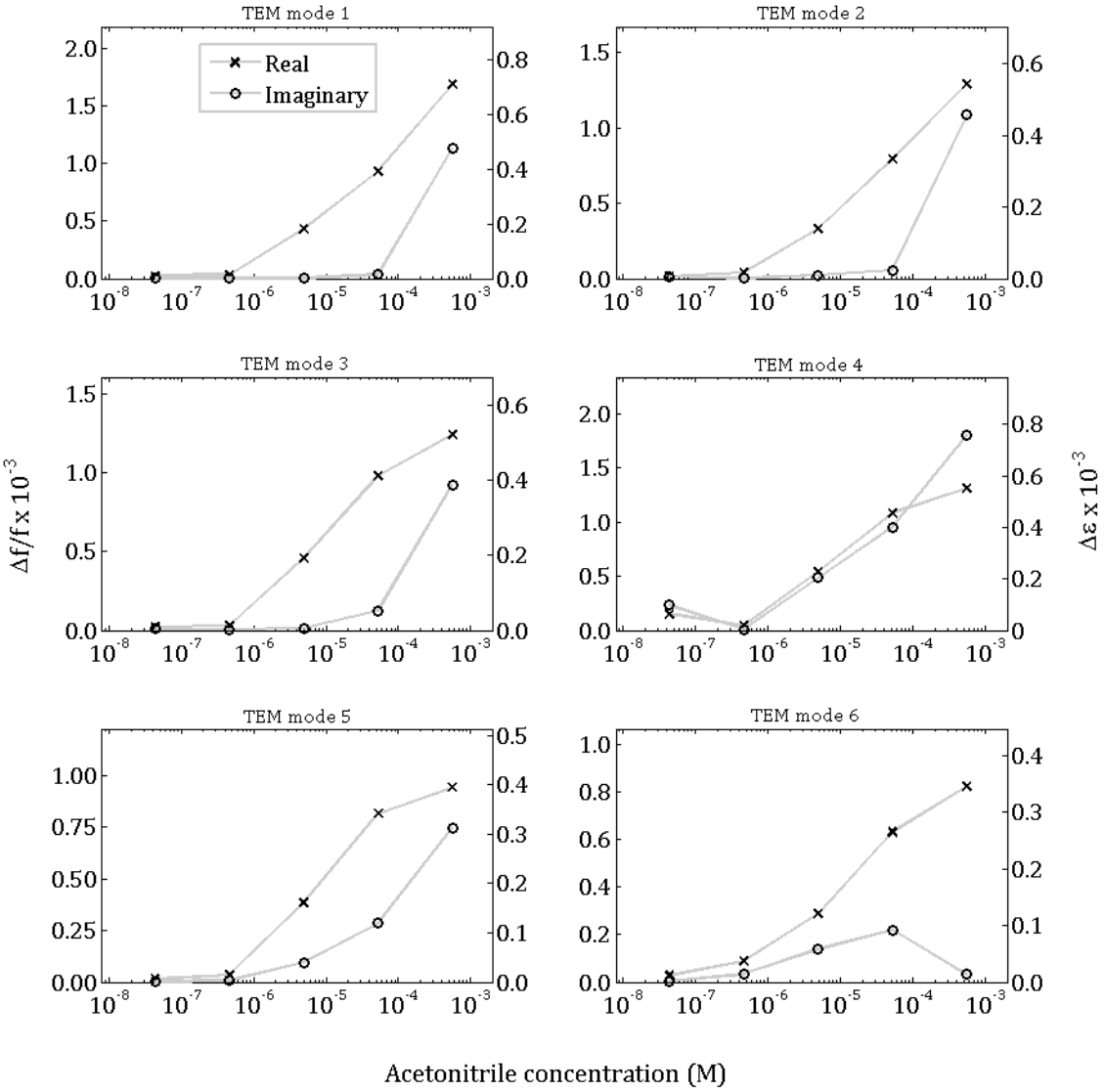

Figure 3.20: Complex frequency and permittivity response of the 8.4 cm non-invasively coupled coaxial resonator with respect to concentration of acetonitrile in toluene. Each subplot represents one of the first six TEM modes of the device. The two traces on each subplot represent the real and imaginary components of both normalised complex frequency change (when read off of the left y-axis) and permittivity (when read off of the right y-axis. Note that the concentration refers to the minor component of acetonitrile dissolved in the major component of toluene.

The complex frequency and permittivity responses for a serial dilution of caffeine in toluene are shown with respect to frequency in Figure 3.21. These data were obtained with the 0.6 GHz non-invasively coupled coaxial resonator embedded in the manifold with a single-phase microfluidic chip and quartz coverpiece. This graph illustrates a different method of interpreting multi-frequency coaxial

resonator, where each trace represents a different concentration of caffeine. Note that concentration refers to the minor component of caffeine dissolved in the major component of toluene.

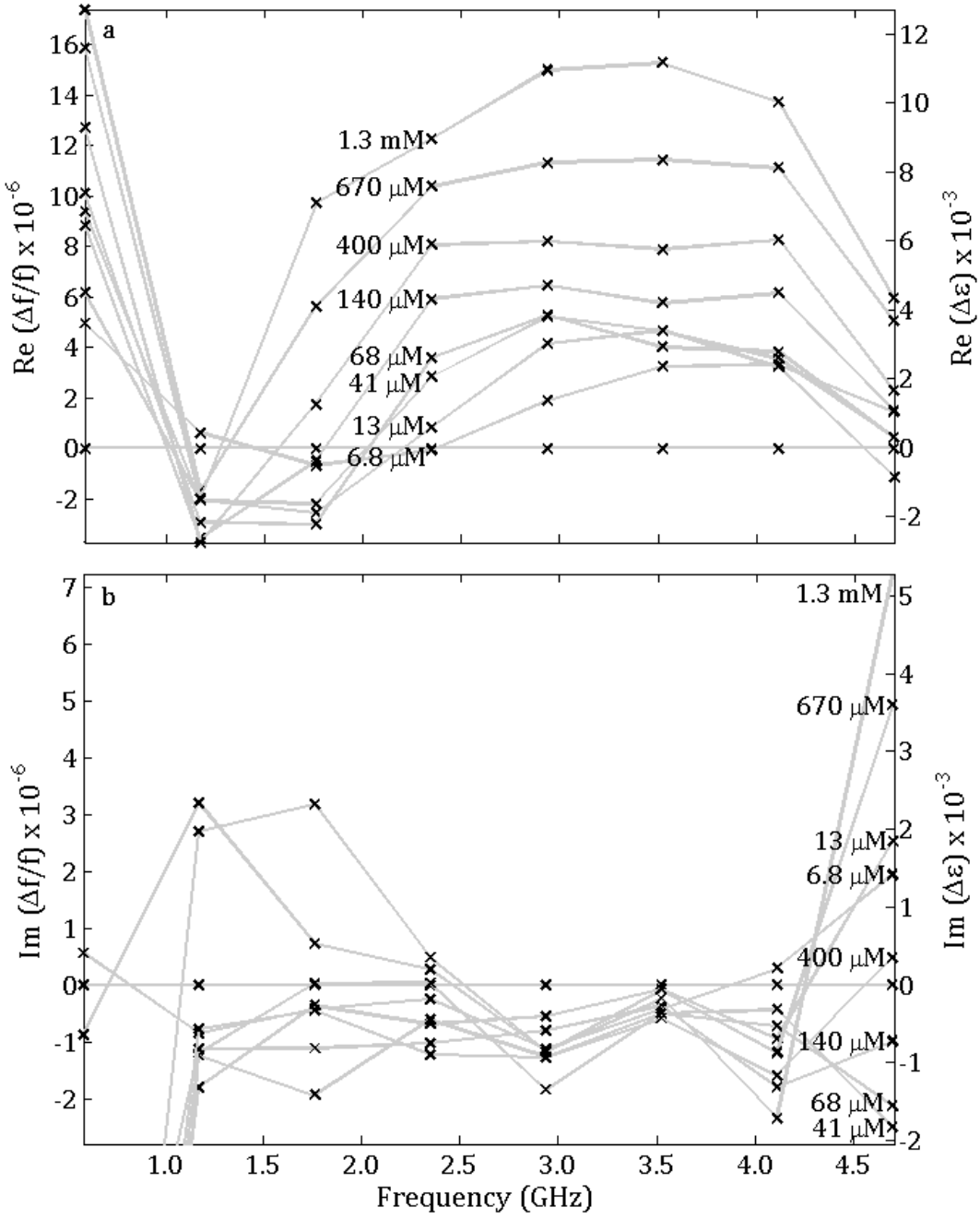

Figure 3.21: Complex frequency response of the 17.5 cm non-invasively coupled coaxial resonator with respect to frequency for a serial dilution of caffeine in toluene. Each trace represents a different concentration of caffeine and each subplot represents either the real or imaginary components of their complex-valued y-axes.

Note that $-\mathrm{Re}\,(\Delta f/f)$ is plotted for the left hand y-axes in Figure 3.20 **a**, and $-\mathrm{Im}\,(\Delta\epsilon)$is plotted for the right hand axis in Figure 3.20 **b**. This approach was used for the sake of brevity, to allow the same traces to be read off of two axes.

The y-axes of these results are similar to those shown in Figure 3.20, in that the data are presented with respect to a reference measurement of pure toluene. This allowed the inversion of frequency data to permittivity values (assuming a small variation in permittivity), and also allows the same traces to be read off of both axes. In this instance, however, the two subplots respectively represent the real and imaginary components of both permittivity and resonant frequency. Each trace represents a different concentration of caffeine; pure toluene is necessarily represented by a flat line. Data are presented in this quasi-spectral manner to illustrate an alternative method of using measurement data.

An organic phase of chloroform and an aqueous phase of water were used to generate segmented flow. At equilibrium, the chloroform was saturated with water, where the solubility of chloroform in water at 20 °C is 0.815% and the solubility of water in chloroform at 20 °C is 0.056%. The liquid phases were segmented on chip, whereupon they flowed the length of an excessively long meandering channel to ensure equilibrium was reached. The equilibrated flow was then interrogated with the embedded 1.25 GHz coaxial resonator using non-invasive coupling. Only the fundamental resonance was interrogated to ensure maximum temporal resolution was attained.

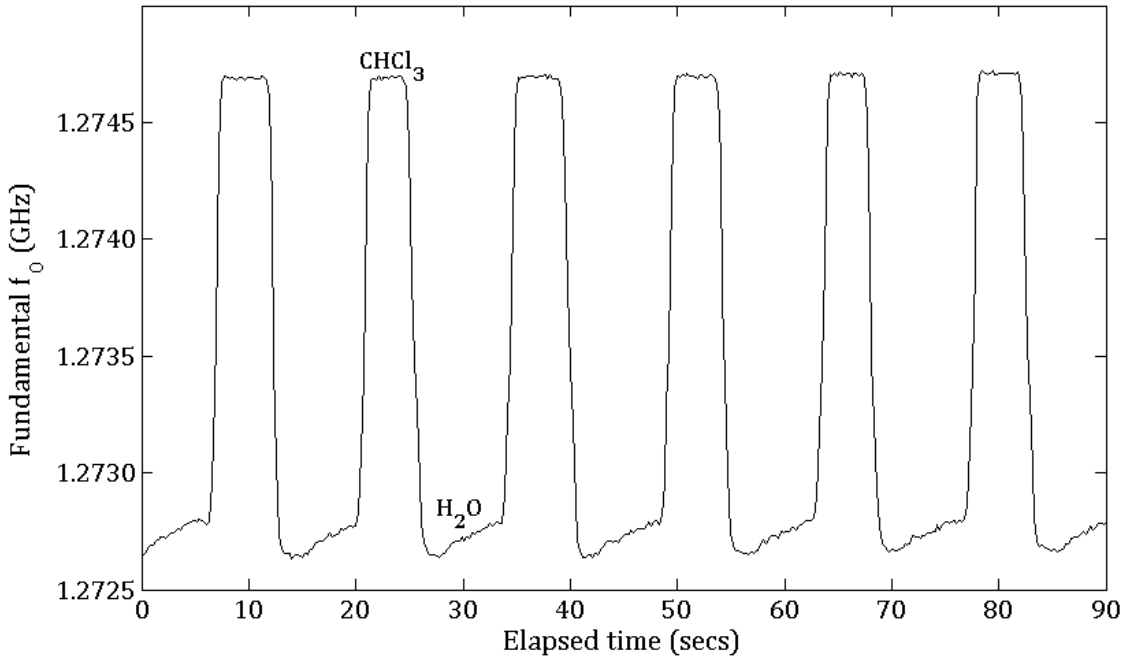

Figure 3.22: Centre frequency trace for a chloroform-water segmented flow, interrogated using the fundamental resonance of the 8.4 cm coaxial resonator embedded in a multiphase microfluidic device.

3.3. Discussion

3.3.1. Invasively coupled resonator

The resonant frequency and quality factor of the first six TEM modes of the unloaded invasively coupled resonator are shown in Table 3.2. The large differences in Q are a consequence of unequal coupling due to the connections part way along the resonator. This is an indication of how sensitivity will vary dramatically between each mode. The fact that this effect was due to the coupling structure could be verified using the same section of coaxial line (i.e. with recesses drilled through the outer conductor) with the non-invasive coupling structure, where the first six modes were all observed to have $Q \approx 750$.

The unequal coupling (and consequent variation in sensitivity between modes) makes the invasive coupling structure unsuitable for the intended applications of this device. In particular, it is necessary to have the receptacles a significant distance from the end of the probe so it can be plumbed in to a (micro)fluidic

environment., which exacerbates the problem of variable coupling strength that is inherent within the invasive coupling design.

The variation of normalised frequency shift with respect to permittivity can be assumed to be linear over small variations in permittivity. Considering the results of Figure 3.15, this assumption holds true given that the relative permittivities of acetic acid and toluene are approximately 6 and 2 respectively and that the largest percentage volume change characterised is 1%. Therefore, any observed non-linear behaviour must instead be due to permittivity being a non-linear function of fluid composition. This reasoning can account for non-linearities but not for any non-monotonic behaviour. It is possible for a bulk liquid to screen the permittivity contribution of very small dissolved species (such as trace biological molecules in water), but it is nonsensical to attribute a drop in permittivity to the addition of a higher permittivity material. This is exactly the effect implied by the non-monotonic results for all modes except the first. That this effect is not displayed consistently across all the measured modes would imply that the coupling (which, being set in from the ends of the probe, will affect each mode differently) could be a cause. The combination of the results of Table 3.2 and Figure 3.15 lead to the conclusion that invasive coupling is incommensurate with the intended aims and applications of this project. Thus, no microfluidic integration or further experiments were performed with the invasively coupled resonator.

3.3.2. T-piece fluid interface with non-invasively coupled resonator

Figure 3.16 clearly illustrates how a series of correlated simulations can be used to invert resonator measurements of a continuous flow regime to obtain permittivity values with respect to time.

The simulated normalised frequency shift attributable to toluene was verified via comparison with a measurement of the pure solvent. The simulated value was within three significant figures of the measured value, which was taken as justification for using the simulated inversion protocol for the continuous flow measurements.

There are numerous unusual features in Figure 3.17. There is a lag between the change in flow composition and resonator response due to the time taken for the solution to reach the resonator from the pumps. The curvature of each step can be attributed to dispersion between the different concentration phases. The permittivity response was systematic in that the calculated data were proportional to the volume fraction of acetic acid, which was anticipated because acetic acid has a higher permittivity than toluene. This is justification for using the single-ended coupling structure over the invasive one, which did not exhibit a monotonic response for a similar test shown in Figure 3.15 and discussed in Section 3.3.1. However, a lack of repeatability was demonstrated for the single-ended coupling with the T-piece interface in Figure 3.17 as permittivity values were different for the same composition, depending on whether the composition had increased or reduced to the volume fraction in question. This effect occurs for all of the different volume fractions used. Similarly, it can be seen that step changes in concentration produce differing changes in permittivity. It is possible that permittivity is a non-linear function of composition, but this would not be dependent on previous composition: permittivity, unlike permeability, does not exhibit hysteresis. The effects in question did not show any correlation with temperature change, which varied erratically but did not exhibit any general upward or downward trend. The flow cell was completely sealed, and care was taken to prevent any bubbles from forming in the system. It is not thought that these effects were due to other solvents remaining within the flow system as the cleaning solvents used (water and acetone) were invariably of higher permittivity than either toluene or acetic acid. The PTFE spacer is sufficiently hydrophobic to prevent ingress of solution between the layers of the coaxial cable.

It is therefore likely that the effects of uneven and inconsistent changes are a consequence of flow. This could be due to the inner geometry of the T-pieces, which could disturb flow in a way that prevents complete circulation of fluid within the flow cell. Also, no specific effort was made to maintain back pressure in the fluidic circuit, so it cannot be assumed that the pumps behaved perfectly and mixed solutions to the programmed concentrations. However, a later experiment with a higher back pressure showed the same variation exhibited in Figure 3.17.

The complex frequency measurements of bulk solvents (Figure 3.18) alone could be used to distinguish between solvents without the need for inversion for permittivity. This could be of use in real-time applications such as industrial process control, where the inversion could be omitted altogether if absolute permittivity values were not required. This would not affect the maximum achievable temporal resolution. Similarly, such an approach could also be of use for monitoring chemical reactions *in situ*. Note that the network analyser used in this experiment could resolve frequencies to sub-kHz accuracy. The fact that frequency resolution is fixed means that bandwidth measurements have significantly higher noise as they are typically three orders of magnitude lower in comparison with resonant frequency measurements.

Statistical measures of the resonant device performance are given in Table 3.4. The data were obtained over the course of several minutes. The low noise of the measurement over this length of time illustrates the temporal stability of the device. Measuring data over this length of time is required for point-of-sampling biochemical applications, but is not something generally required for microwave-frequency measurement techniques.

The significance and usefulness of this particular measurement technique lies in its low resolution limit. This could best be demonstrated through quantifying permittivity changes of decreasing volume fractions of one solvent in another, as attempted for the invasively-coupled probe. The results of Figure 3.19 are intended as a demonstration of the measurement technique only. The T-piece interface has obvious shortcomings for more complex fluid systems, as evidenced by the result in Figure 3.17. Therefore, the data shown throughout Section 3.3.2 have not been taken in an environment which reflects those for which this device is intended to be incorporated. Thus, the ultimate measurement resolution is not best demonstrated with discrete bulk measurements, but rather in a flow environment in a microfluidic device.

3.3.3. Integrated microfluidic device with non-invasively coupled resonator

Figure 3.20 shows complex resonant frequency and permittivity changes for varying composition of acetonitrile in toluene. The imaginary component of

normalised change in complex resonant frequency can be interpreted qualitatively as showing dielectric loss to be proportional to the concentration of acetonitrile. This is to be expected from a brief examination of the permittivity spectra of the two solvents: acetonitrile demonstrates higher permittivity and dielectric loss in comparison with toluene throughout the entire microwave frequency region.

It should be noted that concentration is shown on a logarithmic scale in Figure 3.20, so normalised frequency change and permittivity are clearly non-linear functions of composition within the range of the experiment. Because permittivity and normalised frequency change are linearly proportional to each other over this (very small) range of permittivity, the non-linear response must be a consequence of the relationship between permittivity and concentration. That is, it is implied that the permittivity of an acetonitrile-toluene solution does not vary linearly with concentration at the measured concentrations (560 μM – 43 nM acetonitrile). This is perhaps to be expected from other previously obtained results. In one example, some of the Havriliak-Negami parameters extracted from the dielectric spectra of 2-propanol-water mixtures were shown to vary linearly with changing volume fraction [133]. Note that the Havriliak-Negami equation is an empirical modification of the Debye response that includes an additional exponent for an improved fit to the measured data. It was not possible to extract equivalent parameters from the presented acetonitrile-toluene data because of the relatively narrow frequency range of the coaxial resonator (one order of magnitude, limited by the measurement equipment) in comparison with the dielectric dispersions exhibited by toluene [132] (many orders of magnitude). It would be possible to compare the results of [133] with those obtained here by evaluating the Havriliak-Negami responses at a particular frequency. However, in this case such a comparison would be useless as the smallest change in concentration examined in [10] exceeds the largest investigated here by several orders of magnitude. The permittivity of 2-propanol-water mixtures does not, in fact, vary as a linear function of concentration when evaluated at a constant frequency of 1.25 GHz when concentration is varied by molar fractions of 0.03 and above.

The data presented in Figure 3.20 are a clear demonstration of the suitability of an embedded microfluidic dielectric spectroscopy device for detecting low and trace

concentrations of liquid-liquid mixtures. All of the measured permittivity components (i.e. both real and imaginary components at six discrete frequencies) exhibited a repeatable linear response with respect to log(concentration) over five orders of magnitude. The detection limit of acetonitrile in toluene was shown to be approximately 400 nM. This is considered a vindication of the balanced design methodology described in Section 3.1.1. It demonstrates that highly sensitive measurements can be performed in a robust, adaptable platform without focussing exclusively on the maximisation of quality factor. This performance shows that the embedded microfluidic approach offers a unique and useful alternative to ultra-high quality factor resonators despite the depolarising sample interface and inherently modest quality factors associated with the losses of a coaxial resonator.

Figure 3.21 shows changes in complex resonant frequency and permittivity with respect to caffeine concentration. The effect is generally systematic for the real components of both values, although some modes can be observed to be partially non-monotonic. Using the same interpretation as for the acetonitrile-toluene measurements, these results indicate that increasing caffeine concentration causes a reduction in the overall polarisability of the sample. This would suggest that the addition of a material that is non-polarisable at microwave frequencies will act to reduce the effective (volumetric average of) sample permittivity. One unusual feature of Figure 3.21 is that there is a small increase in permittivity at the second and third modes for some concentrations of caffeine. Again, this appears to be systematic as the effect is reproduced for different samples, but is focused in an unusually small frequency region. A shortcoming of this particular experiment is that is does not exercise the entire dynamic range of the system by not characterising low enough concentrations. Unlike the measured solvent-solvent mixtures, all of the measured concentrations of caffeine were clearly distinguishable from pure toluene. This implies that the limit of detection is below the lowest measured concentration of approximately 6 μM.

In contrast with the real component of sample permittivity, the imaginary component does not exhibit any systematic or meaningful behaviour with respect to caffeine concentration. This result can be therefore be interpreted as meaning

that caffeine has little effect on dielectric loss in the microwave region given that imaginary permittivity is a measure of dielectric loss.

Figure 3.22 shows resonant frequency of the fundamental TEM of the 8.4 cm coaxial resonator with respect to time for a segmented flow of chloroform and water. Because the real component of permittivity of water exceeds that of chloroform by a factor of approximately 20, this result clearly illustrates how a decrease in resonant frequency can be interpreted as demonstrating an increase in polarisability. Unlike Figure 3.20 and Figure 3.21, the change in resonant frequency does not vary linearly with permittivity because the change in permittivity is very large. The fluid sample was not brought into contact with the aperture of the sensor. The field distribution of the open-ended coaxial resonator meant that the gap between the probe aperture and the microfluidic channel caused the sample to cross lines of evanescent electric field. This allowed polarisation charges to accumulate and therefore cause depolarisation. This meant that the measured polarisability (as described in Chapter 2) was not a function of sample polarisability alone. This effect is constant for small changes in permittivity (which is why permittivity values could be calculated for acetonitrile and caffeine dissolved in toluene) but is exaggerated for large changes. Such non-linear behaviour is manifested in the measured response of a segmented flow of chloroform and water, where first order perturbation theory does not hold because of the large variation in permittivity. It is for this reason that permittivity values have not been calculated. This effect was circumvented by the empirical inversion used to obtain permittivity values for bulk solvents as shown in Figure 3.19, except it required measurements to be taken relative to air. Such measurements were not practical in segmented flow within the time limits of this project, although that is not to say that it is impossible. Potential implementations for invertable segmented flow measurements are discussed in the section on future work.

Figure 3.22 also demonstrates the temporal stability of the probe when embedded in the microfluidic interface. The aqueous fluid segment measurements are rising, which can be attributed to a slight temperature difference between the fluidics and the microfluidic manifold. Segmented flow is characterised by a continually-

refreshing fluid interface, which means sample temperature will equilibrate in far less time than in single-phase measurements. A similar effect is not observed in the organic phase measurements because the temperature dependence of the permittivity of water vastly exceeds that of chloroform. This is a direct example of the need for improved temperature control, particularly for the highly temperature-dependent aqueous samples anticipated in biological applications.

Prior to this paragraph, most of Sections 3.3.2 and 3.3.3 have been concerned with very specific aspects of the presented data. A more general perspective is also necessary. The caffeine measurements vindicate the considerable efforts in developing a method for obtaining multi-frequency information with a single resonator. The sensitivity of resonator methods is highly desirable, but measurements performed at a single frequency are like to be ignored upon being judged spurious. Consider the caffeine-toluene measurements at 1.75 GHz in Figure 3.21. If measurements had not been performed at any other frequency, a reasonable conclusion would be that this measurement technique could not be used for characterising the composition of solvent-solvent systems. If the rest of the available frequency information is also considered, systematic effects can be observed with respect to both frequency and concentration whilst simultaneously retaining the sensitivity of a resonant technique over a broadband one. This is particularly important when more complex systems such as blood are considered: the data presented in this work are from artificially simple chemical systems, whereas complexity will be vastly increased for biological applications.

The error of the measured frequency data can be used to estimate the limit of detection and resolution of the embedded microfluidic device in terms of permittivity by considering that normalised frequency change and permittivity are linear over small changes in permittivity. If error is taken as the maximum noise of all measured frequency components at the 99% confidence interval, the calculated permittivity components have a resolution of 2×10^{-4} and a limit of detection of 1.0002. The permittivity resolution and the acetonitrile detection limit of 400 nM can be used to compare this device with various other techniques discussed earlier, as shown in Table 3.6.

Table 3.6: Comparison of device resolution and sensitivity. Note that several examples of detection are given in [11, 13, 15]. Only the highest molar sensitivity has been included for the sake of brevity.

Paper	ε resolution	Molar Sensitivity
Gubin *et al.* [16]	-	150 μM BSA in water
Sharforost *et al.* [105]	-	750 μM BSA in water
Sato *et al.* [134]	-	30 mM propan-2-ol in water
Kapilevich *et al.* [46]	-	800 μM $MgSO_4$ in water
Song *et al.* [60]	-	50 mM ethanol in water
Folgero *et al.* [50]	~ 0.001	-
Hoog-Antonyuk *et al.*[59]	~ 0.01	-
This work	2×10^{-4}	400 nM acetonitrile in toluene

It is necessary to use measures of both permittivity resolution and molar sensitivity due to the various ways in which the other authors have presented their data. Note that [14], which is probably the most sophisticated microfluidic dielectric spectroscopy technique discussed in the Literature section, has not been included because the error treatment was concerned with the accuracy of the transmission line model and quantitative error data was not provided in terms of permittivity or composition. Where several examples of solute detection were given (as in [16], [46], [105]), the highest demonstrated molar sensitivity (i.e. the lowest detected concentration) is quoted in Table 3.6. The resolution of [60] could not be established given the lack of quantitative error analysis. The performance of the non-invasively coupled coaxial resonator and the PTFE microfluidic interface compares favourably with all other existing techniques.

4. CAPILLARY-PERTURBED COAXIAL RESONATOR

Chapter 2 introduced perturbation theory, as well as various spectroscopic methods for characterising the dielectric and/or magnetic properties of a material. Although resonator perturbation is most commonly used for dielectric spectroscopy, a change in complex resonant frequency can in fact be affected by various intrinsic or extrinsic material properties, or some combination thereof. Intrinsic properties can be electrical (complex permittivity, electrical conductivity) or magnetic (complex permeability); extrinsic properties include the shape and volume of a given sample. This project is largely concerned with developing sensing techniques for monitoring fluidic (bio)chemical and pharmaceutical processes. Although shape affects depolarisation, it will depend on the vessel in which the fluidic sample is contained and is constant for each device developed here. Instead, this chapter concentrates on dielectric and magnetic characterisation.

Several important points were raised within the consideration of existing spectroscopic methods for simultaneously characterising the dielectric and magnetic properties of a material in isolation from each other. Whilst such an approach is well established for broadband techniques [67–77], [122], they lack the accuracy and sensitivity of their resonant counterparts [22]. This is chiefly because broadband techniques require careful and frequent calibration of the measurement equipment used to interrogate the sensor, whereas resonant

techniques are sometimes preferred as they have a lesser dependence on Vector Network Analyser (VNA) calibration and therefore have lower systematic error.

Existing resonant techniques [80–83] offer great potential but suffer from different problems. One approach, using an analytical deconvolution, was heavily calibration dependent and required the use of several waveguides to obtain a significant amount of frequency dependence information [81–83]. Another approach, which sought to exploit the field distributions of different modes to isolate electric and magnetic field effects, managed to separate magnetic properties from electric ones, but not vice versa [80]. It is proposed that a coaxial resonator incorporating the coupling structure introduced in Chapter 3 can be perturbed in such a way that it allows electric and magnetic deconvolution. This does not suffer from any of the problems associated with existing techniques, but allows a microfluidic sample interface and retains most of the advantages of the evanescently-perturbed coaxial resonator.

4.1. Methods

4.1.1. Electromagnetic design

The non-invasive coupling structure developed and tested in Chapter 3 allows multi-modal measurements to be taken in order to extract information on the frequency-dependence of sample permittivity. It was shown to compare favourably with related and alternative measurement techniques in terms of sensitivity, versatility and robustness. It also compares favourably with the existing techniques for simultaneous dielectric and magnetic characterisation. This approach is virtually calibration independent and offers a large number of available modes with a single section of coaxial waveguide (potentially >15). This means it is better suited to the intended applications of this project than previously stipulated methods.

Consider a cylindrical sample passed orthogonally through the centre of a coaxial resonator. As its cross-section tends towards zero, the sample will occupy electric field maxima and magnetic field minima for all even TEM modes, and magnetic field maxima and electric field minima for all odd TEM modes. This is illustrated in

Figure 4.1, where colourmaps of electric and magnetic field are shown for the first two TEM modes of the coaxial resonator.

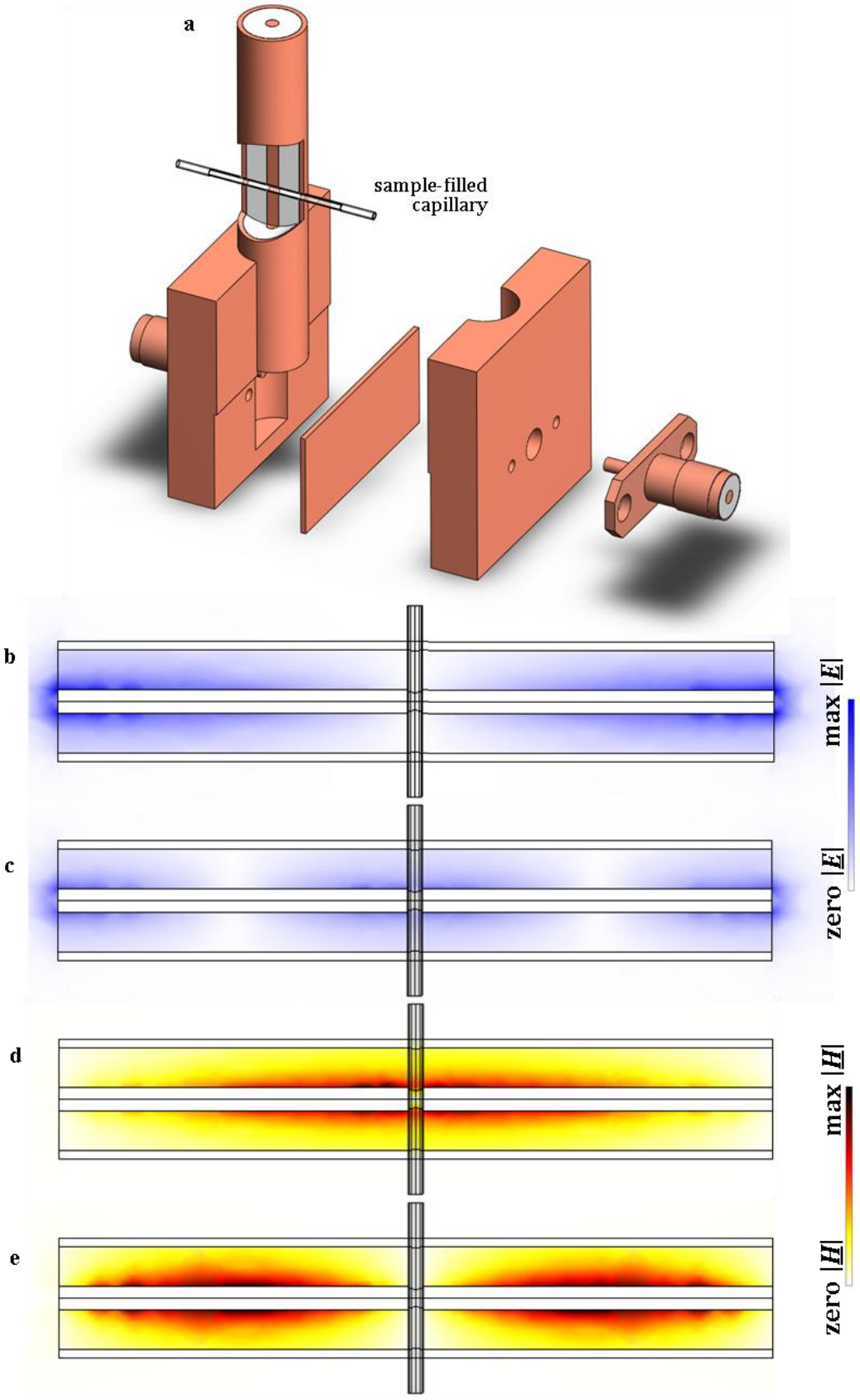

Figure 4.1: Device construction and field distributions. ***a*** *shows a cutaway view of the resonator perturbed with a sample-filled quartz capillary.* ***b*** *and* ***c*** *show cross-sectional colourmaps of electric field magnitude for the first and second TEM modes of the device, respectively.* ***d*** *and* ***e*** *show the equivalent colourmaps of magnetic field magnitude. It can be seen that the sample perturbs zero electric field (**b**) and maximum magnetic field (**d**) for the first TEM mode, and maximum electric field (**c**) and zero magnetic field (**e**) for the second TEM mode.*

The liquid-filled capillary is positioned so that it only occupies either electric or magnetic field depending on which mode is interrogated. In practice, a sample cannot have an infinitely small cross section (as required for total field separation) so it cannot be completely isolated from either field. The sample and capillary must cross lines of electric field and will therefore accumulate charge at their boundaries. Hence, the sample will experience some degree of depolarisation. The design procedure must therefore optimise resonator perturbation in some fashion in order to maximise field separation and minimise depolarisation.

The initial design of this device uses the non-invasive coupling structure from the previous chapter. In Section 3.1.1, it was stated that the coupling structure allowed the user to change the coaxial resonator as desired, for example to adjust the frequency of the available sensing modes. From a practical perspective, this is extremely useful when assembling a device that requires a drilled hole in which to mount the sample-filled capillary. This is useful because the perturbation can be adjusted by changing the resonator rather than having to remake a complete coupled sensor. Such an approach was adopted to simplify the experimental aspects of this work.

It would be equally feasible to fabricate a variation on this design with a simpler, fixed end-coupling design. This is akin to the end-coupled design shown in Figure 3.5 **a**. Such a design was not adopted for the previous coaxial resonators because of the difficulties associated with perturbing the evanescent field whilst using adjacent feedlines at both ends for transmission coupling. This is clearly not a problem for perturbation as shown in Figure 4.1. An implementation of this

approach is shown in Figure 4.2, where coupling is achieved with SMA tab connectors.

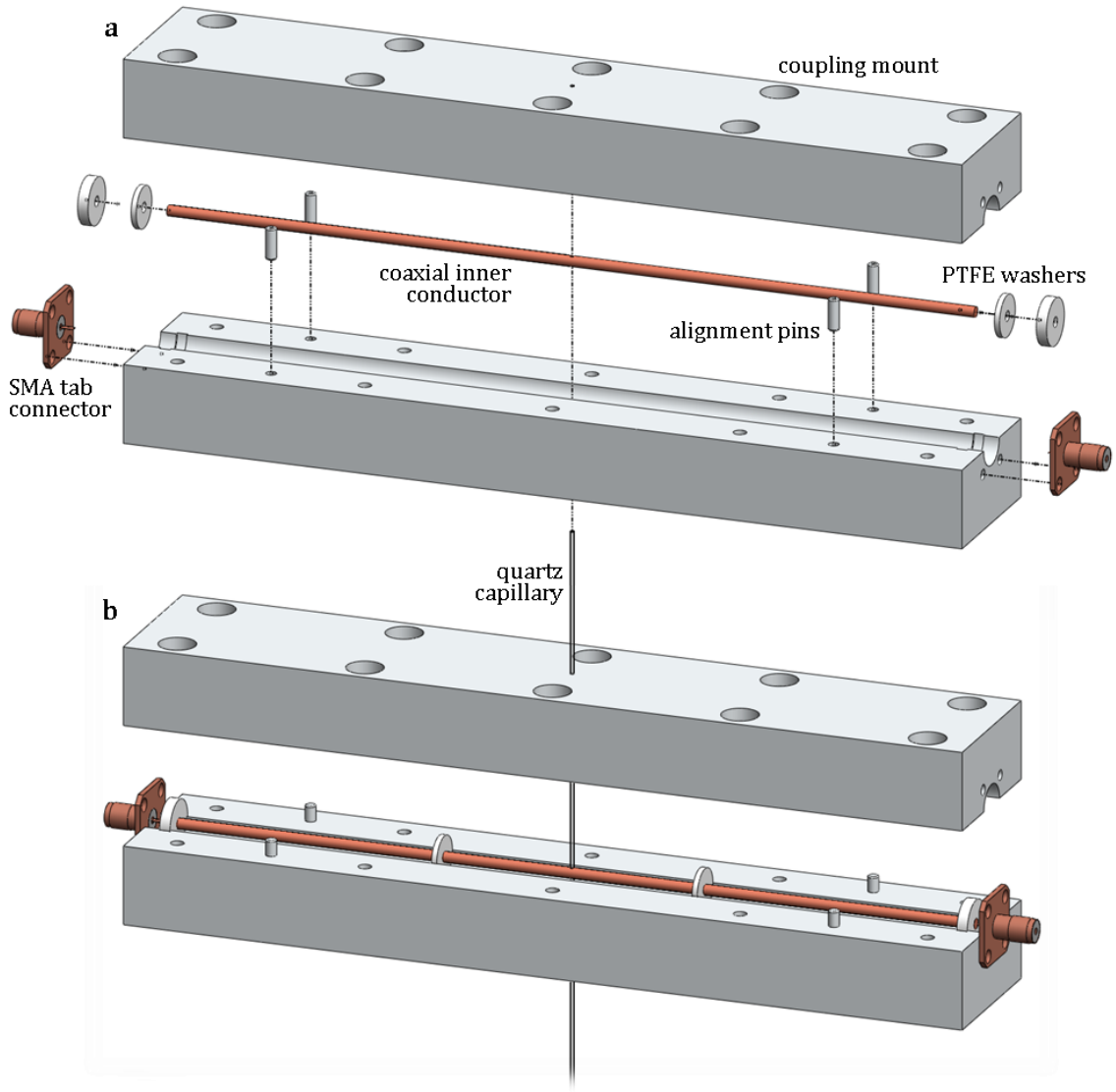

Figure 4.2: Gap-coupled air-spaced open-ended half-wavelength coaxial resonator for simultaneous dielectric and magnetic characterisation of a liquid-filled quartz capillary passing orthogonally through the centre of the resonator. The coupling mount doubles as the outer conductor of the coaxial cable.

The coupling strength could be adjusted by bending the copper tab. This would make it possible to optimise coupling for every individual measurement, but also confines the user to a more restrictive microfluidic interface and a fixed set of harmonic TEM sensing modes. This design still allows multi-modal measurements

for the deconvolution of electrical and magnetic properties, in addition to extracting frequency-dependence information for the two properties.

This approach would also allow sensitivity to be improved. This is because increasing quality factor can lead to higher sensitivity measurements of material properties, which can be achieved by using lower resistivity conductors (such as silver) and lower loss dielectric spacers. Although PTFE has a very low dielectric loss, air- or even vacuum-spaced coaxial cable (if it were possible to hermetically seal the device) would give improved performance. In addition to this enhancement of performance, one of the motivations for using a weakly-coupled resonator was to reduce the calibration dependence of the measurement inversion. In this work, the calculation of permittivity and permeability is not attempted due to time constraints (although it could be) so it would not be particularly detrimental to use the stronger coupling that could be achieved with simple capacitive coupling as shown in Figure 4.2. Indeed, large perturbations (for example, with a polar solvent such as water) will cause a large increase in insertion loss, which can lead to a resonance becoming unmeasurable if its power transmission reduces to a level close to the noise floor of the spectral measurement. This would necessitate stronger coupling (such as the end coupling shown in Figure 4.2) in order to achieve a measurable perturbation since increased coupling strength reduces insertion loss.

4.1.2. Perturbation optimisation

This section shows, firstly, how dielectric properties can be extracted from electric sensing mode measurements and, secondly, how the magnetic sensing mode response is a function of conductivity but not of complex permittivity for a non-magnetic sample. The combination of these results demonstrates the principle of electric and magnetic deconvolution on which the capillary-perturbed coaxial resonator is based. Whilst the finite element modelling in COMSOL gives better agreement with the experimental results, the simplified analytical approach that follows gives the correct dependencies on the geometrical factors (e.g. coaxial line cross-section and capillary dimensions), which are important in the optimisation of this design.

Consider a coaxial resonator as represented in Figure 4.3. If all fields have $e^{j\omega t}$ time dependence, the electric and magnetic field amplitudes can be written as:

$$E_r(r,z) = E_0 \frac{a}{r} \cos\frac{n\pi z}{l}, \tag{4.1}$$

$$H_\varphi(r,z) = j\frac{E_0}{\eta_0}\frac{a}{r}\sin\frac{n\pi z}{l}, \tag{4.2}$$

where E_0 is the peak magnitude of electric field E_r (located at the ends of the resonator) for the nth TEM mode. η_0 is the vacuum impedance (i.e. η_0 = 376.7 Ω). Co-ordinates and all other dimensions are labelled in Figure 4.3.

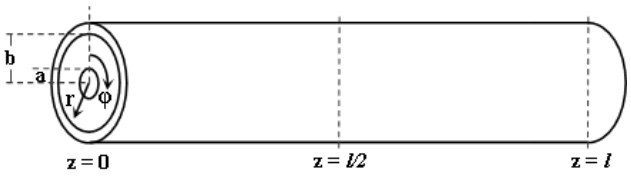

Figure 4.3: Air-filled coaxial resonator schematic (not to scale). The hole for the liquid-filled capillary is perpendicular to the conductors' axis and located halfway along the length of the resonator (z = l/2).

From first order perturbation theory, the normalised change in centre frequency can be written as:

$$\frac{\Delta f_0}{f_0} \simeq -\frac{\int E\, dp}{4U}, \tag{4.3}$$

where dp is the dipole moment of a volume element of the fluid and U is the time-averaged stored energy. Evaluating the right-hand side of Equation 4.3 as shown in Appendix 1 allows the expression for normalised change in centre frequency to be rewritten in terms of sample permittivity and device dimensions:

$$\frac{\Delta f_0}{f_0} \simeq -(\varepsilon_1 - 1)\Gamma_E, \tag{4.4}$$

where

$$\Gamma_{\mathrm{E}} = \frac{d^2(b-a)}{4abl \cdot \ln(b/a)}, \tag{4.5}$$

where d is the inner diameter of the capillary, a is the diameter of the coaxial inner conductor, b is the inner diameter of the coaxial outer conductor and l is the length of the coaxial resonator. By a similar process, the normalised change in half-power bandwidth can be shown to be dependent on the dielectric loss of the sample:

$$\frac{\Delta f_{\mathrm{B}}}{f_0} \simeq 2\varepsilon_2 \Gamma_{\mathrm{E}}. \tag{4.6}$$

These expressions can be used to theoretically predict the change in complex resonant frequency for a sample of known permittivity.

It is obvious from Maxwell's equations that an alternating magnetic field will induce an electric field in a conducting material. It is not possible to induce an electric dipole (defined as $\underline{\nabla} \times \underline{E} = 0$) since the induced electric field necessarily has a non-zero curl. Physically, this means that the induced electric field distribution will consist of concentric circles. This is not an alternating field and therefore cannot be used to quantify alternating polarisation mechanisms such as dipolar reorientation or the associated losses. This can be proven by demonstrating that the magnetic field response depends on conductivity but not on either component of complex permittivity.

The quality factor of a resonator Q can be defined as:

$$Q = \frac{2\pi f_0 U}{P}, \tag{4.7}$$

where P is the time-averaged power dissipation. Evaluation of the right-hand side of Equation 4.7 allows an expression for change of inverse quality factor to be derived. This change is caused by a change in power dissipation rather than stored energy given that the latter is constant. Power dissipation depends on

conductivity, so evaluating the right-hand side of Equation 4.7 as shown in Appendix 1 gives the result:

$$\Delta Q^{-1} = \sigma f_0 \Gamma_{\mathrm{H}}, \tag{4.8}$$

where

$$\Gamma_{\mathrm{H}} = \frac{\mu_0 \pi^3 d^4 (b-a)}{4abl \cdot \ln(b/a)}, \tag{4.9}$$

where μ_0 is vacuum permeability. Equations 4.8 and 4.9 can be used for a theoretical prediction of the change of inverse quality factor for a sample of known conductivity. This can be achieved using the approximation for resonant frequency $f_0 = nc/2l\sqrt{\varepsilon_{\mathrm{r}}}$, where n is mode number and ε_{r} is the relative permittivity of the coaxial spacer. In practice, however, it is likely that f_0 will be known to a greater degree of accuracy than ε_{r} so Equation 4.8 is probably best used in its given form.

It can be seen that a conductive liquid, such as saline, will interact with both electric and magnetic sensing modes from Equations 4.4, 4.6 and 4.8. The ability to deconvolve electric and magnetic field effects will be proven if it can be demonstrated that two conditions are satisfied for a conducting liquid such as an ionic solution. The conditions are that the electric sensing mode response must be a function of complex permittivity only and that the magnetic sensing mode response must be a function of conductivity only.

As the title of this chapter may imply, the coaxial resonator was to be perturbed with a capillary. The capillary dimensions corresponding to optimal perturbation were determined with finite element modelling in COMSOL. The primary motivation for using quartz capillaries was because of their extremely low value of dielectric loss. Capillary action provides an extremely effective method of introducing the sample to the resonator without having to physically manipulate the sensor: the quartz tube will readily fill with a wide range of organic and aqueous liquids by dipping the end of an empty capillary in a liquid sample. Capillary action draws up the liquid sample and fills the tube and thereby the

sensing volume of the resonator. This means the resonator and the capillary do not need to be touched, filled or otherwise disturbed. This is particularly useful because it means that the reference (empty capillary) and sample measurements (filled capillary) are taken from an identical volume. This is significant because any useful data from the sensor will be taken from differences between the reference and sample volumes.

Resonator simulations were performed in COMSOL. Eigenmode simulations were used to investigate the effects of varying capillary dimensions on the behaviour of the resonator. The ability to take aqueous-phase measurements was vital considering the intended point-of-sampling applications, and potentially problematic due to the large permittivity of water.

An appropriate optimisation figure of merit was therefore required to give the maximum decrease in centre frequency in the electric sensing (second TEM) mode upon the introduction of water into the capillary. It was also required to give the minimum centre frequency change in the magnetic sensing (first TEM) mode under the same conditions. The sample would interact with the second TEM mode but not the first if the water was of sufficient purity (i.e. no with no ionic content) and cross-section (i.e. tending towards zero). It is desirable to maximise the frequency shift of the electric sensing mode because it will give increased measurand resolution when the power transmission spectrum of the sensor is characterised by a network analyser of fixed frequency resolution.

In practice, the sample cannot be completely removed from the magnetic field because of its finite cross-section, so the magnetic field response due to any corresponding interaction must also be accounted for by the figure of merit. Hence, the optimisation figure of merit was taken as the frequency change in the second TEM mode divided by the frequency change in the first TEM mode. It is vitally important for this figure of merit to be maximised to ensure maximum sensitivity and unambiguous deconvolution of electric and magnetic field effects. These values (referred to as modal ratios) are shown in Table 4.1 for the available dimensions of quartz capillary from VitroCom (NJ, USA).

Table 4.1: The change in centre frequency affected by the introduction of water was simulated for the first two TEM modes of the resonant coaxial device. The simulations were repeated for several quartz capillaries, where the simulated dimensions were those available for purchase. The outer diameter (O.D.) and inner diameter (I.D.) are shown for each capillary. The modal ratios were obtained by dividing the response of the second TEM mode by the first for a figure of merit for the difference in sensitivity between the modes. The maximisation of this figure represents an optimisation with respect to field separation. This is necessary for the deconvolution of the electrical and magnetic properties of a material under test.

O.D./I.D. (μm)	400/300	700/500	1000/800
Modal ratio	250	440	110

It can be seen that a capillary of inner and outer diameters of 500 μm and 700 μm, respectively, gave the highest ratio. This unusual result could be because of increasing capillary diameter affecting an increase in electric field perturbation and a decrease in field separation.

4.1.3. Experimental

The sensor using the single-ended coupling structure with a separate coaxial section (Figure 4.1) was used instead of the purpose-built coaxial structure formed from a single block of aluminium (Figure 4.2) because of the time constraints of the project. A length of RG401 50 Ω coaxial cable was used to form the half-wavelength resonator. This was open circuited at both ends to allow capacitive coupling to the evanescent field. The coaxial cable was cut and polished to a length of 3.8 cm for a fundamental TEM resonance at ~ 2.8 GHz, giving two modes in the frequency region of interest (0.5 to 6 GHz, the upper limit set by the network analyser used to perform the measurement). More modes could have been used to further examine the frequency dependence of permittivity and permeability. However, the minimum number of modes required (for magnetic and electric sensing, respectively) were used for maximum frequency separation between the sensing modes. This was considered necessary because of the fact that separating mode dependencies could cause two modes to overlap and possibly lead to degeneracy (that is, where two modes have the same resonant frequency). For

example, two adjacent modes could overlap if the centre frequency of the higher mode decreased as a function of permittivity and the centre frequency of the lower mode increased as a function of permeability. This device clearly has potential for obtaining multi-frequency information on both the electric and magnetic properties of the material. This chapter is restricted to the simplest case where the different properties are characterised by one mode apiece because the use of many modes for multi-frequency determination of complex permittivity has already been demonstrated.

RG401 coaxial cable is comprised of copper conductors (of 6.35 mm outer diameter) and a polytetrafluoroethylene (PTFE) spacer (of 1.6 mm inner diameter and 5.4 mm outer diameter). The resonator was constructed from cable of this size so that the previously designed single-ended coupling structure (*cf.* Chapter 3) could be used to perform power transmission measurements of the resonator. A copper cap was placed over the uncoupled end of the resonator. An image of the complete assembled device is in Figure 4.4.

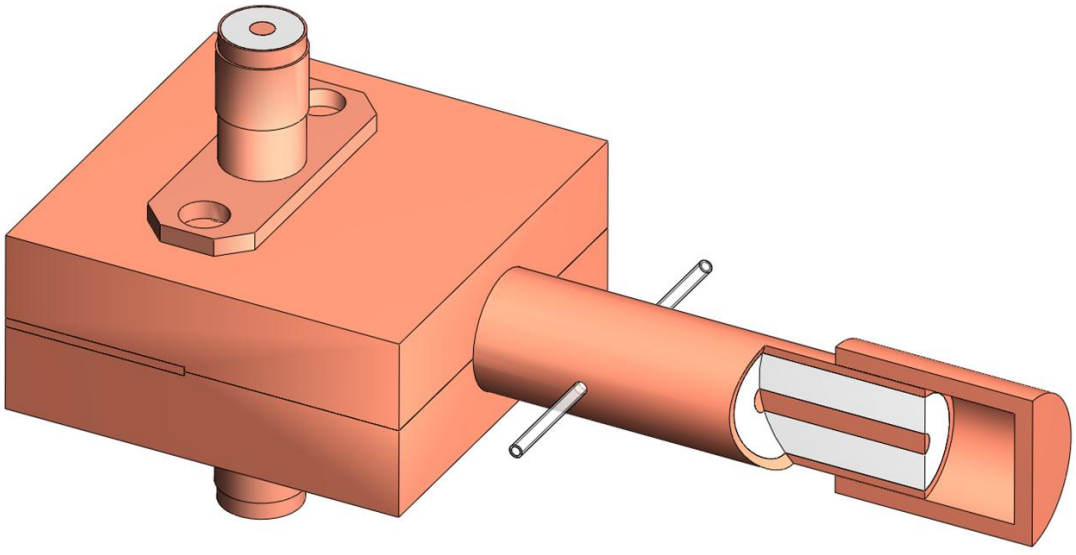

Figure 4.4: Cutaway schematic showing a conducting cap placed over the uncoupled end of the coaxial resonator in order to prevent accidental perturbation and increase field confinement.

The cap was placed over the uncoupled end of the resonator for increased confinement of the evanescent field, which increased sensitivity by reducing the effective volume of the resonator and increasing its Q factor. Note that the cap

does not short circuit the coaxial conductors (which would cause a quarter rather than a half-wavelength resonance). This was considered acceptable as the evanescent field at the uncoupled end was not to be perturbed for any of the measurements presented in this chapter. Including the cap shown in Figure 4.4, the first two TEM modes of this resonator had unperturbed quality factors of approximately 1200.

A ZVL vector network analyser (VNA) (Rohde and Schwarz, Munich, Germany) was used to measure the transmission coefficient of the assembled device. The shortest, highest available quality cables and the fewest, highest available quality connectors were used to connect the resonant devices to the VNA. The data were exported to LabVIEW (National Instruments, TX, USA), where a Lorentzian curve was fitted to the peak of each resonance in real-time. The fitted curve data were then used to measure the resonant frequency and bandwidth of all modes. As with the measurements reported in Chapter 3 that were performed with an E5071B network analyser, the measurement period of this experimental setup was limited by the USB 2.0 data transfer rate from the network analyser and the PC performing the curve fitting algorithms, and the maximum measurement rate was 20 Hz.

The resonator was mounted on a hot plate for temperature control. This was capable of maintaining a specified temperature to within 0.1 K, regulated by a control loop with a period of approximately 40 seconds. This is a reasonably significant temperature variation, but the liquid sample is effectively buffered from such changes by the large thermal mass of the resonant device. The samples and capillaries were stored on the hot plate overnight prior to measurement to allow thermal equilibration. Under these circumstances, the sample, capillary and resonator were considered to be at the same temperature for the duration of the measurement, which was experimentally verified with an infra-red thermometer. All measurements were taken at a slightly elevated temperature of 303 K, which was used to ensure the hot plate (rather than the laboratory environment) was the dominant thermal source.

Deionised (DI) water was obtained with an ELGA Purelab UHQ system for Type I purified water. The highest available purity salts were obtained from Sigma

Aldrich (Sigma Aldrich, MO, USA) and were used as supplied. Magnetite was synthesised according to the procedure described in Section 2.6.4. Stock solutions and suspensions were made and serially diluted with the same batch of solvent. Quartz capillaries of 700 μm outer diameter, 500 μm inner diameter and 10 cm length were obtained from VitroCom (NJ, USA) and used as provided.

For each sample, an empty capillary was introduced into the resonator and a reference air measurement was recorded. The sample was then introduced via capillary action. This was achieved by tilting a liquid-filled Eppendorf tube to dip the end of the capillary in the sample without touching the capillary with the sample vessel. Sample measurements were then recorded. In each instance, 100 data were logged for each reference and sample measurement to provide a sufficiently large dataset for statistical analysis. New quartz capillaries were used for each sample due to difficulties in cleaning them effectively.

The quantification of ionic content of an electrolytic solution is easily achieved with existing techniques such as conductivity measurements. These usually require direct contact to the liquid (unlike our method, which is non-invasive) and cannot distinguish between anions or cations that have the same charge. Practical experience has shown that ionic content can be a significant obstacle to microwave frequency dielectric spectroscopy, particularly at low GHz frequencies. Therefore, the presented approach is not intended to supersede existing conductivity techniques, but rather to render microwave-frequency resonant methods more useful by determining additional information. Furthermore, ionic solutions are convenient for demonstrating simultaneous electrical and magnetic characterisation given that they interact with both fields via different polarisation mechanisms.

The device shown in Figure 4.2 was successfully fabricated and assembled, but time restrictions meant experiments to compare its performance with the single-ended coupling approach were not possible.

4.2. Results

COMSOL simulations yielded the result that the introduction of pure water into the capillary-perturbed coaxial resonator would affect a centre frequency change of 118 MHz at the second TEM mode. The measured change was 115 MHz.

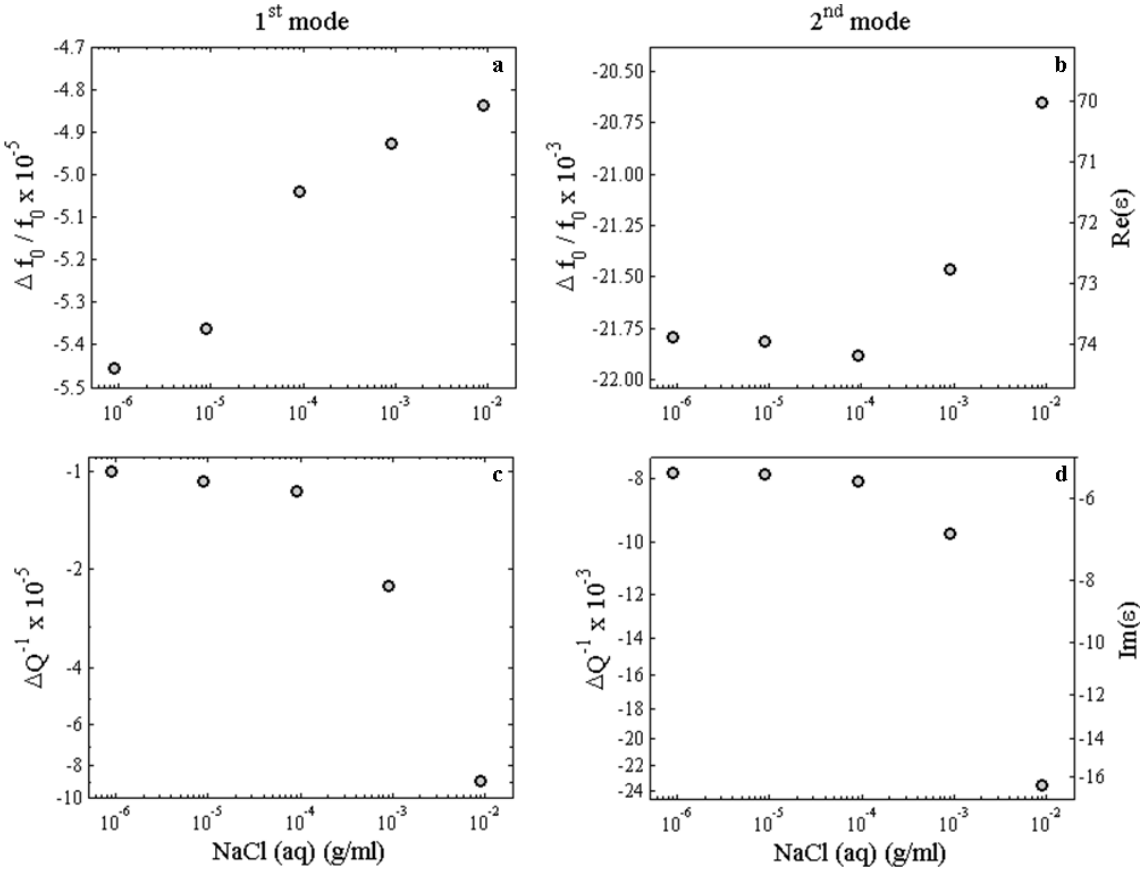

*Figure 4.5: Measurement data for serial dilutions of aqueous NaCl solutions. The change in centre frequency is shown with respect to NaCl concentration for the (**a**) first and (**b**) second TEM sensing modes, representing electrical and magnetic sensing respectively. Likewise, the change in inverse quality factor is shown with respect to NaCl concentration for the (**c**) first and (**d**) second TEM sensing modes. Note that logarithmic y-axes have been used in (**c**) and (**d**) to emphasise that there is still a discernable shift between the lowest measured concentrations. Measured estimates of complex permittivity are shown on the right y-axes of the electric sensing modes responses. Error bars are too small to be visible.*

Values of $\Delta f_0/f_0$ and ΔQ^{-1} are shown with respect to concentration for increasing dilute saline solutions in Figure 4.5. An empirical model of the permittivity variation of aqueous sodium chloride solutions with respect to frequency, concentration and temperature was developed in [135]. This model fitted a Debye-type dispersion equation to measurement data taken from all existing sources of information, and as such is considered the most complete source available. Unfortunately, the sodium chloride concentrations were invariably high: only the highest of the concentrations presented here was within the valid range of the model (taken as the range of data to which the model was fitted). This meant the literature values could not be used as a comparison for the presented measurements. However, this did mean that the response for the highest concentration could be used to calculate complex permittivity from the other measurements.

Complex permeability was not calculated from the magnetic sensing mode response because the sample was not magnetic.

Error bars are too small to be observed. Measurement uncertainty, limits of detection and measurement error are listed in Table 4.2. The same device has been used to measure each solution so any geometric uncertainty (for example, that due to fabrication tolerances) is constant and therefore irrelevant. The temperature can be assumed to be constant, as discussed in Section Experimental4.1.3. The only source of variation between each measurement is the capillary. Simple repeatability measurements (i.e. measuring ten different empty capillaries) have shown the measurement uncertainty due to volume variation to be approximately ±1%. The limits of detection are the smallest changes in centre frequency and quality factor that can be distinguished above the reference measurement error. Measurement error is the highest experimental value of noise (one standard deviation).

Table 4.2: Device characteristics.

Measurement uncertainty u	Detection limit $\Delta f_0/f_0$	Detection limit ΔQ^{-1}	Max. error $\Delta f_0/f_0$	Max. error ΔQ^{-1}
± 1 %	8×10^{-7}	2×10^{-6}	4×10^{-5}	2×10^{-5}

The two quantities of interest from these experiments are changes in centre frequency and in inverse quality factor. Modal ratios of these quantities are obtained by dividing the either one of the measured quantities at the second TEM mode by the same quantity measured at the first TEM mode. Such modal ratios are shown in Figure 4.6. These quantities represent a measure of the difference in sensitivity between the modes.

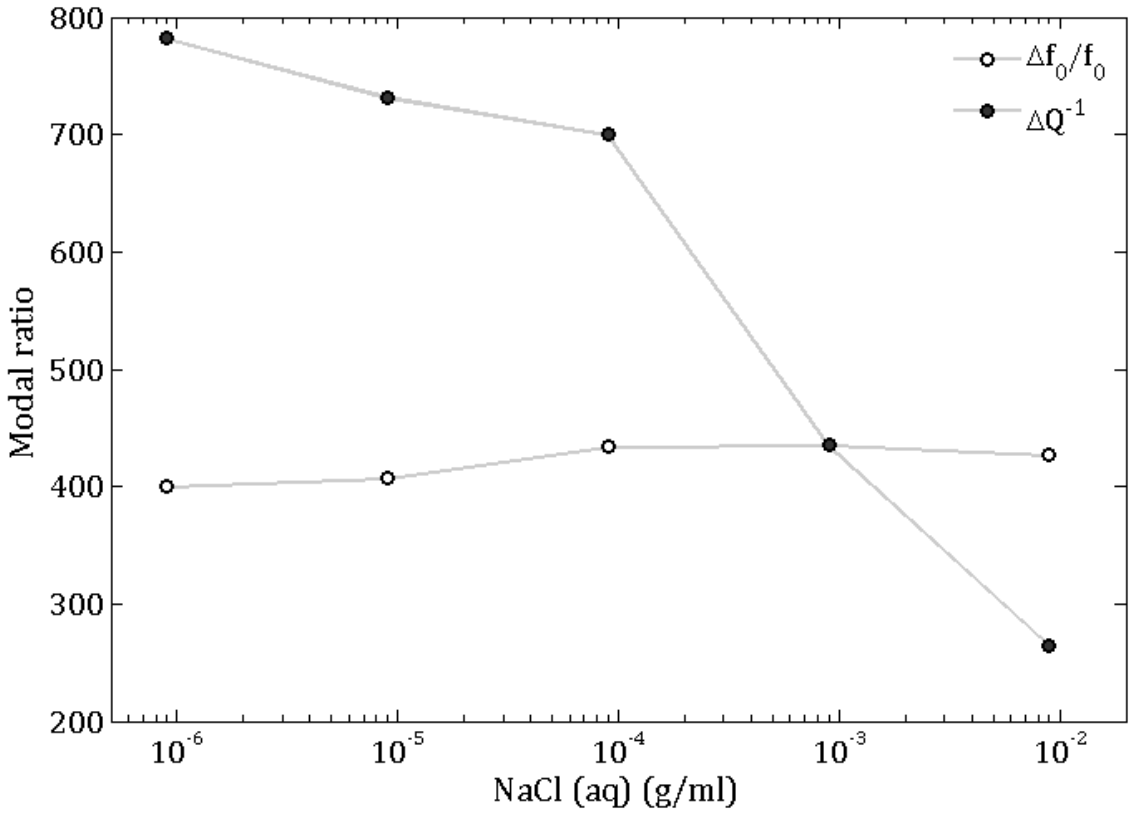

Figure 4.6: Modal ratios have been computed for changes in both centre frequency and inverse quality factor at all concentrations of aqueous NaCl solutions. The modal ratios were obtained by dividing the response of the second TEM mode by the first for a figure of merit for the difference in sensitivity between the modes. The data are joined to emphasise that there are coincident markers at 10^{-3} g/ml NaCl. Error bars are too small to be visible.

Changes in inverse quality factor for all salts are shown with respect to concentration in Figure 4.7. Serial dilutions of three salts have been used: sodium chloride, calcium chloride and sodium acetate.

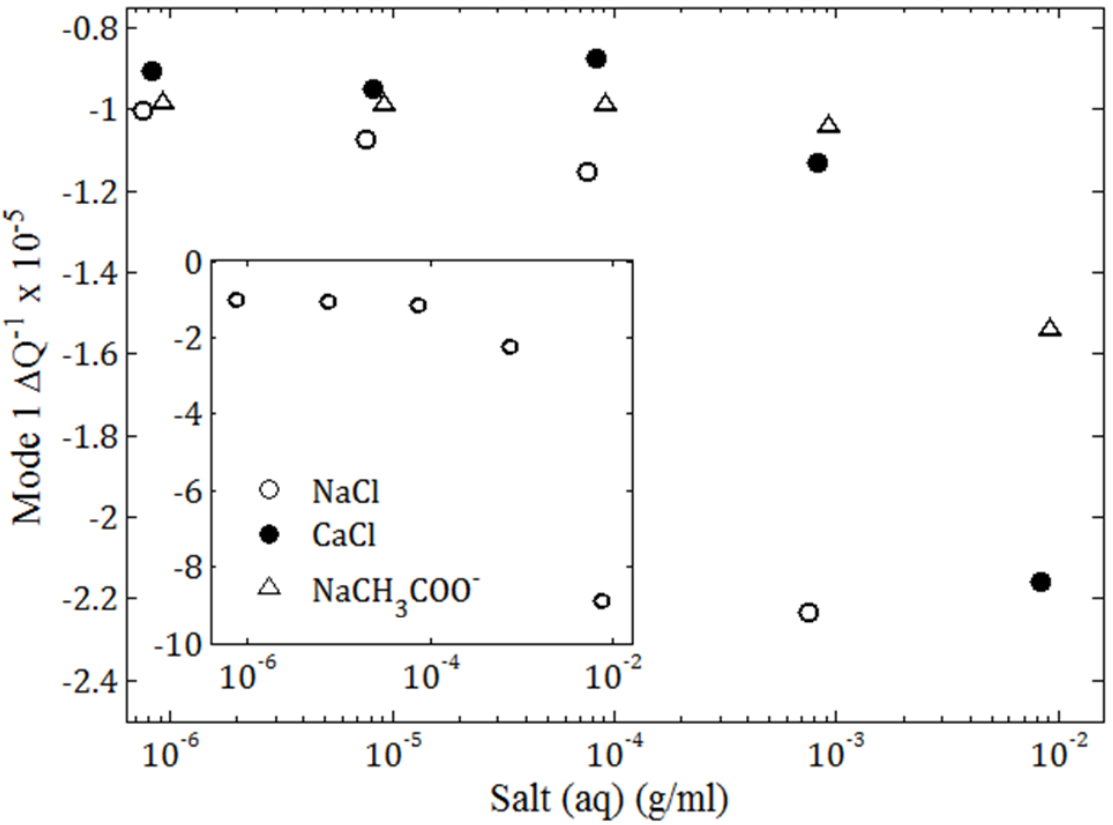

Figure 4.7: The change in inverse quality factor is shown for the magnetic sensing (first TEM) mode for several aqueous salt solutions. Note that different cations (sodium and calcium) and different anions (chloride and acetate) can each be distinguished from each other. The highest NaCl concentration gives a much larger change of inverse quality factor that all other salts and concentrations and has therefore been excluded from the main figure. The inset includes this datum as part of the full NaCl dilution series, where the axes are of the same quantities and units as the main figure.

To investigate the characterisation of magnetic liquids, a 5 mg/ml suspension of magnetite in hexane was prepared according to the synthesis described in Section 2.6.4. Using the same experimental procedure as above, measurements were obtained for pure hexane and the magnetite suspension to investigate the effects of adding a solid ferromagnetic phase to a liquid system. Hexane was chosen as the solvent because it is extremely non-polar and demonstrates a very low dielectric constant across the entire microwave frequency region, meaning that any relative changes due to the suspended particles would be more easily detected. The resulting data are plotted in Figure 4.8.

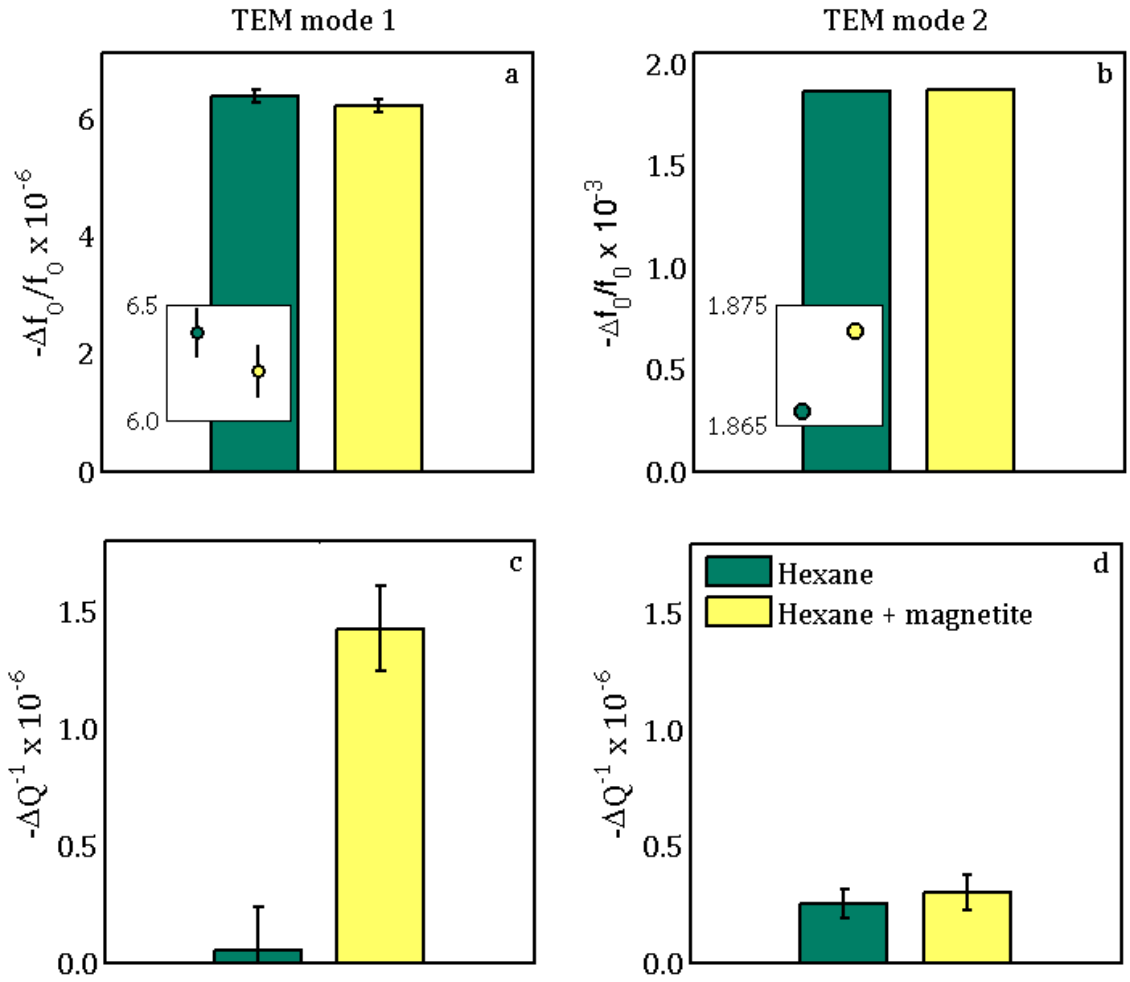

*Figure 4.8: Comparison of the change in centre frequency (***a** *and* **b***) and in inverse quality factor (***c** *and* **d***) of the first two TEM modes for hexane (green) and magnetite suspended in hexane (yellow). The first TEM mode is for magnetic sensing; the second TEM mode for electric sensing. Error bars represent the 95% confidence interval. The insets in* **a** *and* **b** *have the same axis quantities and units as the main figures, and are included to illustrate whether the measured quantities are distinguishable at the given confidence interval (in* **b***, the error bars are too small to be seen).*

The use of the capillary-perturbed coaxial resonator for temporal binding studies was also investigated. Non-specific binding was attempted before targeted binding (such as with molecularly imprinted polymers) for the simplest possible dynamic chemical system. A 5 mg/ml suspension of 5 μm diameter Si100 (silica) in deionised water and aqueous solutions of propranolol were prepared separately. Their concentrations were adjusted so that, when added together, each sample would have the same volume of water and suspended silica particles, but varying

concentration of propranolol. Concentrations of 10 – 100 μM propranolol (i.e. comfortably above the limits of detection) were used to ensure a measureable signal. Empty capillary reference measurements were taken as the liquids were being mixed together. After being added together and mechanically excited to ensure mixing, each sample was introduced into the resonator via capillary action in the same manner as the previous experiments. The ends of the capillary were sealed with wax to prevent evaporation, where a small region of air was maintained between the wax and the liquid sample to prevent foreign species interfering with the measurement. Changes in centre frequency and quality factor were then logged with respect to time.

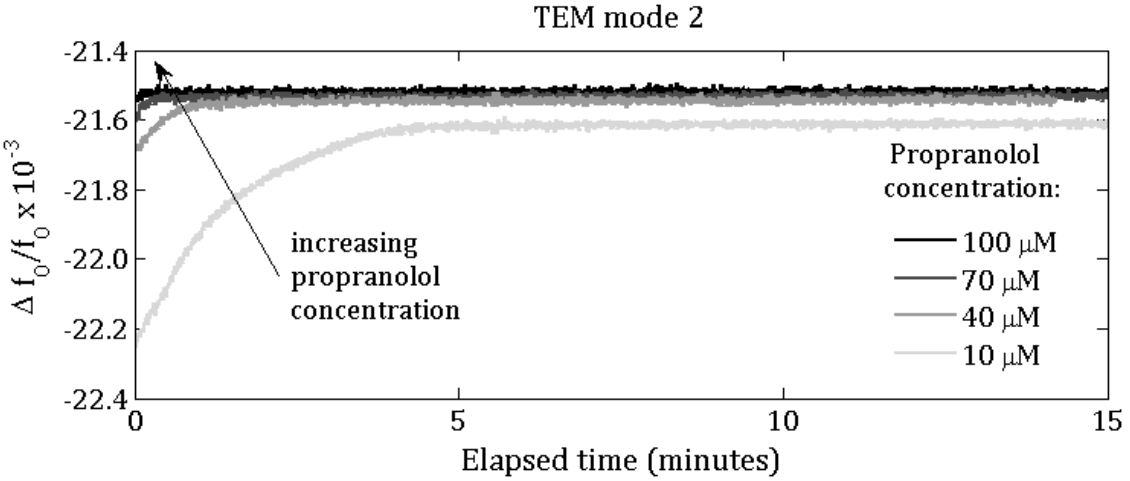

Figure 4.9: Change in centre frequency with respect to time for varying concentrations of propranolol in an aqueous suspension of silica microparticles.

Inverse quality measurements have not been included because they did not show any meaningful results. It should be noted that these results could not be reproduced. Similar experiments were performed several times, resulting in traces of tending downwards rather than upwards; no change in $\Delta f_0/f_0$ or erratic and unpredictable variation in $\Delta f_0/f_0$ over many orders of magnitude.

4.3. Discussion

In Section 4.1.2, it was shown that the normalised change of centre frequency ($\Delta f_0/f_0$) is proportional to the real component of either permittivity or permeability, depending on the sensing mode being interrogated. Likewise, the change of inverse quality factor (ΔQ^{-1}, where $Q = f_0/f_B$) is proportional to the

imaginary component of either permittivity or permeability, depending on the sensing mode interrogated. The response of the magnetic sensing mode is also a function of sample conductivity. Calculating $\Delta f_0/f_0$ and ΔQ^{-1} allows the electric and magnetic sensing modes to be compared in order to demonstrate electric and magnetic deconvolution.

The centre frequency response will be considered first. Figure 4.5 **a** shows the magnetic sensing (first TEM) mode to exhibit very small changes in comparison with the electric sensing mode. This is to be expected given that Na^+ and Cl^- ions do not have any magnetic polarisability. However, the centre frequency response does also show a linear trend with logarithmic concentration. One physical interpretation of this result could be that these results show increasing magnetic polarisability for decreasing NaCl concentration. Such an explanation is clearly nonsensical given that all components of the solution are non-magnetic, so the results in Figure 4.5 **a** shall be treated as negligible. The centre frequency response of the second TEM model can be seen in Figure 4.5 **b.** This exhibits a non-monotonic response above the limit of detection. The saline solutions were obtained by serial dilution with the same batch of deionised water and measured at a constant temperature. Therefore, it would be reasonable to expect any permittivity variation above the limit of detection to be monotonic. This expectation may not be valid for large changes in composition measured using a depolarising geometry. However, such depolarisation (occurring when the sample capillary is oriented parallel to the sensing field and therefore crosses field lines) can account for non-monotonicity in the change of inverse quality factor but not in centre frequency. Therefore, any non-monotonic response above the limit of detection does not have any meaningful interpretation. Whilst the responses shown in Figure 4.5 **a** and **b** are above the limit of detection, such responses are in line with the author's experience characterising ionic solutions with microwave-frequency resonators, where quality factor changes exhibit systematic variation but centre frequency changes do not.

However, of note is the fact that $\Delta f_0/f_0$ is much greater for the electric sensing mode (Figure 4.5 **b**) in comparison with the magnetic sensing mode (**a**). Values of approximately -21 x 10^{-3} (ignoring non-systematic variation) correspond to a 130

MHz decrease in centre frequency. From experience, this is an extremely large change. It is to be expected given the high real permittivity of water, which is roughly 75 at the frequencies considered. The far smaller values for the magnetic sensing mode (approximately -5×10^{-5}) imply that the electrical properties of the sample are not being interrogated, since the presence of water (with the correspondingly large value of real permittivity) would exaggerate any such response. This can be investigated qualitatively using the modal ratio, as introduced in Section 4.1.2.

The quotient of the electric and magnetic sensing mode responses (i.e. TEM mode 2 response divided by the TEM mode 1 response) is shown for changes in both centre frequency and inverse quality factor in Figure 4.6. The modal ratio for centre frequency change is approximately 440 over the entire range of measured concentrations. The response is not completely linear, but any deviation is an artefact of the non-systematic responses discussed above. This experimental modal ratio corresponds with the simulated value for deionised water. This means that the expected amount of field separation occurs, but does not conclusively prove that the modes are interrogating different loss mechanisms. The modal ratio for the change of inverse quality factor is also shown in Figure 4.6, and clearly demonstrates a dependence on salt concentration. This means that the different modes must be interrogating different loss mechanisms because, otherwise, their responses would have to be proportional (from perturbation theory) and the modal ratio would be constant with respect to concentration. Instead, the ratio tends toward unity at high concentrations, which can be interpreted as increasing competition between the different loss mechanisms being interrogated by the two sensing modes. An inverse quality factor modal ratio value of approximately 800 was extracted from simulations. This was obtained for DI water in the same way as the value for centre frequency. The saline solution response approaches this estimated value as the salt concentration tends toward zero. The combination of these results proves that satisfactory mode separation occurs for dielectric and magnetic deconvolution.

The change of inverse quality factor can be seen to vary with NaCl concentration for both sensing modes in Figure 4.5 **c** and **d**. The magnetic sensing mode

response is the smaller of the two, but still exhibits significant systematic variation. However, the modal ratio for change in inverse quality factor demonstrated that the two modes were interrogating different loss mechanisms. Therefore, any responses observed in the imaginary frequency component of either mode must be due to different causes. The electric sensing mode response is to be expected given the dielectric losses associated with dipolar reorientation within an ionic solution. The magnetic sensing mode losses can only be attributed to induced eddy currents for two reasons: the sample occupies maximal magnetic field but exhibits negligible change in magnetic polarisability.

Figure 4.7 shows how this measurement technique can also be used to distinguish different salts. The change of inverse quality factor for the magnetic sensing mode is probably the most useful measured quantity given that it is dependent on conductivity but not on electric polarisability or dielectric loss. This essentially removes the permittivity of the solvating medium from the measurement, which is particularly useful for high permittivity solvents such as water. This is significant for the aqueous samples commonly encountered in biological applications because, particularly for depolarising resonators for dielectric characterisation, the large permittivity of water can drive the resonator response into non-linearity and mask subtle effects of trace concentrations.

The solutions of three salts (sodium chloride, calcium chloride and sodium acetate) were serially diluted. These particular salts were chosen to show that this technique can differentiate between cations (sodium and calcium) and between anions (chloride and acetate). In Figure 4.7, the changes in inverse quality factor with respect to concentration for sodium acetate and sodium chloride are different. Dissociation of the salts into ions means that the cations and anions behave independently, meaning that the conductivity contribution of sodium is the same for both serial dilutions (i.e. it is unaffected by the cation). The differences in ΔQ^{-1} can therefore be attributed to the different anions, which is to be expected given that the acetate and chloride ions will have different ion mobilities as described by the Einstein relations [136]. The differences between the responses of sodium chloride and calcium chloride can similarly be attributed to the different cation.

Being able to differentiate between cations and anions could find use in point-of-care applications for identifying an unknown salt solution independently of the solvating medium. A practical implementation of this approach could be for a user to dilute the sample by a known amount and then compare the resulting plot of ΔQ^{-1} with a lookup table of previously characterised solutions.

More generally, the capabilities of the presented device could also render it useful for metamaterial and ferrofluid research. The latter application is demonstrated in Figure 4.8, which shows the centre frequency (**a** and **b**) and inverse quality factor (**c** and **d**) changes in the first two TEM modes for hexane and a 5 mg/ml suspension of magnetite in hexane. The electric sensing mode results show the two to be distinguishable in their respective changes in centre frequency but not in quality factor, since their error bars overlap for the latter. The magnetic mode response shows the somewhat surprising result where the two samples are clearly distinguishable in inverse quality factor (**c**) but not in centre frequency (**a**). There are two possible reasons for this.

The first possible explanation for the results in Figure 4.8 is that ferrofluids exhibit ferromagnetic resonance, due to the Larmor precession of superparamagnetic magnetic dipoles. At the resonant frequency, susceptibility goes from a positive value to a negative one, meaning permeability transitions from a value above 1 to a value below 1. At this point, the imaginary component of permeability is non-zero. This effect occurs at low GHz frequencies [122], [137], [138]. If the first TEM mode corresponded to the ferromagnetic resonant frequency, it would explain why a difference was observed in imaginary permeability but not in real permeability. The electric sensing mode would be entirely isolated from such responses, so the slight increase in polarisability without any measurable difference in loss would reasonably correspond to a diffuse suspension.

The second possible explanation for the results in Figure 4.8 is that the apparent lack of magnetisation is because the magnetic field of the coaxial resonator is not high enough to cause measurable magnetisation of the superparamagnetic particles. This would mean the particles would simply behave as conducting

particles, leading to a similar interpretation of the results as for the ionic solutions characterised in Figure 4.5. Specifically, the lack of change in centre frequency of the magnetic sensing mode would imply there is no magnetisation. The change in inverse quality factor of the magnetic sensing mode must therefore be due to conductivity, which must be contributed by the suspended particles as hexane is non-conducting. One could also expect the electric sensing mode to exhibit a similar dependence of inverse quality factor on conductivity, since its response is a function of both dielectric and conductive losses. However, it is important to distinguish that the electric sensing mode characterised the entire sample whereas the magnetic sensing mode only characterised the suspended phase. The magnetite could be sufficiently diffuse to not give a discernable change above the electric sensing measurement noise.

The second explanation of the ferrofluid results seems entirely coincidental, but whether either reason (or indeed any other reason) is valid requires further experimental verification. To this end, it would be extremely useful to obtain broadband permeability spectra of the ferrofluid.

The temporal measurements of non-specific propranolol-silica binding shown in Figure 4.9 illustrate the great potential of the capillary-perturbed coaxial resonator measurement technique. In particular, each concentration shows a systematic trend towards some equilibrium value, which is all the more significant because each measurement was taken with a different capillary, causing a slightly different sample volume for each measurement. The results seem to show a decrease in permittivity as propranolol is extracted from solution to bind to the surface of the silica microparticles. The time taken for binding varies with concentration as higher concentration solutions are able to fill the available binding sites quicker. However, these results should not be considered reliable because it has not been possible to reproduce them. This technique is undoubtedly capable of performing interesting, useful measurements, but more rigorous work is required for quantitative analysis.

5. SPLIT-RING RESONATOR

The notion of using a split-ring resonator for dielectric spectroscopy is well established. There are two main types of split-ring resonator, as discussed in Literature and Theory, and they differ in whether or not they have a planar implementation. The planar version is usually etched onto conductor-clad circuit board, where the resonator is formed by a C-shaped section of transmission line. The alternative is to take a metal tube and machine a gap in the conductor. Both versions are illustrated in Figure 5.1, where resonant frequency is a function of ring radius.

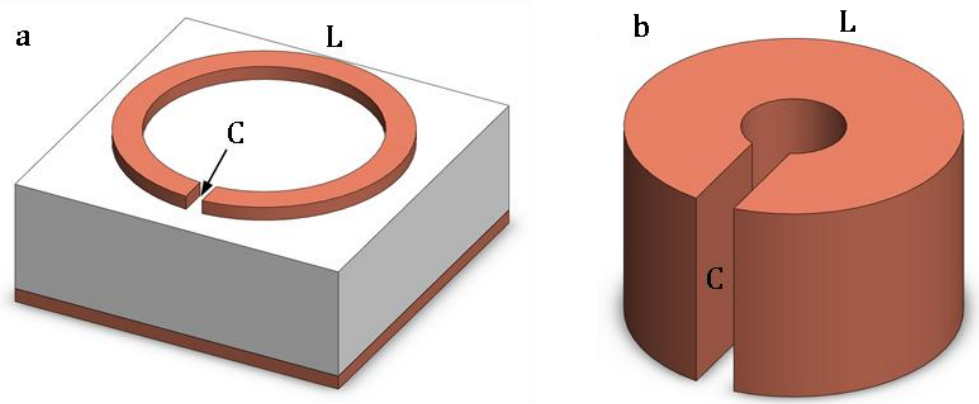

Figure 5.1: Typical implementations of the split-ring resonator. **a** *shows a planar structure and* **b** *shows an alternative fabricated from a conducting tube, where the approximate locations of the inductive (L) and capacitive (C) regions are also labelled.*

A (square) example of Figure 5.1 **a** was described in [19], where thin film samples could be detected when deposited in the capacitive loop gap region. An example of Figure 5.1 **b** is described in [58], where a liquid-filled capillary was passed through the loop gap to assess the composition of an acetonitrile-toluene mixture. Further examples and analysis of split-ring resonators are given in [139–145].

The split-ring resonator can be described by an equivalent parallel LC circuit. In both cases shown in Figure 5.1, the inductive region is approximately bounded by the circumference of the ring, and the capacitive region is the region between the two parallel faces either side of the gap in the loop. Therefore, in order to perform dielectric spectroscopy it is necessary to perturb the electric field within the loop gap.

These implementations of the split-ring resonator are both problematic in different ways. The planar approach is relatively simply to fabricate using standard PCB etching techniques. However, it suffers from extremely high conductor losses due to the thin conducting layer, which is less than skin depth and vastly increases resistance in the low GHz region. In addition to this, the corners of the etched conductors cause current bunching and further exacerbate the conductor losses. The second approach typically has an electric field region that occupies a much large volume. It is difficult to perturb the capacitive region effectively if the resonator is to be perturbed with a fluid-filled channel, as intended. The reason for this is that the length and width (i.e. the surface area) of the conductors bounding the loop gap will generally be much bigger than the distance between them. To pass a fluidic channel (particularly a microfluidic channel) through this region would diminish sensitivity, which will scale with the fraction of the electric field volume that is perturbed. Note that for the planar implementation, the sample perturbation is a function of the width of the transmission line (which essentially forms the width of a capacitor).

An example of how a split-ring resonator could be perturbed with a microfluidic capillary is shown in Figure 5.2.

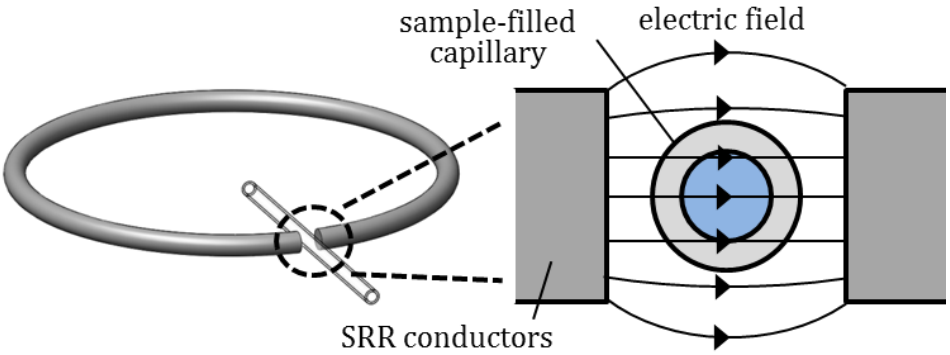

Figure 5.2: View of the electric field distribution in the loop gap of a split-ring resonator. Depolarisation charges (which will give rise to a depolarising electric field) will accumulate on the inner and outer boundaries of the capillary because it crosses electric field lines.

It can be seen in Figure 5.2 that the obvious way of introducing a fluidic sample into the loop gap of a split-ring resonator will always cause depolarisation because the capillary is orientated perpendicularly to the lines of electric field. This problem is common to all of the split-ring resonators discussed in this chapter.

Figure 5.3: Split-ring resonator formed from a single piece of curved wire. This geometry is similar to those seen in Figure 2.8, including having a capacitive region located in the loop-gap and an inductive region opposite the loop-gap. The single wire approach is simpler to fabricate and less lossy than the planar implementation (Figure 2.8 ***a****), but demonstrates reduced electric field confinement in comparison with Figure 2.8* ***b****.*

An alternative method to those shown in Figure 5.1 would be to use wire formed into a ring, which could alleviate the problems with both existing techniques. A simple example is shown in Figure 5.3. This method is low cost, simple to fabricate, and could be embedded in an appropriate recess in a microfluidic device. This approach would greatly reduce the problem of conductor losses associated with etched planar split-ring resonators, particularly if high conductivity wire, such as silver, is used. An issue with the wire resonator approach is that the electric field confinement suffers because the surface area of the faces bounding the loop gap is comparable to the gap separation. This means that much of the electric field will exist as evanescent fringing fields rather than as the uniform field within a parallel-plate capacitor. This would imply that passing a fluidic channel through the loop gap would not perturb a large fraction of the volume occupied by electric field. A solution to this would be to extend the conductors to form a larger capacitive region. Two potential examples are shown in Figure 5.4.

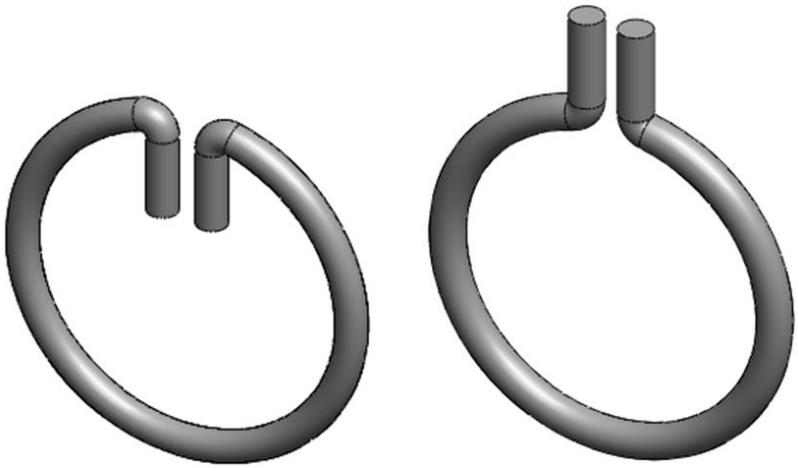

Figure 5.4: Split-ring resonators with extended conductors to enlarge the capacitive region and increase electric field confinement. Although the conductors could be orientated to any direction in 3D space, the simplest approach is to maintain the extensions in the same plane as the ring and have them protrude directly in to or out of the ring.

Investigating and optimising this novel idea will form the bulk of this chapter. The way the capacitive and inductive regions are effectively isolated from each other makes it possible to orientate the extended conductors in any direction in three-dimensional space. For the purposes of integration, it would seem prudent to use a planar device rather than pointing the conductors upwards or downwards. To

have the extensions protruding into the ring is obviously more compact, which would be beneficial on a planar microfluidic chip where space is likely to be at a premium. Whether such extensions have an adverse effect on the magnetic field distribution of the device has not been investigated due to time constraints of this project, though it would certainly be a worthwhile task.

5.1. Methods

5.1.1. Electromagnetic design

There are two main aspects of split-ring resonator design: the resonator and the coupling. They are discussed in that order within this section.

A split-ring resonator with extended conductors can be fully described by the dimensions labelled in Figure 5.5.

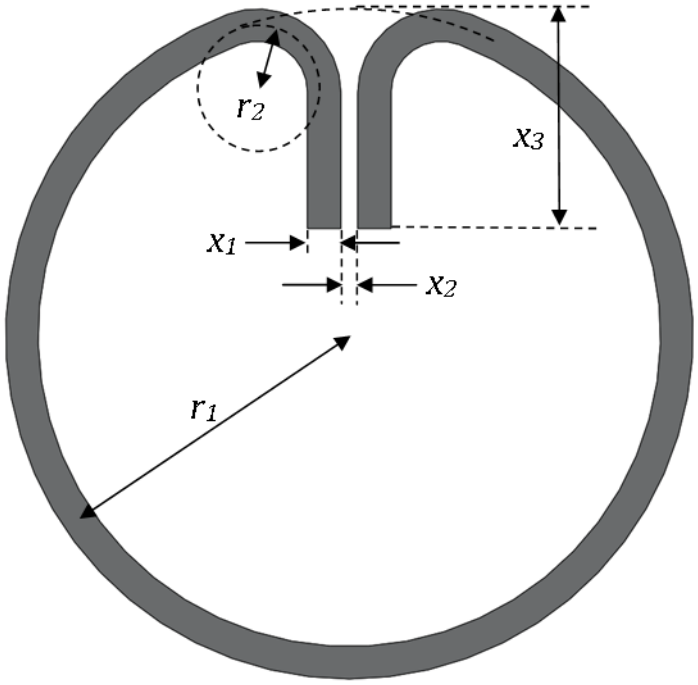

Figure 5.5: Split-ring resonator dimensions. Note that, as a matter of convenience, the radii r_1 and r_2 and the leg length x_3 are taken from the centre of the wire but the leg separation x_2 is not.

The centre frequency of the split-ring resonator is set by the ring radius r_1. The extended legs will also have a minor effect on centre frequency (i.e. a longer

protrusion will decrease centre frequency), but this is not a primary concern. The leg separation x_2 is analogous to the separation of a parallel plate capacitor: reducing this value will increase the electric field magnitude within the gap. The thickness of the wire x_1 will be the diameter for circular cross-section wire and the width for square cross-section wire. The radius of curvature r_2 depends on how the ring is formed. In practice, it can never be zero since the wire would snap, but it is desirable to minimise this radius in order to maximise electric field uniformity. The dimension x_3 describes the length of the extended conductors. Note that the volume occupied by the electric field is also a function of leg width x_1 and radius of curvature r_2 (*cf.* Figure 5.6 **a**).

This structure will have electric and magnetic field distributions as shown in Figure 5.6.

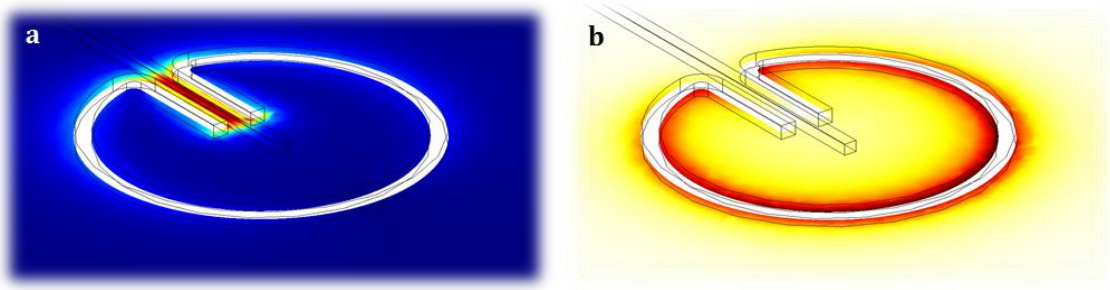

*Figure 5.6: (**a**) Electric field colourmap (blue = zero |E|, red = maximum |E|) and (**b**) magnetic field colourmap (white = zero |H|, brown = maximum |H|) for the split-ring resonator with extended conductors.*

It can be seen that the majority of the electric field energy is stored in the parallel region between the two extended conductors (Figure 5.6 **a**). Within this region, the field is formed of straight lines from one conductor to the other, where the direction of the field varies with sinusoidal excitation. The magnetic field is distributed away from the loop gap around the rest of the ring (Figure 5.6 **b**). It is particularly focussed about the ring on the opposite side to the loop gap. The field lines form concentric circles around the wire.

Three design considerations were highlighted for optimally sensitive dielectric characterisation with this structure. First, did the use of square cross-section wire improve the performance of the sensor? Second, did the extended legs improve

the performance of the sensor? Third, what ring dimensions gave optimal sensitivity? Coupling considerations (such as the effects of coupling on dynamic range, as discussed for the evanescently-perturbed coaxial resonator) were treated separately. The reason for this was that coupling could be affected easily and in many different ways depending on the application. Because the coupling conditions were expected to vary widely, and to be adjusted empirically, the split-ring resonator design deliberately did not account for a fixed set of coupling conditions.

As with the design procedures of the previous chapters, it is necessary to define a figure of merit that can be used to assess whether the novel aspects of this structure offer an enhancement in sensitivity. The split-ring resonator with extended conductors was suggested as a method for increasing field confinement and thereby sensitivity by ensuring that a larger fraction of the electric field volume was perturbed. An appropriate figure of merit can be defined according to first order perturbation theory, where the normalised change in centre frequency and bandwidth can be written as:

$$\frac{\Delta f_0}{f_0} = \frac{\mathrm{Re}(\mathbf{p}E_0)}{4U}, \tag{5.1}$$

$$\frac{\Delta f_B}{f_0} = \frac{\mathrm{Im}(\mathbf{p}E_0)}{2U}, \tag{5.2}$$

where U is the time-averaged stored energy, defined as:

$$U = \frac{1}{2}\varepsilon_0 \int E^2 dV, \tag{5.3}$$

and $\mathbf{p}$ is induced electric dipole moment, defined as:

$$\mathbf{p} = \alpha \varepsilon_0 E_0 V_S \tag{5.4}$$

where α is sample polarisability and V_S is the volume of electric field occupied by the sample.

If the resonator is to be perturbed with a liquid-filled capillary of inner diameter a, the sample volume becomes $V_S = \pi a^2 L_{eff}$, where L_{eff} is the effective length of the sample in maximal electric field. For the split-ring resonator with extended conductors, L_{eff} is the length of the legs, assuming the sample runs the entire length of the capacitive section. Substituting Equations 5.3 and 5.4 into 5.1 and 4.3 gives:

$$\frac{\Delta f_0}{f_0} = \frac{\mathrm{Re}(\alpha) V_S}{2\int \frac{E^2}{{E_0}^2} dV}$$

$$= \frac{1}{2}\mathrm{Re}(\alpha)\frac{V_S}{V_{eff}}$$

$$= \frac{1}{2}\mathrm{Re}(\alpha)\beta, \qquad 5.5$$

$$\frac{\Delta f_B}{f_0} = \frac{\mathrm{Im}(\alpha) V_S}{\int \frac{E^2}{{E_0}^2} dV}$$

$$= \mathrm{Im}(\alpha)\frac{V_S}{V_{eff}}$$

$$= \mathrm{Im}(\alpha)\beta, \qquad 5.6$$

where the effective volume V_{eff} (that is, the volume occupied by maximum electric field) is defined as:

$$V_{eff} = \int \frac{E^2}{{E_0}^2} dV. \qquad 5.7$$

The filling factor β can therefore be defined as $\beta = V_S/V_{eff}$, which quantifies the fraction of the effective volume occupied by the dielectric sample. Increasing filling factor β will increase the corresponding changes in centre frequency and inverse quality factor for a given perturbation, thereby enhancing sensitivity. β also describes any improvement in field confinement, i.e. when V_{eff} decreases for constant V_S.

The centre frequency and quality factor of various designs were obtained via simulations performed in COMSOL. Each simulation was performed for the

idealised case where the split-ring resonator was placed in the centre of a hollow, vacuum-filled, conducting cavity with a 38 mm inner diameter and 30 mm depth. The dimensions of the cavity were identical for each simulation and set so that the lowest frequency cavity resonance was significantly above the mode of the split-ring resonator to be interrogated, to avoid degeneracy. The experimental setup described in later sections will be seen to correspond to the simulated environment. The results of various dimension split-ring resonators are given in Table 5.1. The conductivity of the split-ring resonators was set to the default value for silver at 300 K.

Table 5.1: The effect of varying dimensions on split-ring resonator centre frequency, quality factor and stored energy. Leg length = n/a denotes a ring without extended conductors. The cylindrical cavity had a 38 mm inner diameter and 30 mm depth.

	a	**b**	**c**	**d**	**e**
Ring radius r_1 (mm)	12.5	12.5	12.5	10.0	7.5
Wire profile	circle	circle	square	circle	circle
Wire thickness x_1 (mm)	1.0	1.0	1.0	1.0	1.0
Leg separation x_2 (mm)	1.5	1.5	1.5	1.5	1.5
Leg length x_3 (mm)	n/a	6.0	6.0	6.0	6.0
f_0 (GHz)	1.76	1.54	1.52	1.85	2.37
Q	1520	1410	1200	1710	1900
Stored energy U (10^{-11} J)	4.9	4.7	2.9	-	-

The wire thickness and gap separation were kept constant throughout the simulations. The wire thickness was kept constant at 1.0 mm as it was the only dimension available in both circular and square cross-sections, and allowed a consistent comparison to be made between the two profiles. The gap separation was kept at a constant value of 1.5 mm primarily as a matter of convenience, since the initial practical experiments were to be of split-ring resonators perturbed with quartz capillaries of 1.0 mm outer diameter. Again, maintaining a constant value for this dimension also allowed a consistent comparison whilst other parameters were varied. However, the wire thickness and gap separation do offer additional degrees of freedom for further optimisation for the intended applications of this

device, where it is envisaged that the split-ring resonator would be embedded in a microfluidic chip.

The simulated centre frequency and quality factor data can also be plotted with respect to ring radius, as shown in Figure 5.7. Trendlines can be fitted to the data to extract simple design equations for such resonators, at least within the range of simulated values (i.e. 7.5 mm ≤ r_1 ≤ 15 mm).

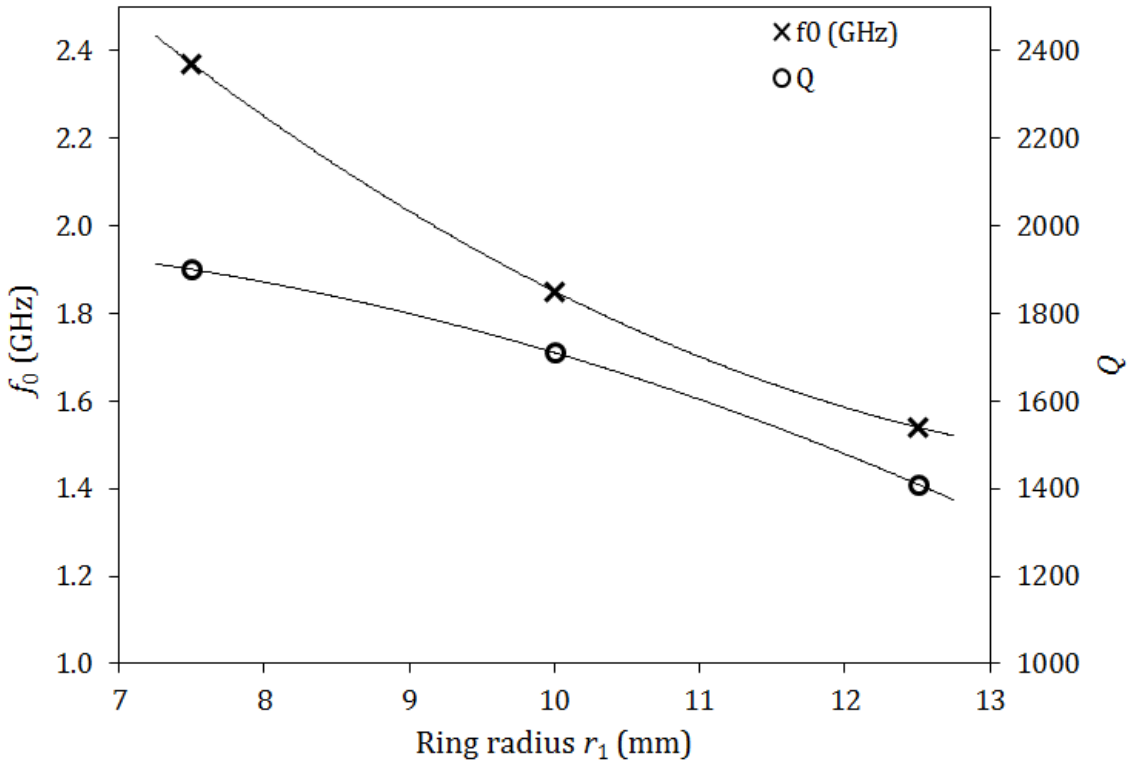

Figure 5.7: Simulated values of centre frequency and quality factor plotted with respect to ring radius r_1. The equations of the fitted trendlines, given below, can be used to estimate centre frequency and quality factor in the region 7.5 mm ≤ r_1 ≤ 15 mm. These equations hold for circular cross-section wire of 1.0 mm thickness, where the split-ring resonator has a leg separation of 1.5 mm and leg length of 6.0 mm.

The trendlines fitted to the data in Figure 5.7 can be used to estimate the centre frequency and quality factor of a split-ring resonator. Equations 5.8 and 5.9 can be used to estimate f_0 and Q, respectively:

$$f_0 = 0.0168{r_1}^2 - 0.502r_1 + 5.19, \qquad 5.8$$

$$Q = -8.8{r_1}^2 + 78r_1 + 1810, \qquad 5.9$$

where f_0 is in GHz and r_1 is in mm. Note that Equations 5.8 and 5.9 only hold for the conditions given in the caption of Figure 5.7.

Introducing extended conductors was expected to increase sensitivity over a split-ring resonator with no legs (**b** compared with **a** in Table 5.1). Similarly, a square cross-section wire was expected to have increased sensitivity over circular cross-section wire (**c** compared with **b** in Table 5.1). However, it can be seen that Q decreases in both of these cases. Any improvement in field confinement must therefore be described by changes in the filling factor β.

It was not possible to directly quantify the ratio V_S/V_{eff} for filling factor in the COMSOL simulations. However, by inspection of Equations 5.3 and 5.7, it is obvious that filling factor and therefore sensitivity are inversely proportional to stored energy U for a given excitation and sample volume. It is for this reason that stored energy was included in Table 3.3. The introduction of extended conductors yielded a slight increase in sensitivity in comparison with a split-ring resonator with no legs (**b** compared with **a** in Table 3.3). However, the use of extended conductors formed from square cross-section wire (case **c**) gave a marked increase in sensitivity in comparison with the other cases.

Stored energy was not computed for cases **d** and **e** in Table 3.3 because only ring radius varied between them. The effective volume was constant, so quality factor is an appropriate figure of merit for comparing the effects of reducing radius. It can be seen that sensitivity increases as radius decreases. Note that, from a practical perspective, such rings become increasingly difficult to manufacture accurately when radius is decreased.

Two methods of performing transmission coupling (via capacitive and inductive methods) are shown in Figure 5.8.

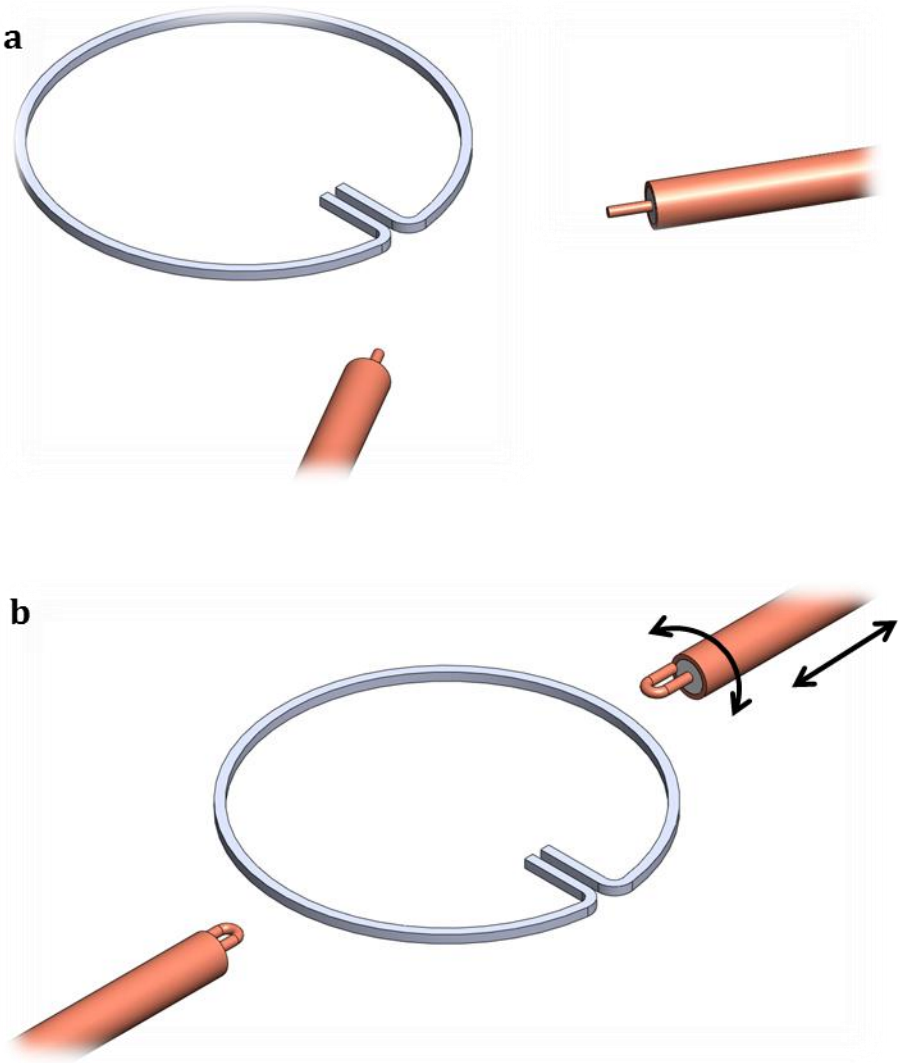

*Figure 5.8: (**a**) Capacitive and (**b**) inductive transmission coupling to a silver split-ring resonator.*

For coaxial resonators, capacitive coupling is generally preferred because it can be used at higher frequencies, where inductive coupling loops tend to act as resonators at sufficiently high frequencies. However, the use of extended conductors and square cross-section wire in the split-ring resonator both increased electric field confinement. This made capacitive coupling much less effective. The coupling structure shown in Figure 5.8 **a** suffered from high crosstalk between the connectors. This reduced the dependence of power transmission on the dielectric properties of the loop gap and rendering the structure unusable. Conversely, the magnetic field distribution of the split-ring resonator made inductive coupling much simpler and far less prone to crosstalk. This also meant that higher coupling strengths (i.e. approaching critical coupling) were achievable. This reason, together with the potential for high filling factors

according to Equations 5.5 and 5.6, made the split-ring resonator suitable for greatly increased power handling. This would allow simultaneous heating and characterisation, which could be of use in biomedical and chemical synthesis applications. However, for the purposes of this work, variable inductive couplings were used. Loops were inserted through the sides of the cavity as shown in Figure 5.8 **b** so they could be moved closer to the split-ring resonator and reoriented as labelled. These two variables allowed the same coupling strength to be maintained for all split-ring resonators, regardless of ring diameter. This allowed measurements to be performed under the same conditions with different split-ring resonators, allowing measurements to be rigorously compared. In practice, this was achieved by moving the coupling loops until a specified value of insertion loss (e.g. 30 dB) was achieved. This is valid because insertion loss varies as a function of coupling strength.

5.1.2. Microfluidic design

The simplest method for perturbing a split-ring resonator was to pass a capillary through the loop gap. This was realised using quartz capillaries in a similar fashion to the capillary-perturbed coaxial resonator, where the empty capillary was inserted into the resonator for a reference measurement, before being filled via capillary action for the sample measurement. This removed the need for pumps or manual insertion of the liquid, and meant the sample could be introduced without touching or otherwise disturbing the resonator setup.

The split-ring resonators were mounted in the centre of an aluminium cavity on top of a piece of polystyrene foam. Polystyrene has a very low dielectric constant and its foam is mostly air by volume, meaning it is effectively invisible to microwave frequency measurements. The cavity was designed so that its lowest mode was above that of the split-ring resonator to avoid degeneracy. Inductive coupling loops were then inserted through holes drilled in the sides of the cavity. The feedlines were oriented at 180° from each other to maximise their separation and thereby minimise crosstalk. The capillary could be inserted through another hole drilled in the cavity. Assuming the top of the polystyrene foam block was level with the underside of this hole, the capillary would lie flat and parallel to the split-

ring resonator inside the extended loop gap region. A schematic view of this resonator setup is given in Figure 5.9.

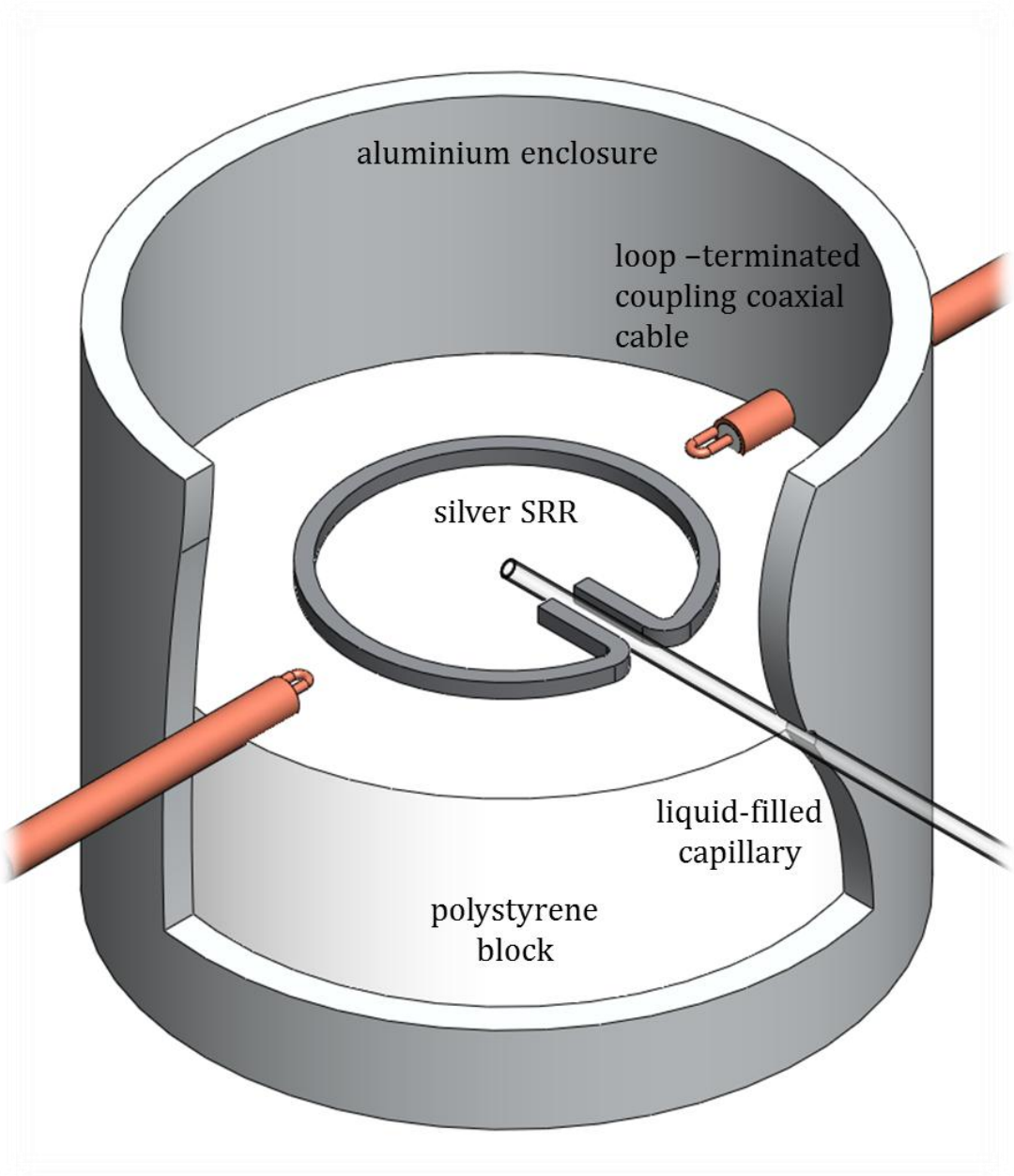

Figure 5.9: Cutaway schematic view of the split-ring resonator perturbed with a liquid filled capillary. The polystyrene block fits tightly into the cavity and forms a rigid platform on which to mount the resonator. The split-ring resonator was also secured to the polystyrene block with a small piece of tape opposite the loop gap.

The cavity can be seen to have an open top. It was possible to cover this with a conducting plate to completely shield the resonator from external interference, which caused a slight decrease in centre frequency but no significant change in

quality factor. It was therefore necessary to be consistent in the use of such a cover. To leave the cover off was not deemed to be detrimental to the performance of the sensor as long as reasonable precautions were taken not to disturb or electrically interfere with the resonator. It was decided to leave the cavity open to allow the filling of the sample capillary to be visually monitored, which is of critical importance for maximum sensitivity and unambiguous results.

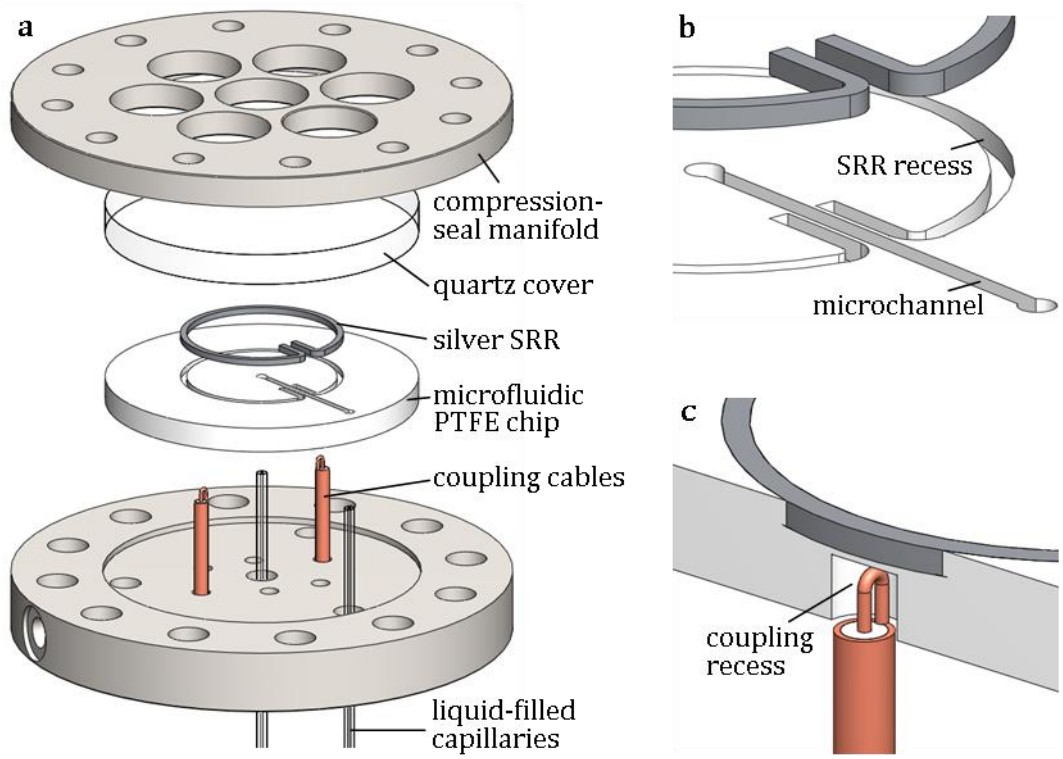

*Figure 5.10: (***a***) Exploded view of the split-ring resonator embedded in a compression-sealed PTFE microfluidic device, with (***b***) a close-up schematic view of the liquid-filled microchannel perturbing the split-ring resonator and (***c***) a cutaway view of the recess for inductive coupling to the resonator. The manifold is similar to those discussed in Chapter 3; the upper half uses several smaller holes rather than one large viewing hole in order to spread force more evenly over the surface of the device to reduce the likelihood of shattering the quartz cover.*

The split-ring resonator is ultimately intended for point-of-sampling applications. Capillary perturbation is sufficient for proof-of-principle experiments, but lacks the robustness of an integrated microfluidic device. Instead, the split-ring resonator could be embedded in a recess milled into a PTFE disc. Additional fluidic channels (for example, passing through the extended loop gap region) could also

be milled into the surface of the chip. This could be compression sealed in a similar manner to the evanescently-perturbed coaxial resonator. A schematic view of this resonator setup is given in Figure 5.10.

The integrated microfluidic approach is more difficult to couple to, given that the resonator is completely enclosed within compressed solid material. Side coupling (as shown in Figure 5.9) could potentially be achieved by milling large recesses into the PTFE chip and the quartz cover to clamp the coupling cables in place. Preliminary investigations showed that this approach could not reliably form a gas-tight compression seal, and the quartz cover was easily shattered due to the additional stresses. However, the inductive coupling loops did not necessarily have to be oriented in the same plane as the split-ring resonator. They could be rotated about the edge of the split ring as long as the loops remained perpendicular to the magnetic field lines of the resonator. The embedded approach shown in Figure 5.10 **c** meant the coupling loops could then be reoriented or moved closer to the ring to vary coupling strength in the same manner as for the capillary-perturbed approach. The thin layer of PTFE shown between the coupling recess and the split-ring resonator was probably not necessary, particularly as it was likely to reduce coupling strength, but could be required to provide extra support to the wire ring to maintain an effective compression seal.

5.1.3. Resonator perturbation

In Section 2.2.1, it was shown that the polarisation (i.e. dipole moment per unit volume) of a material was proportional to the internal electric field. For the purposes of resonator measurements, however, this is caused by an external field that is affected by depolarisation due to the shape of the material under test. The internal field magnitude E due to an external field $\mathbf{E}_0$ can be written:

$$E = \frac{E_0}{1 + N(\varepsilon_\mathrm{r} - 1)}. \qquad 5.10$$

N is the (dimensionless) depolarisation factor dependent on the shape of the sample in relation to the applied field. Long, thin shapes parallel to the applied field do not cause significant depolarisation and therefore have $N \approx 1$. For a

cylindrical sample perpendicular to the applied electric field (i.e. as for the capillary-perturbed split-ring resonator), $N \approx \frac{1}{2}$. Equation 5.10 therefore becomes:

$$E = \frac{2E_0}{\varepsilon_r + 1}. \tag{5.11}$$

The macroscopic sample dipole moment is:

$$p = (\varepsilon_r - 1)\varepsilon_0 E V_S, \tag{5.12}$$

where ε_r is the relative permittivity of the sample and V_S is the volume it occupies. Substituting for E, the dipole moment can be written as:

$$p = 2\frac{\varepsilon_r - 1}{\varepsilon_r + 1}\varepsilon_0 E_0 V_S. \tag{5.13}$$

Comparing this with the general form of dipole moment (Equation 5.4), it is obvious that the macroscopic polarisability of a cylindrical sample oriented perpendicularly to the applied electric field is:

$$\alpha = 2\frac{\varepsilon_r - 1}{\varepsilon_r + 1}, \tag{5.14}$$

where both α and ε_r are complex valued. This expression allows measurements of change in centre frequency and quality factor to be used to extract permittivity according to Equations 5.5 and 5.6.

Clearly, non-linear responses of centre frequency and quality factor with respect to permittivity are to be expected. This means that, for a given (frequency) measurement resolution, sensitivity will be reduced as permittivity increases. This is an inevitable consequence of utilising a depolarising geometry.

5.1.4. Experimental

Split-ring resonators were fabricated from silver-coated copper wire. The various types of wire required were obtained from the Scientific Wire Company (Essex, UK). The thickness of the silver layer was greater than the skin depth at low GHz

frequencies, so all resonators had an effective conductivity identical to that of silver. In the presented experiments, a wire thickness of 1.0 mm and leg separation of 1.5 mm was used throughout. Resonators of varying ring diameter (15, 20, 25 mm) and cross-section (circular, square) were fabricated by manually twisting wire around a former, as shown in Figure 5.11.

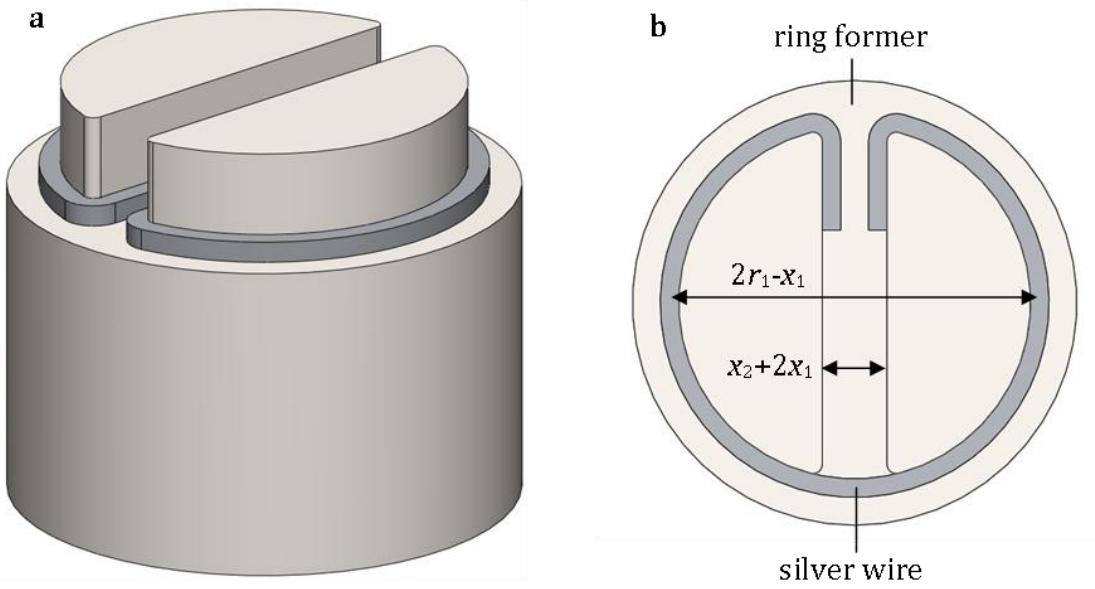

Figure 5.11: (a) Trimetric and (b) top views of the ring former used to fabricate the resonators from silver wire. The dimensions of the ring former are shown in terms of the wire thickness x_1, leg separation x_2 and ring radius r_1 as defined in Figure 5.5.

The cavity (for mounting the resonators) was precision machined from aluminium to have an inner diameter of 38 mm and a depth of 30 mm. Holes were drilled through the cavity walls in order to accept the coupling cables and quartz capillary. A 1.2 mm hole drilled at a depth of 15 mm (facing towards the centre of the cavity) was used to accept the capillaries. Two 4 mm holes for the coupling cables were also drilled through the cavity walls. These were positioned at the same height but oriented 90 degrees either side of the capillary hole about the axis of the cylindrical cavity. A block of polystyrene foam was cut to a radius slightly larger than 38 mm and a thickness of 14.5 mm and subsequently tightly packed into the cavity. This ensured the resonators would be positioned in the centre of the cavity. Semi-rigid RG402 coaxial cable was used to form the coupling cables. The outer conductor and spacer were cut away (and filed for a smooth finish) to expose a length of inner conductor, which was twisted and soldered to the outer conductor

to form the inductive coupling loop. The other end of the coupling cables were terminated with SMA connectors. Quartz capillaries of 0.8 mm inner diameter and 1.0 mm outer diameter were sourced from VitroCom (NJ, USA). The resonant sensor was then assembled according to Figure 5.9.

An Agilent E5071B VNA (Agilent, CA, USA) was used to measure the power transmission coefficient of the assembled resonant devices. The shortest, highest available quality cables and the fewest, highest available quality connectors were used to connect the resonant devices to the VNA. The data were exported to LabVIEW (National Instruments, TX, USA), where a Lorentzian curve was fitted to the peak of each resonance in real-time. The fitted curve data were then used to measure the resonant frequency and bandwidth of all modes. For each split-ring resonator, the distance of coupling loops from the ring was adjusted to maintain an insertion loss of 20 dB, ensuring the coupling was symmetric and the loops remained parallel to the plane of the resonator.

HPLC-grade solvents (Sigma Aldrich, MO, USA) were used for all presented experiments. Fresh (previously unopened) samples were used for each test, and were used as supplied. Standard health and safety and fluid handling precautions were followed throughout.

For each sample, an empty capillary was introduced into the resonator and a reference air measurement was recorded. The sample was then introduced via capillary action by tilting a liquid-filled Eppendorf tube in such a way to dip the end of the capillary in the sample without touching the capillary with the sample vessel. Sample measurements were then recorded. In each instance, 100 data points were logged for each reference and sample measurement to provide a sufficiently large dataset for statistical analysis. New quartz capillaries were used for each sample due to difficulties in cleaning them effectively.

The capillary method of perturbation for the split-ring resonator was tested, but time constraints meant that the embedded microfluidic approach was not.

5.2. Results

Initial, unloaded measurements of the split-ring resonators of various dimensions were taken first. Measured and simulated centre frequency and quality factor are tabulated in Table 5.2.

Table 5.2: The effect of varying dimensions on the measured centre frequency and quality factor of the split-ring resonator. Simulated results are included for comparison. Leg length = n/a denotes a ring without extended conductors. All rings had a wire thickness of 1.0 mm and a leg separation of 1.5 mm.

	a	**b**	**c**	**d**	**e**
Ring radius r_1 (mm)	12.5	12.5	12.5	10.0	7.5
Wire profile	circle	circle	square	circle	circle
Leg length x_3 (mm)	n/a	6.0	6.0	6.0	6.0
Simulated f_0 (GHz)	1.76	1.54	1.52	1.85	2.37
Measured f_0 (GHz)	1.72	1.40	1.35	1.58	n/a
Simulated Q	1520	1410	1200	1710	1900
Measured Q	1580	1420	1300	1520	n/a

Rings **a**, **b** and **c** were used to perform dielectric measurements of several solvents of known permittivity. The power transmission spectra are shown in Figure 5.12.

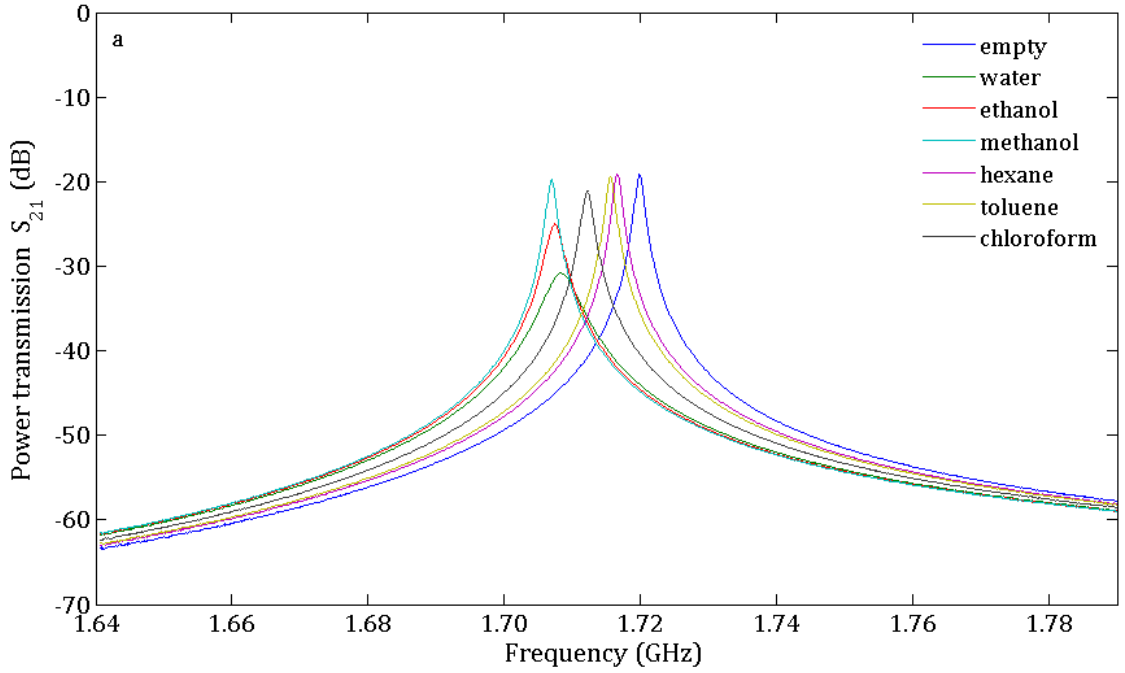

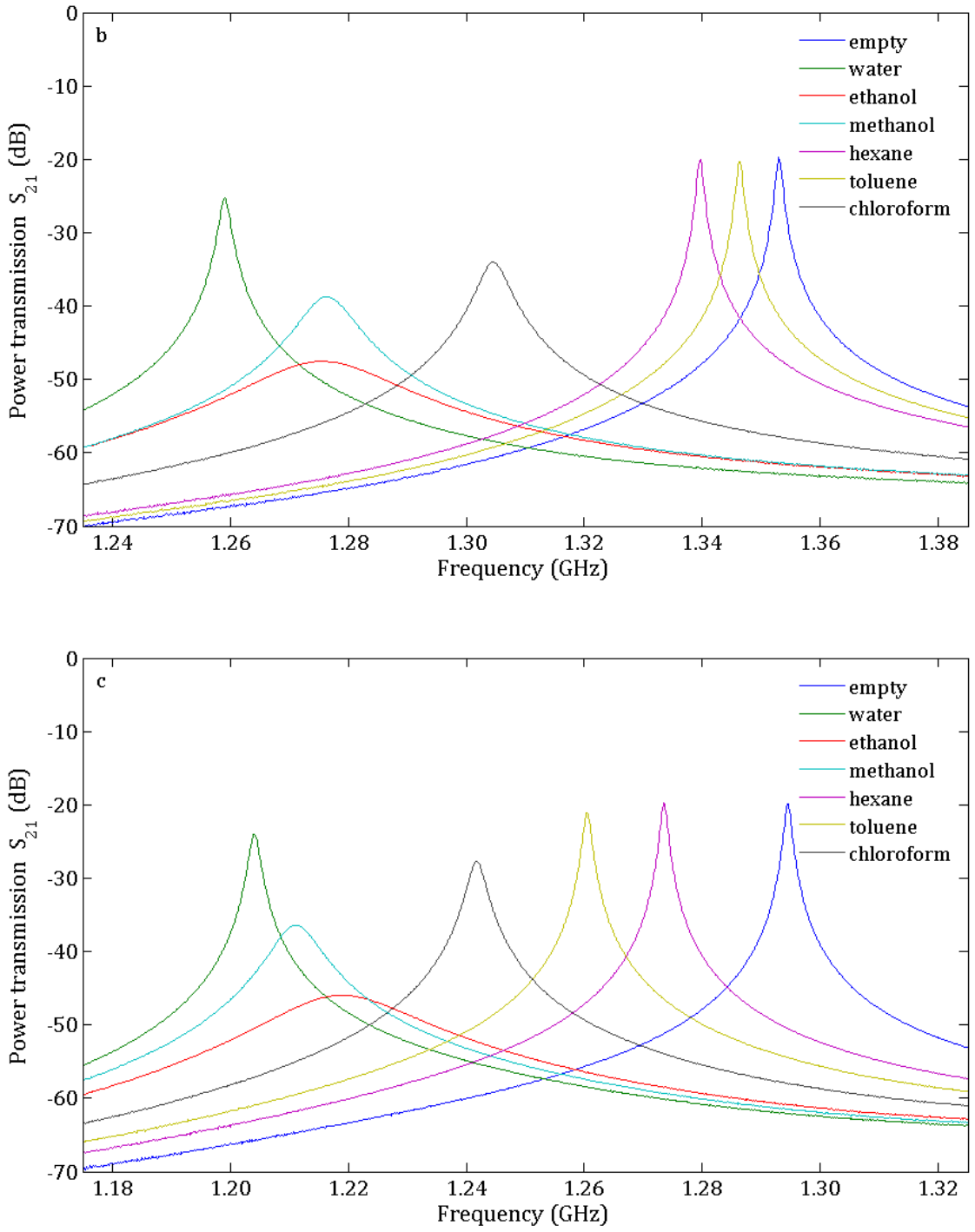

*Figure 5.12: Resonator power transmission spectra for various solvents. The subplots **a**, **b** and **c** correspond to the rings **a**, **b** and **c** of dimensions given in Table 5.2. Note that the x-axis of each subplot has the same range (150 MHz), allowing comparison of the different changes in centre frequency and quality factor between the resonators.*

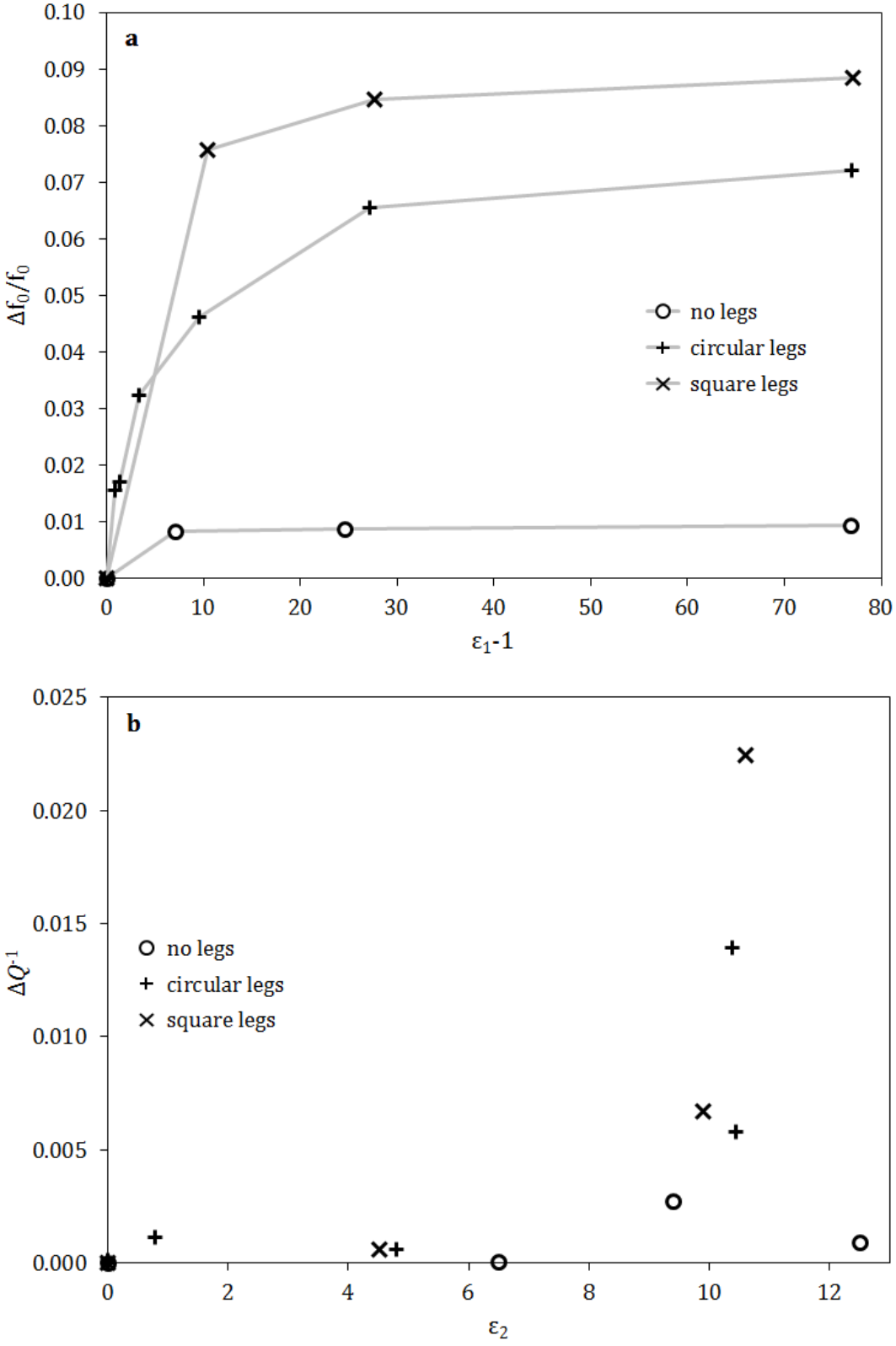

*Figure 5.13: Changes in (**a**) centre frequency and (**b**) inverse quality factor with respect to the permittivity of the measured solvents. The legend refers to the extended conductors of the rings. No legs, circular cross-section legs and square*

*cross-section legs correspond to the rings **a**, **b** and **c**, respectively, as given in Table 5.2. Although the data are discrete, they are shown joined in subplot* **a** *for clarity.*

The changes in centre frequency and inverse quality factor of rings **a**, **b** and **c** were also plotted with respect to permittivity in order to investigate the effects of depolarisation, as shown in Figure 5.13. Permittivity data at the relevant frequencies were obtained from the Debye-type responses given in [6], [39], [132].

An alternative way of interpreting the measured data is to compute the filling factor. This can be computed from complex frequency measurements according to Equations 5.5 and 5.6 if the complex polarisability is known. This can be computed from permittivity values of the appropriate solvents taken from literature [6], [39], [132] according to Equation 5.14. Filling factor was computed in this way for measurements obtained with each resonator, as shown in Table 5.3. Given that the filling factor represents a constant of proportionality between changes in complex frequency and components polarisability, it was expected to be the same for the respective real and imaginary components of these two quantities (i.e. identical for Equations 5.5 and 5.6). In order to examine whether the split-ring resonators demonstrated such behaviour, the filling factor was computed from both centre frequency and quality factor measurements. Only three solvents (encompassing a large range of permittivities) are shown for brevity.

Table 5.3: Filling factors for different solvents and resonators. These were obtained using measured values of the change in complex frequency and permittivity values taken from literature. Rings **a**, **b** *and* **c** *correspond to the dimensions given in Table 3.3. β_1 was the filling factor computed from the real components of complex frequency shift and polarisability; β_2 was the filling factor computed from the imaginary components.*

	ring **a**		ring **b**		ring **c**	
filling factor $\beta \times 10^{-3}$	β_1	β_2	β_1	β_2	β_1	β_2
ethanol	9.4	13	51	81	83	140
methanol	9.3	16	70	130	90	170
water	9.6	13	74	190	91	210

5.3. Discussion

Table 5.2 shows that the measured values of unloaded centre frequency and quality factor agree very closely with the simulated values. Several of the rings show the somewhat surprising result of having a quality factor higher that predicted. This is probably due to having a ring radius r_1 slightly smaller than expected rather than demonstrating any unusual loss-reducing mechanism. Note that the split-ring resonator with r_1 = 7.5 mm could not be made accurately using the wire former method shown in Section 5.1.4 and therefore could not be coupled to. In particular, this was because x_2 was kept constant (to allow the performance of the different rings to be compared) and r_2 does not scale with ring diameter. The combination of these two factors meant that the angle between the extended conductors and the main ring was much smaller than for the other resonators. These sharp bends may have led to fractures within the wire, which would massively decrease conductivity. However, not being able to couple to the resonator is entirely a consequence of the fabrication procedure. The associated problems would be alleviated, for example, if the split-ring resonator was formed from sputtered metal rather than a bent wire. In Figure 5.10 **b**, the micromachined recess for embedding a wire split-ring resonator could be filled with highly conductive sputtered material such as gold. If the recess was filled from the bottom up, the discrete layers formed as a consequence of the sputtering process would not introduce any discontinuities and therefore would not significantly reduce conductivity because the main direction of flow of charge is around the circumference of the ring (i.e. parallel to the sputtered layers).

It is obvious from Figure 5.12 that, for rings of constant wire thickness and loop gap, the change in centre frequency and quality factor is greatly increased for split-ring resonators with extended conductors (**b** and **c**) compared to those without (**a**). This is a vindication of the hypothesis that such structures would increase electric field confinement and therefore increase sensitivity by increasing the filling factor of the resonator.

Figure 5.13 shows the changes in centre frequency and inverse quality factor for measurements of several solvents of known permittivity, as obtained with several

different resonators. Note that this comparison serves to investigate the effects of the geometry of the extended conductors rather than the effects of reducing ring radius. Two factors contributed to this decision: that the rings could not be made very accurately, and that the extended conductors offered a more elegant way of enhancing sensitivity. The low cost and simple fabrication procedure of the presented split-ring resonators are greatly appealing.

Both types of ring with extended conductor offer significant enhancements over the resonator with no such modification, as expected. The square cross-section resonator exhibited an increased response to changes in permittivity over the entire measured range in comparison with the circular cross-section one, but also demonstrates increased non-linearity. This could be advantageous or detrimental, depending on the application. For analytical chemistry applications where the bulk sample material is an organic solvent, the square-cross section rings offer enhanced sensitivity (i.e. increased change in complex frequency for a given change in permittivity) at lower permittivities ($\varepsilon_1 < \sim 20$). For biomedical applications where a wider range of permittivities are likely to be encountered (particularly for aqueous samples), the more uniform sensitivity of the circular cross-section split-ring resonator could be more appropriate.

The data obtained from the change in inverse quality factor is more problematic. Two of the three resonators (both with circular cross-section wire) exhibit a non-monotonic response with respect to the imaginary component of permittivity. The resonator with square cross-section wire demonstrates a greatly exaggerated response at higher values of imaginary permittivity. It is possible that errors could have occurred due to fluid handling: for example, ionic contaminants could affect quality factor but not centre frequency measurements. However, reasonable precautions were followed (akin to those used in previous chapters) so this seems unlikely. The standard error of the measurements was greatest for the lowest loss liquids (hexane and toluene), which have loss comparable to that of the quartz capillary.

Changing volume between capillaries was accounted for by taking measurements with respect to the empty capillary. It is true that the differing volumes

encountered could lead to different levels of depolarisation, but this would be expected to manifest itself in the measurements of both components of complex permittivity. Clearly, it does not. Therefore, this source of error does not satisfactorily explain the response shown in Figure 5.13 **b**.

An obvious discrepancy in the theory used to predict the degree of depolarisation due to the sample geometry is that it does not account for the additional depolarisation due to the capillary containing the sample. This effect, however, is likely to be consistent between each experiment given that the permittivity of the quartz capillary is fixed. However, it could be that the depolarisation due to the capillary gives rise to a screening effect that means low loss solvents cannot be measured effectively.

Filling factor was also computed for several solvents using the split-ring resonators. As filling factor is the constant of proportionality between the complex frequency shift and complex permittivity, it was expected to be constant and to be the same when calculated from either the real or imaginary components of resonant frequency and permittivity. This is implicitly shown to be false by the non-linear responses plotted in Figure 5.13 and explicitly expressed in Table 5.3.

Filling factor is a characteristic measure of sensitivity for each resonator, but its variation is also a measure of the non-linearity of the resonator. Resonators **b** and **c** offer a significant enhancement in sensitivity over resonator **a**. Resonator **c** appears to exhibit less variation in both β_1 and β_2, but this is simply because the sample permittivity is sufficiently high to take the resonator response into the highly non-linear region (*cf*. Figure 5.13 **a**) where large changes in permittivity affect reduced changes in complex frequency. A similar argument applies to the low variation in β_1 and β_2 for resonator **a**.

In Table 5.3, β_2 is consistently lower than β_1, but the factor by which it is reduced varies. It should be noted that there is a significant difference between ε_1 and ε_2 for each solvent: water, for example, demonstrates an extremely large value of ε_1 (leading to a large depolarisation and consequent non-linearity in real frequency shift) but a moderately low value of ε_2 ($\varepsilon_1/\varepsilon_2 \approx 15$). If the depolarisation analysis

does not properly describe the relationships between polarisability and the two components of permittivity, the difference between ε_1 and ε_2 will exaggerate any differences between the real and imaginary components of frequency shift.

An extended analysis can be applied to the depolarising geometry where a liquid-filled capillary is oriented perpendicularly to an applied electric field, where the capillary also contributes to depolarisation[146]. This gives the general result for the polarisability α of a cylindrical sample of complex permittivity ε_S confined within a capillary of inner diameter a, outer diameter b and complex permittivity ε_C:

$$\alpha \approx 2\frac{(\varepsilon_S+\varepsilon_C)(\varepsilon_C-1)+(\varepsilon_S-\varepsilon_C)(\varepsilon_C+1)q^2}{(\varepsilon_S+\varepsilon_C)(\varepsilon_C+1)+(\varepsilon_S-\varepsilon_C)(\varepsilon_C-1)q^2}, \qquad 5.15$$

where $q = a^2/b^2$. This provides an alternative expression for polarisability that can be substituted into Equations 5.5 and 5.6. Note that this analysis assumes the capillary occupies a uniform field and, as such, will only be applied to the square cross-section split-ring resonator as it demonstrates greatly enhanced field confinement over the circular cross-section alternative. Schematic cross-sectional views of the electric field distribution in the capacitive region of split-ring resonators with different wire profiles are shown in Figure 5.14.

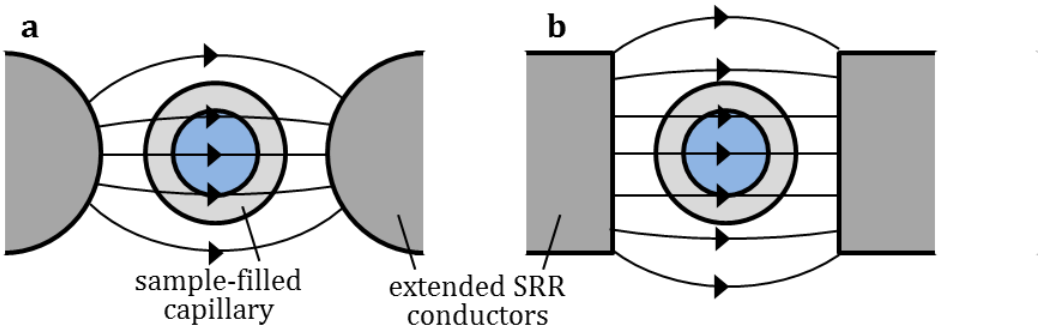

*Figure 5.14: Electric field distribution in the capacitive sensing region of split-ring resonators with (**a**) circular and (**b**) square wire profiles.*

(This analysis was not included earlier in the chapter precisely because it is not applicable to the majority of the tested resonators.) Therefore, filling factor can be recalculated for split-ring resonator **c**. The new filling factors, as calculated from

the respective real and imaginary components of complex resonant frequency and permittivity, shall be written as γ_1 and γ_2 rather than β_1 and β_2 for clarity.

Table 5.4: Recalculated filling factors for different solvents using split-ring resonator **c**. *These were obtained using measured values of the change in complex frequency and permittivity values taken from the literature. γ_1 was the filling factor computed from the real components of complex frequency shift and polarisability according to Equation 5.15; γ_2 was the filling factor computed from the imaginary components.*

	ethanol		methanol		water	
	γ_1	γ_2	γ_1	γ_2	γ_1	γ_2
filling factor $\gamma \times 10^{-3}$	101	240	110	270	112	300

A potentially more useful method of interpreting this data, and to compare the different analyses of polarisability, is to examine changes in centre frequency and inverse quality factor with respect to polarisability. These are shown in Figure 5.15 **a** and **b**.

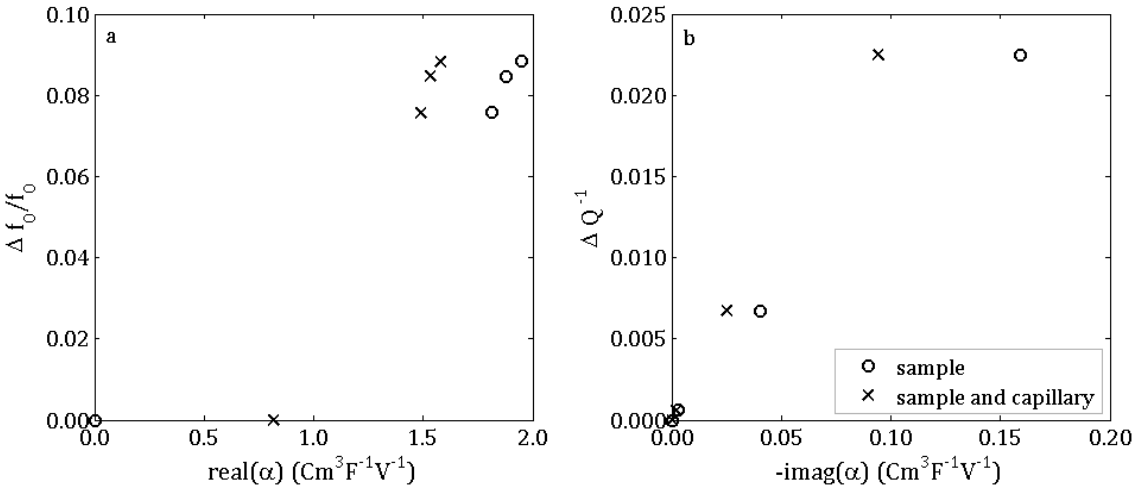

*Figure 5.15: Changes in (***a***) centre frequency and (***b***) inverse quality factor with respect to polarisability. The different traces represent different analyses of polarisability, distinguished by whether the depolarisation contribution of the capillary was considered. Measurements were obtained with a square cross-section split-ring resonator.*

Of particular note are the empty measurements (i.e. those exhibiting zero centre frequency change) in Figure 5.15 **a**. The polarisation analysis including the contribution of the capillary agrees better with the other measurements: the response of centre frequency change is linear with polarisation, as expected. Conversely, the polarisation analysis excluding the contribution of the capillary does not exhibit a linear response as it cannot account for the fact that depolarisation still occurs when the sample has zero permittivity.

This behaviour is not demonstrated in the inverse quality factor responses in Figure 5.15 **b**. This is to be expected, given that the dielectric loss of quartz is extremely low, so its inclusion in the depolarisation analysis has little effect on the imaginary component of complex resonant frequency shift. The change in inverse quality factor remained the same for polarisabilities that were, in fact, smaller than predicted by the incomplete depolarisation analysis. However, this apparent increase in sensitivity is due to a more refined interpretation of results and is not representative of any improvement in physical performance.

6. DISCUSSION

6.1. Comparison with cavity techniques

This discussion is a holistic consideration of the three measurement techniques developed in this work in the context of existing methods, and of the implications for microwave-frequency spectroscopy. In-depth analysis of individual results and the limitations of each new technique are included in the discussion sections of the relevant chapters.

In Chapter 2, the difficulties associated with the perturbation of cavity resonators were cited as a reason why it would be inappropriate to combine them with a microfluidic interface. For this work to be relevant, it is necessary to show that the presented measurement techniques do not suffer the same problem. Throughout the course of this work, two main methods of microfluidic sample interfacing were investigated. The capillary-perturbed coaxial resonator and split-ring resonator both utilised a fluidic interface of a rigid capillary situated so that it passed through maximum electric or magnetic field, depending on the resonator and mode of excitation. The sample could be introduced via capillary action, meaning that the resonator and microchannel did not need to be removed and replaced or otherwise disturbed. This provided a simple and cost-effective method of inserting a fixed volume of fluid into a resonator. The second approach utilised a PTFE microfluidic device. Microchannels were machined in a PTFE disc before a gasket film and quartz cover layer were placed on top and compression sealed within a brass manifold. The evanescently-perturbed coaxial resonator could then be

embedded in the underside of the PTFE device for continuous flow characterisation of the fluidic sample. It was also proposed that the split-ring resonator could be fitted in an appropriately sized recess that had a channel passing through its capacitive region. Implementing the evanescently-perturbed coaxial resonator in a compression-sealed microfluidic device greatly improved its sensitivity and resolution, despite the additional depolarisation caused by the inclusion of a thin PTFE layer over the probe aperture. This improvement was due to the vastly reduced variation in temperature as the thermal mass of the fluid sample was much less than that of the entire microfluidic device, which would otherwise affect measurement repeatability due to the temperature dependence of permittivity of most solvents. The compression-sealed PTFE approach also provided a flexible platform (suitable for rapid prototyping) for integrating more complex microfluidic circuits, such as a phase separator. It is possible that, for a future mass-produced implementation of an embedded split-ring resonator, the resonator itself would be best produced by sputtering or otherwise depositing the conductor in the microfluidic substrate. This approach may be more suitable for existing fabrication techniques as opposed to bending a wire into shape as the latter approach is likely to cause fractures in the wire, particularly as the ring radius is reduced to increase the quality factor (and therefore the sensitivity) of the device.

A cavity resonator, however, is not particularly well suited to being perturbed with microfluidic chips. One reason is that a large chip would cause a significant perturbation of the electric field, reducing quality factor (if the dielectric loss of the chip material is taken into account) and therefore sensitivity. Also, the motivation for using a chip rather than, say, a liquid-filled capillary is to exploit microfluidic handling techniques for additional sample processing such as mixing. To do so within a cavity, however, would be inadvisable as the entire circuit would occupy some fractional volume of electric field and hence contribute to the complex resonant frequency response of the resonator. It could then be problematic to extrapolate which part of the circuit was contributing to a measured response, particularly if composition varied throughout the course of the microfluidic circuit.

It would be possible to use a solid capillary interface to perturb a cavity resonator, in a similar fashion to that described above for the capillary-perturbed coaxial and split-ring resonators. For a cylindrical cavity, this would be achieved by orienting the capillary axis along that of the cavity, as previously demonstrated in [147], [148]. However, the split-ring resonator capillary perturbation in Chapter 5 was used for the sake of simplicity, but was not the intended final implementation of the device. An embedded microfluidic implementation would not rely on the user being careful to not disturb the sample capillary whilst filling it via capillary action. Similarly, the capillary perturbation was only included in Chapter 4 for the sake of obtaining magnetic and dielectric information simultaneously. For the capillary-perturbed coaxial resonator, however, flexible PEEK or PTFE tubing could equally be used for a continuous flow system as the capillary is rigidly held in place in the hole drilled through coaxial cable. This would be beneficial for point-of-sampling applications, where the user could syringe the sample into the resonator rather than filling the sensor via capillary action.

These examples are relevant to the microfluidic perturbation of a cavity resonator in that the large dimensions required for accessible microwave-frequency resonances would make it difficult to ensure that a flexible capillary remained along the cavity axis. The larger thermal mass associated with a cavity resonator makes it more difficult to achieve and maintain a consistent temperature throughout its volume, although this also means it is less prone to random thermal fluctuations. Whilst continuous flow measurements could probably be achieved with a cavity resonator perturbed with a solid tube, as in [147], [148], it would also require extensive temperature control using apparatus unsuitable for a portable device.

For the sake of a completely integrated point-of-sampling device (one that included a microfluidic sample interface, microwave-frequency sensor and associated electronics for automated measurements), a cavity resonator cannot be suitably miniaturised given that the resonant frequency of its sensing modes are defined by the cavity dimensions [22]. Despite all of these factors, it is possible to obtain extremely high quality factors with cavity resonators. This (together with the corresponding increase in sensitivity) occurs because of the use of low

resistivity conductors and because the unperturbed electric and magnetic fields are occupied by air rather than by some lossy microfluidic substrate [57]. The use of a cavity resonator for multimodal measurements (to extrapolate frequency dependence information or to allow the deconvolution of electric and magnetic sample properties) therefore has potential for extremely accurate reference measurements.

6.2. Comparison with existing microfluidic microwave-frequency methods

The benefits of dielectric spectroscopy in relation to other spectroscopic methods were discussed in Chapter 2. It was shown to be useful for a variety of biological and chemical applications [12], [14], [34], [37], [38], [122], [137], [149], [150] and, additionally, had potential for non-destructive, non-contact and label-free measurements of all states of matter (and combinations thereof, such as colloids and suspensions) [6], [9], [151], [152]. Each of the presented techniques addresses some of the shortcomings associated with existing microfluidic microwave-frequency sensors [9], [11–20]. The primary advantage of the new devices is that they allow non-contact measurements. The sample does not come into contact with a metal conductor at any point, but remains in contact with either PTFE or quartz (both of which are chemically inert) throughout the entire measurement procedure. Existing broadband techniques [14], [12], [9], [13], [11], [15] usually exploit a coplanar waveguide, where the centre conductor is fragile, exposed to the sample and prone to come away from the substrate. If this happens, the fully integrated approach means that the whole device cannot be reused. The integrated microfluidic interfaces of the new devices are not permanently bonded to the resonant sensors. The most expensive and time-consuming part of the fabrication process is to form the resonator and coupling structure owing to the precision with which they must be made. To have a replaceable and low-cost microfluidic interface is a key advantage for the intended point-of-sampling applications. From experience, problems in operation are most likely to occur in the microfluidic parts of an integrated device, rather than the electronics. One of the most commonly occurring problems is with channel blockages. These can usually be removed by sonication or by pumping through an appropriate cleaning solvent such as acetone, but this type of operation is

undesirable for the intended applications. To have an easily replaceable microfluidic interface would be preferential for non-expert point-of-sampling operation.

Resonant microwave-frequency sensors have also previously been combined with microfluidic techniques [16–20]. Of the published examples, few are suitable for continuous-flow measurements. Many of the unique fluid behaviours observed at the microscale arise as a consequence of the motion of a fluid through a channel, so measurement techniques without the capacity for continuous flow (as in [105] and [104], for example) cannot be considered truly microfluidic. Microchannels have been used to perturb whispering gallery mode [16] and split-post [17] dielectric resonators at microwave frequencies. At higher frequencies (i.e. THz and above), whispering gallery modes can also be excited in microsphere resonators [153], [154]. The discussion of evanescent filling factor and spatial resolution that follows is formulated in terms of microwave-frequency techniques, but equally applies to the higher frequency methods.

The approach described in [17] implemented a circular microchannel that ensured the sample remained parallel to the electric field distribution to minimise any depolarisation. This microchannel was embedded in the resonator itself. To use part of the electromagnetic structure to form the microfluidic channel is less of a disadvantage here than for the coplanar waveguide broadband techniques as the sample is not in contact with a conductor. This fluidic interface was somewhat restrictive but not completely prohibitive. Sapphire (from which the dielectric pucks were formed) is fragile, expensive and notoriously difficult material to machine and bond. In [17], the discs were bonded using spin-coated Teflon AF, which was sufficient for proof-of-principle experiments although its reliability was not extensively tested. It is for these reasons that, despite the elegant electromagnetic design of the sapphire split-post resonator, it is not suitable for low cost, point-of-sampling applications. Forming the dielectric resonator from a different material could solve these issues and allow the advantages of a non-depolarising geometry to be fully realised. However, the new measurement techniques have other advantages. For example, the evanescently-perturbed coaxial resonator has a far greater number of available sensing modes and a less

restrictive fluid interface. The split-ring resonator is simpler to perturb and could be suitable for selective, highly localised heating. The capillary-perturbed coaxial resonator can be used to extrapolate the frequency-dependent electric and magnetic properties of a sample simultaneously.

The whispering gallery mode dielectric resonator with an integrated microchannel [16] was formed of a resonator bolted to a separate microfluidic substrate that had an embedded microchannel. There are several problems with this approach. The microfluidic substrate covered the entire dielectric resonator, which had two effects. Firstly, the microfluidic chip perturbed the entire evanescent field of the mode, reducing Q and therefore sensitivity. The volume occupied by a capillary, for example, would be far smaller. Secondly, it provides additional surface area on which depolarisation charges can accumulate to oppose the sensing field and thereby reduce sensitivity.

Another problem with the whispering gallery mode resonator approach lies in the fact that the electric field is mostly contained within the dielectric resonator, whereas the sample is only used to perturb the evanescent field. This means the sensor has a reduced filling factor and a correspondingly reduced sensitivity. A similar criticism could be levelled at the evanescently-perturbed coaxial resonator. There is, however, an important difference in the fraction of the evanescent field that is perturbed: it is significantly higher for the evanescently-perturbed coaxial resonator technique. The evanescent field of the whispering gallery mode essentially follows the circumference of the dielectric resonator, so only a small fraction is perturbed if the channel passes across the top of the resonator. This also leads to poor spatial resolution as the sample must be homogeneous as the channel crosses both edges of the resonator. The sensitivity of the whispering gallery mode approach could be greatly increased if the channel followed the circumference of the dielectric resonator. The capillary-perturbed coaxial resonator and the split-ring resonator both have significantly higher filling factors because they do not utilise evanescent sensing fields.

Spatial resolution is a topic frequently encountered in the development of microwave microscopes [155], [156]. Such devices use highly-localised

evanescent fields to attempt to quantify electric properties and topology of a sample. These devices scan an open-ended coaxial resonator (where [155] also has a pointed tip attached to the end of the inner conductor) over the sample under test. The use of evanescent sensing fields allows the distinction of features that are orders of magnitude smaller than the wavelength of operation. These devices are provided as an example of how evanescent fields can be used to enhance the spatial resolution of a sensor. In comparison with microwave microscopes, continuous flow sensors can be thought of as moving the sample relative to the probe rather than the other way around. The microfluidic implementation of the whispering gallery mode resonator described in [16] negates any improvement in resolution because, if the sample is not homogeneous across the resonator, its variation cannot be extracted from a single measurement.

From a practical perspective, the microfluidic interface of the whispering gallery mode resonator could also be unreliable as there is no method for aligning the channel with the resonator. Given that the channel had a cylindrical cross-section of 200 μm diameter, any movement of the channel relative to the resonator would cause a wildly different perturbation. The open geometry is simple to perturb but prone to interference: a resonance change could be caused by the operator holding the unit in their hand, for example.

6.3. Comparison of the new measurement techniques

The three new measurement techniques presented in this work each have their own advantages and disadvantages. To compare the three is somewhat contrived as a greater period of time was spent developing and testing the evanescently-perturbed coaxial resonator, but such a comparison is useful for exploring potential applications.

The evanescently-perturbed coaxial resonator has been used to characterise a segmented flow and a variety of solvents and mixtures in a compression sealed microfluidic device. It has also been proposed that the split-ring resonator would be appropriate for this type of integration. However, care must be employed if additional flow functionality is included in the planar microfluidic device. The

electric sensing fields of both devices is not completely localised within the designated sensing volume (the channel over the coaxial aperture, or the channel in the capacitive region of the split-ring resonator). Although these fields decay rapidly to a negligible magnitude, it is possible for a channel outside of the sensing regions to affect a measurable perturbation. In addition, the magnetic field of the split-ring resonator occupies a large volume fraction of the entire microfluidic device. In the same way that the ionic content of a liquid could be assessed by the magnetic sensing modes of the capillary-perturbed coaxial resonator, an ionic sample could interact with the magnetic field of the split-ring resonator. This interaction could cause an ambiguous change in complex resonant frequency and could possibly heat the sample at higher power levels. These are undesirable effects that could be reduced with appropriate shielding. The simplest way of implementing this would be to use a polished metal sheet (rather than a quartz or PTFE disc) as the coverplate for the microfluidic device.

It is possible that the increased field confinement caused by this approach would increase the quality factor and therefore sensitivity of both devices; although it would also mean that the microfluidic operation could not be visually monitored or irradiated with an ultraviolet source.

The potential for accidental perturbation (which would be most important if fluid composition or temperature were changing on-chip) is most significant for the split-ring resonator. For this reason, the evanescently-perturbed coaxial resonator is more suitable for performing additional complex on-chip fluid processing. It also allows for complex permittivity information to be obtained at multiple frequencies. The high electric field confinement and adjustable coupling of the split-ring resonator make it most suitable for heating (and simultaneous heating and sensing) applications. It also has the simplest construction and, of the three devices, is the one best suited for mass production. A compromise is necessary, however, if the ability to perform multi-frequency measurements is also important.

Of the three devices, the capillary-perturbed coaxial resonator suffers from the most restrictive fluid interface but also allows the most information to be extracted. The fluid interface could be considered an advantage for point-of-

sampling applications where extensive sample processing was not required, but simplicity for non-expert operation was required. Under such circumstances, it could be that the ability to deconvolve electric and magnetic field interactions would negate the need for complex sample processing given that ionic and dielectric effects could be separated. Such applications could include disease diagnosis in deprived regions.

The spatial resolution of the capillary-perturbed coaxial resonator can be improved more readily that the other two techniques. However, this may not always be an advantage. When characterising suspensions, it is necessary to have an even dispersion throughout the entire sensing volume for unambiguous measurements. As the sensing volume is reduced, it becomes more likely that homogeneity will not be preserved, for example with low volume fraction dispersions of relatively large solid particles, which could be anticipated for geological measurements performed in the field.

Despite all of the above practical considerations, the ultimate figure of merit for determining which of the three new methods is best is probably sensitivity. This requires further experimentation for the capillary-perturbed coaxial resonator and the split-ring resonator: a serial dilution of one solvent in another could be consecutively characterised by the three methods in continuous flow to determine the lowest possible limit of detection.

7. CONCLUSION

Microwave-frequency measurements are highly useful for the dielectric and magnetic characterisation of liquids and suspensions across a range of scientific disciplines [12], [14], [34], [37], [38], [122], [137], [149], [150]. In comparison with broadband techniques (i.e. those yielding a continuous spectra), resonant methods generally have improved accuracy and reduced uncertainty [21], [22], but can only obtain data at a single, discrete frequency. Some resonator techniques allow multi-frequency data measurements though exploitation of two or three higher order modes [81], [82], [157]. A novel coupling structure for the overmoded coaxial resonator was introduced in Chapter 3. This was designed to give optimal weakly-coupled transmission measurements from one end of the device, allowing the other end to be perturbed evanescently. This method could be used to simultaneously interrogate upwards of fifteen modes. The overmoded coaxial resonator can therefore be seen to combine the accuracy and sensitivity of resonant methods with the multi-frequency capabilities of broadband methods.

An adaptation of the planar split-ring resonator [19] was also introduced in Chapter 5. This was formed of a single piece of wire where the two ends of the ring were bent inwards to form a parallel capacitive region. This had the effect of increasing field confinement and filling factor, and therefore dielectric measurement sensitivity, over an equivalent split-ring resonator without the extended conductors.

Additionally, it should be remembered that dielectric spectroscopy is a subset of microwave-frequency spectroscopy, where magnetic-field interactions can also be quantified. Previous work has yielded simultaneous measurements of dielectric and magnetic material properties using both broadband [67], [69], [70], [158] and resonant [80–83] techniques, where same considerations of accuracy, sensitivity and availability of frequency information still apply. In Chapter 4, the capillary-perturbed coaxial resonator was introduced. This exploited the differences in field pattern between TEM modes to provide the capability for simultaneous dielectric and magnetic sensing at many different frequencies, rather than the two or three frequencies available with cavity techniques.

The confinement of fluids in channels of micron-scale cross-sectional dimensions leads to behaviour not observed at the macroscale [10]. Fluid handling and controllability issues associated with microwave-frequency resonator techniques (for example, retaining a constant sample temperature for an extended length of time) can be addressed through the adoption of suitable microfluidic techniques. Basic microfluidic sample interfaces have been realised for both broadband [9], [11–15] and resonant [16–20] dielectric spectroscopy techniques. In this work, different microfluidic interfaces were investigated for each of the new sensing techniques as appropriate. These methods, together with a LabVIEW graphical user interface that allowed rapid time-dependent measurements to be obtained with a vector network analyser, gave much greater control of the fluid regimes used to perturb the resonant sensors. This means that the hitherto unfulfilled potential of microwave-frequency spectroscopy for the *in situ* characterisation of chemical and biological processes can now be realised.

The evanescently-perturbed coaxial resonator demonstrated multi-modal operation for highly accurate measurements at numerous discrete frequencies. The resonator response was shown for bulk solvents; with respect to concentration for liquid-liquid mixtures and dissolved species, and also for segmented flows of immiscible fluids.

The capillary-perturbed coaxial resonator was the first example of a resonant technique being used for simultaneous dielectric and magnetic characterisation

with a microfluidic sample interface. The resonator response was shown with respect to concentration for several salt solutions, and used to demonstrate adequate separation of electric and magnetic field effects due to the interaction of ionic content with both fields. Measurements of a magnetic nanoparticle suspension suggested that such particles exhibited negligible magnetisation at the frequency of interrogation, although this interpretation was somewhat speculative. The resonant device was also used to non-invasively characterise non-specific adsorption with respect to time. These measurements were not easily reproducible, but offered a tantalising hint of what such a device could be capable of. The ability to separate electric and magnetic field effects is particularly useful because the cause of the changes affected in centre frequency and bandwidth for most resonant dielectric spectroscopy techniques (where the sample occupies both electric and magnetic field) cannot be distinguished.

Various split-ring resonators were investigated to demonstrate the improvement in performance offered by extending the conductors to form an elongated capacitive region. The use of square cross-section wire was also shown to improve filling factor and therefore sensitivity. An extended analysis of the depolarisation due to having the sample oriented perpendicularly to the sensing electric field allowed a more rigorous interpretation of the results (specifically, the non-linearity arising as a consequence of depolarisation).

Each of the presented techniques offers a unique contribution to the field of microfluidic microwave-frequency measurements.

7.1. Further work

Each of the three new measurement techniques are ripe for development in three areas: (bio)chemical/pharmaceutical applications, electromagnetic design and microfluidic design. Each technique is discussed in turn.

7.1.1. Evanescently-perturbed coaxial resonator

The single-ended coupling structure was designed to couple to coaxial cable of 6.35 mm outer diameter. This was chosen as a compromise between being big

enough to allow standard microwave components to be used to connect to the device, whilst being small enough to give a probe aperture suitable for microfluidic perturbation. In reality, it may be preferable to reduce the diameter of the coaxial resonator (which does not affect its resonant frequency) to enhance the spatial resolution of the device. The coupling structure for such a device could be designed using the same procedure described in Chapter 3. It is possible that the effects of changing the probe aperture diameter could provide an extra degree of freedom for optimising the filling factor of the device for a microfluidic channel of given dimensions.

Of the sample interfaces considered, the compression-sealed PTFE one offers the most scope for implementing more complex microfluidic circuits. For any passive or active device that can be realised in the planar, micromilled substrate (be it PTFE or some other low loss material), the evanescently-perturbed coaxial resonator can be included at any point in the fluidic circuit by fixing it in place in a recess underneath the desired location. For example, it could be used in conjunction with a phase separator [98] to monitor how efficiently the two constituent phases of a segmented flow were being separated. It may be necessary to use two resonators: one to ensure breakthrough was not occurring on the organic outlet and one to ensure the entire organic phase was being extracted before the aqueous outlet. A conceptual diagram of this device shown in Figure 7.1

The evanescently-perturbed coaxial resonator could be used to investigate the varying composition of an individual fluid partition in segmented flow. Composition can vary as fluid recirculates within each partition. This causes (a) rapid mixing and (b) the inter-partition fluid interface to continually refresh. Given that partition recirculation is a function of path length for a fixed fluid velocity, it is necessary to perform measurements at different distances along the channel if changing composition is to be characterised. There are two ways this can be achieved. Firstly, the probe could be moved. This is inherently impractical for a device embedded in a compression-sealed manifold. Secondly, the segmented flow could be passed back over the same probe. This could be achieved by delivering the carrier (organic) phase of the segmented flow with a push-pull pump, which would allow a train of fluid partitions to be moved back and forth

about the probe aperture. This 'back and forth' principle was first introduced in [159].

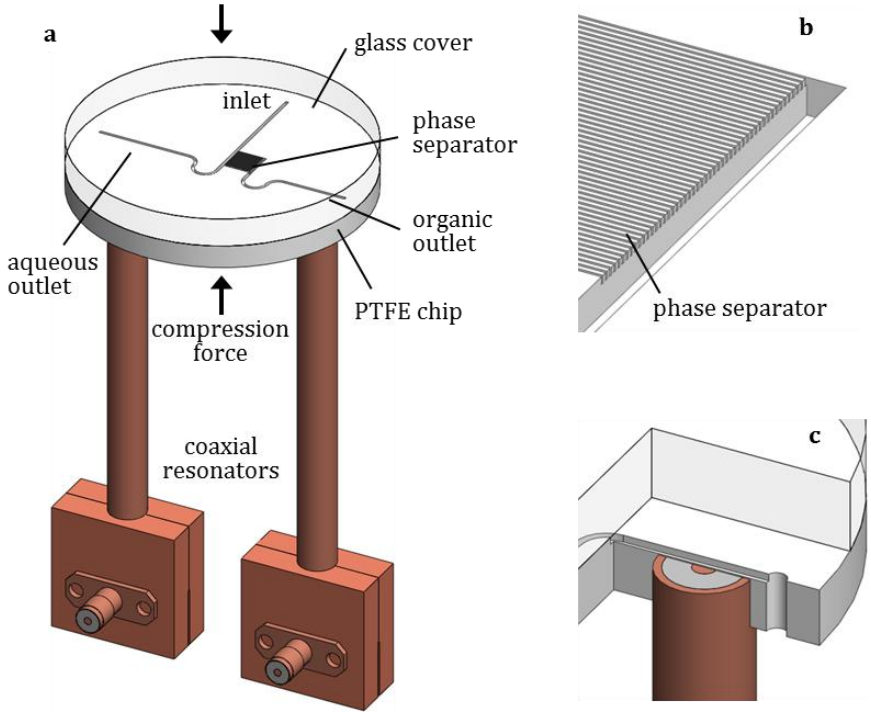

*Figure 7.1: Schematic diagram (***a***) showing two evanescently-perturbed coaxial resonators used to interrogate the outlets of a phase separator. It is assumed the inlet channel carries a segmented flow of two immiscible liquids. The phase separator is a linear array of fifty small channels that will carry the liquid with the lower contact angle upon application of an appropriate pressure difference between the outlet channels. It is envisaged that the compression-seal manifold used throughout this work would be used to provide the compression forces labelled, although it is not shown for clarity. Also shown are (***b***) a close-up view of the phase separator channel array and (***c***) a cutaway view exposing one of the resonators.*

7.1.2. Capillary-perturbed coaxial resonator

The device used to obtain the measurements presented in Chapter 4 was comprised, in part, of the single-ended transmission coupling structure and a piece of RG401 (PTFE spaced) coaxial cable. A second device was also discussed. This device was air-spaced to reduce dielectric losses and had adjustable end couplings that allowed the coupling coefficient to be manually adjusted for maximum

dynamic range for an arbitrary material under test. Time constraints meant that this could not be adequately tested, so further optimisation is necessary to see if it is advantageous.

It is possible that the filling factor (and therefore sensitivity) of this method could be optimised through variation of the radial dimensions of the coaxial resonator. For a coaxial resonator of inner conductor radius a and outer conductor inner radius b perturbed with a sample in the form of a capillary aligned parallel to the electric field, the volume occupied by the sample scales with $b - a$ whereas the total volume occupied by electric field scales with $b^2 - a^2$.

Independently of the coupling methodology, it may transpire that different capillaries (varying in material and in radial dimensions) give the optimum response for resonators of different fundamental frequency (i.e. of different length). For example, a much longer resonator would be required to yield multi-frequency information for both the electric and magnetic sensing modes using the equipment available. It could also be beneficial to use flexible capillaries in order to perform continuous flow measurements: a back and forth segmented flow could be implemented with a push-pull pump, as described in Section 7.1.1.

The capillary-perturbed coaxial resonator has a less flexible microfluidic interface than the evanescently-perturbed alternative, but it can also be used to obtain more information. For example, it could be used to characterise ferrofluids (e.g. to monitor selective binding to the surface of functionalised magnetic nanoparticles) or to analyse the properties of and distinguish between erythrocytes.

The use of a square or rectangular cross-section coaxial device, as shown in Figure 7.2, could result in reduced depolarisation. For a circular cross-section device, the radial electric field distribution means that passing a cylindrical capillary through the centre of the resonator must always cross some lines of electric field and therefore cause depolarisation. The use of flat conductors could reduce this effect by increasing the electric field uniformity in the parallel regions. However, this approach would experience current bunching at the edges of the conductors. This will cause the electric field to distort in the regions close to the conductor edges,

which will be a sizable effect given that the radial dimensions are likely to be small. Current bunching could also lead to a significant drop in electric field magnitude at the midpoints of the conductor faces. This would mean a sample passed through the centre of the resonator would occupy a smaller volume fraction of the electric field, reducing the filling factor and therefore sensitivity of the device.

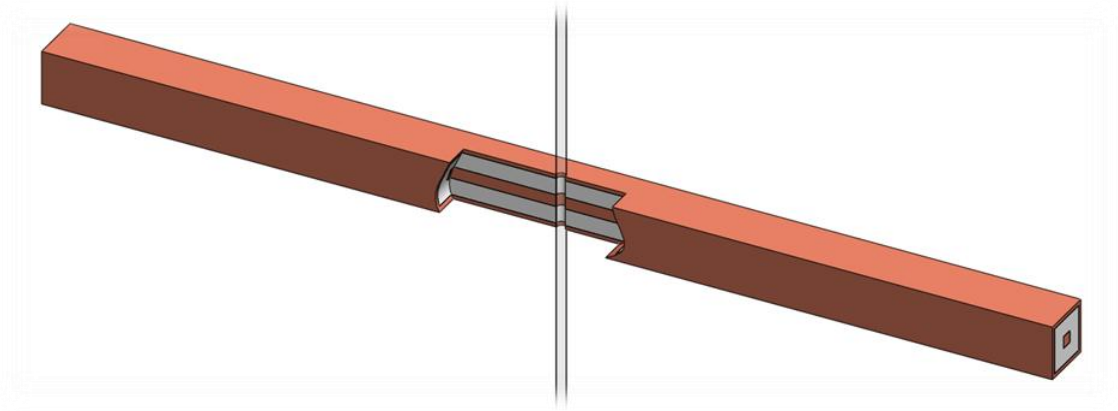

Figure 7.2: Cutaway view of a square cross-section coaxial resonator. It is suggested that this device could reduce the depolarisation encountered in the circular cross-section capillary-perturbed coaxial resonator of Chapter 4.

7.1.3. Split-ring resonator

The split-ring resonator only allows resonator measurements at a single frequency. It does, however, possess other advantages that could be useful in other applications. The most immediately obvious improvement of the split-ring resonator would be to improve the fluid handling capabilities by embedding it in a compression-sealed microfluidic manifold in a similar fashion to that used for the evanescently-perturbed coaxial resonator.

The adjustable inductive coupling means that near-critical coupling can readily be achieved. This is of relevance to heating applications, where critical coupling is necessary to maximise power transfer from the feedlines to the resonator. The resonator would then deliver power to a sample in its capacitive region according to the dielectric loss of the material. It would then be possible to simultaneously perform dielectric spectroscopy whilst heating the material, as first demonstrated with a cavity resonator in [160]. There are many high-power heating applications for the split-ring resonator, as evidenced by microwave-assisted chemistry.

The applicability of this device for biomedical applications could be improved by pointing the extended outer conductors out of the centre of the split-ring resonator, rather than inwards. Such a device could then be used to pinch a material between the extensions or to be injected into animal tissue in order to perform cauterisation. However, injecting this device would require pointed tips, which would focus the electric field at the wire tips rather than in the parallel capacitive region. This could be achieved via other, simpler, means and is unlikely to be advantageous. It would be preferable to heat the material within the parallel capacitive region rather than just at the tips of the wire, which would require the wire itself to not be pointed. Instead, a separate needle tip could be added to the ends of the resonator wire. This could be a cap formed of a plastic with low dielectric loss. Alternatively, it may be possible to deposit biocompatible microneedles on the ends of the wire that would dissolve upon insertion into an aqueous environment such as human tissue.

7.1.4. Long-term projections

Dielectric spectroscopy has the potential to be a powerful tool in the laboratory, but experimental difficulties have traditionally restricted such measurements to specialist groups. The ability to characterise fluids in a microfluidic environment with respect to time is tremendously enabling. Any one of the three new techniques could be used to this end, although each has its own particular benefits.

Extensive chemical studies have not yet been undertaken. A particularly exciting aspect of these systems is that they allow reactions to be monitored *in situ*. Perhaps more significantly, such measurements can be non-contact, non-destructive, non-invasive and label-free. This approach could fundamentally change the way analytical chemistry is performed: the usual current practice is to perform an experiment and characterise the remains. The ability to directly and non-invasively access the kinetics of a reaction provides additional information not currently available. One implication of routinely obtaining such information could be speeding up the time taken to perform chemical syntheses. It may not be necessary, for example, to wait 24 hours for equilibrium to be obtained.

Of course, only proof-of-principle results have been achieved throughout this work. Nevertheless, the use of these measurement techniques in a 'chemical multimeter' remains a worthy aim. This term is used by way of analogy with its electrical equivalent, where the basic quantities of voltage, current and resistance can be measured to a usable degree of accuracy with a low-cost, portable, durable and battery powered unit without requiring any great degree of knowledge or expertise. The chemical multimeter would allow a small fluidic sample to be identified via its dielectric and magnetic properties. A reading would be available instantly and could be logged with respect to time if composition was changing. As well as the obvious biological and chemical applications, such a device could be of use in applications as diverse as geology, sports science and forensics.

If this long-term aim is to be realised, much more work is necessary. It may be that one of the resonant sensors is reasonably close to being usable in a chemical multimeter, as long as it could be mass produced. The implementation of all of the associated electronics, such as a miniaturised network analyser, may take far longer to realise. A possible solution could be to avoid using a dedicated instrument: for example, the National Instruments PXI chassis (National Instruments, Texas, US) allows the necessary vector network analyser functionality with standard modules and boards [8]. A multitone readout system for low-cost, high-speed measurements with microwave-frequency resonators was recently developed by [8] and simultaneously by [161]. The accuracy of the system in [8] was comparable to that of a calibrated network analyser, but also offered a sampling rate of up to 500 Hz. Although this value was limited by the data transfer rate of the system, no theoretical reason exists as to why the sampling rate could not be close to the bandwidth of the resonant sensor itself [8]. For example, the coaxial and split-ring resonators in this work have bandwidths in the order of 1 MHz.

APPENDIX 1

In Chapter 4, the capillary-perturbed coaxial resonator was introduced as a method for simultaneously quantifying the dielectric and magnetic properties of a liquid-phase sample. It was stated that evaluating the right-hand side of Equation 4.3 gave Equation 4.4, although the workings were not shown. They are given in full in Section A1.1, where Equations 4.3 and 4.4 correspond to Equations 4.3 and 4.4, respectively. Similarly, it was also stated that evaluating the right-hand side of Equation 4.7 gave Equation 4.8. The full workings are given in Section A1.2, where equations 4.7 and 4.8 correspond to Equations 4.7 and 4.8, respectively.

A1.1 Electric sensing mode

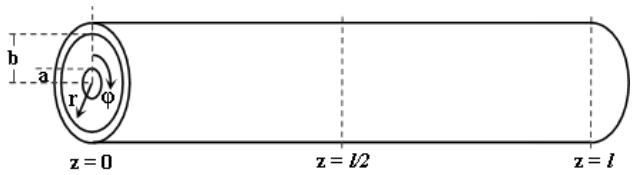

Figure 0.1: Coaxial resonator schematic (not to scale). The hole for the liquid-filled capillary is perpendicular to the conductors' axis and located halfway along the length of the resonator (z = l/2).

Consider a coaxial resonator as represented in Figure 4.3. If all fields have $e^{j\omega t}$ time dependence, the electric and magnetic field amplitudes can be written as:

$$E_r(r,z) = E_0 \frac{a}{r} \cos\frac{n\pi z}{l}, \qquad 0.1$$

$$H_\varphi(r,z) = j\frac{E_0}{\eta_0}\frac{a}{r}\sin\frac{n\pi z}{l}, \qquad 0.2$$

where E_0 is the peak magnitude of electric field E_r (located at the ends of the resonator) for the nth TEM mode. η_0 is the vacuum impedance (i.e. η_0 = 376.7 Ω). Co-ordinates and all other dimensions are labelled in Figure 4.3.

For the electric sensing (i.e. even TEM) modes, the fields at the centre of the resonator (z=l/2) are:

$$n \text{ even} \begin{cases} E_r = E_0 \frac{a}{r}\cos\frac{n\pi}{2} = E_0\frac{a}{r}(-1)^{n/2} \rightarrow |E_r| = E_0\frac{a}{r} \\ H_\varphi = 0. \end{cases} \qquad 0.3$$

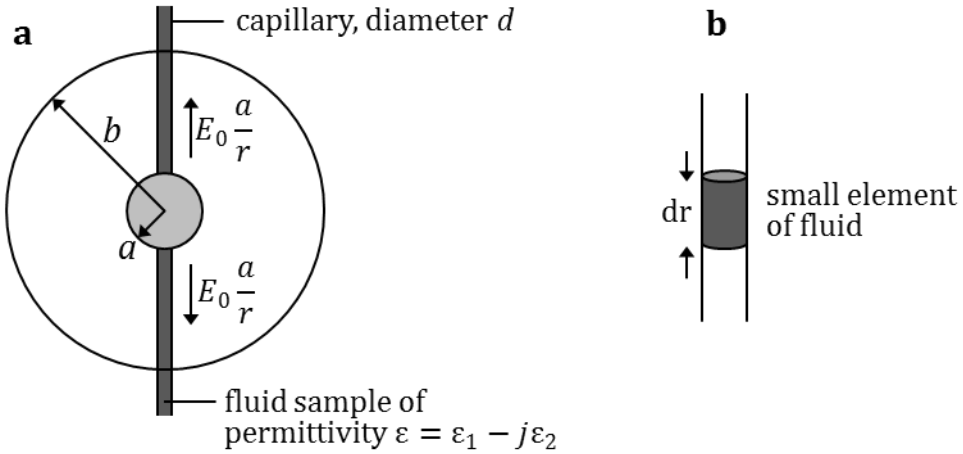

*Figure 0.2: (**a**) Cross-sectional schematic through the centre of the capillary-perturbed coaxial resonator (z = l/2) and (**b**) schematic of a small element of the fluidic sample under test.*

The dipole moment dp of a fluid element of volume dV and permittivity $\varepsilon = \varepsilon_1 - j\varepsilon_2$ (as shown in Figure 0.2) is:

$$dp = (\varepsilon - 1)\varepsilon_0 \mathrm{E}\, dV = (\varepsilon - 1)\varepsilon_0 E_0 \frac{a}{r}\frac{\pi d^2}{4} dr. \qquad 0.4$$

where ε_0 is vacuum permittivity. Hence, the dipole energy $E\,dp$ is:

$$E\ dp = E_0 \frac{a}{r}(\varepsilon_1 - 1)\varepsilon_0 E_0 \frac{a}{r}\frac{\pi d^2}{4} dr. \quad 0.5$$

Hence,

$$\int E\ dp = 2(\varepsilon_1 - 1)\varepsilon_0 {E_0}^2 \pi \left(\frac{ad}{2}\right)^2 \int_a^b \frac{dr}{r^2}, \quad 0.6$$

where the factor of two arises because there are two fluid sections: one either side of the centre conductor. Evaluating the integral:

$$\int E\ dp = \frac{1}{2}(\varepsilon_1 - 1)\varepsilon_0 {E_0}^2 \pi a^2 d^2 \frac{b-a}{ab}. \quad 0.7$$

The time averaged stored energy U is given by:

$$\begin{aligned} U &\approx \frac{1}{2}\varepsilon_0 \int E^2\ dV \\ &= \frac{1}{2}\varepsilon_0 {E_0}^2 a^2 \int_a^b \frac{2\pi r\ dr}{r^2} \int_0^l \cos^2 \frac{n\pi z}{l} dz \\ &= \frac{1}{2}\varepsilon_0 \pi a^2 \ln\left(\frac{b}{a}\right) l {E_0}^2. \end{aligned} \quad 0.8$$

From first order perturbation theory, the normalised change in centre frequency can be written as:

$$\frac{\Delta f_0}{f_0} \simeq -\frac{\int E\ dp}{4U}. \quad 0.9$$

Substituting Equations 0.8 and 4.3 into Equation 4.4 gives:

$$\frac{\Delta f_0}{f_0} \simeq -(\varepsilon_1 - 1)\Gamma_{\mathrm{E}}, \quad 0.10$$

where

$$\Gamma_{\mathrm{E}} = \frac{d^2(b-a)}{4abl \cdot \ln(b/a)}. \qquad 0.11$$

Hence,

$$\frac{\Delta f_{\mathrm{B}}}{f_0} \simeq 2\varepsilon_2 \Gamma_{\mathrm{E}}. \qquad 0.12$$

These expressions can be used to theoretically predict the change in complex resonant frequency for a sample of known permittivity.

A1.2 Magnetic sensing mode

For odd TEM modes, the fields at the centre of the resonator (z=l/2) are:

$$n \text{ odd} \begin{cases} E_r = 0 \\ H_\varphi = j\dfrac{E_0}{\eta_0}\dfrac{a}{r} \rightarrow \left|H_\varphi\right| = \dfrac{E_0}{\eta_0}\dfrac{a}{r}. \end{cases} \qquad 0.13$$

Considering the fluid volume element in Figure 0.2 **b**, it is necessary to divide the fluid element into strips parallel to the magnetic field, as shown in

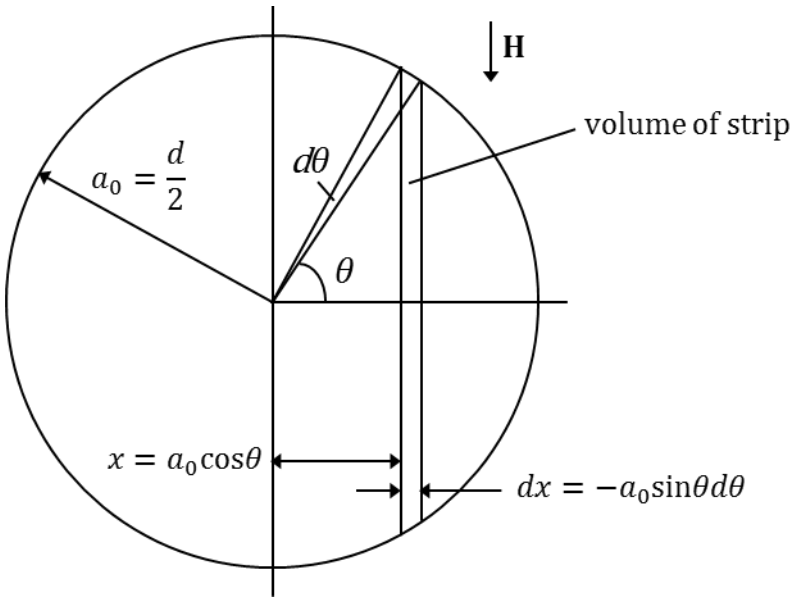

Figure 0.3: Cross-sectional view of the fluid volume element shown in Figure 0.2 **b**. *The element is divided into strips parallel to magnetic field, which forms concentric circles about the coaxial centre conductor.*

The volume of the fluid element strip in Figure 0.3 is:

$$\begin{aligned} dV &= \mathrm{d}r \cdot dx \cdot 2a_0 \sin\theta \\ &= -2a_0 \sin^2\theta dr d\theta. \end{aligned} \tag{0.14}$$

The induced electric field at the position of the strip is:

$$\begin{aligned} E &= j\omega\mu_0 Hx \\ &= j\omega\mu_0 H a_0 \cos\theta, \end{aligned} \tag{0.15}$$

where μ_0 is the vacuum permeability. The time-averaged power dissipation dP in the element dV is:

$$\begin{aligned} dP &= \frac{1}{2}\sigma|E|^2 \mathrm{dV} \\ &= \frac{1}{2}\sigma(\omega\mu_0 H_0)^2 a^2 \cdot -2{a_0}^4 \int_0^{\pi/2} \sin^2\theta\cos^2\theta \, d\theta \int_a^b \frac{dr}{r^2}, \end{aligned} \tag{0.16}$$

where σ is the conductivity of the sample. It can be written that:

$$\begin{aligned} \int \sin^2\theta\cos^2\theta d\theta &= \frac{1}{4}\int \sin^2 2\theta \, d\theta \\ &= \frac{1}{8}\int (\cos 4\theta - 1) d\theta \\ &= \frac{1}{8}\left[\frac{\sin 4\theta}{4} - \theta\right]. \end{aligned} \tag{0.17}$$

Therefore, the total power dissipation is:

$$\begin{aligned} \langle P\rangle &= 2\sigma(\omega\mu_0 H_0)^2 a^2 {a_0}^4 \frac{\pi}{16}\frac{b-a}{ab} \\ &= \frac{\pi}{8}\sigma(\omega\mu_0 H_0)^2 {a_0}^4 a\left(1 - \frac{a}{b}\right). \end{aligned} \tag{0.18}$$

The quality factor of a resonator Q can be defined as:

$$Q = \frac{2\pi f_0 U}{P}. \tag{0.19}$$

The time averaged stored energy U is given by:

$$U \approx \frac{1}{2}\mu_0 \int H^2 \, dV$$

$$= \frac{1}{2}\mu_0 \int_{r=a}^{b} \int_{z=0}^{l} {H_0}^2 \frac{a^2}{r^2} 2\pi \mathrm{r} \, \mathrm{dr} \, \mathrm{dz} \cdot \sin^2 \frac{n\pi z}{l}$$

$$= \frac{1}{4}\mu_0 {H_0}^2 \pi a^2 l \ln\left(\frac{b}{a}\right). \qquad 0.20$$

Substituting Equations 0.18 and 0.20 into Equation 4.7 and rearranging gives:

$$\Delta Q^{-1} = \sigma f_0 \Gamma_{\mathrm{H}}, \qquad 0.21$$

where

$$\Gamma_{\mathrm{H}} = \frac{\mu_0 \pi^3 d^4 (b-a)}{4abl \cdot \ln(b/a)}. \qquad 0.22$$

Equations 4.8 and 4.9 can be used for a theoretical prediction of the change of inverse quality factor for a sample of known conductivity.

BIBLIOGRAPHY

[1] J.D. Jackson, *Classical Electrodynamics*, 3rd ed. New Jersey: Wiley, 1999.

[2] C. Kittel, *Introduction to Solid State Physics*, 7th ed. New York: Wiley, 1996.

[3] H. Fröhlich, *Theory of Dielectrics*. Oxford: Oxford University Press, 1949.

[4] J.B. Hasted, *Aqueous Dielectrics*. London: Chapman and Hall, 1973.

[5] P. Cicmanec, "Cavity perturbation method for measurement of permittivity and conductivity of medium lossy semiconductors and dielectrics," *Solid-State Electronics*, vol. 14, no. 2, pp. 153-166, Feb. 1971.

[6] J. Barthel, K. Bachhuber, R. Buchner, and H. Hetzenauer, "Dielectric spectra of some common solvents in the microwave region. Water and lower alcohols," *Chemical Physics Letters*, vol. 165, no. 4, pp. 369-373, Jan. 1990.

[7] J. F. Rouleau, J. Goyette, T. K. Bose, and M. F. Frechette, "Performance of a microwave sensor for the precise measurement of water vapor in gases," *IEEE Transactions on Dielectrics and Electrical Insulation*, vol. 7, no. 6, pp. 825-831, 2000.

[8] J. Naylon, "Microwave resonant sensors," PhD thesis, Cardiff University, 2011.

[9] K. Grenier, D. Dubuc, P.-E. Poleni, M. Kumemura, H. Toshiyoshi, T. Fujii, and H. Fujita, "Integrated Broadband Microwave and Microfluidic Sensor Dedicated to Bioengineering," *IEEE Transactions on Microwave Theory and Techniques*, vol. 57, no. 12, pp. 3246-3253, Dec. 2009.

[10] G. M. Whitesides, "The origins and the future of microfluidics," *Nature*, vol. 442, no. 7101, pp. 368-373, Jul. 2006.

[11] J. C. Booth, J. Mateu, M. Janezic, J. Baker-Jarvis, and J. A. Beall, "Broadband permittivity measurements of liquid and biological samples using microfluidic channels," in *IEEE MTT-S International Microwave Symposium Digest*, 2006, pp. 1750-1753.

[12] G. R. Facer, D. A. Notterman, and L. L. Sohn, "Dielectric spectroscopy for bioanalysis: From 40 Hz to 26.5 GHz in a microfabricated wave guide," *Applied Physics Letters*, vol. 78, no. 7, pp. 996-998, 2001.

[13] J. Mateu, N. Orloff, M. Rinehart, and J. C. Booth, "Broadband permittivity of liquids extracted from transmission line measurements of microfluidic channels," in *IEEE MTT-S International Microwave Symposium Digest*, 2007, pp. 523-526.

[14] J. C. Booth, N. D. Orloff, J. Mateu, M. Janezic, M. Rinehart, and J. A. Beall, "Quantitative permittivity measurements of nanoliter liquid volumes in microfluidic channels to 40 GHz," *Instrumentation and Measurement, IEEE Transactions on*, vol. 59, no. 12, pp. 3279-3288, Dec. 2010.

[15] M. Giraud-Carrier, K. Moon, E. Teng, A. R. Hawkins, K. F. Warnick, and B. A. Mazzeo, "Broadband RF impedance spectroscopy in micromachined microfluidic channels," in *Engineering in Medicine and Biology Society,EMBC, 2011 Annual International Conference of the IEEE*, 2011, pp. 4042-4045.

[16] A. I. Gubin, A. A. Barannik, N. T. Cherpak, S. A. Vitusevich, A. Offenhäusser, and N. Klein, "Whispering-gallery mode resonator technique for characterization of small volumes of biochemical liquids in microfluidic channel," in *Proceedings of the European Microwave Conference*, Manchester, 2011, pp. 615-8.

[17] A. Porch, A. Masood, J. Naylon, A. Sulaimalebbe, and D.A. Barrow, "Sapphire dielectric resonators for microfluidic compositional analysis," in *Proceedings of MicroTAS*, Groningen, 2010, pp. 2011-3.

[18] R. Göritz, A. Masood, O.K. Castell, D.A. Barrow, C.J. Allender, and A. Porch, "Microwave compositional analysis of solvent matrices in microcapillary manifiold systems," in *Proceedings of MicroTAS*, Paris, 2007, pp. 1689-91.

[19] M. Labidi, J. B. Tahar, and F. Choubani, "Meta-materials applications in thin-film sensing and sensing liquids properties," *Optics Express*, vol. 19, no. S4, p. A733, May 2011.

[20] A. Masood, Oliver K. Castell, David A. Barrow, Christopher J. Allender, and A. Porch, "Split ring resonator technique for compsitional analysis of solvent matrices in microcapillary systems," in *Proceedings of MicroTAS*, San Diego, 2008, pp. 1636-1638.

[21] A. P. Gregory and R. N. Clarke, "A review of RF and microwave techniques for dielectric measurements on polar liquids," *IEEE Transactions on Dielectrics and Electrical Insulation*, vol. 13, no. 4, pp. 727-743, 2006.

[22] National Physical Laboratory, *A Guide to the characterisation of dielectric materials at RF and microwave frequencies*. London: The Institute of Measurement and Control, 2003.

[23] Gauglitz, G and Vo-Dinh, T, *Handbook of Spectroscopy*. Weinheim: Wiley-VCH, 2003.

[24] S. K. Sia, V. Linder, B. A. Parviz, A. Siegel, and G. M. Whitesides, "An integrated approach to a portable and low-cost immunoassay for resource-poor settings," *Angewandte Chemie International Edition*, vol. 43, no. 4, pp. 498-502, Jan. 2004.

[25] C. D. Chin, T. Laksanasopin, Y. K. Cheung, D. Steinmiller, V. Linder, H. Parsa, J. Wang, H. Moore, R. Rouse, G. Umviligihozo, E. Karita, L. Mwambarangwe, S. L. Braunstein, J. van de Wijgert, R. Sahabo, J. E. Justman, W. El-Sadr, and S. K. Sia, "Microfluidics-based diagnostics of infectious diseases in the developing world," *Nature Medicine*, vol. 17, no. 8, pp. 1015-1019, Jul. 2011.

[26] D. Proudnikov and A. Mirzabekov, "Chemical methods of DNA and RNA fluorescent labelling.," *Nucleic Acids Research*, vol. 24, no. 22, pp. 4535-4542, Nov. 1996.

[27] Long, D.A., *The Raman effect: a unified treatment of the theory of Ramen scattering by molecules*. Chichester: Wiley, 2002.

[28] M. N. Afsar, J. R. Birch, R. N. Clarke, and G. W. Chantry, "The measurement of the properties of materials," *Proceedings of the IEEE*, vol. 74, no. 1, pp. 183-199, 1986.

[29] E. I. Izgorodina, M. Forsyth, and D. R. MacFarlane, "On the components of the dielectric constants of ionic liquids: ionic polarization?," *Physical Chemistry Chemical Physics*, vol. 11, no. 14, pp. 2452-2458.

[30] Barsoukov, E. and Macdonal, J.R., *Impedance Spectroscopy*, 2nd ed. New Jersey: Wiley, 2005.

[31] P. J. Hore, *Nuclear Magnetic Resonance*. OUP Oxford, 1995.

[32] D. I. Hoult, C. N. Chen, and V. J. Sank, "The field dependence of NMR imaging. II. Arguments concerning an optimal field strength," *Magnetic Resonance in Medicine*, vol. 3, no. 5, pp. 730-746, Oct. 1986.

[33] A. M. C. van Dinther, C. G. P. H. Schroën, F. J. Vergeldt, R. G. M. van der Sman, and R. M. Boom, "Suspension flow in microfluidic devices — A review of experimental techniques focussing on concentration and velocity gradients," *Advances in Colloid and Interface Science*, vol. 173, pp. 23-34, May 2012.

[34] A. Bonincontro and C. Cametti, "Interfacial characterization of mesoscopic particle suspensions by means of radiowave dielectric spectroscopy: a minireview," *Colloids and Surfaces A: Physicochemical and Engineering Aspects*, vol. 246, no. 1–3, pp. 115-120, Oct. 2004.

[35] J. C. Booth, J. Mateu, M. Janezic, J. Baker-Jarvis, and J. A. Beall, "Broadband permittivity measurements of liquid and biological samples using microfluidic channels," in *IEEE MTT-S International Microwave Symposium Digest*, 2006, pp. 1750-1753.

[36] E. Benoit, O. Prot, P. Maincent, and J. Bessière, "Applicability of dielectric measurements in the field of pharmaceutical formulation," *Bioelectrochemistry and Bioenergetics*, vol. 40, no. 2, pp. 175-179, 1996.

[37] S. Egot-Lemaire, J. Pijanka, J. Sulé-Suso, and S. Semenov, "Dielectric spectroscopy of normal and malignant human lung cells at ultra-high frequencies," *Physics in Medicine and Biology*, vol. 54, no. 8, pp. 2341-2357, 2009.

[38] M. Kent, A. Peymann, C. Gabriel, and A. Knight, "Determination of added water in pork products using microwave dielectric spectroscopy," *Food Control*, vol. 13, no. 3, pp. 143-149, 2002.

[39] M. Xu, E. M. Eyring, and S. Petrucci, "Dielectric relaxation of chloroform and chloroform-cyclohexane mixtures at Gigahertz and Terahertz frequencies. The inertial term," *Journal of Molecular Liquids*, vol. 73–74, pp. 41-48, 1997.

[40] F. F. Hanna, K. N. Abdel-Nour, A. M. Ghoneim, and F. Hufnagel, "Dielectric relaxation of polar molecules in mixtures of non-polar solvents.," *Journal of Molecular Liquids*, vol. 31, no. 1, pp. 51-65, Jun. 1985.

[41] S. Schwerdtfeger, F. Köhler, R. Pottel, and U. Kaatze, "Dielectric relaxation of hydrogen bonded liquids: Mixtures of monohydric alcohols with n-alkanes," *Journal of Chemical Physics*, vol. 115, no. 9, pp. 4186-4194, 2001.

[42] H. P. Schwan, "Electrode polarization impedance and measurements in biological materials," *Annals of the New York Academy of Sciences*, vol. 148, no. 1, pp. 191-209, Feb. 1968.

[43] S. Mashimo, T. Umehara, and H. Redlin, "Structures of water and primary alcohol studied by microwave dielectric analyses," *The Journal of Chemical Physics*, vol. 95, no. 9, pp. 6257-6260, 1991.

[44] U. Kaatze and V. Lönnecke-Gabel, "Dielectric spectroscopy on binary mixtures of organic solvents," *Journal of Molecular Liquids*, vol. 48, no. 1, pp. 45-60, 1991.

[45] U. Kaatze and R. Pottel, "Dielectric and ultrasonic spectroscopy of liquids. Comparative view for binary aqueous solutions," *Journal of Molecular Liquids*, vol. 49, no. C, pp. 255-248, 1991.

[46] B. Kapilevich and B. Litvak, "Optimized microwave sensor for online concentration measurements of binary liquid mixtures," *IEEE Sensors Journal*, vol. 11, no. 10, pp. 2611-2616, 2011.

[47] L. D. Landau, E. M. Lifshitz, and L. P. Pitaevskiĭ, *Electrodynamics of continuous media*. Butterworth-Heinemann, 1984.

[48] D. K. Misra, "Quasi-static analysis of open-ended coaxial lines," *IEEE Transactions on Microwave Theory and Techniques*, vol. 35, no. 10, pp. 925-928, 1987.

[49] C. Gabriel, T. Y. A. Chan, and E. H. Grant, "Admittance models for open ended coaxial probes and their place in dielectric spectroscopy," *Physics in Medicine and Biology*, vol. 39, no. 12, pp. 2183-2200, 1994.

[50] K. Folgero, T. Friiso, J. Hilland, and T. Tjomsland, "A broad-band and high-sensitivity dielectric spectroscopy measurement system for quality determination of low-permittivity fluids," *Measurement Science and Technology*, vol. 6, no. 7, pp. 995-1008, Jul. 1995.

[51] K. Folgero, "Broad-band dielectric spectroscopy of low-permittivity fluids using one measurement cell," *IEEE Transactions on Instrumentation and Measurement*, vol. 47, no. 4, pp. 881-885, 1998.

[52] A. Raj, W. S. Holmes, and S. R. Judah, "Wide bandwidth measurement of complex permittivity of liquids using coplanar lines," *IEEE Transactions on Instrumentation and Measurement*, vol. 50, no. 4, pp. 905-909, 2001.

[53] J. Hefti, A. Pan, and A. Kumar, "Sensitive detection method of dielectric dispersions in aqueous-based, surface-bound macromolecular structures using microwave spectroscopy," *Applied Physics Letters*, vol. 75, no. 12, pp. 1802-1804, Sep. 1999.

[54] M. D. Janezic and J. A. Jargon, "Complex permittivity determination from propagation constant measurements," *IEEE Microwave and Guided Wave Letters*, vol. 9, no. 2, pp. 76-78, Feb. 1999.

[55] U. C. Hasar, "A new microwave method for electrical characterization of low-loss materials," *IEEE Microwave and Wireless Components Letters*, vol. 19, no. 12, pp. 801-803, Dec. 2009.

[56] D. Kajfez and P. Guillon, *Dielectric Resonators*. Artech House, 1986.

[57] D. M. Pozar, *Microwave Engineering*, 3rd ed. New York: Wiley, 2005.

[58] A. Masood, Oliver K. Castell, David A. Barrow, Christopher J. Allender, and A. Porch, "Split ring resonator technique for compsitional analysis of solvent matrices in microcapillary systems," in *Proceedings of MicroTAS*, San Diego, 2008, pp. 1636-1638.

[59] N. A. Hoog-Antonyuk, W. Olthuis, M. J. J. Mayer, D. Yntema, H. Miedema, and A. van den Berg, "On-line fingerprinting of fluids using coaxial stub resonator technology," *Sensors and Actuators B: Chemical*, vol. 163, no. 1, pp. 90-96, 2012.

[60] C. Song and P. Wang, "A radio frequency device for measurement of minute dielectric property changes in microfluidic channels," *Applied Physics Letters*, vol. 94, no. 2, p. 023901, 2009.

[61] D. K. Wood, S.-H. Oh, S.-H. Lee, H. T. Soh, and A. N. Cleland, "High-bandwidth radio frequency Coulter counter," *Applied Physics Letters*, vol. 87, no. 18, p. 184106, 2005.

[62] G. A. Ferrier, S. F. Romanuik, D. J. Thomson, G. E. Bridges, and M. R. Freeman, "A microwave interferometric system for simultaneous actuation and detection of single biological cells," *Lab on a Chip*, vol. 9, no. 23, pp. 3406-3412, Dec. 2009.

[63] M. Nikolic-Jaric, S. F. Romanuik, G. A. Ferrier, G. E. Bridges, M. Butler, K. Sunley, D. J. Thomson, and M. R. Freeman, "Microwave frequency sensor for detection of biological cells in microfluidic channels," *Biomicrofluidics*, vol. 3, no. 3, p. 034103, 2009.

[64] C. Gasparovic and N. A. Matwiyoff, "The magnetic properties and water dynamics of the red blood cell: a study by proton-NMR lineshape analysis," *Magnetic Resonance in Medicine*, vol. 26, no. 2, pp. 274-299, Aug. 1992.

[65] M. Zborowski, G. R. Ostera, L. R. Moore, S. Milliron, J. J. Chalmers, and A. N. Schechter, "Red blood cell magnetophoresis," *Biophysical Journal*, vol. 84, no. 4, pp. 2638-2645, Apr. 2003.

[66] J. Baker-Jarvis and P. Kabos, "Dynamic constitutive relations for polarization and magnetization," *Physical Review E*, vol. 64, no. 5, p. 056127, Oct. 2001.

[67] A. M. Nicolson and G. F. Ross, "Measurement of the Intrinsic Properties of Materials by Time-Domain Techniques," *IEEE Transactions on Instrumentation and Measurement*, vol. 19, no. 4, pp. 377-382, 1970.

[68] Weir, W.B., "Automatic measurement of complex dielectric constant and permeability at microwave frequencies," *Proceedings of the IEEE*, vol. 62, no. 1, pp. 33-6, 1974.

[69] T. L. Blakney and W. B. Weir, "Comments on 'Automatic measurement of complex dielectric constant and permeability at microwave frequencies'," *Proceedings of the IEEE*, vol. 63, no. 1, pp. 203-205, 1975.

[70] R. A. Shelby, D. R. Smith, and S. Schultz, "Experimental Verification of a Negative Index of Refraction," *Science*, vol. 292, no. 5514, pp. 77 -79, Apr. 2001.

[71] D. R. Smith, S. Schultz, P. Markoš, and C. M. Soukoulis, "Determination of effective permittivity and permeability of metamaterials from reflection and transmission coefficients," *Physical Review B*, vol. 65, no. 19, p. 195104, Apr. 2002.

[72] V. V. Varadan and A. R. Tellakula, "Effective properties of split-ring resonator metamaterials using measured scattering parameters: Effect of gap orientation," *Journal of Applied Physics*, vol. 100, no. 3, pp. 034910-034910-8, Aug. 2006.

[73] Hasar, U.C., "A microwave method for accurate and stable retrieval of constitutive parameters of low- and medium-loss materials," *IEEE Microwave and Wireless Components Letters*, vol. 20, no. 12, pp. 696-8, 2010.

[74] Hasar, U.C., "A microwave method for noniterative constitutive parameters determination of thin low-loss or lossy materials," *IEEE Transactions on Microwave Theory and Techniques*, vol. 57, no. 6, pp. 1595-601, 2009.

[75] Belhadj-Tahar, N.-E., Dubrunfaut, O., and Fourrier-Lamer, A., "Broad-band microwave characterization of a tri-layer structure using a coaxial discontinuity with applications for magnetic liquids and films," *IEEE Transactions on Microwave Theory and Techniques*, vol. 46, no. 12, pp. 2109-16, 1998.

[76] Clerjon, S., Bayard, B., Vincent, D., and Noyel, G., "X-band characterization of anisotropic magnetic materials: application to ferrofluids," *IEEE Transactions on Magnetics*, vol. 35, no. 1, pp. 568-82, 1999.

[77] Clerjon, S., Vincent, D., and Noyel, G., "Complex microwave susceptibility of a ferrofluid with mag-hematite particles: Nonreciprocal phenomena in magnetic liquids," *IEEE Transactions on Magnetics*, vol. 34, no. 3, pp. 719-23, 1998.

[78] Fannin, P.C., MacOireachtaigh, C., and Couper, C., "An improved technique for the measurement of the complex susceptibility of magnetic colloids in the microwave region," *Journal of Magnetism and Magnetic Materials*, vol. 322, no. 16, pp. 2428-33, 2010.

[79] Usanov, D.A., Skripal, Al.V., Skirpal, An.V., and Kurganov, A.V., "Interaction of microwave radiation with magnetic liquid layer placed in waveguide," *Journal of Magnetism and Magnetic Materials*, vol. 252, pp. 183-5, 2002.

[80] Penaranda-Foix, F.L., Plaza-Gonzalez, P.J., Garcia-Banos, B., and Polo-Nieves, D., "A nondestructive method of measuring the dielectric and magnetic properties of laminate materials in open cavities," in *IEEE IMS 2004*, 2004, vol. 3, pp. 1821-3.

[81] Lin, M., Wang, Y., and Afsar, M.N., "Precision measurement of complex permittivity and permeability by microwave cavity perturbation technique," in *IRMMW-THz 2005 conference*, 2005, vol. 1, pp. 62-3.

[82] Lin, M., Duane, M.H., and Afsar, M.N., "Cavity-perturbation measurement of complex permittivity and permeability of common ferrimagnetics in microwave-frequency range," *IEEE Transactions on Magnetics*, vol. 42, no. 10, pp. 2885-7, 2006.

[83] Dimri, M.C., Kashyap, S.C., and Dube, D.C., "Complex permittivity and permeability of Co2U (Ba4Co2Fe36O60) hexaferrite bulk and composite thick films at radio and microwave frequencies," *IEEE Transactions on Magnetics*, vol. 42, no. 11, pp. 3635-40, 2006.

[84] Klein, O., Donovan, S., Dressel, M., and Gruner, G., "Microwave cavity perturbation technique: Part I: Principles," *International Journal of Infrared and Millimeter Waves*, vol. 14, no. 12, pp. 2423-57, 1993.

[85] R. A. Waldron, "Perturbation theory of resonant cavities," *Proceedings of the IEE Part C: Monographs*, vol. 107, no. 12, p. 272, 1960.

[86] R. G. Carter, "Accuracy of microwave cavity perturbation measurements," *Microwave Theory and Techniques, IEEE Transactions on*, vol. 49, no. 5, pp. 918-923, 2001.

[87] G. M. Whitesides, "The origins and the future of microfluidics," *Nature*, vol. 442, no. 7101, pp. 368-373, Jul. 2006.

[88] L. Johansson, S. Johansson, F. Nikolajeff, and S. Thorslund, "Effective mixing of laminar flows at a density interface by an integrated ultrasonic transducer," *Lab on a Chip*, vol. 9, no. 2, pp. 297-304.

[89] G. G. Yaralioglu, I. O. Wygant, T. C. Marentis, and B. T. Khuri-Yakub, "Ultrasonic mixing in microfluidic channels using integrated transducers," *Analytical Chemistry*, vol. 76, no. 13, pp. 3694-3698, 2004.

[90] C.-C. Chang and R.-J. Yang, "Electrokinetic mixing in microfluidic systems," *Microfluidics and Nanofluidics*, vol. 3, no. 5, pp. 501-525, Jun. 2007.

[91] F. Jiang, K.S. Drese, S. Hardt, M. Küpper, and F. Schönfeld, "Helical flows and chaotic mixing in curved micro channels," *American Institute of Chemical Engineering Journal*, vol. 50, no. 9, pp. 2297-2305, 2004.

[92] T. Scherr, C. Quitadamo, P. Tesvich, D.S.-W. Park, T. Tiersch, D. Hayes, J.-W. Choi, K. Nandakumar, and T. Monroe, "A planar microfluidic mixer based on logarithmic spirals," *Journal of Micromechanics and Microengineering*, vol. 22, no. 5, p. 055019, 2012.

[93] Tsung Sheng Sheu, Sin Jhih Chen, and Jyh Jian Chen, "Mixing of a split and recombine micromixer with tapered curved microchannels," *Chemical Engineering Science*, vol. 71, pp. 321-332, 2012.

[94] A. A. Mouza, C.-M. Patsa, and F. Schönfeld, "Mixing performance of a chaotic micro-mixer," *Chemical Engineering Research and Design*, vol. 86, no. 10, pp. 1128-1134, Oct. 2008.

[95] A. Günther and K. F. Jensen, "Multiphase microfluidics: from flow characteristics to chemical and materials synthesis," *Lab on a Chip*, vol. 6, no. 12, pp. 1487-1503.

[96] H. Song, J. D. Tice, and R. F. Ismagilov, "A microfluidic system for controlling reaction networks in time," *Angewandte Chemie International Edition*, vol. 42, no. 7, pp. 768-772, Feb. 2003.

[97] O. K. Castell, C. J. Allender, and D. A. Barrow, "Continuous molecular enrichment in microfluidic systems," *Lab on a Chip*, vol. 8, no. 7, pp. 1031-3, May 2008.

[98] O. K. Castell, C. J. Allender, and D. A. Barrow, "Liquid–liquid phase separation: characterisation of a novel device capable of separating particle carrying multiphase flows," *Lab on a Chip*, vol. 9, no. 3, pp. 388-96, 2009.

[99] P. Yager, T. Edwards, E. Fu, K. Helton, K. Nelson, M. R. Tam, and B. H. Weigl, "Microfluidic diagnostic technologies for global public health," *Nature*, vol. 442, no. 7101, pp. 412-418, Jul. 2006.

[100] S.-Y. Teh, R. Lin, L.-H. Hung, and A. P. Lee, "Droplet microfluidics," *Lab on a Chip*, vol. 8, no. 2, pp. 198-220.

[101] U. Kaatze, R. Pottel, and A. Wallusch, "A new automated waveguide system for the precise measurement of complex permittivity of low-to-high-loss liquids at microwave frequencies," *Measurement Science and Technology*, vol. 6, no. 8, pp. 1201-1207, Aug. 1995.

[102] J. Mateu, N. Orloff, M. Rinehart, and J. C. Booth, "Broadband permittivity of liquids extracted from transmission line measurements of microfluidic channels," in *IEEE MTT-S International Microwave Symposium Digest*, 2007, pp. 523-526.

[103] Booth, J.C., "private communications," Sep. 2011.

[104] A. Taeb, S. Gigoyan, G. Rafi, S. Safavi-Naeini, and M. Neshat, "A Low Cost and Sensitive Sensor Based on the Whispering Gallery Mode at D-Band," in *Proceedings of the European Microwave Conference*, Manchester, 2011, pp. 619-22.

[105] E. N. Shaforost, N. Klein, S. A. Vitusevich, A. Offenhäusser, and A. A. Barannik, "Nanoliter liquid characterization by open whispering-gallery mode dielectric resonators at millimeter wave frequencies," *Journal of Applied Physics*, vol. 104, p. 074111, 2008.

[106] T. Eriksson, S. Björkman, and P. Höglund, "Clinical pharmacology of thalidomide," *European Journal of Clinical Pharmacology*, vol. 57, no. 5, pp. 365-376, Aug. 2001.

[107] Chiarotti, M. and Fucci, N., "HPLC analysis of cocaine diastereoisomers by chiral stationary phase," *Forensic Science International*, vol. 44, no. 1, pp. 37-41, 1990.

[108] Y. Hayashi, L. Livshits, A. Caduff, and Y. Feldman, "Dielectric spectroscopy study of specific glucose influence on human erythrocyte membranes," *Journal of Physics D: Applied Physics*, vol. 36, no. 4, pp. 369-374, Feb. 2003.

[109] Colella, L, Beyer, C., Fröhlich, J., Talary, M., and Renaud, P., "Microelectrode-based dielectric spectroscopy of glucose effect on erythrocytes," *Bioelectrochemistry*, vol. 85, pp. 14-20, 2012.

[110] K. Kaminski, E. Kaminska, S. Pawlus, P. Wlodarczyk, M. Paluch, J. Ziolo, A. Kasprzycka, W. Szeja, K.L. Ngai, and J. Pilch, "Dielectric properties of two diastereoisomers of the arabinose and their equimolar mixture," *Carbohydrate Research*, vol. 344, no. 18, pp. 2547-53, 2009.

[111] Y. Luk, C.J. Allender, and T. Wirth, "Molecular imprinted polymers binding low functionality templates," *Tetrahedron Letters*, vol. 51, no. 45, pp. 5883-5, 2010.

[112] O. K. Castell, D. A. Barrow, A. R. Kamarudin, and C. J. Allender, "Current practices for describing the performance of molecularly imprinted polymers can be misleading and may be hampering the development of the field," *Journal of Molecular Recognition*, vol. 24, no. 6, pp. 1115-1122, Nov. 2011.

[113] C. J. Allender, O. K. Castell, P. R. Davies, S. Fiddy, J. Hedin-Dahlström, and M. Stockenhuber, "A glimpse of the inner workings of the templated site," *Chemical Communications*, no. 2, pp. 165-167.

[114] B. Sellergren, *Molecularly Imprinted Polymers: Man-Made Mimics of Antibodies and Their Applications in Analytical Chemistry*. Elsevier, 2001.

[115] H. Zhang, T. Piacham, M. Drew, M. Patek, K. Mosbach, and L. Ye, "Molecularly imprinted nanoreactors for regioselective Huisgen 1,3-dipolar cycloaddition reaction," *Journal of the American Chemical Society*, vol. 128, no. 13, pp. 4178-4179, 2006.

[116] Castell, O.K., Allender, C.J., and Barrow, D.A., "Novel biphasic separations utilising highly selective molecularly imprinted polymers as biorecognition solvent extraction agents," *Biosensors and Bioelectronics*, vol. 22, no. 4, pp. 526-533, 2006.

[117] Q. A. Pankhurst, J. Connolly, S. K. Jones, and J. Dobson, "Applications of magnetic nanoparticles in biomedicine," *Journal of Physics D: Applied Physics*, vol. 36, no. 13, p. R167-R181, Jul. 2003.

[118] Gupta, A.K. and Gupta, M., "Synthesis and surface engineering of iron oxide nanoparticles for biomedical applications," *Biomaterials*, vol. 26, no. 18, pp. 3995-4021, 2005.

[119] S. Mornet, S. Vasseur, F. Grasset, and E. Duguet, "Magnetic nanoparticle design for medical diagnosis and therapy," *J. Mater. Chem.*, vol. 14, no. 14, pp. 2161-2175.

[120] Irène Brigger, Catherine Dubernet, and Patrick Couvreur, "Nanoparticles in cancer therapy and diagnosis," *Advanced Drug Delivery Reviews*, vol. 54, no. 5, pp. 631-51, 2002.

[121] S. Sun, "Recent advances in chemical synthesis, self-assembly, and applications of FePt nanoparticles," *Advanced Materials*, vol. 18, no. 4, pp. 393-403, Feb. 2006.

[122] P. C. Fannin, S. W. Charles, and T. Relihan, "On the broadband measurement of the permittivity and magnetic susceptibility of ferrofluids," *Journal of Magnetism and Magnetic Materials*, vol. 167, no. 3, pp. 274-280, Mar. 1997.

[123] Davis, L.E. and Smith, P.A., "Q of a coaxial cavity with a superconducting inner conductor," *IEE Proceedings A*, vol. 138, no. 6, pp. 313-9, 1991.

[124] C. Gao and X.-D. Xiang, "Quantitative microwave near-field microscopy of dielectric properties," *Review of Scientific Instruments*, vol. 69, no. 11, p. 3846, 1998.

[125] Massood Tabib-Azar and Yaqiang Wang, "Design and fabrication of scanning near-field microwave probes compatible with atomic force microscopy to image embedded nanostructures," *Microwave Theory and Techniques, IEEE Transactions on*, vol. 52, no. 3, pp. 971-979, 2004.

[126] W. Saleh and N. Qaddoumi, "Potential of near-field microwave imaging in breast cancer detection utilizing tapered rectangular waveguide probes," *Computers & Electrical Engineering*, vol. 35, no. 4, pp. 587-593, Jul. 2009.

[127] R. Inoue, Y. Odate, E. Tanabe, H. Kitano, and A. Maeda, "Data analysis of the extraction of dielectric properties from insulating substrates utilizing the evanescent perturbation method," *IEEE Transactions on Microwave Theory and Techniques*, vol. 54, no. 2, pp. 522-531, 2006.

[128] D. K. Misra, "Quasi-static analysis of open-ended coaxial lines," *IEEE Transactions on Microwave Theory and Techniques*, vol. 35, no. 10, pp. 925-928, 1987.

[129] J.-H. Kim, B. Enkhbayar, J.-H. Bang, B.-C. Ahn, and E.-J. Cha, "New formula for the reflection coefficient of an open-ended rectangular waveguide with or without an infinite flange," *Progress In Electromagnetics Research M*, vol. 12, pp. 143-153, 2010.

[130] C. Gao, F. Duewer, and X.-D. Xiang, "Quantitative microwave evanescent microscopy," *Applied Physics Letters*, vol. 75, no. 19, pp. 3005-3007, 1999.

[131] A. P. Gregory and R. N. Clarke, "Dielectric metrology with coaxial sensors," *Measurement Science and Technology*, vol. 18, no. 5, pp. 1372-1386, 2007.

[132] V. A. Santarelli, J. A. MacDonald, and C. Pine, "Overlapping dielectric dispersions in toluene," *The Journal of Chemical Physics*, vol. 46, no. 6, pp. 2367-2375, 1967.

[133] S. Schwerdtfeger, F. Köhler, R. Pottel, and U. Kaatze, "Dielectric relaxation of hydrogen bonded liquids: Mixtures of monohydric alcohols with n-alkanes," *Journal of Chemical Physics*, vol. 115, no. 9, pp. 4186-4194, 2001.

[134] T. Sato and R. Buchner, "Dielectric relaxation spectroscopy of 2-propanol–water mixtures," *The Journal of Chemical Physics*, vol. 118, no. 10, pp. 4606-4613, Mar. 2003.

[135] Peyman, A., Gabriel, C., and Grant, C.H., "Complex permittivity of sodium chloride solutions at microwave frequencies," *Bioelectromagnetics*, vol. 28, no. 4, pp. 264-274, 2007.

[136] N. W. Ashcroft and N. D. Mermin, *Solid state physics*. Holt, Rinehart and Winston, 1976.

[137] Bellizzi, G., Bucci, O.M., and Capozzoli, A., "Broadband spectroscopy of the electromagnetic properties of aqueous ferrofluids for biomedical applications," *Journal of Magnetism and Magnetic Materials*, vol. 322, no. 20, pp. 3004-13, 2010.

[138] P. C. Fannin, "Use of ferromagnetic resonance measurements in magnetic fluids," *Journal of Molecular Liquids*, vol. 114, no. 1–3, pp. 79-87, Sep. 2004.

[139] M. Mehdizadeh, T. K. Ishii, J. S. Hyde, and W. Froncisz, "Loop-Gap Resonator: A Lumped Mode Microwave Resonant Structure," *IEEE Transactions on Microwave Theory and Techniques*, vol. 31, no. 12, pp. 1059-1064, Dec. 1983.

[140] M. Mehdizadeh and T. K. Ishii, "Electromagnetic field analysis and calculation of the resonance characteristics of the loop-gap resonator," *IEEE*

Transactions on Microwave Theory and Techniques, vol. 37, no. 7, pp. 1113-1118, Jul. 1989.

[141] W Froncisz and J.S. Hyde, "The loop-gap resonator: a new microwave lumped circuit ESR sample structure," *Journal of Magnetic Resonance (1969)*, vol. 47, no. 3, pp. 515-521, 1982.

[142] W. Piasecki and W. Froncisz, "Field distributions in loop-gap resonators," *Measurement Science and Technology*, vol. 4, no. 12, pp. 1363-1369, Dec. 1993.

[143] W. N. Hardy and L. A. Whitehead, "Split-ring resonator for use in magnetic resonance from 200–2000 MHz," *Review of Scientific Instruments*, vol. 52, no. 2, pp. 213-216, Feb. 1981.

[144] H.-J. Lee, H.-S. Lee, K.-H. Yoo, and J.-G. Yook, "DNA sensing based on single element planar double split-ring resonator," in *Microwave Symposium Digest, 2009. MTT '09. IEEE MTT-S International*, 2009, pp. 1685-1688.

[145] H.-J. Lee, J. H. Lee, H.-S. Moon, Ik-Soon Jang, Jong-Soon Choi, Jong-Gwan Yook, and Hyo-Il Jung, "A planar split-ring resonator-based microwave biosensor for label-free detection of biomolecules," *Sensors and Actuators B: Chemical*, vol. 169, pp. 26-31.

[146] A. Masood, "Microwave resonators for highly sensitive compositional analysis: applications for solvents in microcapillary systems," PhD thesis, Cardiff University, 2010.

[147] K. H. Hong and J. A. Roberts, "Microwave properties of liquids and solids using a resonant microwave cavity as a probe," *Journal of Applied Physics*, vol. 45, no. 6, pp. 2452-2456, Jun. 1974.

[148] G. K. Johri and J. A. Roberts, "Study of the dielectric response of water using a resonant microwave cavity as a probe," *Journal of Physical Chemistry*, vol. 94, no. 19, pp. 7386-7391, 1990.

[149] G. Bellizzi, O. M. Bucci, and I. Catapano, "Microwave Cancer Imaging Exploiting Magnetic Nanoparticles as Contrast Agent," *IEEE Transactions on Biomedical Engineering*, vol. 58, no. 9, pp. 2528-2536, Sep. 2011.

[150] I. Mălăescu and I. Hrianca, "Relaxation processes of magnetite-based ferrofluids in rf magnetic fields," *Journal of Magnetism and Magnetic Materials*, vol. 157–158, no. 0, pp. 585-586, May 1996.

[151] P. Cicmanec, "Cavity perturbation method for measurement of permittivity and conductivity of medium lossy semiconductors and dielectrics," *Solid-State Electronics*, vol. 14, no. 2, pp. 153-166, Feb. 1971.

[152] J. F. Rouleau, J. Goyette, T. K. Bose, and M. F. Frechette, "Performance of a microwave sensor for the precise measurement of water vapor in gases," *IEEE Transactions on Dielectrics and Electrical Insulation*, vol. 7, no. 6, pp. 825-831, 2000.

[153] M.L. Gorodetsky, A.A. Savchenkov, and V.S. Ilchenko, "Ultimate Q of optical microsphere resonators," *Optics Letters*, vol. 21, no. 7, pp. 453-455, 1996.

[154] D.W. Vernooy, V.S. Ilchenko, H. Mabuchi, E.W. Streed, and H.J. Kimble, "High-Q measurements of fused-silica microspheres in the near infrared," *Optics Letters*, vol. 23, no. 4, pp. 247-249, 1998.

[155] C. Gao, F. Duewer, and X.-D. Xiang, "Quantitative microwave evanescent microscopy," *Applied Physics Letters*, vol. 75, no. 19, pp. 3005-3007, Nov. 1999.

[156] D. E. Steinhauer, C. P. Vlahacos, S. K. Dutta, B. J. Feenstra, F. C. Wellstood, and S. M. Anlage, "Quantitative imaging of sheet resistance with a scanning

near-field microwave microscope," *Applied Physics Letters*, vol. 72, no. 7, pp. 861-863, Feb. 1998.

[157] M.C. Dimri,, V.K. Tripathi, S.C. Kashyap, Y.H. Jeong, and D.C. Dube, "Theoretical modeling and experimental verification of the permeability measurements of thick films at microwave frequencies," *IEEE Transactions on Instrumentation and Measurement*, vol. 58, no. 9, pp. 2911-5, 2009.

[158] W. B. Weir, "Automatic measurement of complex dielectric constant and permeability at microwave frequencies," *Proceedings of the IEEE*, vol. 62, no. 1, pp. 33-36, 1974.

[159] S. Jakiela, T.S. Kaminski, O. Cybulski, and P. Gartecki, "Parallel micro-chemostats in an automated droplet microfluidic system," in *Proceedings of MicroTAS*, Seattle, 2011, pp. 2083-5.

[160] J. Naylon, S. Gooding, C. John, A. Morgan, O. Squires, J. Lees, D.A. Barrow, and A. Porch, "Efficient microwave heating and dielectric characterization of microfluidic systems," in *Proceedings of MicroTAS*, Groningen, 2010, pp. 2092-4.

[161] T. Hermann, G.R. Olbrich, and P. Russer,, "A novel system for real-time measurement of the electrical properties of a cavity resonator," in *Proceedings of the European Microwave Conference*, 2008, pp. 67-70.